
THE UNIVERSITY *of* EDINBURGH

This thesis has been submitted in fulfilment of the requirements for a postgraduate degree (e. g. PhD, MPhil, DClinPsychol) at the University of Edinburgh. Please note the following terms and conditions of use:

- This work is protected by copyright and other intellectual property rights, which are retained by the thesis author, unless otherwise stated.
- A copy can be downloaded for personal non-commercial research or study, without prior permission or charge.
- This thesis cannot be reproduced or quoted extensively from without first obtaining permission in writing from the author.
- The content must not be changed in any way or sold commercially in any format or medium without the formal permission of the author.
- When referring to this work, full bibliographic details including the author, title, awarding institution and date of the thesis must be given.

# Interacting active particles and cellular automata: microscopic models of stochastic nonequilibrium systems

Matthew James Metson


Doctor of Philosophy
The University of Edinburgh
2023

# Lay summary

The Universe is a process: it is forever evolving and changing. Equivalently, the Universe may be viewed as a large collection of small processes which continuously feed into and out of each other. In order to gain a feel for this notion, we consider the everyday example of a river. The river is fed by a source, such as a lake, from which water flows downstream. Perhaps it flows gently down a channel before reaching a drop. The flow of water off the drop constitutes a waterfall, and the crashing of water into the pool below creates a stable collection of whirlpools. Thereafter, the river carries on its journey one process at a time, until, eventually, the water flows out into a sink, such as the sea.

In the above description, we see how the river comprises a sequence of processes, where one process feeds into the next one by the flow, or *current*, of water. In fact, it is currents that are the defining feature of *all* processes: in the absence of currents things are static, and static things cannot sensibly be described as processes. For example, a snapshot of the river shows its state at a given point in time, and is therefore not a process. On the other hand, a recording of the river (a series of consecutive snapshots) shows the sequence of states the river moves through, and it is this sequence that allows us to see currents, or a process, unfolding. Rivers aside, other examples of processes include electricity (currents of charge) traffic flow (currents of vehicles), weather systems (currents of air, moisture, and heat), and biological organisms (complex networks of molecular/cellular currents). Even objects which appear to be completely static, such as stones, are in fact processes: the molecules that make up the stone are in a constant state of vibration (molecular currents), and weathering causes the stone's form to morph by the gradual removal of material over long time scales (also molecular currents).

With the above in mind, there are three categories that the Universe's processes fall into. The first category is that of *equilibrium* processes. An example of this is placing a cold block of material in a warm room. After a while, the block warms up to the temperature of the room, at which point equilibrium has been established: the room warms the block at the same rate at which the block leaks warmth back into the room.

The second category is that of the *nonequilibrium stationary state*. We return to the river for an example. Simultaneously, the lake feeds the channel, the channel

feeds the waterfall, the waterfall feeds the whirlpools, and the whirlpools feed the river's remaining processes before it finally drains into the sea. Because of this, the river appears *stationary*: from one second to the next, it is hard to discern any difference in its appearance; the channel, the waterfall and the whirlpools all maintain their physical forms, as does the river in its entirety.

The third category is that of *relaxation* towards equilibrium or nonequilibrium stationary states. The warming-up of the block after it was placed in the room is an example of relaxation towards equilibrium. In the case of the river, suppose a period of heavy rainfall sustains an increase in the lake's water level. This causes the flow rate into the river to increase, and as a consequence the river relaxes to a new nonequilibrium stationary state in which the channel is deeper and the waterfall and whirlpools are more violent.

The second and third categories described above are *nonequilibrium* processes. What's remarkable is that the vast majority of the Universe consists of nonequilibrium processes but, unlike equilibrium – for which physicists have a complete theoretical description – nonequilibrium is poorly understood: no general approach may be applied to an arbitrary nonequilibrium system in order to ascertain its properties. The Universe, therefore, remains a very puzzling place to us.

Given the above, one has to consider nonequilibrium systems on a case-by-case basis in order to understand them. In this thesis, two classes of nonequilibrium system are studied in order to better grasp their behaviours. The first class consists of *active particles* – objects such as animals and bacteria that are capable of moving in a set direction over an extended period of time. Such directed motion is a form of current, and hence active particles are nonequilibrium objects. When multiple active particles interact with each other, striking collective behaviours often emerge; the flocking of birds, schooling of fish, and clustering of bacteria are all examples of this. Two systems comprising *persistent random walkers* – active particles whose motion is inspired by bacteria – are studied in this thesis in an attempt to better understand precisely how collective behaviours such as those stated above are able to emerge.

The second class of system we study is that of *cellular automata*. A cellular automaton is a system which starts in some initial configuration and thereafter evolves in time according to a prescribed set of rules. It is often the case that surprisingly simple rule sets which encode for nonequilibrium behaviours lead to the emergence of complex phenomena. Cellular automata therefore yield insight into how complex forms such as biological organisms are able to emerge from physical laws which describe atoms and molecules. In this thesis, a cellular automaton's rules are modified in order to investigate its emergent properties and how these contrast to those of its predecessor.

# Abstract

The broad focus of this thesis is the statistical physics of nonequilibrium systems – systems which violate the condition of detailed balance. Detailed balance is the property that the probability fluxes between all pairs of states of a system cancel exactly, and is the defining feature of the *equilibrium* stationary state. Nontrivial flux cancellations – which arise as a result of probability currents in a system's state space – are also possible: when this happens, a system is said to be in a *nonequilibrium* stationary state. As a consequence of this increased complexity, establishing a general theory of nonequilibrium systems remains one of physics' great outstanding challenges.

One route to understanding nonequilibrium systems is to consider simplified microscopic models. The benefits to this are twofold: firstly, microscopic models allow us to probe nonequilibrium processes at the most fundamental level; and secondly, by pooling together the results of various such models, we can begin to establish connections between them with a view to extracting general principles.

In this thesis, we will consider two kinds of nonequilibrium system when developing microscopic models. The first kind is active systems. Active systems – those which comprise particles that can execute motion using energy they extract from their environment – are inherently out of equilibrium. In the presence of interactions, active particles often exhibit intriguing emergent behaviours – such as collective motion – which are absent in systems of passive particles. Not only, therefore, do they hold strong scientific interest, but their ubiquity in nature provides a pool of inspiration for physicists from which models may be developed and studied.

The dearth in the literature of $N$-body microscopic models of active systems, where $N \geq 2$, is a major problem if we wish to fundamentally understand how their macroscopic complexity emerges from interactions at the level of individual particles. In this thesis, we shall devote much time to the analysis of microscopic active systems in an attempt to address this. To this end, two models of interacting *persistent random walkers* (PRWs) will be discussed. The PRW is an active particle which moves by executing a series of linear 'runs' at speed $\gamma$ interspersed by random reorientation events,

known as 'tumbles', which occur at rate $\omega$. Interacting PRW systems are of interest in the active-matter community as they are often inspired by and have applications to bacterial motion.

The first model consists of a dilute gas of excluding PRWs in an arbitrary number of dimensions. The *jamming probability* – the probability of finding a pair of adjacent PRWs mutually blocking each other – is derived via a first-passage approach in order to investigate the nature of multiparticle clustering. This yields the surprising result of a vanishing critical density for clustering in the model's thermodynamic limit.

The second PRW model generalises the exclusion interaction to an active *recoil* interaction, whereby PRWs are instantaneously displaced upon contact according to an arbitrary distribution. The nonequilibrium stationary states of a one-dimensional two-PRW system featuring recoils are derived exactly using a generating-function approach, revealing a variety of rich behaviours. These include *reentrant* states, for which an effective attraction exists between the walkers within a finite range of tumble rates but is otherwise repulsive, as well as highly nontrivial boundary behaviours, for which a novel technique was developed in order for an exact characterisation to be established.

The second kind of nonequilibrium system we shall consider is the cellular automaton (CA). A CA consists of a lattice whose sites are associated with a discrete variable. For all sites, this variable is updated in discrete time steps according to a prescribed function whose input is the site's local environment. Thus, given some initial configuration, the CA evolves through a deterministic trajectory of configurations. Engineering the update function to enforce broken detailed balance allows for the possibility of complex emergent phenomena. The CA, therefore, constitutes an alternative approach for the nonequilibrium physicist regarding the examination of emergent complexity from microscopic rules for which detailed balance does not hold.

In the final chapter of this thesis, a one-dimensional CA of binary variables is modified such that two of its eight possible update rules are made stochastic. We then assess the changes this effects on the state space via simulations, revealing a pattern in the configurational structure of each sector (subspace). From this we establish a lower bound on the number of sectors of the model; we find that this lower bound is related to the Fibonacci numbers and asymptotically grows as $(\sqrt[4]{\phi})^L$, where $\phi$ is the golden ratio and $L$ is system size. This growth rate, it turns out, is substantially slower than the stochastic automaton's deterministic predecessor.

Taking together the above-described models and the results we derive from them, it is hoped that this thesis constitutes a small step forward in our understanding of nonequilibrium systems.

# Declaration

I declare that this thesis was composed by myself, that the work contained herein is my own except where explicitly stated otherwise in the text, and that this work has not been submitted for any other degree or professional qualification except as specified.

Parts of this work have been published in [1–3].

(*Matthew James Metson, 2023*)

# Acknowledgements

First and foremost, I would like to thank my principal supervisor, Richard Blythe, and my second supervisor, Martin Evans, for the invaluable guidance you have given me throughout the last five years. It has been the utmost pleasure working with you both.

I would like also to thank the wider School, right the way down from the many students I have taught, to all the wonderful PhD students who I have shared this experience with, to all those who have taught and assisted me with PhD life (academic or otherwise), and to those steering the helm at the top. I could not have asked for a better environment to carry out my research. Additionally, I would like to thank the Postgraduates in Physics & Astronomy Society for bringing together what is a wonderful community of PhD students, and for leaving me with memories that I will forever cherish. We bounced back so strongly after the pandemic and I hope future cohorts can keep the ball rolling.

Thank you to all those with whom I shared the legendary call centre. It's been an absolute blast.

Thank you to the Scottish Centre for Doctoral Training in Condensed Matter Physics for providing me with so much opportunity. I would like to thank Chris Hooley, Debra Thompson, and Julie Massey in particular for providing help and support when needed, as well as for making things run so smoothly through what have been bizarre and difficult times.

Thank you to the brilliant people who made my first year in Roxburgh Place so much fun.

Thank you to the many amazing people I have been fortunate enough to meet and share experiences with at the various schools, conferences, and workshops I have attended during my studies.

I am grateful for Holyrood Park, the Pentland Hills, and the Innocent Railway Tunnel for providing me with space to think, as well as so much more.

I am grateful to The Everest restaurant for providing heaps and heaps of delicious curry throughout the pandemic and beyond.

I am grateful to the Auld Hoose for supplying me with much needed Plum Porter.

I am grateful to King Gizzard and the Lizard Wizard, whose music accompanied me through much of the writing process.

Thank you to Viktor Škultéty for much stimulating and useful discussion, as well as for being an icon to me throughout this experience.

Thank you to Jenny Harnett for being enduringly patient with me throughout the writing process. Thank you also for the many lovely moments we have shared since we met.

Thank you to Rory Claydon and Hector Leong for sharing the PhD experience with me so closely. We have grown so much together.

I would also like to thank my parents, Tracey and Keith, as well as my siblings, Jake, Toby and Albertina. Your company, especially at Christmas, brings me so much. Finally, I am immeasurably grateful for Tracey and Keith, who raised and supported me in a way that has allowed me to prosper. This document would not exist otherwise.

# Contents

# List of Figures

# List of Tables

# Chapter 1

# Introduction: nonequilibrium statistical mechanics; stochastic processes; and active matter

A general theory of nonequilibrium statistical mechanics remains as one of modern physics' great outstanding challenges. Treatment of the equilibrium case began as far back as 1860 [4, 5], when Maxwell published his seminal works on the dynamical theory of gases in which the first derivation of the Maxwell-Boltzmann distribution for the speeds of ideal gas particles at thermodynamic equilibrium was given. Boltzmann further developed these ideas later that decade [6] when he presented the first description of the celebrated Boltzmann distribution for a general system in equilibrium. Given a system in thermal equilibrium with a heat bath at temperature $T$, the probability of finding the system in some configuration $\mathcal{C}$ with associated energy $E(\mathcal{C})$ is

$$P(\mathcal{C}) = \frac{1}{Z} \mathrm{e}^{-\frac{E(\mathcal{C})}{k_B T}}, \tag{1.0.1}$$

where $Z$, the partition function, is the normalisation

$$Z = \sum_{\mathcal{C}} \mathrm{e}^{-\frac{E(\mathcal{C})}{k_B T}}, \tag{1.0.2}$$

and where $k_B$, the Boltzmann constant, defines the energy scale. This theory has been highly successful at predicting the properties of systems at equilibrium. By facilitating a microscopic description of classical thermodynamics [7–9], this

theoretical framework has provided us deeper insights into many fields of physics. In particular, the theory of phase transitions developed in the 20th century provides an accurate description of the transitions between different states of matter, made possible by mathematical techniques such as Ginzburg-Landau theory and the renormalisation group [10, 11]. Beyond condensed matter [10, 12, 13], these ideas have usefully been applied in other fields of physics, such as astrophysics [14] and particle physics [15]. Remarkably, the framework of equilibrium statistical mechanics is so powerful that it has found applications in areas such as machine learning [16, 17], linguistics [18] and economics [19], which lie outwith the domain of physics entirely.

Despite these successes, statistical mechanics is mostly incomplete. This is because, as we shall see, equilibrium is not the norm; most physical systems are, in fact, *out of* equilibrium. Examples from day-to-day life include electronic circuits, motor vehicles, weather systems, biological organisms and ecosystems. Generally speaking, nonequilibrium systems are more complex than those of equilibrium, since irreversible energy exchange with the environment (in contrast with equilibrium systems, where energy exchange is reversible) allows for nontrivial probability currents in the system's state space to become established (we shall see this more rigorously in the sections that follow). Thus, a nonequilibrium generalisation of the Boltzmann distribution, if found, would constitute an enormous leap forward in understanding.

With a general description of nonequilibrium statistical mechanics currently out of reach, alternative approaches to understanding nonequilibrium systems must be taken. One approach is to study and solve microscopic models of such systems [20–23]. This has the benefit that if a solution is found, we gain access to a fundamental understanding of the properties of the system under study, and how or whether said properties are a consequence of being out of equilibrium. By pooling together the results of such studies, we can begin to identify common features amongst them, thus giving us clues as to what general principles might underpin them.

One of the first major examples of the above-described approach was the solution of the totally asymmetric simple exclusion process (TASEP) with open boundaries [24–26]. This may be regarded as a nonequilibrium analogue of the Ising model in that it constitutes a simple model whose solution requires what are now considered standard techniques of the field. Briefly, the TASEP as studied in [24–26] comprises a one-dimensional lattice with a reservoir that injects particles

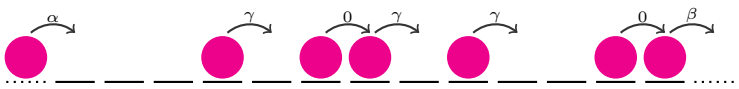


**Figure 1.1** *The dynamics of the open-boundary TASEP, where solid lines represent lattice sites and where dotted lines represent reservoirs. Particles hop to their right adjacent site given that it is unoccupied, and are blocked otherwise. In the former case, particles enter from the left reservoir at rate $\alpha$, enter the right reservoir at rate $\beta$, and otherwise hop with rate $\gamma$. The third-from-left particle and the second-from-right particle are blocked, shown as rate* 0*.*

at rate $\alpha$ at one end (given that the receiving site is empty) and a reservoir that absorbs particles with rate $\beta$ at the other end. Hops are only allowed to the nearest neighbour in the direction of the absorbing reservoir (again, given that the receiving site is empty); such hops occur at rate $\gamma$. The dynamics is sketched out in fig. 1.1. Since the reception and absorption of particles at each end is an irreversible process, the TASEP is out of equilibrium.

Using matrix-product methods [27], it is possible to derive all configurational probabilities of the TASEP. We shall explore these ideas more thoroughly later but, briefly, this works as follows. One supposes that the configurational probabilities of the system may be expressed in terms of a product of matrices, where the $i$th matrix is chosen to reflect the occupancy of site $i$. In the case of open boundaries, an inner product is then taken to give the associated probability. The matrices are chosen to enforce a *cancellation mechanism* which reflects how probability flows through the system. Once this has been established, the nonequilibrium partition function may be computed as a normalisation factor (in the same way as eq. (1.0.2) was for the case of equilibrium), from which the system's macroscopic properties can be derived. The resultant phase diagram is shown in fig. 1.2.

The impacts of the above work were manifold. Despite the simplicity of the model, the solution revealed a rich phase diagram, illustrating how complex behaviours can arise out of simple rules in nonequilibrium systems. In addition to this, these results demonstrated the feasibility of tackling nonequilibrium lattice models analytically, triggering a field of research that remains active to the present day.

In this thesis, we take the model-based approach to probing nonequilibrium systems described in the preceding paragraphs. Much like the TASEP, our focus will also be lattice-based models. To set the stage for this, we will give a brief

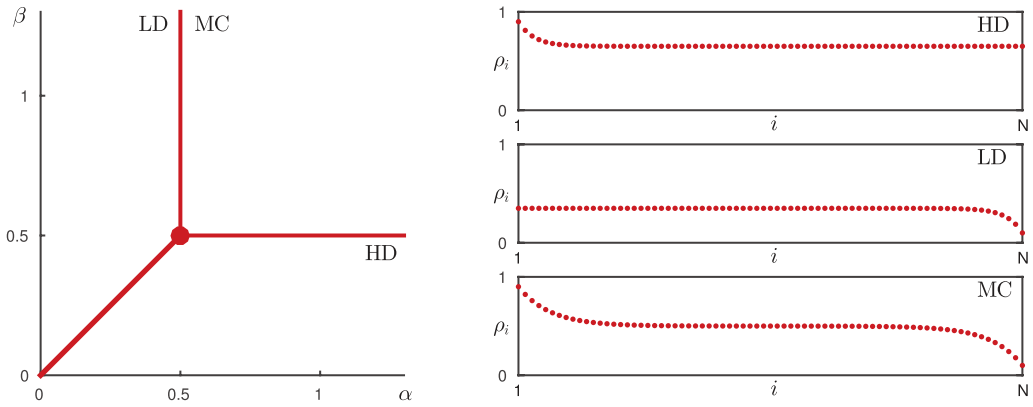


**Figure 1.2** *(Reproduced from [28].) The left panel shows the TASEP phase diagram for different rates $\alpha$ and $\beta$ as measured in units of the hop rate, that is, we have set $\gamma = 1$. We see a rich structure comprising a low-density (LD) phase, a high-density (HD) phase, and a maximum-current (MC) phase. The right panel shows the density profiles through the system in each of the three phases, where $\rho_i$ is the mean occupation number at site $i$.*

introduction to nonequilibrium statistical mechanics in section 1.1, and, at an intuitive level, what it means for a system to be out of equilibrium. We will then move on to section 1.2, where we will introduce *stochastic processes* and *master equations*. These are central concepts to the models studied in this thesis, and will allow us to develop the notion of nonequilibrium more rigorously. Next, in section 1.3, we will look at areas of application for these ideas; in particular, those of *active matter* and *cellular automata*, the categories under which the models investigated in this thesis fall. Finally, we will outline the structure of the remainder of this thesis in section 1.5.

## 1.1 Nonequilibrium statistical mechanics

We will proceed with this introduction by familiarising the reader with the fundamentals of nonequilibrium statistical mechanics [29, 30]. To do this, it is best to think about any arbitrary system in terms of its *state space* – the set of all states of the system. We will then introduce *stochastic processes*, which feature in all of the models examined in this thesis. In combination with what we know about state spaces, this will allow us to develop mathematical techniques for solving nonequilibrium models, with a particular emphasis on *master equations*. These ideas are central to the works featured in this thesis and it is hoped,

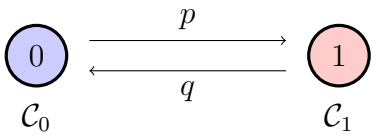


**Figure 1.3** *The state space of a bit. In continuous time, $p$ and $q$ are the transition rates – the transition probabilities per unit time – between the two states $\mathcal{C}_0$ and $\mathcal{C}_1$, whilst in discrete time, $p$ and $q$ are transition probabilities (where $1-p$ and $1-q$ are the self-transition probabilities).*

therefore, that this section will stand the reader in good stead for what is to come.

### 1.1.1 State spaces

As mentioned above, we must begin with the notion of a *state space* in order to gain a fundamental understanding of what it means to be out of equilibrium. A state space is the set of all states, or configurations, as well as the set of possible transitions between them, of a system. (The terms 'state' and 'configuration' will hereon be used interchangeably.) Each state is specified by its unique combination of state variables. A very simple example of a state space is that of a bit, whose values can be 0 or 1. The states that comprise the state space in this case are simply $\mathcal{C}_0$ and $\mathcal{C}_1$, where the subscripts refer to the value the bit can take. This setup, along with the possible transitions between the states, is shown schematically in fig. 1.3.

To understand state spaces more deeply, we consider a more complex example in fig. 1.4. The arrows show the allowed transitions between states; specifically, if there exists a sequence of transitions to state $\mathcal{C}'$ starting from state $\mathcal{C}$, then $\mathcal{C}$ is said to *communicate* with $\mathcal{C}'$. The states/configurations of the system then fall into two categories. The first such category is that of *transient* configurations: a configuration $\mathcal{C}'$ is transient if it communicates with $\mathcal{C}$ when $\mathcal{C}$ does not communicate with $\mathcal{C}'$ such that $\mathcal{C}'$ can never be returned to. All states in subsets $A$ and $C$ of the figure are transient since none of the states in subset $B$ communicate with them. This leads us onto our second category, known as *recurrent* configurations, which comprise all other configurations. All states in subset $B$ of the figure are recurrent since all such states can be accessed from each other, i.e. they all communicate.

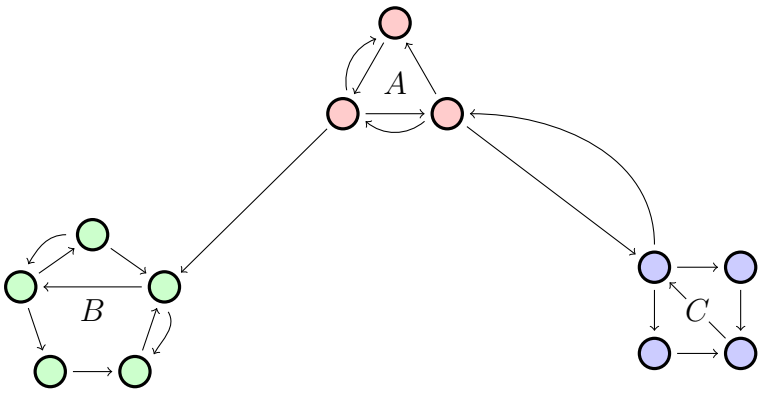


**Figure 1.4** *An example of an arbitrary state space featuring both transient and recurrent configurations. Configurations and possible transitions are depicted as coloured circles and arrows, respectively. In this example, the configurations in subsets A and C are transient since the system always relaxes to the recurrent configurations of subset B, irrespective of its initial condition.*

The nature of the system's state space is crucial to understanding the evolution of the system from some initial condition. We know from the above arguments that the state space depicted in fig. 1.4 guarantees that the associated system relaxes to subset $B$ in the limit of infinite time. The endpoint of such a relaxation – where all configurations are recurrent – is known as *stationarity*, the *stationary state*, or the *steady state*. (These three terms will be used interchangeably throughout this thesis.) Stationarity is characterised by a time-independent probability distribution over the recurrent configurations, the details of which depend on the transition rates. As an example, we return to the bit depicted in fig. 1.3. Clearly, both configurations are recurrent. Working in continuous time such that $p$ and $q$ are rates, we see that the mean time spent in $\mathcal{C}_0$ is $\frac{1}{p}$ and that the mean time spent in $\mathcal{C}_1$ is $\frac{1}{q}$. It follows, therefore, that the stationary distribution is $P(\mathcal{C}_0) = \frac{q}{p+q}$ and $P(\mathcal{C}_1) = \frac{p}{p+q}$, as intuition dictates.

Sometimes there are multiple disjoint subsets of the state space, each of whose member configurations are recurrent; we shall refer to such subsets interchangeably as *subsapces* or *sectors* in this thesis[1]. In such cases, stationarity can depend on the initial conditions. This is demonstrated in fig. 1.5. Starting from subset $P$, it is only possible to relax to stationarity in subset $R$; however, starting from subset $Q$, it is possible for the system to relax to either of subsets $S$ or $T$. By our above definition, subsets R, S and T are subspaces/sectors. We note that subspace $R$ features a single cycle of transitions through its member

[1]To be completely clear, the more general term 'subset' refers to any arbitrary set of states.

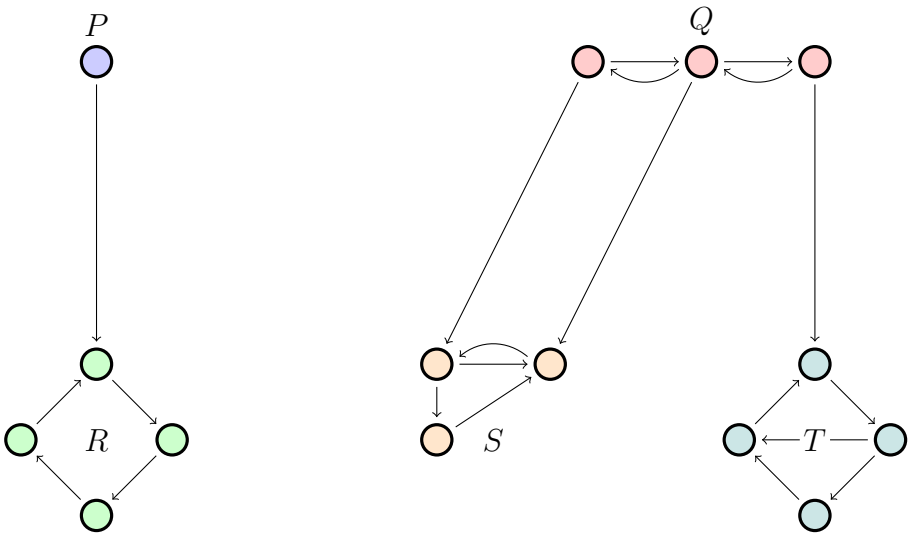


**Figure 1.5** *A second example of a state space, this time featuring disjoint subspaces and periodic behaviour. Configurations and possible transitions are depicted as coloured circles and arrows, respectively. In this example, the initial configuration of the system determines which subspaces the system is able to relax into: if initiated in subset $P$, then the system must relax into subspace $R$; and if initiated in subset $Q$, then relaxation into either of subspaces $S$ and $T$ is possible. We note also the periodic set of transitions in subspace $R$.*

configurations. In discrete time, this is known as *periodic* behaviour. This is different from the behaviours seen in subspaces $S$ and $T$, for in the former case the time evolution is predictable, whilst in the latter two cases it is impossible to say with certainty which configuration the system will be in at some arbitrary time.

### 1.1.2 The defining features of nonequilibrium systems

We now move onto what defines a nonequilibrium system. Specifically, the question we are asking is 'In relation to state spaces, what characterises a system that is out of equilibrium?'. It turns out that it is much easier to ask the reverse question: 'What characterises a system *in* equilibrium?'. We will see why in what follows.

As we saw above, the nature of the stationary state of a system depends on the transition rates. This is particularly important when it comes to equilibrium systems: a system is said to be in equilibrium if it is stationary such that the probability fluxes between all pairs of configurations cancel exactly. This

condition is known as *detailed balance*, and it may be shown that, if satisfied, the system obeys the Boltzmann distribution given in eq. (1.0.1) [31]. We will develop these ideas more rigorously in the next section. For now, however, we will give an intuitive feel for these notions.

Consider the bit in fig. 1.3 once more. To reiterate, stationarity is reached when the probabilities of finding each configuration are the same at all future times. This implies that the stationary probability flux between the two configurations of the bit must cancel exactly, and thus that the system is at equilibrium. (In the situation where the fluxes do not cancel there must be a flow of probability, and hence the bit is not yet stationary.) In fact, equilibrium is a necessary consequence of stationarity when there are precisely two configurations (there is no way other than pairwise balance for stationarity to be achieved). The introduction of a third recurrent configuration, however, allows for probability currents in the stationary state, and therefore for an absence of detailed balance. It is instructive to consider a ternary bit, or trit, whose possible values are 0, 1 and 2; an example state space of a trit is shown in fig. 1.6. We see that a stationary state can be achieved here without detailed balance. As long as the flux into $\mathcal{C}_1$ from $\mathcal{C}_0$ is equal to the flux exiting $\mathcal{C}_1$ into $\mathcal{C}_2$, and as long as both cyclic permutations of the previous statement also hold, then the state will be stationary. Thus, we have demonstrated that it is possible to achieve a stationary state *without* detailed balance; such a system is said to be *out of* equilibrium. The precise nature of the stationary state in this example (i.e. the probability distribution of configurations $\mathcal{C}_0$, $\mathcal{C}_1$ and $\mathcal{C}_2$) depends on the values of the transition rates $p$, $q$ and $r$. We remark finally of the contrast between the bit and the trit presented here regarding time-reversal symmetry: since the trit exhibits a net direction of flux – a current – it does *not* exhibit time-reversal symmetry; systems that fulfil detailed balance, such as the bit, exhibit no currents, and hence are time-reversible. This distinction is extremely important.

A more general feel for how equilibrium and nonequilibrium stationary states differ can be gained by looking at the examples given in fig. 1.7. Figure 1.7a shows an equilibrium state, where detailed balance follows from the symmetries of the system. Figure 1.7b, on the other hand, depicts a nonequilibrium state. This can be seen by identifying, for example, the absence of a reverse transition from bottom-right to top-left; this tells us immediately that detailed balance has been violated. As we did with the trit, we note how loops of time-irreversible probability current can arise due to the set of allowed transitions.

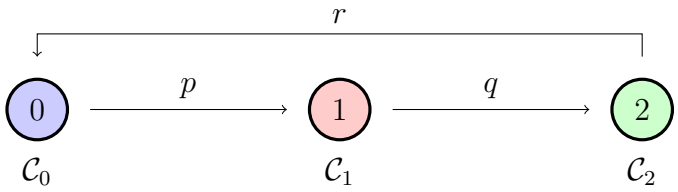


**Figure 1.6** *An example state space of a trit, analogous to that of the bit in fig. 1.3. One sees in this example that stationarity can be achieved by a probability current through the configurations – made possible by the presence of more than two recurrent states. Like all nonequilibrium systems, this means it breaks time-reversal symmmetry.*

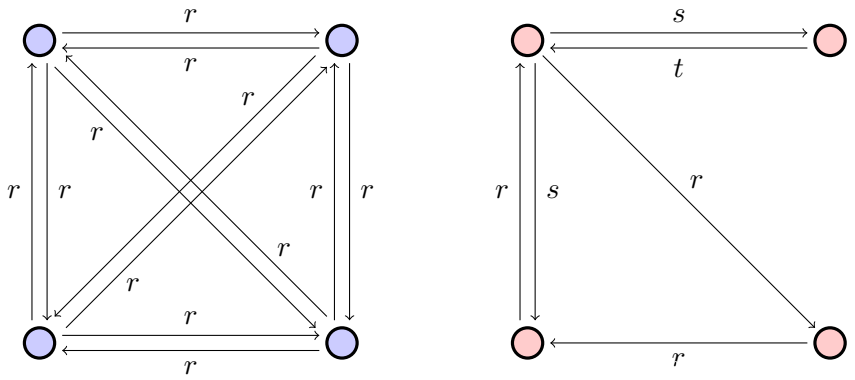


**(a)** *An equilibrium stationary state.*

**(b)** *A nonequilibrium stationary state.*

**Figure 1.7** *Two examples of stationary states, where coloured circles represent configurations and possible transitions are shown as arrows labelled with rates. By rotational invariance, each configuration in fig. 1.7a is equiprobable and, given that all rates are identical, we conclude that all fluxes must balance pairwise. The stationary state in fig. 1.7a thus satisfies detailed balance and is one of equilibrium. The same cannot be said for fig. 1.7b, since detailed balance is violated: for example, there is a transition from top-left to bottom-right, but there is no transition in the reverse direction. The stationary state in fig. 1.7b is therefore out of equilibrium.*

In reality, the system under study will likely be significantly more complex than the examples given in this introduction. If a system has $N_C$ possible configurations, the total number of possible transitions in the system is $\mathcal{O}(N_C^2)$. For increasing $N_C$, therefore, one sees how rapidly the state space complexifies. This gives us a feel for how exceptional equilibrium stationary states are in the context of all possible stationary states, for only special choices of the transition rates give rise to detailed balance.

Before rounding off this section, we note that the description of nonequilibrium systems given above is incomplete. The relaxation process of a system to any stationary state, equilibrium or nonequilibrium, is also a nonequilibrium process, since detailed balance is absent (and any kind of flux balance, for that matter). Relaxation will not concern us in this thesis, for we will look exclusively at steady-state dynamics.

## 1.2 Stochastic processes

### 1.2.1 Definitions and examples

Stochasticity is an imperative feature of nonequilibrium models. It is therefore paramount that we give an introduction to this concept. The information in this section can be found in [31–34].

We start with the definition of a stochastic process. Let $X$ be an arbitrary random variable. A stochastic process is then defined as a sequence of outputs of $X$, $(X_{t_1}, ..., X_{t_N})$, where $t_i$ for $i = 1, ..., N$ serves as an index. In discrete-time processes, $t_i$ indexes the $i$th time step of the process. For example, assigning the output of a fair coin flip as 1 for heads and as $-1$ for tails, the first 10 coin flips might constitute the stochastic process $(-1, -1, 1, -1, 1, -1, 1, 1, 1, -1)$, where the $i$th position in this sequence corresponds to the $i$th coin flip, or time step. In a continuous-time process, $t_i$ is a continuous value on the real number line. Finally, a stochastic process is said to be *Markovian* or a *Markov process* if $X_{t_{i+1}}$ depends only on $X_{t_i}$ – i.e., all that is necessary to predict the future state is knowledge of the current state; knowledge of the history that led to the current state is not required. All stochastic processes considered in this thesis are Markov processes.

Stochastic processes occur ubiquitously in physics, and as such physicists have developed numerous tools and techniques for their study. A well-known application of stochastic processes to physics is the Langevin formulation of Brownian motion [35], wherein the thermal fluctuations of a fluid's constituent particles exert forces on a larger particle immersed in the fluid, thereby causing random motion of the latter. One can write down Newton's second law for the large particle as

$$m\frac{\mathrm{d}\boldsymbol{v}}{\mathrm{d}t} = -\gamma\boldsymbol{v} + \boldsymbol{\eta}(t), \tag{1.2.1}$$

where the first term on the right-hand side models viscous drag and, importantly, the second term is a continuous-time zero-mean stochastic process which models the random forces exerted by the immersing fluid's constituent particles.

Whilst the above equation was simple to write down, its analytical solution would necessarily be parametrised by $\boldsymbol{\eta}(t)$. For general Langevin equations, it is rare to find such solutions. An alternative to the Langevin approach is to instead consider the probability distribution of $\boldsymbol{v}$, $P(\boldsymbol{v}(t), t)$. This is known as the Fokker-Planck approach and, given a Langevin equation, there exists a procedure for finding a partial differential equation for the time evolution of $P(\boldsymbol{v}(t), t)$ [30]. The Fokker-Planck approach is generally more convenient from an analytical point of view, but there are subtleties to consider regarding the nature of the noise. Specifically, integrals over stochastic processes depend on where in the interval $[t, t + \mathrm{d}t]$ the noise $\eta(t)$ is evaluated. When the coefficient of the noise in the Langevin equation is a function of the dependent variable – known as multiplicative noise – this distinction becomes important, for it changes the form of the associated Fokker-Planck equation. This is sometimes known as the Itô-Stratonovich dilemma, and has the drawback that the correct choice for evaluation is not always obvious. In the converse case, where the coefficient of the noise term is *not* a function of the dependent variable – known as additive noise – this is no longer a problem. An extended technical discussion can be found in [36].

Ultimately, the problems that arise in the above approaches stem from phenomenologically inserting noise to approximate large numbers of events, such as the collisions described in the example of Brownian motion. One has to be wary that this might fail to capture all of the necessary physics. One way to circumvent this is to consider all events individually, thus enabling us to encode correct physics at a fundamental level. This is the approach taken with *master equations*, which we devote the next section to. For now, we remark that the drawback to using master equations is that it usually entails a large increase in complexity, since the

details of all individual particles must be kept track of. Owing to the absence of ambiguity, however, this approach is invaluable.

### 1.2.2 Master equations

Central to this thesis are *master equations*. As noted above, master equations are a tool, amongst others, for describing the time evolution of stochastic phenomena. Specifically, master equations describe the time evolution of the *probabilities* of the possible configurations of a stochastic system in terms of the probabilities of all other system configurations and the transition rates between said configurations. Mathematically, given some configuration, $\mathcal{C}$, and its associated probability at time $t$, $P(\mathcal{C}, t)$, the time evolution of the latter is given by

$$\frac{\mathrm{d}P(\mathcal{C}, t)}{\mathrm{d}t} = \sum_{\mathcal{C}' \neq \mathcal{C}} [W(\mathcal{C}' \to \mathcal{C})P(\mathcal{C}', t) - W(\mathcal{C} \to \mathcal{C}')P(\mathcal{C}, t)], \tag{1.2.2}$$

where, for example, $W(\mathcal{C} \to \mathcal{C}')$ is the transition rate from configuration $\mathcal{C}$ to configuration $\mathcal{C}'$. As a reminder, by transition rate we mean the probability per unit time of a transition occurring. This form of the master equation applies in continuous time, and a rigorous derivation of it can be found in [34], for example. Intuitively, eq. (1.2.2) can be understood as follows: the rate of change of $P(\mathcal{C}, t)$ is equal to the rate of entering $\mathcal{C}$ from all other configurations (the $W(\mathcal{C}' \to \mathcal{C})P(\mathcal{C}', t)$ terms) minus the rate of entering all other configurations from $\mathcal{C}$ (the $W(\mathcal{C} \to \mathcal{C}')P(\mathcal{C}, t)$ terms). We remark that no reference is made to the history of the system in eq. (1.2.2) since the rates depend only on the two configurations involved in the corresponding transitions. Equation (1.2.2) only applies, therefore, to Markov processes.

In discrete time, the analogous master equation reads

$$P(\mathcal{C}, t+1) - P(\mathcal{C}, t) = \sum_{\mathcal{C}' \neq \mathcal{C}} [M(\mathcal{C}' \to \mathcal{C})P(\mathcal{C}', t) - M(\mathcal{C} \to \mathcal{C}')P(\mathcal{C}, t)], \tag{1.2.3}$$

where the time step has been scaled to $\Delta t = 1$ and where, for example, $M(\mathcal{C} \to \mathcal{C}')$ is the transition probability from configuration $\mathcal{C}$ to configuration $\mathcal{C}'$.[2] Note that one can include self-transitions $\mathcal{C} \to \mathcal{C}$ in the above sum (which are perfectly

[2]Dividing both sides of the discrete master equation by an arbitrary $\Delta t$ and subsequently taking $\Delta t \to 0$ recovers eq. (1.2.2).

legitimate in discrete time), but since such terms would cancel we need not bother.

For continuous-time processes, an alternative and commonly used master-equation formalism is known as the 'quantum Hamiltonian formalism' [27, 37], so called because the master equation takes a form reminiscent of the Schrödinger equation:

$$\frac{\mathrm{d}}{\mathrm{d}t}\left|P(t)\right\rangle = -H\left|P(t)\right\rangle . \tag{1.2.4}$$

To see where this comes from, and precisely what is meant by $|P(t)\rangle$ and $H$, we note that, for example, $\sum_{\mathcal{C}'\neq\mathcal{C}} W(\mathcal{C}'\to\mathcal{C})P(\mathcal{C}',t)$ may be recast as a matrix equation by indexing each configuration. Indexing configurations $\mathcal{C}$ with $i$ and indexing configurations $\mathcal{C}$' with $j$ allows us to re-express eq. (1.2.2) as

$$\begin{aligned}\frac{\mathrm{d}P_i(t)}{\mathrm{d}t} &= \sum_{j\neq i}[W_{ij}P_j(t) - W_{ji}P_i(t)] \\ &= \sum_{j\neq i} W_{ij}P_j(t) - \left[\sum_{j\neq i} W_{ji}\right] P_i(t) \\ &= -\sum_j H_{ij}P_j(t),\end{aligned} \tag{1.2.5}$$

where

$$H_{ij} = \begin{cases} -W_{ij} & i\neq j \\ \sum_{j\neq i} W_{ji} & i=j \end{cases} . \tag{1.2.6}$$

Inserting the identity operator into eq. (1.2.4) and projecting onto state $i$ as

$$\frac{\mathrm{d}}{\mathrm{d}t}\left\langle i|P(t)\right\rangle = -\sum_j \left\langle i\right| H \left|j\right\rangle \left\langle j|P(t)\right\rangle \tag{1.2.7}$$

recovers the form seen in eq. (1.2.5). Thus, eq. (1.2.2) may be recast as eq. (1.2.4) when the off-diagonal elements $H_{ij} = H_{\mathcal{C}\mathcal{C}'}$ are the negated transition rates $-W_{ij} = -W(\mathcal{C}'\to\mathcal{C})$ and when the diagonal elements $H_{ii} = H_{\mathcal{C}\mathcal{C}}$ are the total rate out of $\mathcal{C}$, $\sum_{j\neq i} W_{ji} = \sum_{\mathcal{C}'\neq\mathcal{C}} W(\mathcal{C}\to\mathcal{C}')$. The matrix $H_{ij}$ comprising the above elements is commonly referred to as the *Markov matrix*. In the present formalism, it is often known simply as the Hamiltonian.

The similarities between stochastic processes and quantum systems is much-studied. In particular, it can be shown that exact mappings exist between lattice-based models of classical particles and quantum-spin-chain models [37]. One example of this is the symmetric simple exclusion process, whose Hamiltonian $H$ has an isomorphic structure to the spin-$\frac{1}{2}$ Heisenberg model [37]. Such

mappings are useful as they enable us to use long-established techniques from quantum mechanics to solve lattice-based models of stochastic processes. There are some caveats, however, in that the Hamiltonians of stochastic systems need not have the same structure as those for quantum systems; the columns of $H$, for example, necessarily sum to zero for stochastic systems due to the conservation of probability. We see this via

$$\begin{aligned} 0 &= \frac{\mathrm{d}}{\mathrm{d}t}\left(\sum_i P_i(t)\right) \\ &= -\sum_i \sum_j H_{ij} P_j(t) \\ &= -\sum_j \left(\sum_i H_{ij}\right) P_j(t). \end{aligned} \tag{1.2.8}$$

Since $\{P_j(t)\}$ is arbitrary, we conclude that $\sum_i H_{ij} = 0$. Conversely, $H$ is Hermitian in quantum mechanics, but no such constraint on its columns is necessary. Furthermore, the elements of $|P(t)\rangle$ are such that $0 \leq P_i(t) \leq 1$ in the stochastic case, but the corresponding requirement in quantum mechanics is $0 \leq |P_i(t)|^2 \leq 1$, since the elements correspond not to probabilities, but to probability amplitudes.

Some consideration has to be made for subtleties such as the above. An extended account is given in [37].

### Solving the continuous-time master equation and finding stationary states

A solution to the master equation is best sought using the quantum Hamiltonian formalism. Assuming no Jordan blocks, the solution to eq. (1.2.4) is

$$|P(t)\rangle = \sum_n a_n \mathrm{e}^{-\lambda_n t} |n\rangle \,, \tag{1.2.9}$$

where $\{|n\rangle\}$ is the set of eigenvectors of the Hamiltonian with corresponding eigenvalues $\{\lambda_n\}$, and where $\{a_n\}$ is a set of constants to be determined by initial conditions. It can be shown that the real parts of $\{\lambda_n\}$ are always positive or zero by the Perron-Frobenius theorem [38], with any zero eigenvalues corresponding to stationary states whose contributions are the only ones that survive in the limit $t \to \infty$. If there are multiple zero eigenvalues, the stationary state is determined by the initial conditions – as discussed previously. If we wish only to find the

stationary state of a system and not the full system dynamics, it is simplest to solve eq. (1.2.2) or eq. (1.2.4) with a vanishing left-hand side.

In order to gain a better feel for master equations, we will look at an example system. The simplest stochastic system we can investigate is the bit, since there are only two states. Physically, the states of the bit could represent the spin-up and spin-down states of a spin-$\frac{1}{2}$ fermion. In the quantum Hamiltonian formalism, the master equation for the bit reads

$$\frac{\mathrm{d}}{\mathrm{d}t}\begin{pmatrix} P_0(t) \\ P_1(t) \end{pmatrix} = -\begin{pmatrix} +T_{10} & -T_{01} \\ -T_{10} & +T_{01} \end{pmatrix}\begin{pmatrix} P_0(t) \\ P_1(t) \end{pmatrix}, \tag{1.2.10}$$

where, for example, $T_{10}$ is the transition rate to state 1 from state 0. As described, we must find the eigenvectors and eigenvalues of the above matrix. The characteristic equation reads

$$\lambda[\lambda - (T_{01} + T_{10})] = 0, \tag{1.2.11}$$

and hence the eigenvalues are

$$\lambda_0 = 0 \qquad \text{and} \qquad \lambda_1 = T_{01} + T_{10}. \tag{1.2.12}$$

The associated right eigenvectors are

$$|\psi_0\rangle = \begin{pmatrix} T_{01} \\ T_{10} \end{pmatrix} \qquad \text{and} \qquad |\psi_1\rangle = \begin{pmatrix} 1 \\ -1 \end{pmatrix}, \tag{1.2.13}$$

respectively. The general solution is thus

$$\begin{pmatrix} P_0(t) \\ P_1(t) \end{pmatrix} = a_0\begin{pmatrix} T_{01} \\ T_{10} \end{pmatrix} + a_1\mathrm{e}^{-\lambda_1 t}\begin{pmatrix} 1 \\ -1 \end{pmatrix}. \tag{1.2.14}$$

It remains to fix the constants of integration $a_0$ and $a_1$. To do this, we must now find the left eigenvectors of the transition matrix. These are

$$\langle\phi_0| = \begin{pmatrix} 1 & 1 \end{pmatrix} \qquad \text{and} \qquad \langle\phi_1| = \begin{pmatrix} T_{10} & -T_{01} \end{pmatrix}. \tag{1.2.15}$$

Noting the biorthogonality property $\langle\phi_k|\psi_l\rangle = \lambda_1\delta_{k,l}$, then given some initial condition $|P(0)\rangle$ it is possible to calculate $a_0$ and $a_1$ via

$$\langle 0|P(0)\rangle = a_0\lambda_1 \qquad \text{and} \qquad \langle 1|P(0)\rangle = a_1\lambda_1. \tag{1.2.16}$$

More generally,

$$\langle 0|P(t)\rangle = a_0\lambda_1 \qquad \text{and} \qquad \langle 1|P(t)\rangle = a_1 \mathrm{e}^{-\lambda_1 t}\lambda_1, \tag{1.2.17}$$

which yields the time-dependent normalisation

$$Z(t) = (a_0 + a_1 \mathrm{e}^{-\lambda_1 t})\lambda_1. \tag{1.2.18}$$

The particular solution is therefore

$$\begin{pmatrix} P_0(t) \\ P_1(t) \end{pmatrix} = \frac{a_0}{Z(t)} \begin{pmatrix} T_{01} \\ T_{10} \end{pmatrix} + \frac{a_1}{Z(t)} \mathrm{e}^{-(T_{01}+T_{10})t} \begin{pmatrix} 1 \\ -1 \end{pmatrix}, \tag{1.2.19}$$

which, in the long-time limit, approaches the stationary state

$$\lim_{t\to\infty} \begin{pmatrix} P_0(t) \\ P_1(t) \end{pmatrix} = \frac{1}{T_{01}+T_{10}} \begin{pmatrix} T_{01} \\ T_{10} \end{pmatrix}. \tag{1.2.20}$$

This is simple to verify by solving eq. (1.2.10) with the temporal derivative set to zero.

Before moving on, we note from the above that we can define a characteristic time scale over which the system approaches stationarity: the *relaxation time*, $\tau$. In this example, from eq. (1.2.19) we see that

$$\tau = \frac{1}{T_{01}+T_{10}}. \tag{1.2.21}$$

In the general case, we have multiple time scales over which the system relaxes corresponding to the reciprocal decay constants $\{\lambda_n\}$ in eq. (1.2.9). Then, the relaxation time is defined by

$$\tau = \frac{1}{\mathrm{Re}[\lambda_{\min}]}, \tag{1.2.22}$$

where $\lambda_{\min}$ is the nonzero eigenvalue with the smallest real part (since this is associated with the slowest mode of decay).

### Revisiting detailed balance

We conclude this section with a more rigorous discussion of detailed balance and its relation to equilibrium and nonequilibrium stationary states. There, we stated that equilibrium stationary states are defined by detailed balance: 'a system

is said to be in equilibrium if it is stationary such that the probability fluxes between all pairs of configurations cancel exactly'. In a continuous-time process, this translates as

$$W(\mathcal{C}' \to \mathcal{C})P(\mathcal{C}', t) = W(\mathcal{C} \to \mathcal{C}')P(\mathcal{C}, t) \tag{1.2.23}$$

for all distinct $\mathcal{C}$ and $\mathcal{C}'$. Now let us look at the stationary continuous-time master equation, taken by setting the left-hand side of eq. (1.2.2) to zero:

$$0 = \sum_{\mathcal{C}' \neq \mathcal{C}} [W(\mathcal{C}' \to \mathcal{C})P(\mathcal{C}') - W(\mathcal{C} \to \mathcal{C}')P(\mathcal{C})]. \tag{1.2.24}$$

Clearly, enforcing eq. (1.2.23) in eq. (1.2.24) yields stationarity (all summands are zero). One of the consequences of detailed balance is that the dynamics of an equilibrium system is reversible in the sense that the probability of traversing a trajectory through state space is exactly equal to that of its reverse. The statements about time-reversibility in equilibrium systems as alluded to earlier reflect this fact.

As was discussed at length in the previous section, detailed balance is just one way in which stationarity can be achieved; there are many nontrivial cancellations, corresponding to nonequilibrium states, that also satisfy eq. (1.2.24). To demonstrate this, we revisit the nonequilibiurm trit featured in fig. 1.6, setting $p = q = r$ for simplicity. By symmetry, the stationary state is $P(\mathcal{C}_0) = P(\mathcal{C}_1) = P(\mathcal{C}_2) = \frac{1}{3}$. The stationary master equation for $\mathcal{C} = \mathcal{C}_0$ is then

$$\begin{aligned}
&[W(\mathcal{C}_1 \to \mathcal{C}_0)P(\mathcal{C}_1) - W(\mathcal{C}_0 \to \mathcal{C}_1)P(\mathcal{C}_0)] + [W(\mathcal{C}_2 \to \mathcal{C}_0)P(\mathcal{C}_2) - W(\mathcal{C}_0 \to \mathcal{C}_2)P(\mathcal{C}_0)] \\
&\quad = \left[0 - \frac{r}{3}\right] + \left[\frac{r}{3} - 0\right] \\
&\quad = 0.
\end{aligned} \tag{1.2.25}$$

The master equations for $\mathcal{C}_1$ and $\mathcal{C}_2$ are seen to be identical by cyclically permuting the indices. In all cases, one sees a violation of detailed balance due to a nontrivial cancellation of terms, this being a consequence of the flux loop in the trit's state space.

## 1.3 Applications: active matter

Having now introduced the notions of nonequilibrium and stochastic processes, we move on to consider some pertinent physical examples. We shall focus on those most relevant to the investigations of this thesis, starting in this section with *active matter*.

In recent years, the scientific community has become increasingly interested in active matter [39–43]. The field of active matter concerns particles, or collections thereof, which consume energy in order to perform directed motion. Since the energy flow in such instances is time-irreversible, active particles are inherently out of equilibrium. The most notable examples of active matter come from biology, for this is the basis upon which all living organisms function. A fish, for example, may be modelled as an active particle because the energy it uses to swim is sourced from food in its local environment (the same can be said for birds, bacteria, etc.). Outwith the domain of biology, self-phoretic particles – those which directly convert chemical energy in their environment into motion (as opposed to the more-convoluted metabolic route) – are also active.

Broadly speaking, what makes active systems of interest to physicists are the emergent behaviours they exhibit when multiple, and often large numbers of, active particles coexist and interact with each other and/or their environment. Empirically, an extensive range of emergent behaviours are observed depending on the nature of the particles' motility as well as the nature of the interactions they experience (as we shall see shortly). Examples of this include collective motion – such as the flocking of birds or the schooling of fish – and clustering – as seen in some bacterial populations. For physicists, pinning down the precise nature of these behaviours has been a major challenge of the last three decades, but much progress has been made.

### 1.3.1 Different approaches to active matter

There are various approaches to studying active matter. Firstly, we can classify active systems as being either *wet* or *dry*; into which class an active system falls is related to momentum conservation, where wet systems conserve momentum, and dry systems do not. Additionally, we can classify active systems as being *microscopic* or *macroscopic*, based on whether we are describing the active

constituents at the level of individuals or at the level of whole populations, respectively. These two classification types can be thought of as lying on two 'orthogonal' axes such that there are a total of four classes of active systems: dry microscopic; dry macroscopic; wet microscopic; and wet macroscopic. The models of active matter considered in this thesis are of the dry microscopic variety (though we will also encounter the dry macroscopic variety in a continuum limit), and as such we will devote most of this section to systems of this type.

### 1.3.2 Modelling dry active matter

We begin by discussing dry active matter. As stated above, the term 'dry' comes from the fact that we do not rigorously consider momentum exchange with a surrounding fluid, unlike in wet systems; thus, the only conservation law that is imposed for dry macroscopic active systems with fixed particle number is conservation of mass.

#### Vicsek model

A seminal example of a dry active system is that of the Vicsek model [44]. The essence of the model is captured by the following rule, as stated in [44]: 'at each time step a given particle driven with a constant absolute velocity assumes the average direction of motion of the particles in its neighbourhood of radius $r$ with some random perturbation added'. Specifically, the dynamics are simulated as follows. Particles inhabit continuous space in a square cell with periodic boundaries. The square is measured in discrete units and has side length $L$ as measured in said units. The system is initialised at time $t = 0$ with $N$ randomly-oriented, randomly-distributed particles, all of which have fixed speed $v$. The particle density, $\rho$, is given by $\frac{N}{L^2}$. Denoting the position, orientation, and velocity of particle $i$ by $\boldsymbol{x}_i$, $\theta_i$, and $\boldsymbol{v}_i$ (pointing in the direction of $\theta_i$), respectively, the system is updated at each discrete time step $t$ according to

$$\boldsymbol{x}_i(t+1) = \boldsymbol{x}_i(t) + \boldsymbol{v}_i(t)\Delta t, \tag{1.3.1}$$

where $\Delta t = 1$, and

$$\theta_i(t+1) = \langle \theta_i(t) \rangle_r + \Delta\theta_i, \tag{1.3.2}$$

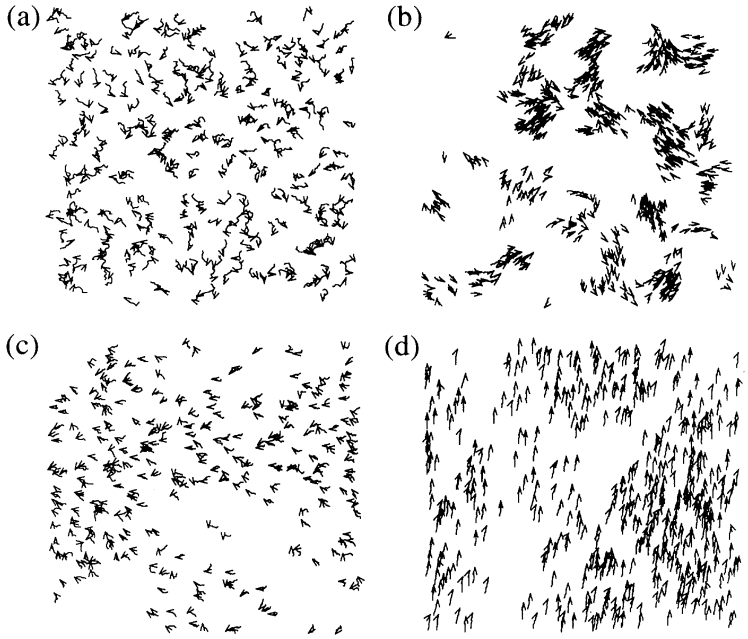


**Figure 1.8** *(Reproduced from [44].) Various collective behaviours for different parameter choices of the Vicsek model. In all cases, the particle number is* $N = 300$ *and arrows indicate velocities. Panel (a) shows particles shortly after initialisation for* $\rho \approx 6.12$ *(*$L = 7$*) and* $\eta = 2.0$*. Panel (b) shows a low-density, low-noise scenario in which* $\rho = 0.48$ *(*$L = 25$*) and* $\eta = 0.1$*. Coherent groupings are observed which move in random directions. Panel (c) features the same parameter choice as panel (a), but shows a still after some time has passed. The particles appear to move somewhat randomly but show some degree of correlation. For* $\rho = 12$ *(*$L = 5$*) and* $\eta = 0.1$*, i.e. high density and low noise, ordering occurs. This is shown in panel (d).*

where the average is over all particle orientations within an interaction radius $r$ (including particle $i$ itself) and where $-\frac{\eta}{2} \leq \Delta\theta_i \leq +\frac{\eta}{2}$, this being the random perturbation. Though superficially simple, this model exhibits a variety of behaviours owing to the three free parameters at a given system size and interaction radius: $v$, $\eta$, and the particle density $\rho$. Examples of the various kinds of collective behaviours that emerge from this model's dynamics are shown in fig. 1.8.

### Toner-Tu model

The rich variety of behaviours that emerge from the Vicsek model exemplifies how active systems are able to generate complexity out of simple rules. As a consequence of this, interest in the model quickly grew. Toner and Tu [45, 46]

later wrote down a continuum description (that is, a description that is of the dry *macroscopic* type) of a large universality class of models which includes the Vicsek model. This description consists of the Landau-style expansion

$$\frac{\partial \boldsymbol{v}}{\partial t}+(\boldsymbol{v}\cdot\boldsymbol{\nabla})\boldsymbol{v} \\ = \alpha\boldsymbol{v}-\beta|\boldsymbol{v}|^2\boldsymbol{v}-\boldsymbol{\nabla}P+D_L\boldsymbol{\nabla}(\boldsymbol{\nabla}\cdot\boldsymbol{v})+D_1\boldsymbol{\nabla}^2\boldsymbol{v}+D_2(\boldsymbol{v}\cdot\boldsymbol{\nabla})^2\boldsymbol{v}+\boldsymbol{f}, \tag{1.3.3}$$

where terms in a vector field of velocities $\boldsymbol{v}$ and its gradients reflect underlying system symmetries, and the continuity equation

$$\frac{\partial\rho}{\partial t}+\boldsymbol{\nabla}\cdot(\boldsymbol{v}\rho)=0, \tag{1.3.4}$$

where $\rho$ is the density field, which reflects conservation of mass. Here, $\beta > 0$ and $\alpha$ may obey $\alpha > 0$ (corresponding to the ordered phase) or $\alpha < 0$ (as in the disordered phase). The coefficients $D_L$, $D_1$, and $D_2$ are diffusion constants, $\boldsymbol{f}$ is a Gaussian noise term, and the pressure $P = P(\rho)$ is expanded in powers of $\rho$ relative to the mean number density $\rho_0$ as

$$P(\rho)=\sum_{n=1}^{\infty}\sigma_n(\rho-\rho_0)^n, \tag{1.3.5}$$

where $\{\sigma_n\}$ is a set of further coefficients. We make clear that all of the foregoing constants are phenomenological.

One of Toner and Tu's key observations was that the Vicsek model is very similar to the two-dimensional XY model. In general, the latter consists of a lattice in which continuously-oriented spins interact both with each other and an external field, but the version of this model in which there is no external field and nearest-neighbour interactions only (as considered in [47]) is in fact a limiting case of the Vicsek model wherein each particle has zero velocity. What is striking is that the two-dimensional XY model described here, as a consequence of the Mermin-Wagner theorem for equilibrium systems [48, 49], exhibits no long-range order at finite temperature – in stark contrast to what is seen in the Vicsek model (as was demonstrated in fig. 1.8). Toner and Tu demonstrated that this difference arises from the nonequilibrium nature of the Vicsek particles, which is reflected in the self-advection $(\boldsymbol{v}\cdot\boldsymbol{\nabla})\boldsymbol{v}$ term on the left-hand side of eq. (1.3.3): two particles which were once far away from each other are able to interact with each other at later times, thus stabilising the ordered phase.

Toner and Tu went on to derive exactly the scaling exponents of their model in two dimensions using renormalisation-group techniques, rigorously proving the thermodynamic stability of the Vicsek model's ordered phase. Their work was later built upon when a continuum description was derived directly from a coarse-graining of the Vicsek model, meaning all phenomenological parameters in the Toner-Tu theory were related back to microscopic variables [50, 51]. With these descriptions, a comprehensive characterisation of the phase space is possible, revealing details of the phase transitions the system exhibits and intriguing spatiotemporal structures such as sound waves in the ordered phase.

### Persistent exclusion process

An alternative means of studying dry active systems is to take the underexplored lattice-based approach. This was the route taken in [52–54] with regards to the *persistent exclusion process* (PEP). As motivated in [52], the PEP encodes the motility pattern of *Escherichia coli* bacteria [55, 56] on a lattice. This motility pattern is known as *run-and-tumble* motion, and is detailed in what follows. We will elaborate on the PEP thereafter.

In the early 1970s, Berg, Brown and Anderson probed samples of *E. coli* via microscopy [55, 56]. By tracking individual bacteria in isotropic solutions (so as to eliminate chemotactic biases), they were able to identify two distinct modes of motion: *runs* and *twiddles*, or *tumbles* as the latter are now more commonly known. Bundles of flagella – threadlike appendages attached to the main body of the bacterium – collectively move to induce these two forms of motion. The former mode consists of uninterrupted linear swim trajectories, whilst the latter consists of a reorientation of the bacterium (with no preferred direction), occurring on shorter time scales and involving little translational motion. Both run and tumble times were found to be exponentially distributed. A typical trajectory for a single bacterium is shown in fig. 1.9.

The above work inspired numerous theoretical models in the decades that followed. Schnitzer [57] derived a continuous-space description of run-and-tumble motion in one dimension which closely resembles the telegraph model of diffusion, and was able to predict behaviours resembling those of wild-type[3] individuals in the presence of chemotactic gradients. Later, Tailleur and Cates [58] devised a

[3]'Wild-type' refers to strains that are found in the wild as opposed to those bred in the laboratory.

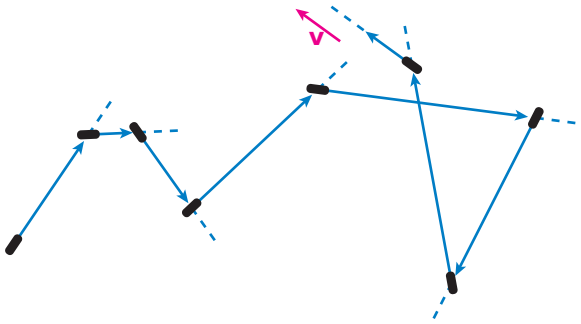


**Figure 1.9** *(Reproduced from [41].) Schematic trajectory for an E. coli bacterium in two dimensions, depicting the exponentially distributed run lengths (consistent with Poisson-distributed run terminations for constant-velocity runs), and the random reorientations after the occurrence of twiddles.*

procedure which allows one to map the description proposed by Schnitzer onto an effective equilibrium free energy for a system of many interacting particles, thus making it amenable to techniques from thermodynamics and equilibrium statistical mechanics. Via mean-field theory, they were subsequently able to predict phase separation into dense and sparse domains for certain parameter choices.

This phase-separation phenomenon would later become known as *motility-induced phase separation* (MIPS). It is speculated that MIPS may play a role in the formation of *biofilms* [59–61] – dense clusters of microorganisms that can be found on surfaces such as rocks and other biological organisms. As a consequence of this and the work presented in [58], interest in modelling MIPS at the population level grew rapidly. More information about these developments can be found in [41]).

In the years following [58], the lesser-explored lattice-based approach to modelling MIPS also emerged. This began in 2011 when Thompson et al. presented exact solutions to two variants of the PEP for non-interacting and zero-range-interacting particles on a one-dimensional lattice [52]. The term PEP was coined later, however, when Soto and Golestanian simulated persistent particles which experience an exclusion interaction on one- and two-dimensional lattices [53]. Specifically, particles occupy sites on the lattice, and each particle has a direction of motion associated with it which aligns to one of the lattice's principal directions. Each particle stochastically hops, with fixed mean rate $\gamma$, to the site adjacent to it and parallel to its direction of motion. An exclusion interaction is implemented such that a hop is rejected when the target site is occupied;

no more than one particle, therefore, can occupy a particular lattice site at a given time. Finally, particles may stochastically reorient with fixed mean rate $\alpha$. For persistence, we require $\alpha \ll \gamma$; this ensures that multiple lattice sites are traversed between reorientations. In this way, the motion resembles that of run-and-tumble particles in continuous space. On-lattice particles such as these are often referred to as *persistent random walkers* (PRWs, 'walkers', or 'particles' when the context is clear) and, in conjunction with an exclusion interaction, constitute the PEP. The authors of [53] observed MIPS in their simulations, and were able to characterise the size distribution of clusters (dense domains) over a range of parameter choices.

Further progress on the PEP was made by Slowman, Evans and Blythe (SEB) [54] when they sought to probe MIPS at the level of individual particles. They achieved this by giving an exact solution to a two-body problem on a periodic one-dimensional lattice of $L$ sites. The dynamics of a single PRW in this model is identical to that described above: hops are made stochastically to adjacent sites in a given direction with mean rate $\gamma$, and reversals occur stochastically with mean rate $\omega = \frac{\alpha}{2}$ ($\alpha$ gives the total rate of reorientations, including those which leave the walker's direction unchanged). And similarly, walkers interact via exclusion: both particles are forbidden from occupying the same site at a given instant; hops are instead rejected if an attempt is made to do so, and the walker remains on its current site. Much of the work presented in this thesis was inspired by this model, and as such we will summarise its results below.

There are four distinct subsets in the state space of this model corresponding to the directional combinations of both particles: $++$, $+-$, $--$, and $-+$.[4] Here, $+$ and $-$ denote right- and left-moving particles, respectively. The aim, then, was to solve for the stationary distributions for the separation, $n$, of the particles in each of these four subsets: $P_{++}(n)$, $P_{+-}(n)$, $P_{--}(n)$, and $P_{-+}(n)$. SEB solved this problem by writing down a set of coupled stationary master equations for the above distributions which were transformed into algebraic equations via a method involving generating functions. This facilitated an exact solution in both discrete and continuous space.

By analogy with the Boltzmann distribution, these results can be used to derive

[4]For clarity, these subsets are not subspaces/sectors since all such subsets communicate with one another.

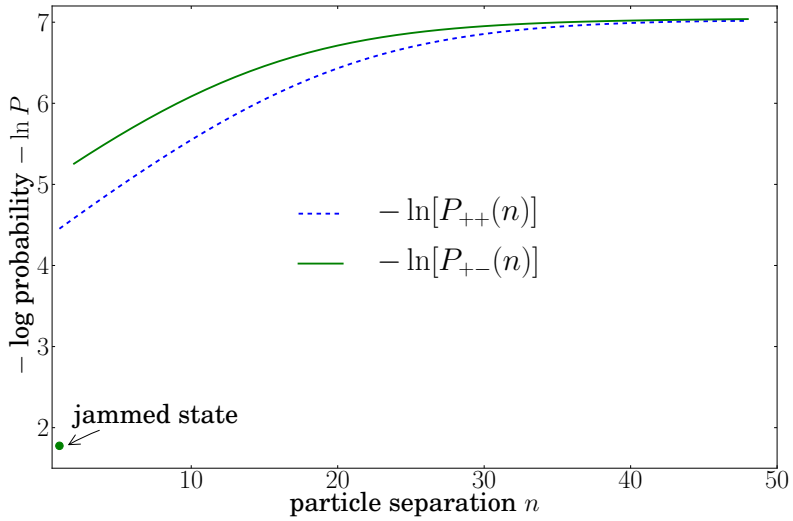


**Figure 1.10** *(Reproduced from [54].) The effective potentials $V_{+\pm}(n)$ corresponding to the distributions $P_{+\pm}(n)$ for $L = 100$ and $\omega = \frac{1}{100}$. This reveals a rich structure comprising a jammed piece, linear pieces, and constant pieces.*

an *effective* pair potential. With a suitable normalisation, we can write

$$P_{+\pm}(n) = \mathrm{e}^{-V_{+\pm}(n)}, \tag{1.3.6}$$

where $V_{+\pm}(n)$ are the dimensionless effective potentials. Physically, these effective potentials emerge as a consequence of the nonequilibrium dynamics, and give us great insight into how complexity is able to arise in active systems at a fundamental level. The rich structure exhibited by these potentials is shown in fig. 1.10. Importantly, we note the *jammed* piece, which arises as a consequence of the particles blocking each other's motion and manifests as a pair of delta functions at the domain boundaries in the stationary distribution (its fingerprint is indicated in fig. 1.10). We will make clear the significance of jammed states in chapter 3.

Though insightful in their own right, the effective potentials derived in [54] raise further important questions. How are the potentials modified if we increase the particle number? How are the potentials modified in higher dimensions? How are the potentials modified in the case of generalised interactions? Though the approach taken in [54] is exact and ensures that the physics is correct at the microscopic scale (which cannot be said of all hydrodynamic theories), one has to concede that the above questions are challenging to answer with said approach. Some progress, however, has been made: generalisations include [62], in which

the authors solve for the time-dependent solution of the dynamics; and [63], in which the authors solve for the stationary solution when the tumble time is finite (instantaneous tumbling is an approximation to real biological contexts). Further progress detailing an exact stationary solution in the case of a generalised 'recoil' interaction forms the topics of chapters 4 and 5 (previously published in [2, 3]).

It is the major goal of nonequilibrium statistical mechanics to bridge the gap between microscopic dynamics and emergent behaviours at the macroscopic level. Only by studying models of the type described above can we make progress on this front, since the mathematical techniques required to study such systems in generality are currently lacking. Until more sophisticated methods are developed, we must proceed by studying specific cases and looking for connections between them.

### 1.3.3 Contrasting dry active matter with wet active matter

In the preceding section, we discussed dry microscopic systems, and touched upon some examples of dry macroscopic systems. We now move on to discuss wet active systems – in which momentum is conserved – and how they contrast with their dry counterparts. Given the content of this thesis (as alluded to previously), we only include this for completeness; this will therefore be a brief discussion only. For more extended discussions, we point the reader to the many review papers [39–43] that cover the topic.

We will make the contrast between wet and dry active matter by looking at two alternative macroscopic formulations of active fluids. Firstly, we will write down a simple model of a dry polar active fluid and explain its workings. We will then write down an alternative model from the viewpoint of wet polar active systems, highlighting the key differences regarding momentum conservation.

To this end, we start with the model of a dry polar active fluid. This consists of writing down the following pair of phenomenological equations [40]:

$$\frac{\partial \rho}{\partial t} = -\boldsymbol{\nabla} \cdot \left[ -\frac{1}{\gamma_\rho} \boldsymbol{\nabla} \left( \frac{\delta F_p}{\delta \rho} \right) + \mathbf{f}_\rho + v_0 \rho \mathbf{p} \right]; \tag{1.3.7}$$

$$\text{and} \qquad \frac{\partial \mathbf{p}}{\partial t} = -\frac{1}{\gamma_p} \frac{\delta F_\rho}{\delta \mathbf{p}} + \mathbf{f}_p - \lambda (\mathbf{p} \cdot \boldsymbol{\nabla}) \mathbf{p}. \tag{1.3.8}$$

Here, $\rho$ is a particle density, $\mathbf{p}$ is both an associated orientational ordering and

a momentum, $\gamma_\rho$ and $\gamma_p$ are constant kinetic coefficients, $F_\rho$ and $F_p$ are Landau-style free-energy functionals, $\mathbf{f}_\rho$ and $\mathbf{f}_p$ are noise terms, $v_0$ is a constant 'swim' speed of the particles, and $\lambda$ is a phenomenological constant. These equations may be interpreted as follows. Equation (1.3.7) conserves mass since it takes the form of a continuity equation, where the current density is the collection of terms in the square brackets. Equation (1.3.7) may also be interpreted as a driven diffusion equation, with the diffusive piece given by the free-energy term (since it is Laplacian), and where the driving is given by the advective and noise terms. Put more simply, we decompose the right-hand side of eq. (1.3.7) into an equilibrium diffusive current and nonequilibrium driving contributions. This means the free-energy density has to be chosen such that it yields the appropriate diffusive current, thus motivating a Landau-style expansion in terms of $\rho$ and $\mathbf{p}$. We have an analogous setup in eq. (1.3.8) with two key differences. The first is that the right-hand side is not the divergence of a current, which is where momentum conservation is violated (in accordance with what we said earlier for dry systems). The second is that we now have a nonlinear self-advection term; $\mathbf{p}$ is an order parameter that drives itself across the system by virtue of its also being a momentum.

The approach described above phenomenologically captures momentum fluxes in its nonequilibrium driving terms. In wet active matter, a phenomenological approach is *not* taken; the key difference between the wet and dry approaches is that the latter encodes momentum conservation by writing down a second continuity equation. For a wet polar active fluid, we thence have [40]

$$\frac{\partial \rho}{\partial t} + \boldsymbol{\nabla} \cdot (\rho \mathbf{v}) = 0 \tag{1.3.9}$$

$$\text{and} \qquad \frac{\partial g_\alpha}{\partial t} + \partial_\beta \Pi_{\alpha\beta} = 0, \tag{1.3.10}$$

where $\mathbf{g} = \rho m \mathbf{v}$ is the local momentum density, and where $\Pi_{\alpha\beta} = \rho m v_\alpha v_\beta - \sigma_{\alpha\beta}$, for which the first term corresponds to Reynolds stress and the second term corresponds to the system's total stress. In practice, the Reynolds number is often small enough that the Reynolds stress can be neglected entirely.

We have seen above how momentum flux is treated differently in the wet and dry formulations of macroscopic active fluids. Before moving on, we remark that there exists further approaches one can take to modelling macroscopic active systems. Kinetic models, for example, are commonly used to model active suspensions (often suspensions of swimming microorganisms) [64–67]. The kinetic-theory

approach boils down to defining a probability density function $\Psi(\mathbf{r}, \mathbf{p}, t)$, where $\mathbf{r}$ and $\mathbf{p}$ denote position and unit-normalised orientation, respectively. Conservation of particle number is then enforced by the *Smoluchowski equation* [68]

$$\frac{\partial \Psi}{\partial t} + \boldsymbol{\nabla} \cdot (\dot{\mathbf{r}} \boldsymbol{\Psi}) + \boldsymbol{\nabla}_p \cdot (\dot{\mathbf{p}} \boldsymbol{\Psi}) = 0, \tag{1.3.11}$$

whose precise form is determined by writing down appropriate equations for $\dot{\mathbf{r}}$ and $\dot{\mathbf{p}}$. Here, $\boldsymbol{\nabla}_p$ is the gradient operator on the unit sphere. Whilst $\Psi(\mathbf{r}, \mathbf{p}, t)$ gives a full characterisation of the suspension, one usually gives consideration to the concentration, polar order, and nematic order, whose evolution equations are derived by taking moments of the Smoluchowski equation.

## 1.4 Applications: cellular automata

In the previous section, we showed how the formalism and techniques introduced in sections 1.1 and 1.2 can be usefully applied to systems of interacting active particles. In this section, we will shift our focus towards the subject of the final chapter of this thesis – *cellular automata* (CA).

At their heart, CA are discrete-space, discrete-time systems whose physical variables are also discrete and evolve according to a prescribed set of rules. To be more specific, a lattice of $L$ sites (commonly referred to as *cells* in the literature) exists in an arbitrary number of dimensions, $d$, where lattice sites are labelled $i = 0, 1, 2, ..., L-1$. Associated with site $i$ at time $t$ is a physical variable, denoted by $\sigma_i^t$, which can take on a finite number of discrete values. The configuration of the system at time $t$, therefore, is given by $\Sigma^t = \{\sigma_0^t, \sigma_1^t, ..., \sigma_{L-1}^t\}$. A set of rules is then applied which updates sites based on their local configurations to determine $\Sigma^{t+1}$. The same set of rules is then applied to $\Sigma^{t+1}$ to determine $\Sigma^{t+2}$, and so on. The end result is an ordered set of system configurations comprising the trajectory of the automaton. Such trajectories, depending on the update rules, may break detailed balance.

As we shall see, many CA exhibit rich and varied behaviours – even when the rules that govern their updates are simple. That this is possible has implications for the emergence of complexity in physical systems: if we are able to better understand how complexity arises from simple underlying rules in model systems such as CA, we may better understand the emergence of complex forms in nature.

### 1.4.1 Conway's game of life

In order to elucidate the above ideas and demonstrate the relevance of CA in nonequilibrium statistical physics, we will provide context using perhaps the most famous example of a CA – that of Conway's *game of life* [69]. The game of life comprises a two-dimensional square lattice of binary variables; traditionally, the binary states are known as 'dead' and 'live'. At each time step, the status of each site is updated according to the following rules, where by 'neighbours' we mean the eight sites that are either immediately adjacent or immediately diagonal to the site being updated:

1. a dead site that has exactly three live neighbours becomes live;
2. a live site that has either two or three live neighbours remains live;
3. and all other sites, no matter their present status, become dead.

These rules are applied in a *fully parallel* manner [27], meaning that all sites are updated simultaneously when going from $\Sigma^t$ to $\Sigma^{t+1}$. This is in contrast to other updating schemes [27] in which an order of site updates is specified; we will encounter a different type of update scheme briefly towards the end of this section as well as more fully in chapter 6.

#### Emergent behaviours

The game of life is of interest to physicists because, despite the simplicity of its rules, it exhibits many complex emergent phenomena. Some such phenomena are listed below [70].

- *Still lifes*:
  Still lifes are configurations which persist from one time step to the next. The simplest example of a still life is a *block*, which consists of an isolated 2-by-2 square of live sites. A block will persist since each site in the block has precisely three neighbouring live sites.
- *Oscillators*:
  Oscillators are collections of live sites that evolve periodically. Associated with each oscillator is a time period. Other than still lifes (which may

be viewed as oscillators with time period 1), the simplest example of an oscillator is a *blinker*. Starting with three adjacent horizontal live sites, the system updates to three adjacent vertical live sites centred on the same site as that at the previous time step, before returning to the original state. The blinker thus has time period 2.

- *Spaceships*:
  Spaceships are similar in vein to oscillators, only that when the original configuration is returned to its location is translated. The simplest example of a spaceship is a *glider*, whose evolution is depicted in fig. 1.11. Other simple spaceships are shown in fig. 1.12.

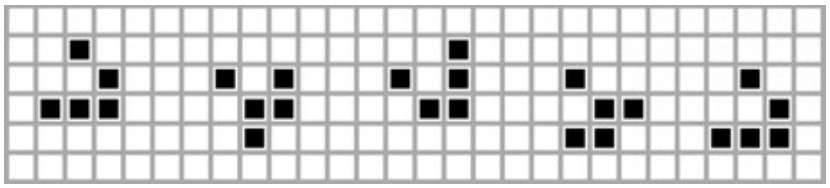

**Figure 1.11** *(Reproduced from [70].) All configurations during the evolution of a glider – the smallest of the game of life's spaceships – arranged chronologically. One sees a repeating pattern that slowly translates: after four time steps the glider is replicated one site right and one site down from its starting position. The initial orientation of the glider determines its direction.*

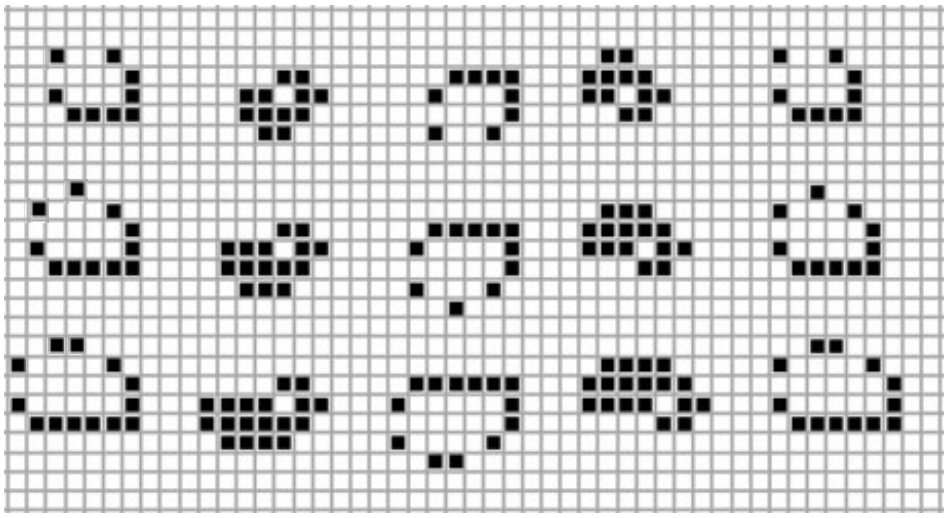

**Figure 1.12** *(Reproduced from [70].) All configurations during the evolution of the lightweight (top), middleweight (middle) and heavyweight (bottom) spaceships, arranged chronologically. As with the glider, one sees repeating patterns that gradually translate.*

Numerous other forms of the types listed above also exist [70], the details of which we will not go into. It suffices to say that such forms can interact and

self-organise into larger-scale forms, and so on. It is hence possible for highly complex and intricate structures to self-organise from the game of life's simple rules which, naturally, is of interest to scientists and mathematicians spanning a wide range of disciplines [70–72]. In mathematics and computer science, for example, the game of life has been proven to be Turing-complete [72, 73], whilst the game of life and various other CA are of interest to biologists due to the emergence of complex phenomena such as self-replicators [73]. We will discuss artificial life more fully at the end of this section.

### Nonequilibrium properties

It is simple to see that the game of life is out of equilibrium. Whilst some subspaces of the state space do exhibit detailed balance, such as those containing isolated blocks or blinkers only, many subspaces do not. A single glider breaks detailed balance, for example, since it constitutes a current; it is unable to reverse its direction, meaning that 'forward' fluxes are not balanced by 'backward' ones. Since detailed balance does not hold in all subspaces, it does not hold for the state space as a whole.

A more complex violation of detailed balance resides in the existence of trajectories whose numbers of live sites grow without bound when the domain size is infinite. The first such example came in 1970 when Gosper [70] discovered the existence of the *glider gun*: a trajectory of configurations in which gliders are emitted periodically and without obstruction. This means the number of gliders, and therefore live sites, grows indefinitely. Guns which emit other kinds of spaceships also exist. In all such cases, flux is directed in the state space, meaning detailed balance is broken.

The game of life is, of course, just one example of a CA, but given the simplicity of their formulation, it is straightforward to design and study CA which break detailed balance. This fact, in conjunction with their simple computational implementations, make CA an invaluable tool with which we can probe nonequilibrium processes at a fundamental level.

#### Sectors

Before moving on to discuss CA more generally, we briefly discuss the game of life's sectors, where we remind the reader that by 'sectors' we mean disjoint, recurrent subsets of a system's state space. It is simple to argue that many configurations in the game of life do not communicate. Consider, for example, a configuration in which a single glider exists amongst no other live forms. Since the glider deterministically translates, said configuration can never, for example, evolve into a configuration comprising a single block. Many other examples exist: a set of $N$ spaceships not bound for collision with each other can never reach a configuration comprising $M \neq N$ such spaceships; a set of oscillators may never evolve into a glider gun; and so on. Additionally, by broken detailed balance, a configuration may communicate with another, but not vice versa: the simplest such example is that of a single live site which immediately 'dies'; the reverse transition is not possible.

We therefore see that the game of life's state space comprises distinct sectors, and into which sector the system ends up in is determined by initial conditions. It is possible to modify the structure of the state space by allowing for stochastic update rules, in which case some sectors are able to mix. In chapter 6, we will focus on indentifying sectors in the context of a one-dimensional stochastic CA with the aim of establishing how the stochasticity effects increased mixing.

### 1.4.2 General cellular automata

In the first instance, the study of CA was motivated by von Neumann [74] in the late 1940s. Von Neumann was interested in self-replicating machines – both from a biological perspective and from the perspective of using them for space exploration. In the early 1950s, Ulam suggested von Neumann focus on discrete models for this purpose [75, 76], out of which the concept of CA was born. The advent of the modern computer several years earlier facilitated much CA research in the subsequent decades, with Conway's game of life propelling CA into public awareness following a magazine article in 1970 [69].

In physics circles, CA research gained traction in the 1980s after Wolfram's seminal papers on fully parallel one-dimensional CA [77–80]. Through empirical work, Wolfram established that four CA classes characterised by form and statistical properties can be identified. The limiting forms of the four classes

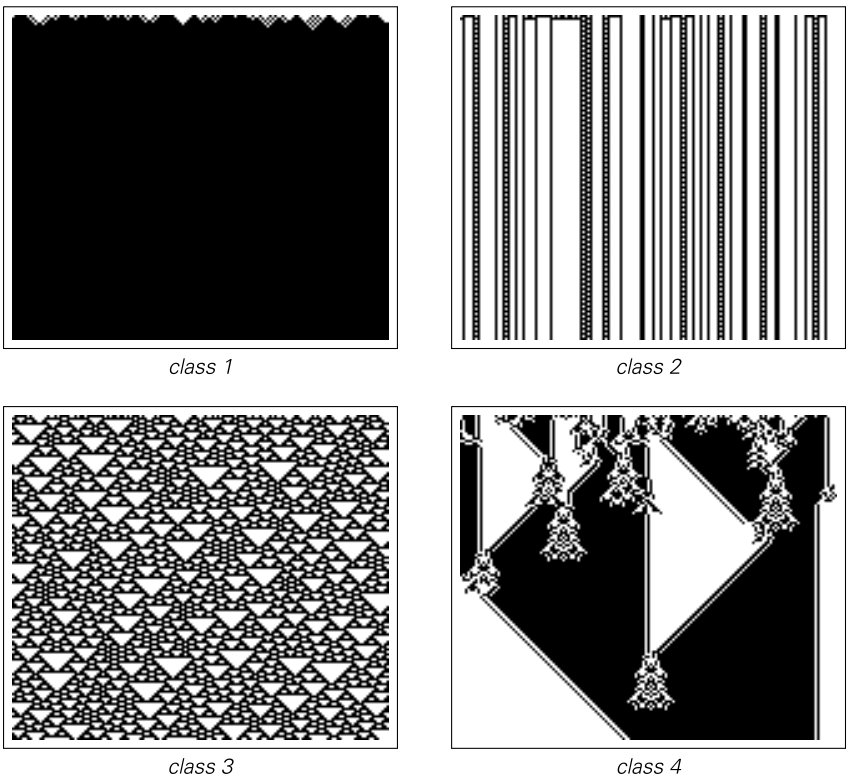


**Figure 1.13** *(Reproduced from [81].) Examples of CA that fall into each of the four classes of one-dimensional CA as described by Wolfram, where the horizontal axis represents space and the vertical axis represents time, starting with $t = 0$ at the top of each subfigure.*

were described by Wolfram as the following:

1. a spatially homogeneous state;
2. a sequence of simple stable or periodic structures;
3. chaotic aperiodic behaviour; and
4. complicated localised structures, some propagating.

We show examples of each class in fig. 1.13. The evolution of CA that belong to class 1 is analogous to evolution towards a limit point in a dynamical system, where all initial conditions converge to the same final configuration. Similarly, the evolutions of class 2 and class 3 CA are analogous to the evolution towards limit cycles and attractors, respectively. Class 4 may be considered intermediate to classes 2 and 3, comprising a mixture of structure and order which can be seen in the right-most panel of fig. 1.13. These ideas lead to an entropic characterisation

of the four classes. To do this, one can define

$$S_i = -\lim_{L\to\infty} \frac{1}{L} \sum_{j=1}^{k^L} p_j \log_k p_j \qquad \text{and} \qquad S_t = -\lim_{T\to\infty} \frac{1}{T} \sum_{m=1}^{k^T} p_m \log_k p_m \ , \quad (1.4.1)$$

to be the limiting entropy per site and limiting entropy per time step for a single site, respectively. Here, we remind the reader that $L$ is the number of sites. We also define $T$ to be the number of time steps, $k$ to be the number of possible values each site can take, $p_j$ to be the probability of spatial configuration $j$, and $p_m$ to be the probability of the single-site temporal sequence $m$. The four classes can then be characterised according to the following:

1. $S_x = 0$, $S_t = 0$;
2. $S_x > 0$, $S_t = 0$;
3. $S_x > 0$, $S_t > 0$; and
4. $S_x$, $S_t$ usually undefined.

The final classification is a consequence of the mixed behaviours of class 4. An account of this classification in terms of information propagation can be found in [78].

The fact that even simple CA such as Wolfram's can exhibit such rich behaviours inspired a wide range of CA-based physical models in the years that followed. Such works include modelling two- and three-dimensional fluids [82–85], surface and interface growth [86, 87], sand-pile dynamics and granular flows [88], traffic flow [88, 89], waves in reaction-diffusion systems [90, 91], forest fires [92–94], and describing rigid-body motion [95]. Some of these CA-based models, such as the forest-fire models, feature stochastic update rules. As alluded to earlier, we shall encounter a stochastic CA in chapter 6.

At the intersection of biology and nonequilibrium physics, the question of the emergence of life has been approached using CA. Arguably the most striking example of this is Chan's Lenia [96, 97], a class of multidimensional CA which was inspired by the 14 open problems in artificial life [98]. Lenia CA are *continuous*, meaning that site values are generally not restricted to be discrete (though they can be, as we shall see). Lenia has been noted for its rich diversity of 'species',

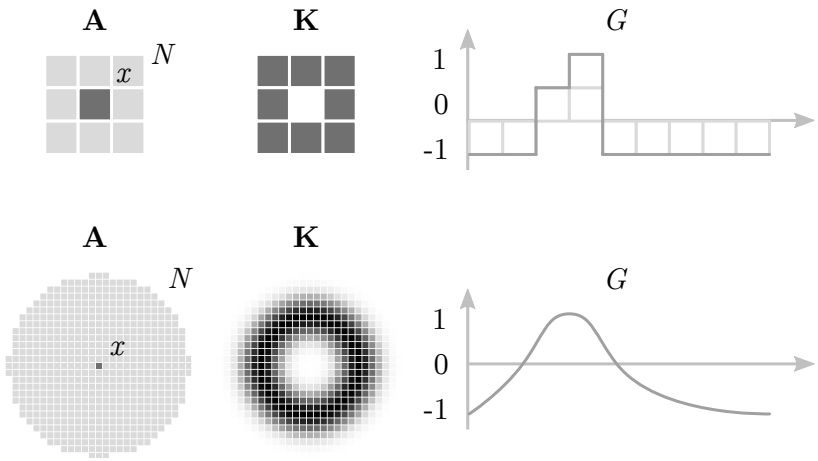


**Figure 1.14** *(Reproduced from [97].) Depictions of the neighbourhoods of $N$ sites for site $x$ over which the kernel $K$ is nonzero, and the mapping functions for both the game of life (top) and an implementation of Lenia (bottom).*

which it generates via the update scheme

$$\mathbf{A}^{t+\mathrm{d}t} = [\mathbf{A}^t + G(\mathbf{K} * \mathbf{A}^t)\,\mathrm{d}t]_0^1 \ . \tag{1.4.2}$$

Here, $\mathbf{A}^t$ is the array of continuous lattice-site values at time $t$, $G$ is a mapping function, $\mathbf{K}$ is a convolution kernel, and $\mathrm{d}t$ is the time increment. The notation $[x]_a^b$ means that $x$ is clipped to the interval $[a, b]$ if its value falls outside this range. In words, eq. (1.4.2) is interpreted as follows. To start, one convolves the array of site values at time $t$ with a chosen kernel, after which the mapping function is applied to the output. Multiplying by the time increment, adding the result to the starting array and clipping the final output to the interval $[0, 1]$ yields an array of continuous site values that constitutes the updated configuration.

To demonstrate the precise workings of Lenia we return to the game of life, which it turns out corresponds to a special choice of eq. (1.4.2) in which $\mathbf{A}^t$, $\mathbf{K}$, $G$ and $\mathrm{d}t$ are discrete. Specifically, $\mathbf{A}^t$ is a lattice of binary values (0 or 1), $\mathbf{K}$ is a square 'ring' (its *Moore neighbourhood*) comprising eight 1s whose effect it is to count the number of 1s immediately surrounding the site to be updated, $G$ encodes the update rules listed in section 1.4.1, and $\mathrm{d}t = 1$. In more general implementations of Lenia, one has freedom over the size of the spatiotemporal increments, the kernel, and the mapping function. The kernel is taken to be ring-like, and the mapping function is taken to be smooth. These facts are depicted in fig. 1.14, and some of Lenia's emergent forms are shown in fig. 1.15. Generalisations to Lenia not stated here are detailed in [97].

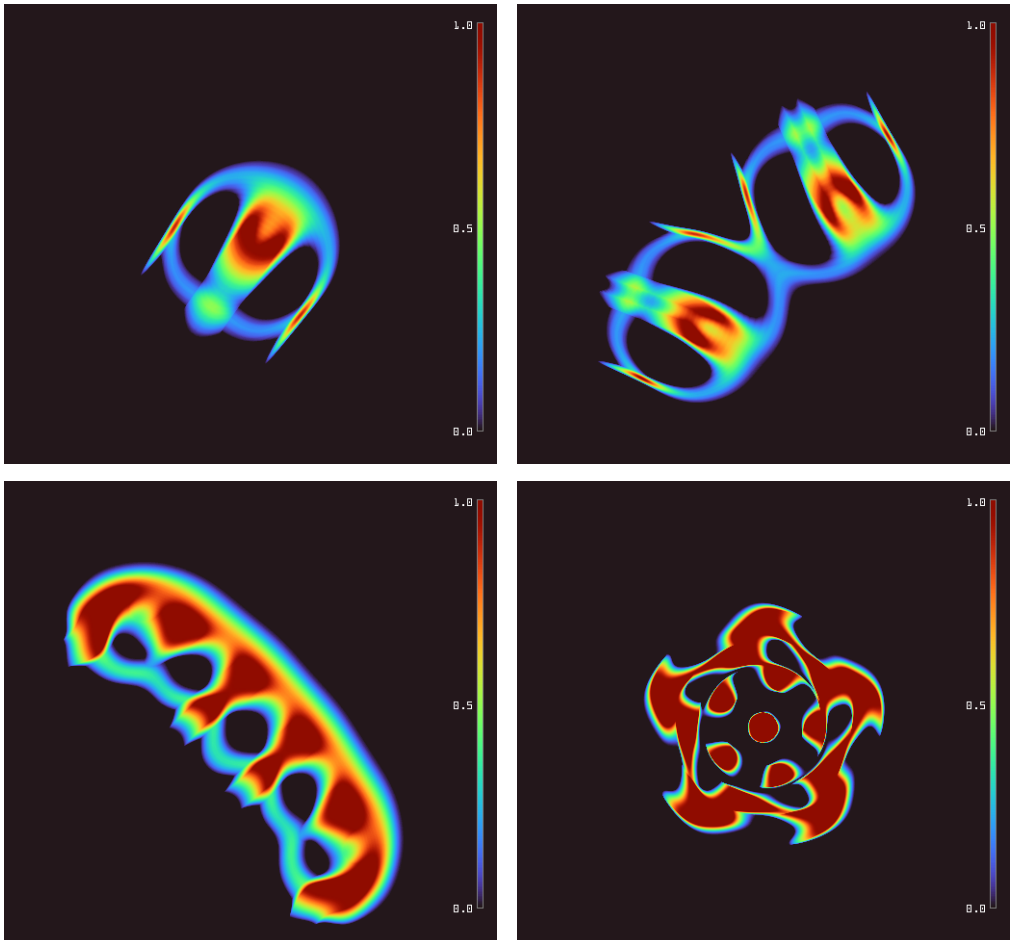


**Figure 1.15** *(Reproduced from [97].) Various forms that emerge in Lenia (eq.* (1.4.2)*). To generate these forms, initial configurations featuring random patches of nonzero site values were generated and simulated. This procedure was repeated with random input distributions and parameters; for some such choices the above forms emerge. We do not quote the precise distribution/parameter choices here as multiple choices lead to the emergence of the same forms (with only minor visual features, such as roughness or brightness relative to the background, affected). The colour bar in each case shown indicates site values. Analogous to the game of life's locomotive glider is Lenia's Orbium (single Orbium shown left; collision of two individuals shown middle-left). Like the glider, Orbium follows a straight-line trajectory. Another locomotive form, Pentaptera (middle-right), and a rotating form, Asterium (right), are also shown.*

Emergent phenomena such as self-organisation, locomotion, self-replication, environmental adaptability, and evolvability – all characteristics of biological life – have been observed in Lenia. That such phenomena are able to arise is of significance regarding the scientific community's understanding of the emergence of biological life, and further serves as a strong demonstration of the utility and ever-present relevance of CA-based modelling.

## 1.5 Outline of this thesis

In this introduction, we began by reviewing state spaces and their relation to (non)equilibrium in terms of (broken) detailed balance. We then introduced the notion of stochastic processes and the master equation formalism which one can use to mathematically describe stochastic processes, before finally moving on to consider applications of the foregoing in active matter and cellular automata. In the remainder of this thesis, we will explore the methods and applications reviewed in this introduction more deeply by considering three microscopic models, the details of which we outline below.

We will begin in chapter 2 by introducing the mathematical toolbox which we will employ to tackle two interacting-PRW models in chapters 3 to 5. We shall demonstrate such methods in the context of simple random-walk problems. We will then finish with a discussion of the techniques employed to simulate all systems studied in chapters 3 to 6.

In chapter 3, we introduce the first model of study featured in this thesis. This model is a multidimensional, many-body generalisation of the one-dimensional SEB model of [54]. We analyse this model by using *backward equations* to solve a *first-passage problem*, from which we determine a density threshold for clustering/MIPS. We show the intriguing result that, in a physically interesting continuum scaling limit, this threshold becomes vanishingly small.

Another important generalisation of [54] is that which features *active* interactions. This is the subject of chapters 4 and 5, where we contrast the emergent effects of active interactions with those of steric exclusion. Specifically, we implement a *recoil* interaction wherein particles are instantaneously displaced upon contact according to an arbitrary probability distribution. We tackle this model with *generating functions*, which we use to develop a novel technique for dealing

with nontrivial boundary behaviours. We go on to show a variety of effective interactions and, interestingly, transitions between them for special parameter choices.

We then move away from PRWs to CA in chapter 6, where we will consider a stochastic generalisation of a one-dimensional CA in order to ascertain how the added stochasticity alters the state space's structure. We conduct our analysis using simulation data, and find that the growth on a lower bound for the number of distinct sectors is related to the Fibonacci numbers and the golden ratio. Due to increased mixing, this growth rate, it turns out, is significantly slower than that of the automaton's deterministic predecessor.

Finally, we make concluding remarks and discuss potential future investigations which follow on naturally from the work presented in this thesis. This is the subject of chapter 7.

# Chapter 2

# Methodologies

A multitude of mathematical and computational techniques can be applied to models of nonequilibrium systems. In this thesis, we will make use of various such techniques. It is the purpose of this chapter to introduce these.

We will begin in chapter 3 by presenting a model of two persistent random walkers on a lattice, and define a *first-passage* problem for the mean elapsed time from some arbitrary starting configuration to one in which the walkers are in contact. This we will tackle by writing down a set of *backward equations* and subsequently solving them. To stand the reader in good stead for chapter 3, we will demonstrate the application of backward equations to a simple first-passage problem involving a single random walker in section 2.1.

In chapters 4 and 5, *generating functions* will be our machinery of choice. There, we will begin with a one-dimensional lattice model of two interacting particles. The set of governing master equations will then be written down and converted to a more amenable form via the use of generating functions and a technique known as the *kernel method*, eventually facilitating the problem's full solution. We will demonstrate the workings of the kernel method in section 2.2, where we will apply it to the same random-walk problem of section 2.1 in order to obtain the same result.

Finally, we will describe the numerical techniques that have been used to simulate the stochastic systems studied in chapters 3 to 6 of this thesis. In particular, we will make frequent use of *Monte Carlo* simulations in order to obtain numerical results and verify our analytical predictions; it is therefore important that our

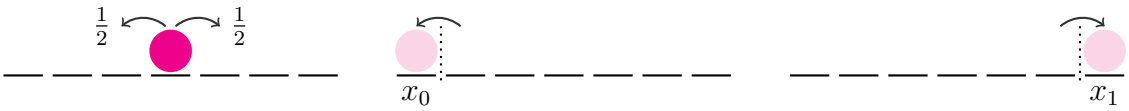


**Figure 2.1** *The dynamics of the discrete-space discrete-time one-dimensional symmetric random walk with absorbing boundaries. Hops occur indiscriminately to nearest-neighbour sites (left panel). Once the walker reaches either boundary it is absorbed and the process terminates (middle, right panels), indicated by faded circles.*

simulations accurately and efficiently capture the necessary physics.

It is the purpose of this chapter to familiarise the reader with the foregoing tools and techniques. This material, it is hoped, will serve as a springboard for the remainder of this thesis.

## 2.1 Absorption time of a symmetric random walker on a bounded domain: a first-passage approach

We will begin with the application of first-passage techniques to the problem of a symmetric random walker on a one-dimensional lattice in discrete time. The domain is such that absorbing boundaries exist at $x_0$ and $x_1$, meaning that when the random walker reaches either of these points the process ceases. The dynamics of the problem is shown pictorially in fig. 2.1.

The question we now ask is as follows: what is the mean time to absorption given some initial position $x$? Such problems – where we wish to calculate the time taken for a specific event to occur – are known as *first-passage* problems, and are studied widely in statistical physics [99, 100]. To begin to answer our question, we note that the mean absorption time starting from position $x$ at time $t = 0$, denoted $T(x)$, must obey the equation

$$T(x) = \Delta t + \frac{1}{2}T(x + \Delta x) + \frac{1}{2}T(x - \Delta x). \tag{2.1.1}$$

Here, $\Delta t$ is the discrete time increment and $\Delta x$ is the lattice spacing. This is an example of a *backward equation*, so called because we are conditioning the final state and not the initial state (as is more often the case in physics). In order to

reach one of the absorbing boundaries from $x$, the time must first be incremented by $\Delta t$ to allow the walker to make its next hop. Since the walk is symmetric, with probability $\frac{1}{2}$ the walker's new position will be $x + \Delta x$ and with probability $\frac{1}{2}$ its new position will be $x - \Delta x$, thus yielding the second and third contributions to the equation's right-hand side.

With the governing equation established, we may now proceed to solve for $T(x)$. Due to its utility later on in this thesis, we will solve for $T(x)$ by taking a continuum limit and thus converting eq. (2.1.1) into an ordinary differential equation. Taking $\Delta x \to 0$ and Taylor-expanding yields

$$0 = \Delta t + \frac{\Delta x^2}{2} \frac{\mathrm{d}^2 T(x)}{\mathrm{d}x^2}. \tag{2.1.2}$$

Taking $\Delta t \to 0$ so as to keep $D = \frac{\Delta x^2}{2\Delta t}$ finite in the limit yields the equation

$$D \frac{\mathrm{d}^2 T(x)}{\mathrm{d}x^2} = -1. \tag{2.1.3}$$

The solution to this equation must be quadratic: $T(x) = ax^2 + bx + c$. In order to determine the constants $a$, $b$ and $c$, we require a pair of boundary conditions. These can be deduced straightforwardly from the physics, since we must have that $T(x_0) = T(x_1) = 0$ (in words, the time taken to reach the absorbing boundaries when already at the absorbing boundaries is zero). Substituting the quadratic ansatz into eq. (2.1.3) tells us immediately that $a = -\frac{1}{2D}$. The boundary conditions then complete our solution to reveal

$$T(x) = -\frac{1}{2D} \left[ x^2 - (x_0 + x_1)x + x_0 x_1 \right]. \tag{2.1.4}$$

The validity of this result is demonstrated in fig. 2.2. Note that for this continuum solution to be accurate when applied to discrete systems, we must have $L \gg 1$. From the definition of the diffusion constant, we see $D \approx \frac{1}{2L^2 \Delta t}$ since $\Delta x = \frac{1}{L-1}$. One therefore scales $\Delta t = \mathcal{O}\left(\frac{1}{L^2}\right)$ such that $D$ remains $\mathcal{O}(1)$, thus yielding convergence for $T(x)$ in the limit $L \to \infty$. Setting $\Delta t = \frac{1}{L^2}$, we have

$$T(x) = -\left[ x^2 - (x_0 + x_1)x + x_0 x_1 \right]. \tag{2.1.5}$$

To summarise, we wrote down the first-passage time to absorption for a symmetric discrete-space discrete-time random walk starting at position $x$, $T(x)$, in terms of $T(x \pm \Delta x)$ after a single time step. We then performed a Taylor expansion

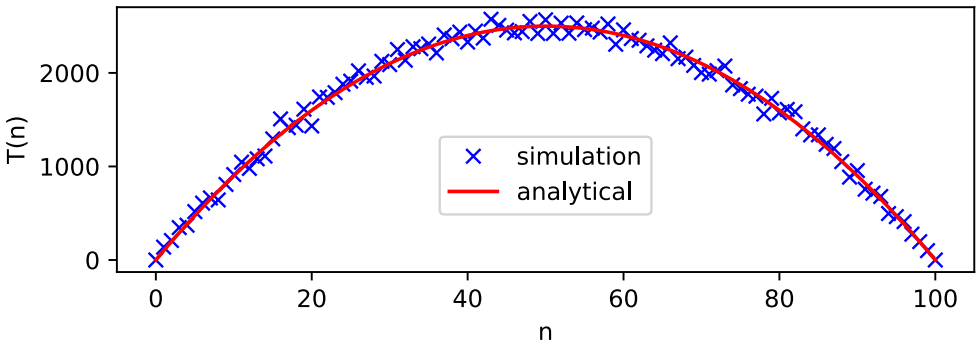


**Figure 2.2** *Demonstration of eq.* (2.1.5) *on a lattice of* $L = 101$ *sites with absorbing boundaries at* $L = 0$ *and* $L = 100$. *In a simulation (see section 2.3) a symmetric random walker is initialised at each site* $n$ *1000 times and the time taken to absorption is measured in each case. The means for all* $n$ *have then been plotted as blue crosses. The red curve represents eq.* (2.1.5)*, where* $x = \frac{n}{L}$ *such that* $x_0 = 0$ *and* $x_1 = 1$. *The diffusion constant may be shown to be* $D \approx \frac{1}{2L^2} = 5 \times 10^{-5}$ *when* $\Delta x = \frac{1}{L-1} = \frac{1}{100}$ *and* $\Delta t = 1$.

to leading order in $\Delta x$ to arrive at an ordinary differential equation, after which boundary conditions motivated by the physics were subsequently used to determine the solution in full. This type of approach is commonplace in first-passage problems. We shall make use of these techniques in chapter 3.

## 2.2 Absorption time of a symmetric random walker on a bounded domain: a generating-function approach

We have seen above one approach to solving the first-passage problem of the mean time taken to reach an absorbing boundary for a symmetric random walker initialised at position $x$ on a one-dimensional lattice. There, a solution was found by taking a continuum limit, thus converting the difference equation in eq. (2.1.1) into a soluble differential equation. What if, though, we wish to find the discrete solution? In this section, we will show how to make use of generating functions to achieve this goal.

To make it clear that we are working on a discrete domain in discrete time, we will update our notation. We shall replace $x$ with $n$, where $n$ is a discrete index that labels lattice sites from $n = 0$ to $n = L$ (the absorption sites) such that

$\Delta x \to \Delta n = 1$. Then, eq. (2.1.1) reads

$$T(n) = \Delta t + \frac{1}{2}T(n+1) + \frac{1}{2}T(n-1). \tag{2.2.1}$$

We may now proceed to solve this, which we do by introducing the *generating function* [101]

$$G(y) = \sum_{n=1}^{L-1} T(n) y^n. \tag{2.2.2}$$

This may be thought of as the discrete-space analogue to the continuous-space Laplace transform, $\mathcal{L}\{f(t)\}(s) = \int_0^\infty f(t)\mathrm{e}^{-st}\,\mathrm{d}t$, where the summation plays the rôle of integration and $y^n$ plays the rôle of $\mathrm{e}^{-st}$. Just as a Laplace-transform solution to a differential equation requires one to multiply all terms by $\mathrm{e}^{-st}$ and integrate over all $t$, so here we shall multiply all terms by $y^n$ and sum over all $n$. Explicitly,

$$\sum_{n=1}^{L-1} T(n) y^n = \Delta t \sum_{n=1}^{L-1} y^n + \frac{1}{2}\sum_{n=1}^{L-1} T(n+1) y^n + \frac{1}{2}\sum_{n=1}^{L-1} T(n-1) y^n. \tag{2.2.3}$$

We now examine each of the terms above one-by-one. The sole term on the left-hand side is $G(y)$. The first term on the right-hand side is the sum of a geometric series; as such, it is easily evaluated as

$$\sum_{n=1}^{L-1} y^n = \frac{y^L - y}{y - 1}. \tag{2.2.4}$$

The second and third terms on the right-hand side require more attention. As an example, we may write

$$\begin{aligned}
\sum_{n=1}^{L-1} T(n+1) y^n &= \frac{1}{y}\sum_{n=1}^{L-1} T(n+1) y^{n+1} \\
&= \frac{1}{y}\sum_{m=2}^{L} T(m) y^m \\
&= \frac{1}{y}[G(y) - T(1)y] \\
&= \frac{1}{y}G(y) - T(1),
\end{aligned} \tag{2.2.5}$$

where we have made use of the boundary condition $T(L) = 0$ introduced in the

previous section. Similarly, one can show

$$\sum_{n=1}^{L-1} T(n-1)y^n = yG(y) - T(L-1)y^L$$
$$= yG(y) - T(1)y^L, \tag{2.2.6}$$

where on the second line we have used $T(L-1) = T(1)$, which follows from symmetry arguments.

With the above facts established, our transformed equation now reads

$$G(y) = \Delta t \frac{y^L - y}{y-1} + \frac{1}{2y}G(y) - \frac{1}{2}T(1) + \frac{y}{2}G(y) - \frac{1}{2}T(1)y^L. \tag{2.2.7}$$

Rearranging for the generating function yields

$$G(y) = \frac{T(1)(1+y^L)(1-y)y + 2\Delta t(y^L - y)y}{(1-y)^3}. \tag{2.2.8}$$

A complete closed-form expression for $G(y)$ requires an explicit expression for $T(1)$. In order to find $T(1)$, we employ the *kernel method* [102], which is described in the following. We note from the definition of the generating function that, for finite $y$ and $L$, it must converge to a finite value everywhere. Hence, $\lim_{y\to 1} G(y)$ must converge, thus requiring that the numerator of eq. (2.2.8), which we will denote $N(y)$, contain a factor of $(1-y)^3$, rendering the generating function's third-order singularity removable.

By identifying the appropriate value of $T(1)$, we can ensure that $N(y)$ and its first two derivatives vanish when $y = 1$, thus guaranteeing the convergence of $G(y)$. It is simple to see that $N(1) = 0$ automatically, so we must look to $N'(y)$. We find

$$N'(y) = T(1)[1 + (L+1)y^L - 2y - (L+2)y^{L+1}] + 2\Delta t[(L+1)y^L - 2y]. \tag{2.2.9}$$

Requiring $N'(1) = 0$ necessitates that

$$T(1) = (L-1)\Delta t. \tag{2.2.10}$$

We must now check that this is consistent with our final requirement: $N''(1) = 0$.

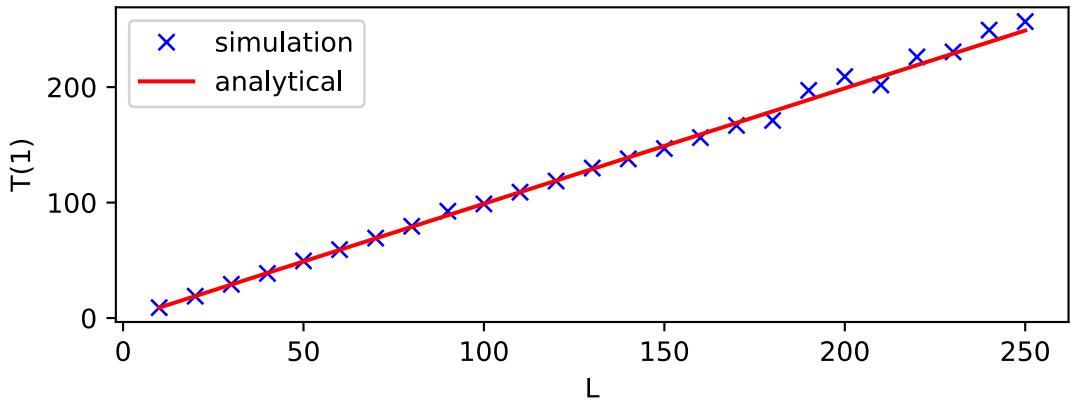


**Figure 2.3** *Demonstration of the validity of eq.* (2.2.10) *for* $\Delta t = 1$. *Simulations (see section 2.3) were run* $10^5$ *times for all lattice sizes* $L = 10$ *to* $L = 250$ *in increments of* 10.

We find

$$N''(y) = T(1)[(L+1)Ly^{L-1} - 2 - (L+2)(L+1)y^L] + 2\Delta t[(L+1)Ly^{L-1} - 2], \quad (2.2.11)$$

which solves $N''(1) = 0$ by the same expression established in eq. (2.2.10). At this point, we can check our calculation by comparing the predicted values of $T(1)$ with simulation data. (For simple problems like that presented here, it may be quicker to simply check the algebra; for algebraically complex problems, such as that which we will see in chapter 4, it can pay to check numerically.) Equation (2.2.10) is shown to be consistent with simulation data in fig. 2.3.

With $T(1)$ correctly established, the generating function can now be written in closed form. We have

$$\frac{G(y)}{\Delta t} = \frac{(L-1)(1+y^L)(1-y)y + 2(y^L - y)y}{(1-y)^3}. \quad (2.2.12)$$

We now have everything we need to determine $T(n)$: all one has to do is expand the denominator term as a power series such that $G(y)$ can be written in polynomial form; then, the $y^n$ coefficients are read off to reveal $T(n)$. We may write $N(y)$ in the form

$$\frac{N(y)}{\Delta t} = (L-1)y - (L+1)y^2 + (L+1)y^{L+1} - (L-1)y^{L+2}. \quad (2.2.13)$$

Further, it can be shown that

$$\frac{1}{(1-y)^3} = \frac{1}{2}\sum_{n=0}^{\infty}(n+2)(n+1)y^n. \quad (2.2.14)$$

Since there are no negative powers of $y$ in the above expansion, and since the generating function by its definition features no power of $y$ greater than or equal to $L$, we may readily drop the appropriate terms in $N(y)$ and $(1-y)^{-3}$ to give

$$\frac{G(y)}{\Delta t} = \sum_{n=0}^{L-2} \frac{(n+2)(n+1)(L-1)}{2} y^{n+1} - \sum_{n=0}^{L-3} \frac{(n+2)(n+1)(L+1)}{2} y^{n+2} \tag{2.2.15}$$

such that only non-vanishing powers of $y$ are written down explicitly. One can, of course, work with the full expression for $G(y)$, but will find that terms of order $y^L$ or higher will vanish. Shifting the summation variables in each case yields

$$\begin{aligned} \frac{G(y)}{\Delta t} &= \sum_{n=1}^{L-1} \frac{(n+1)n(L-1)}{2} y^n - \sum_{n=1}^{L-1} \frac{n(n-1)(L+1)}{2} y^n \\ &= \sum_{n=1}^{L-1} \frac{n}{2} [(n+1)(L-1) - (n-1)(L+1)] y^n \\ &= \sum_{n=1}^{L-1} n(L-n) y^n. \end{aligned} \tag{2.2.16}$$

We thus have

$$\sum_{n=1}^{L-1} \frac{T(n)}{\Delta t} y^n = \sum_{n=1}^{L-1} n(L-n) y^n \tag{2.2.17}$$

from our definition of the generating function. Hence,

$$T(n) = n(L-n)\Delta t. \tag{2.2.18}$$

This is the complete solution. To check the consistency of this result with that derived in the continuum, we take the limit $L \to \infty$ and define $x = \lim_{L\to\infty} \frac{n}{L}$ such that $x$ is a continuous variable. In this regime, the absorbing sites at $n = 0$ and $n = L$ correspond to $x_0 = 0$ and $x_1 = 1$. As for $T(n)$, we may write

$$T(n) = L^2 \Delta t \left(\frac{n}{L}\right)\left(1 - \frac{n}{L}\right). \tag{2.2.19}$$

Thus, setting $\Delta t = \frac{1}{L^2}$,

$$\begin{aligned} T(x) &= \lim_{L\to\infty} \left[L^2 \Delta t \left(\frac{n}{L}\right)\left(1 - \frac{n}{L}\right)\right] \\ &= x(1-x). \end{aligned} \tag{2.2.20}$$

Comparing this with eq. (2.1.5) for $x_0 = 0$ and $x_1 = 1$, we see that the two results are consistent.

In summary, the first-passage time to absorption for a symmetric random walker as described in the previous section was solved via an alternative means involving the kernel method, where the value of $T(1)$ was fixed to ensure the convergence of the generating function. Specifically, we multiplied both sides of eq. (2.2.1) by $y^n$ and summed over $n$ to obtain an equation which can be rearranged for $G(y)$ in closed form. The kernel method and a power-series expansion were then used to write $G(y)$ as a polynomial whose coefficients were read off to reveal the explicit form of $T(n)$.

## 2.3 Monte Carlo methods for simulating stochastic processes

Though most of the work of this thesis is analytical, simulations are required to obtain data and validate our theoretical predictions. We therefore finish this chapter by considering the techniques used to simulate the systems that we study in this thesis. Since all such systems feature stochasticity, pseudo-random sampling is necessary to generate their dynamics. Techniques of this kind are known as *Monte Carlo* methods [103], and we describe their implementation in what follows.

The systems that we will introduce in chapters 3 to 5 feature dynamics closely related to that described in section 1.3.2 in the context of the SEB model [54]. There, particles hop in their direction of motion as a Poisson process with rate $\gamma$, and change direction as a Poisson process with rate $\omega$. Since waiting times between Poisson events are exponentially distributed, an algorithm that samples a waiting time for the next event in the process is required. For example, if we consider a single particle, the time to the next hop is distributed as $\gamma \mathrm{e}^{-\gamma t}$, where $t \geq 0$. Similarly, the time to the next tumble is distributed as $\omega \mathrm{e}^{-\omega t}$. And by the properties of Poisson processes, the time to the next event – hop or tumble – is distributed as $(\gamma + \omega)\mathrm{e}^{-(\gamma+\omega)t}$, where $\gamma+\omega$ is the combined rate. Using these facts, a continuous-time Monte Carlo algorithm known as a *Gillespie algorithm* [104] may be implemented. A pseudo-random number generator may be used to draw a waiting time from the appropriate exponential distribution. For the

case of one particle, one could draw from two distributions: one for hops and one for tumbles. The clock is moved forward to the earliest such event, and a new waiting time for the next event of the type executed is generated. This process continues until the desired simulation time has been reached. An alternative means of simulating the same system would be to draw an event waiting time from a combined distribution as described above, and to then assign the event as a hop or a tumble by, for example, drawing from an appropriately weighted Bernoulli distribution. These ideas can also be used when simulating an arbitrary number of particles, $N$. Again, one can assign waiting-time distributions to each particle, find the next scheduled event, and then update the appropriate waiting time once the clock has moved forward and the event has been executed. Such an approach might be useful if, say, the rates for all particles are different. If the rates are the same for each particle, then a single combined distribution with rate $N(\gamma + \omega)$ may be a better choice. One first draws a waiting time from the combined distribution; a particle is then chosen with probability $\frac{1}{N}$ to execute the next event at the drawn time, and the type of event that occurs is once more determined by drawing from a Bernoulli distribution. An alternative in this case is to have separate waiting-time distributions for hops and tumbles such that the foregoing final step can be dispensed of at the cost of having to determine whether the next event is a hop or a tumble.

The stochastic cellular automaton (CA) of chapter 6 has also been simulated using Monte Carlo techniques. Unlike the systems described above, the cellular automaton updates in discrete time. Conventional CA update deterministically based on a set of local update rules; in the cases we will look at, how the site under consideration updates is determined by the states of its two nearest neighbours. In the stochastic generalisation, however, some of the update rules are altered such that with probability $q$ one update is executed, and with probability $p = 1 - q$ a different update is executed. A simple Monte Carlo algorithm is therefore implemented in which the central site of a local three-site configuration is updated according to a Bernoulli distribution that reflects the stochastic update probabilities. Specifically, the implemented algorithm looks at the state of the site under consideration as well as the states of its nearest neighbours. If, according to the CA's rules, this three-site configuration should yield a deterministic update, said update is executed. If, however, this configuration corresponds instead to a stochastic update rule as described above, then the central site is updated according to a Bernoulli distribution, where one of the possible updates is executed with probability $q$, and where the second

possible update occurs with probability $p$. This procedure is then repeated for all sites to be updated at that time step.

Due to the basic principles that they are built upon, Monte Carlo simulations prove very useful for simulating stochastic systems. By generating pseudo-random stochastic processes, it is possible to accurately simulate a system's stochastic dynamics. Furthermore, due to their simplicity and widespread usage, Monte Carlo simulations are relatively straightforward to implement, and many programming languages incorporate built-in features that are geared towards them. Consideration has to be made, however, for the length of simulation time that is required to accurately determine a property of interest. For example, if one wishes to numerically obtain the stationary state of a system, one has to consider the time taken to reach stationarity as well as allow enough simulation time such that each configuration is visited on many occasions, thus ensuring accuracy of the recorded stationary distribution. One may also have to account for lack of ergodicity: if a system's state space comprises disjoint subspaces then multiple simulation runs are required.

## 2.4 Summary

In this chapter, we have demonstrated the mathematical methods of backward equations and generating functions that we will make use of in chapters 3 to 5. Additionally, we have discussed the Monte Carlo methods that are used to simulate the nonequilibrium systems investigated throughout chapters 3 to 6. Taking this chapter in combination with chapter 1, we now have the background required to begin our investigations.

# Chapter 3

# A first-passage approach to jamming and clustering in a multidimensional many-body system of persistent random walkers

In this chapter, a microscopic model of excluding persistent random walkers (PRWs) is considered. Unlike previous microscopic models of interacting PRWs, where analytical results are limited to one-dimensional domains and to two particles at most, we hereunder present an analytical study of a many-body model in an arbitrary number of dimensions $d$, where $d \geq 2$.

Unlike microscopic models, a multitude of studies exist which explore the emergent features of interacting PRWs at the population level. Field-theoretic and computational work constitutes the primary approaches in such cases, and has been paramount to our current understanding of motility-induced phase separation (MIPS) – the phenomenon in which particles cluster together due to density-dependent motilities (as discussed in the introduction). Whilst much useful information has been garnered using these approaches, they also have their limitations. We will discuss these in detail shortly, but briefly we remark that arguably the biggest limitation is an incomplete understanding of precisely how the emergent phenomena of such systems arise. It is for this reason that microscopic models are invaluable, as they enable us to better understand how population-level features of active systems emerge from processes that occur on

the level of individual particles.

We now outline the structure of this chapter. We will begin in section 3.1 with a brief discussion of the results and limitations of various microscopic and macroscopic studies of PRWs to date, highlighting the need for models which attempt to bridge the gap in understanding between the two paradigms. We will then present the details of the microscopic model considered in this chapter in section 3.2. In section 3.3, the notions of 'sea' and 'channel' states will be introduced as a means of tackling a two-particle problem in an arbitrary number of dimensions $d$, where $d \geq 2$. A generalisation to a dilute gas of $N$ PRWs will thereafter be made in section 3.4, which will lead onto an investigation of multi-particle clustering. Finally, extensions will be discussed and concluding remarks will be made in sections 3.5 and 3.6, respectively.

The work presented in this chapter was published in [1].

## 3.1 Single- and many-body PRW systems

We begin this chapter with a brief review of previous work, starting with the properties of single PRWs. Such work began in the early 1900s when Fürth introduced the PRW as a model for diffusion in various biological settings [105]. Shortly after, Taylor introduced the notion of persistence in order to understand the 'diffusing power' of turbulent flows, which he recognised as being able to transport heat in an analogous way to molecular diffusion [106]. Then, three decades later, Goldstein showed that the continuous-space probability distribution of a single PRW obeys the telegrapher's equation [107] – a partial differential equation which is second-order in both the spatial and temporal variables. By establishing the applicability of single PRWs to a wide range of contexts and providing the first analytical results concerning them, these three works laid the foundations of what was to become a fruitful research topic. Since the work of Goldstein, PRWs have proved useful in modelling photon transport through various media [108–111], have found application in biochemical settings when modelling polymers [112] and molecular motor-driven transport [113], and have proved to be applicable in the context of animal [114] and, most prominently, bacterial motility patterns [52, 57].

### 3.1.1 Derivation of the telegrapher's equation

We will now briefly survey some of the statistical and nonequilibrium properties of single PRWs. For the purpose of providing a pedagogical demonstration of how scaling arguments can be used to rigorously arrive at a continuum description – something we have already touched on in section 2.1 and that we will make frequent use of throughout this thesis – we start by giving a microscopic derivation of the telegrapher's equation. Let $P_+(n,t)$ and $P_-(n,t)$ be the probabilities of finding the PRW moving to the right and left, respectively, at lattice site $n$ and time $t$. Then, the microscopic master equations read

$$\frac{\partial P_+(n,t)}{\partial t} = \gamma P_+(n-1,t) + \omega P_-(n,t) - \gamma P_+(n,t) - \omega P_+(n,t) \tag{3.1.1}$$

$$\text{and} \quad \frac{\partial P_-(n,t)}{\partial t} = \gamma P_-(n+1,t) + \omega P_+(n,t) - \gamma P_-(n,t) - \omega P_-(n,t), \tag{3.1.2}$$

where $\gamma$ is the rate of hopping and $\omega$ is the rate of reversal, as per the notation of chapter 1. Letting $x = an$, where $a = \Delta x$ measures the lattice spacing, the above may be re-expressed as

$$\frac{\partial p_+(x,t)}{\partial t} = \gamma p_+(x-a,t) + \omega p_-(x,t) - \gamma p_+(x,t) - \omega p_+(x,t) \tag{3.1.3}$$

$$\text{and} \quad \frac{\partial p_-(x,t)}{\partial t} = \gamma p_-(x+a,t) + \omega p_+(x,t) - \gamma p_-(x,t) - \omega p_-(x,t). \tag{3.1.4}$$

Taking $a$ to be small, Taylor-expanding the above equations yields

$$\frac{\partial p_+(x,t)}{\partial t} = -a\gamma \frac{\partial p_+(x,t)}{\partial x} + \omega p_-(x,t) - \omega p_+(x,t) \tag{3.1.5}$$

$$\text{and} \quad \frac{\partial p_-(x,t)}{\partial t} = +a\gamma \frac{\partial p_-(x,t)}{\partial x} + \omega p_+(x,t) - \omega p_-(x,t). \tag{3.1.6}$$

We now do two things. Firstly, we differentiate the above equations with respect to $t$. In order to eliminate the mixed derivatives that result on the right-hand side of each equation, we also differentiate the above equations with respect to $x$, and substitute appropriately. Dropping the arguments of $p_\pm(x,t)$ for brevity, this leads to

$$\frac{\partial^2 p_+}{\partial t^2} = a^2\gamma^2 \frac{\partial^2 p_+}{\partial x^2} + a\gamma\omega \frac{\partial (p_+ - p_-)}{\partial x} - \omega \frac{\partial (p_+ - p_-)}{\partial t} \tag{3.1.7}$$

$$\text{and} \quad \frac{\partial^2 p_-}{\partial t^2} = a^2\gamma^2 \frac{\partial^2 p_-}{\partial x^2} + a\gamma\omega \frac{\partial (p_+ - p_-)}{\partial x} + \omega \frac{\partial (p_+ - p_-)}{\partial t}. \tag{3.1.8}$$

The total probability of being at site $n$ is $p := p_+ + p_-$; hence,

$$\frac{\partial^2 p}{\partial t^2} = a^2\gamma^2\frac{\partial^2 p}{\partial x^2} + 2a\gamma\omega\frac{\partial(p_+ - p_-)}{\partial x}. \tag{3.1.9}$$

Finally, from eqs. (3.1.5) and (3.1.6) we deduce

$$a\gamma\frac{\partial(p_+ - p_-)}{\partial x} = -\frac{\partial p}{\partial t}, \tag{3.1.10}$$

yielding

$$\frac{\partial^2 p}{\partial t^2} + 2\omega\frac{\partial p}{\partial t} = a^2\gamma^2\frac{\partial^2 p}{\partial x^2}\ . \tag{3.1.11}$$

This equation becomes exact when we take $a \to 0$. For an appropriate scaling, we must then take $\gamma \to \infty$ such that the product $a\gamma$ is finite and fixed; we denote this limiting value by $\Gamma := \lim_{a\to 0,\gamma\to\infty} a\gamma$. This scaling limit ensures that persistence is maintained at the level of the continuum: if each lattice site is infinitesimally separated, then an infinite number of hops are required to move a finite distance. As for the reversal rate $\omega$, this must remain $\mathcal{O}(1)$: if scaled as $\mathcal{O}(a^\tau)$ for $\tau > 0$, the persistence length – that is, the mean run length between two reversals – diverges such that no reversals are possible; and if scaled as $\mathcal{O}(a^\tau)$ for $\tau < 0$, persistence is lost as reversals occur infinitely quickly. The final form of our equation is thus

$$\frac{\partial^2 p}{\partial t^2} + 2\omega\frac{\partial p}{\partial t} = \Gamma^2\frac{\partial^2 p}{\partial x^2}\ , \tag{3.1.12}$$

which is known as the telegrapher's equation. This has the simple interpretation of being a standard diffusion equation with an additional inertia term, this being the signature of persistence and hence nonequilibrium.

### 3.1.2 Nonequilibrium properties of single PRWs

We now turn to the properties of the PRW that make it a nonequilibrium object. We recall from the introduction that, intuitively speaking, nonequilibrium systems are those which exhibit currents. Thus, we understand the PRW to be a nonequilibrium object based on its trajectory as a series of randomly-oriented runs, where each run is a particle current. At the level of detailed balance, a simple interpretation presents itself. Consider, for example, a PRW moving in the positive direction of a one-dimensional lattice. With some probability per unit time, the walker is able to hop from site $n$ to site $n$+1; however, in order for the walker to transition back to its original state at site $n$, it must do so in

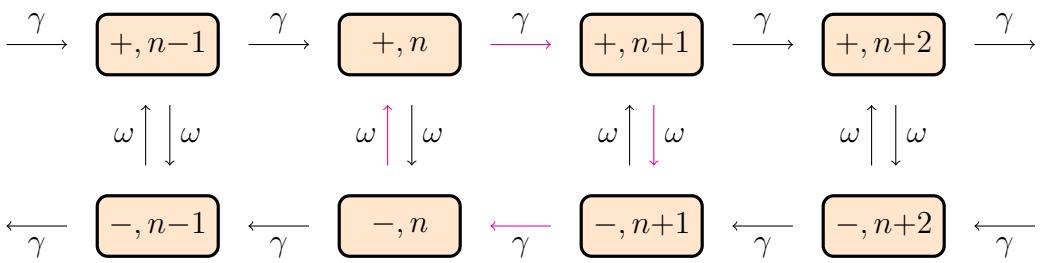


**Figure 3.1** *State space of a single PRW. We observe direct probability flux from state* $(+, n)$ *to state* $(+, n{+}1)$*, but observe no such flux regarding the reverse transition. The quickest route back to state* $(+, n)$ *comprises a reversal, a hop, and a second reversal. This route is marked in magenta.*

multiple steps. Put differently, there is direct probability flux in the first case, and indirect flux in the second case (intermediate configurations must be accessed first). An analogous situation holds for negative-moving walkers. Since detailed balance requires pairwise flux cancellation between all system configurations, it is concluded that the PRW is out of equilibrium. We demonstrate these ideas in fig. 3.1

As a consequence of its nonequilibrium nature, we expect the PRW to exhibit nontrivial physical behaviours. A fundamental example of this is given in [62] wherein the dynamical relaxation spectrum is derived for a PRW on a periodic lattice in one dimension. Fixing $\gamma = 1$ for simplicity, eqs. (3.1.1) and (3.1.2) are solved by the Fourier series

$$\mathbf{g}(k,t) = \sum_{n=1}^{L} \mathrm{e}^{\frac{2\pi i k n}{L}} \begin{pmatrix} P_+(n,t) \\ P_-(n,t) \end{pmatrix}, \tag{3.1.13}$$

where $k = 1, ..., L$ and where $L$ is the number of lattice sites. For all $n$, the above solution recasts the master equations as

$$\frac{\partial \mathbf{g}(k,t)}{\partial t} = \begin{pmatrix} \mathrm{e}^{\frac{2\pi i k}{L}} - (1+\omega) & \omega \\ \omega & \mathrm{e}^{-\frac{2\pi i k}{L}} - (1+\omega) \end{pmatrix} \mathbf{g}(k,t), \tag{3.1.14}$$

where the above matrix constitutes the $n$th block on the diagonal of the Markov matrix in Fourier space for all $n$ (that there is no reference to $n$ in the above equation is a consequence of translational invariance). Thus, the full eigenvalue spectrum comprises the eigenvalues of the above matrix for all values of $k$. One

finds

$$\lambda^{(s)}(k) = -2\sin^2\left(\frac{\pi k}{L}\right) - \omega + s\sqrt{\omega^2 - \sin^2\left(\frac{2\pi k}{L}\right)}\,, \tag{3.1.15}$$

where we observe two distinct 'bands' corresponding to the signs $s = \pm 1$ of the square root. The stationary mode occurs when $k = 0$ and $s = 1$. The corresponding mode for $s = -1$ has eigenvalue $-2\omega$, and is associated with the relaxation of an initial distribution into the state space's + and − subsets via tumbling.

The above spectrum comprises a rich and varied structure. For large values of $\omega$ the spectrum is entirely real. At the special value $\omega = 1$, all eigenvalues corresponding to $s = -1$ coalesce to $-2$. Decreasing $\omega$ further, the bands begin to 'cross' beyond the coalescence point and, since the argument of the square root can be negative, complex-conjugated pairs emerge (at the exceptional points $\omega = |\sin\left(\frac{2\pi k}{L}\right)|$, such pairs coincide on the real line). Finally, all eigenvalues reside on the unit circle centred at $-1$ when $\omega = 0$. These behaviours are depicted graphically in fig. 3.2. The different regimes that arise here realise a 'dynamical transition' in the spatial relaxation times at $\omega = \omega^*(L) = \sin\left(\frac{2\pi}{L}\right)$, corresponding to $k = s = 1$. We have

$$\lambda^{(1)}(1) = -2\sin^2\left(\frac{\pi}{L}\right) - \omega + \sqrt{\omega^2 - \sin^2\left(\frac{2\pi}{L}\right)}\,. \tag{3.1.16}$$

Since the relaxation time associated with this mode is $\tau_{\max} = -(\mathrm{Re}\{\lambda^{(1)}(1)\})^{-1}$, a transition occurs between purely exponential relaxation and oscillatory exponential relaxation at $\omega^*$, manifesting as a cusp as shown in fig. 3.3.

What the above case study emphasises is how complex behaviours are able to emerge when detailed balance is broken – even in very simple PRW systems. The equilibrium analogue to this system – that of the periodic random walker – is much simpler by contrast, with eigenvalue spectrum $-2\sin^2\left(\frac{\pi k}{L}\right)$. The fact that equilibrium is the exception and not the rule is what allows for nontrivial behaviours to emerge; that the PRW system exhibits dynamical transitions is a consequence of its being out of equilibrium for all $\omega < \infty$, allowing one to tune the system's overall behaviour.

The case study presented above is one of many on the nonequilibrium properties of single PRWs. Other exact results in one dimension include mean first-passage times [115] and large-deviation properties [116]. The stationary state, relaxation

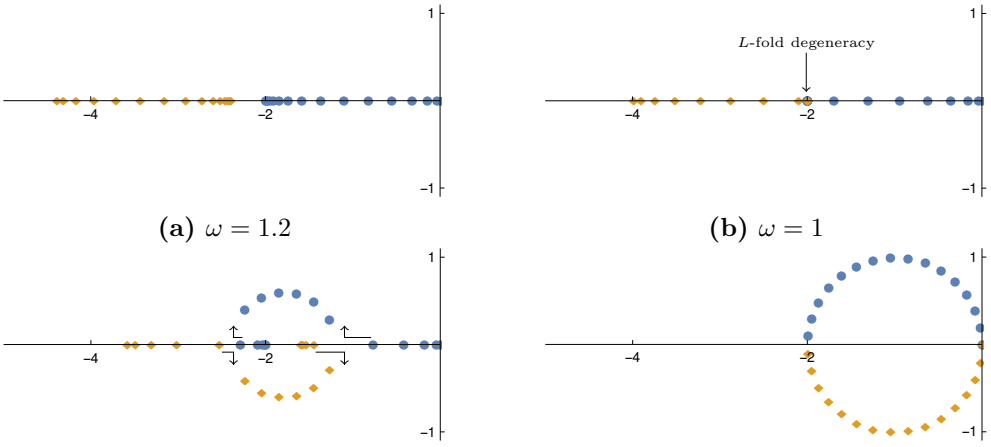


**(a)** $\omega = 1.2$ **(b)** $\omega = 1$

**(c)** $\omega = 0.8$ **(d)** $\omega = 0$

**Figure 3.2** *(Reproduced from [62].) Eigenvalue spectra for various $\omega$, where the horizontal and vertical axes correspond to real and imaginary parts, respectively, and where blue circles and yellow diamonds respectively correspond to the bands $s = +1$ and $s = -1$. The spectrum is entirely real when $\omega$ is large. When $\omega$ crosses over to the persistent regime ($\omega < 1$), an $L$-fold degeneracy occurs at $-2$ before the eigenvalues cross and begin to form conjugated pairs. These pairs form a unit circle at infinite persistence.*

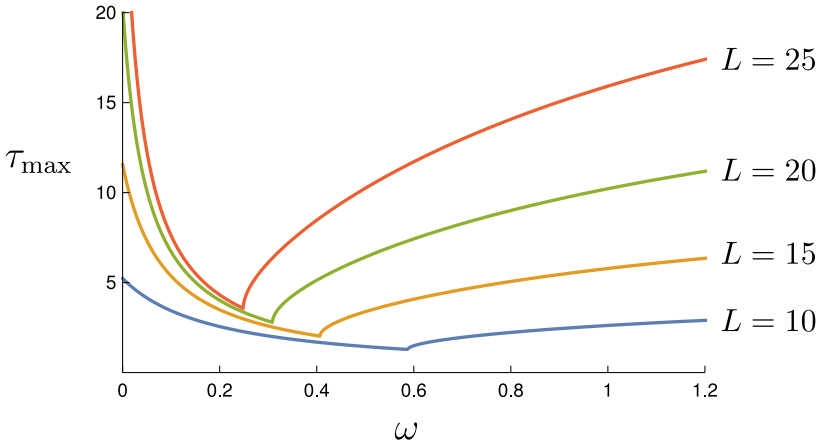


**Figure 3.3** *(Reproduced from [62].) Spatial relaxation times against $\omega$ for varying lattice sizes. A dynamical transition occurs at $\omega = \omega^*(L)$, manifesting as a series of cusps.*

times and first-passage properties have also been solved for in a variant of the dynamics that incorporates a diffusive component [117]. In higher dimensions, the stationary distribution for a particle confined to an harmonic trap [118], the probability of remaining in the upper-half plane [119], the perimeter of the convex hull [120], and large-deviation statistics [121] have also been established.

### 3.1.3 Generalisations to multiple PRWs

Having reviewed the properties and behaviours of single PRWs, we now turn our attention to the problem of multiple PRWs. In particular, in accordance with the topic of this chapter, we are interested in the effects of adding interactions between PRWs.

As mentioned in the introduction, interest in interacting PRWs began when Tailleur and Cates constructed a mapping from a system of many interacting run-and-tumble particles to that of one in equilibrium [58], allowing for analysis via equilibrium techniques. Results concerning these methods are summarised in [41], with perhaps the most striking finding being that of MIPS driven by a feedback between particles accumulating where the propulsion speed is low and this speed decreasing due to crowding from nearby particles. Whilst the methods described above have proven useful at the population level, they tell us little about the precise microscopic origins of emergent phenomena such as MIPS. It is the aim of this chapter to address this problem analytically.

A microscopic approach to understanding MIPS was first attempted by Thompson et al. [52]. Their model consists of a one-dimensional lattice inhabited by PRWs whose hop and tumble rates are site-dependent. Exact microscopic solutions were derived for the non-interacting case and a *zero-range* case in which the hop rate from site $n$ depends on the current configuration of particles at site $n$ only (and not on the configuration of the destination site). This was achieved by deriving conditions for a factorised steady state to exist on a periodic domain; thereafter, exact expressions for the steady state and an effective free energy were determined. With the density-dependent hop rate

$$\gamma_n(m_+, m_-) = \begin{cases} v_0[1-(m_+ + m_-)M^{-1}], & m_+ + m_- < M \\ v_0 M^{-1}, & m_+ + m_- \geq M \end{cases} , \qquad (3.1.17)$$

where $\gamma_n(m_+, m_-)$ denotes the hop rate at site $n$ given that site $n$ is occupied

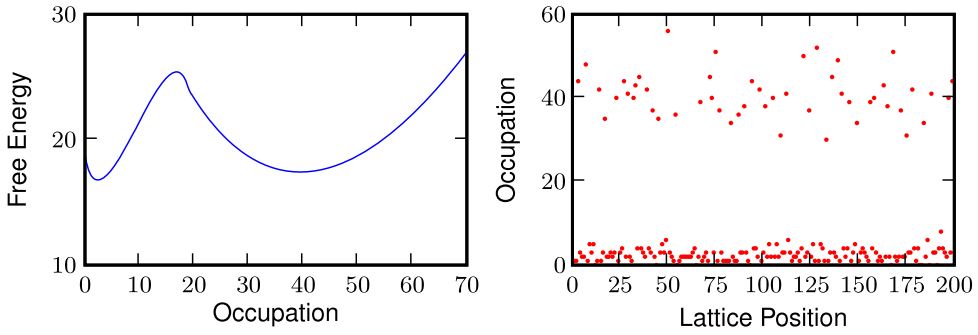


**Figure 3.4** *(Reproduced from [52].) Left: effective free energy as a function of occupation for* $\omega_n = \frac{1}{2}\ \forall n$*,* $M = 20$*,* $v_0 = 10$*, and particle number* 2400 *on a lattice of* $L = 200$ *sites. Right: snapshot of site-occupation numbers for the same set of parameters after the system was allowed to relax for* 1000 *time steps. We observe two minima in the free energy corresponding to the two bands of occupation.*

by $m_+$ right-moving particles and $m_-$ left-moving particles, and where $v_0$ and $M$ are constant, strong agreement with simulation data was found. This is shown in fig. 3.4.

Further progress was made upon the introduction of the persistent exclusion process (PEP) in [53]. This study investigated on-lattice simulation data on periodic one- and two-dimensional domains for excluding PRWs as outlined in the introduction. Specifically, the simulations were run in discrete time using a random-sequential update scheme [27] in which a fixed number of particles are considered, one by one, at each time step. With some predefined probability, the particle under consideration has its direction reset (it tumbles), but otherwise preserves its current direction. The particle then hops to the nearest-neighbour site in its current direction of motion given that said site is empty. At high levels of persistence (small tumble rate), separation into dense multiparticle clusters and dilute regions was observed, reminiscent of MIPS. Using entropic arguments, it was shown that the cluster-size distribution in one dimensions, $F_c(\ell)$, obeys

$$F_c^{(1)}(\ell) = A_c \mathrm{e}^{-\frac{\ell}{\ell_c}}, \tag{3.1.18}$$

where $\ell$ is cluster length and where $A_c$ and $\ell_c$ are constants which may be determined from the parameters of the system. Crucially, this inspired a form for the cluster-size distribution in two dimensions, where clusters are markedly different in that they are not necessarily compact (they may feature holes). The

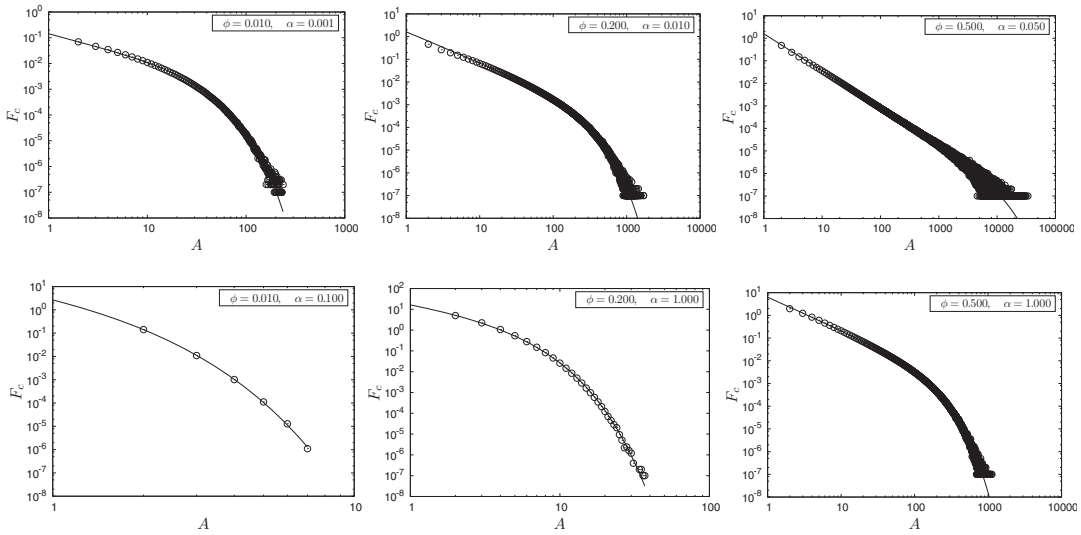


**Figure 3.5** *(Reproduced from [53].) Cluster-size distributions in the PEP in two dimensions for various particle concentrations, $\phi$, and tumble rates, $\alpha$, (including tumbles that maintain a particle's current direction) as determined by simulation data (empty circles). The solid lines indicates fits according to eq.* (3.1.19).

cluster-size distribution in two dimensions,

$$F_c^{(2)}(A) = A^{-\nu} \mathrm{e}^{-\frac{A}{A_c}}, \tag{3.1.19}$$

where $A$ is the cluster area, $\nu$ lies in the range $1 < \nu < 1.5$, and where $A_c$ is the characteristic cluster area, is shown to match simulation data in fig. 3.5 (the values of $\nu$ and $A_c$ in each case shown in fig. 3.5 were determined by fitting simulation data to eq. (3.1.19)).

The model presented above is of interest since it is lattice-based, thereby giving the particles which it hosts a finite size; exclusion is therefore an obvious choice of interaction to implement. Moreover, the methods of [58] (mapping to thermodynamic free energies) cannot be applied to exclusion interactions, thus rendering treatments which appeal directly to interactions at the level of individual particles important. We therefore see the relevance of the SEB model [54] whose results, namely the derivation of two-particle effective potentials, we reviewed in section 1.3.2. Whilst a solution to the many-body generalisation of the PEP has so far eluded the active-matter community [122], a number of further studies at the two-particle level have since yielded further insight. One such example is [63], which builds upon the SEB model by accommodating a biologically realistic finite tumble duration. At the level of the lattice, two length scales emerge in the stationary distribution. The first of these is a jamming

length scale, which we understand as follows. After the walkers tumble out of a jammed state, they proceed to follow each other for, on average, one persistence length. During this time, the stochasticity of the hops means that the walkers do not always occupy adjacent sites, thus 'smearing out' the jammed contribution to the stationary distribution over some length scale as an exponential decay. This feature carries over from SEB. In contrast to SEB, however, a second length scale emerges which relates to the distance covered by a moving particle over the time scale for which its partner tumbles. Like the jamming contribution, this also manifests as an exponential decay in the stationary distribution. Of interest is how these length scales behave in the continuum limit in which runs are ballistic and tumble times remain finite: the former length scale vanishes as its associated exponential components sharpen up to delta functions (as we noted in chapter 1) whilst the latter remains finite. Further work on the two-particle case includes [62] which, in addition to the one-particle case reviewed earlier, solves the time-dependent analogue of the SEB model, and [123], which solves the SEB model by introducing a diffusive component to the dynamics.

Finally, more recent work has attempted to bridge the gap between microscopic and macroscopic descriptions of the PEP, or variants thereof, beyond what was reported in [52, 53]. The work of [124] builds upon [53] by allowing multiple occupancies per site, revealing three parameter-dependent phases: those of particles gases, cluster gases, and a coarsened phase. A full many-body dynamics was shown to admit an exact hydrodynamic description when a diffusive component dominates the directed motion and the reorientation [125], with the key finding being that a homogeneous density field is unstable to phase separation above a critical density that decreases with increasing Péclet number (the ratio of the advective and diffusive length scales) in one dimension. In [126], hydrodynamics, lattice simulations and a field-theoretic description of a microscopic model were used to show that the critical behaviour of MIPS belongs to the Ising universality class with conserved dynamics. Finally, multispecies lattice models were investigated in [127], where it was found generally that the associated mean-field descriptions amount to systems of nonlinear advection-diffusion equations in two dimensions. In this chapter, we aim also to establish a firm link between a microscopic and macroscopic description of the PEP, focussing in particular on the scaling behaviours of MIPS.

## 3.2 The model

We now present the model considered in this work. The model comprises a periodic square/(hyper)cubic lattice of dimension $d \geq 2$ which measures $L$ sites in each of the lattice's principal directions. Particles inhabit the lattice, where the number of particles present in the system is $N$. A $d$-dimensional unit vector $(0, ..., 0, \pm 1, 0, ..., 0)$ specifies the direction of motion of each particle, where the basis vectors are aligned with the lattice's principal directions. Each particle hops, according to a Poisson process with mean rate $\gamma$, to the nearest site which is parallel to its direction of motion unless a second particle is present on the target site; in this case, the hop is rejected and the particle remains on its current site. As with other PEP variants, this encodes the exclusion interaction that the particles undergo. Furthermore, each particle chooses a new, distinct direction of motion according to a Poisson process with mean rate $\omega$, where we choose $\omega \ll \gamma$ such that each particle executes many hops (a run) before changing its direction of motion (a tumble). This choice of $\omega$ fixes the particles as PRWs. Finally, as previously defined in the context of [54], a configuration in which both particles mutually block each other is said to be *jammed*. One of the particles must tumble in order for a pair to exit a jammed configuration. An example of the evolution towards a jammed state is shown in fig. 3.6.

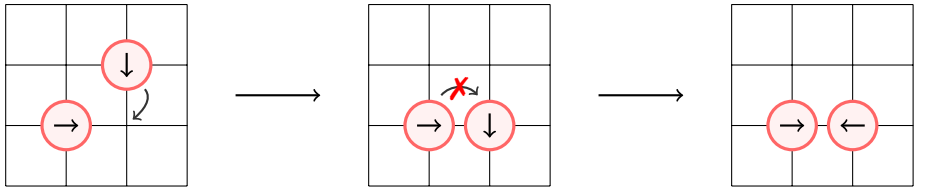


**Figure 3.6** *Showing a possible evolution from an unjammed state to a jammed state on a $4 \times 4$ square lattice inhabited by two PRWs. Lattice sites correspond to intersections of lines. A jammed state comprises particles on adjacent sites with opposing velocities as shown in the right panel above. One of the particles must move off its current site via a tumble in order for a jammed state to be exited.*

We will take $L \gg 1$ in our analysis, allowing us to approximate each particle's trajectory as ballistic. The advantages of this will be discussed in the next section.

Before proceeding, we acknowledge the limitations of this model regarding its discrete directions of motion. We will discuss how one might overcome such limitations towards the end of this chapter, but note here that some PRW systems

exhibit what is known as *directional locking* [128] in which the walkers do indeed fix their motion along discrete directions.

## 3.3 Jamming in a two-particle system: a first-passage approach

The principal aim of this section is to investigate the statistics of jamming for a pair of particles. The importance of this regarding the many-body system lies in the fact that jammed pairs of particles serve as nucleation sites for larger clusters. Thus, by establishing the nature of these nucleation sites, we can begin to understand the emergent phenomenon of MIPS from a fundamental point of view. This goes beyond what previous microscopic PRW models have established, and will form the subject of section 3.4.

### 3.3.1 Jamming probability

To begin our analysis, we define the *jamming probability*, $P_{\mathrm{J}}$. This is simply the average fraction of time that the two-particle system spends in jammed states. Defining $T_{\mathrm{J}}$ to be the mean lifetime of jammed states, and $T_{\mathrm{R}}$ to be the mean time that elapses between the cessation of a jammed state and the formation of a new jammed state, which we hereafter refer to as the mean return time, we have that

$$P_{\mathrm{J}} = \frac{T_{\mathrm{J}}}{T_{\mathrm{J}} + T_{\mathrm{R}}}. \tag{3.3.1}$$

As will be seen later, this quantity is crucial to our analysis. Our next task, therefore, is to calculate $T_{\mathrm{J}}$ and $T_{\mathrm{R}}$. The calculation of $T_{\mathrm{J}}$ is simple: each particle tumbles with rate $\omega$, and hence the total rate of either particle tumbling is $2\omega$; it hence follows that

$$T_{\mathrm{J}} = \frac{1}{2\omega}. \tag{3.3.2}$$

All that remains is to calculate $T_{\mathrm{R}}$. This calculation is more involved, and we will use first-passage techniques to carry it out. We devote the next section to this task.

### 3.3.2 Calculation of the mean return time in $d = 1$

To calculate the mean return time, we look to an analogous calculation in dimension $d = 1$ originally carried out in [54]. We will then modify this in the next section for dimension $d \geq 2$ by introducing the notion of 'sea' and 'channel' states, wherein we embed one-dimensional sub-domains in a multidimensional reservoir.

In [54], Slowman, Evans & Blythe considered a first-passage problem concerning two PRWs in one dimension whose solution we recapitulate in what follows. The aim was to calculate the mean time that elapses between jammed states – the same definition as we have used for $T_{\mathrm{R}}$. In the present one-dimensional case, we use $T_1$ to denote the corresponding quantity.

As in our model, SEB modelled tumbles (which amount to reversals in $d = 1$) as a Poisson process with rate $\omega$. Unlike our model, however, the domain was treated as being continuous by taking the limit $L \to \infty$. In order that the walkers are able to traverse finite distances on the scale of the domain before tumbling, the scaling $\frac{\omega}{\gamma} = \mathcal{O}\left(\frac{1}{L}\right)$ is chosen.[1] With this scaling limit in place, the walker trajectories become ballistic. To see why, we consider that the motion of each walker, when considered on the lattice, constitutes a random walk about a mean drift of velocity $\gamma$ due to the stochastity of the hopping dynamics. From random-walk statistics [99], it follows that each walker strays, between tumble events, an average of $\mathcal{O}(\sqrt{L})$ sites from the mean trajectory described above, since $\mathcal{O}(L)$ sites are traversed on such time scales. We hence conclude that in the chosen scaling limit, each walker strays a distance $\lim_{L\to\infty} \frac{\sqrt{L}}{L} = 0$ from a truly ballistic trajectory when measured as a fraction of the system size. Only after an infinite number of tumbles – $\mathcal{O}(L)$ – does the discrepancy between the stochastic and ballistic trajectories become comparable to the system size.

With this noted, we now proceed with the calculation. There are two contributions to $T_1$ to consider:

$$T_1 = T_{\mathrm{J}} + \frac{1}{2}T_{\mathrm{L}}. \tag{3.3.3}$$

The first contribution, $T_{\mathrm{J}}$, has the same definition as in eq. (3.3.2), and is a

[1] Whilst irrelevant in the calculation that follows, $\gamma = \mathcal{O}(L)$ is the most physical scaling of time in the context of bacterial dynamics, as it permits the walkers to traverse finite fractions of the box size on $\mathcal{O}(1)$ time scales.

consequence of the walkers necessarily following each other after one of them tumbles. The second contribution, $T_{\mathrm{L}}$, is that which results from the recession of the walkers after such a following event. There is a $\frac{1}{2}$ prefactor since either particle can tumble in a following state, but only the trailing walker can tumble to induce a receding state; if the leading walker tumbles then a jammed state is entered once more to give a third contribution of zero. Since $T_{\mathrm{J}}$ is already known, the calculation of $T_1$ boils down to the calculation of $T_{\mathrm{L}}$. We approach this calculation by setting up a coupled first-passage problem for the quantities $T_{\mathrm{A}}(x)$ and $T_{\mathrm{F}}(x)$, defined to be the mean times to jammed states from configurations in which the walkers are approaching each other and following each other, respectively, from some initial separation $x$, where $x \in (0, L)$. Once solved, $T_{\mathrm{L}}$ is given by $T_{\mathrm{L}} = T_{\mathrm{A}}(L)$.

Now, since tumbles obey Poisson statistics, waiting times to leave approaching/following configurations are distributed as $2\omega e^{-2\omega t}$. Thus, the probability that neither particle tumbles in an arbitrary time interval $\delta t$ is the sum over all probabilities of tumbling after $t = \delta t$, given by $\int_{\delta t}^{\infty} 2\omega e^{-2\omega t}\,\mathrm{d}t = e^{-2\omega\delta t}$. If this is the case, then we have

$$T_{\mathrm{A,no\text{-}tumbles}}(x) = \delta t + T_{\mathrm{A}}(x - 2\delta t), \tag{3.3.4}$$

where we have scaled the units of time according to $\gamma = 1$. Alternatively, the probability of tumbling in the infinitesimal interval $\delta t'$ to $\delta t' + \mathrm{d}(\delta t')$, where $\delta t' + \mathrm{d}(\delta t') < \delta t$, is $2\omega e^{-2\omega\delta t'}\,\mathrm{d}(\delta t')$. If this is the case, we have

$$T_{\mathrm{A,tumble}}(x) = \delta t' + T_{\mathrm{F}}(x - 2\delta t'). \tag{3.3.5}$$

We may therefore write down the following equation for $T_{\mathrm{A}}(x)$:

$$T_{\mathrm{A}}(x) = e^{-2\omega\delta t}\left[\delta t + T_{\mathrm{A}}(x - 2\delta t)\right] + \int_0^{\delta t} \mathrm{d}(\delta t')\, 2\omega e^{-2\omega\delta t'}\left[\delta t' + T_{\mathrm{F}}(x - 2\delta t')\right]. \tag{3.3.6}$$

This is simply a sum of the probabilities of tumbling at each future time weighted by the mean waiting times to the next jamming event. Since $\delta t$ is arbitrary, we may take it to be very small; this permits us to Taylor-expand the above equation to first order in $\delta t$. The first term becomes

$$e^{-2\omega\delta t}\left[\delta t + T_{\mathrm{A}}(x - 2\delta t)\right] \approx T_{\mathrm{A}}(x) + \left[1 - 2\omega T_{\mathrm{A}}(x) - 2\frac{\mathrm{d}T_{\mathrm{A}}(x)}{\mathrm{d}x}\right]\delta t\ . \tag{3.3.7}$$

To expand the integral, we need only keep zeroth-order terms in the integrand, for these will become first-order terms upon integration. The only term that survives in the integrand is $2\omega T_{\mathrm{F}}(x)$, and so

$$\int_0^{\delta t} \mathrm{d}(\delta t')\, 2\omega e^{-2\omega\delta t'} \left[\delta t' + T_{\mathrm{F}}(x - 2\delta t')\right] \approx 2\omega T_{\mathrm{F}}(x)\delta t. \tag{3.3.8}$$

Combining the facts presented above gives

$$T_{\mathrm{A}}(x) \approx T_{\mathrm{A}}(x) + \left[1 - 2\frac{\mathrm{d}T_{\mathrm{A}}(x)}{\mathrm{d}x} + 2\omega\left(T_{\mathrm{F}}(x) - T_{\mathrm{A}}(x)\right)\right]\delta t, \tag{3.3.9}$$

leading to

$$1 - 2\frac{\mathrm{d}T_{\mathrm{A}}(x)}{\mathrm{d}x} + 2\omega\left(T_{\mathrm{F}}(x) - T_{\mathrm{A}}(x)\right) = 0. \tag{3.3.10}$$

To convert this to a differential equation entirely in $T_{\mathrm{A}}(x)$, we must eliminate $T_{\mathrm{F}}(x)$.

Much like jammed states, the lifetime of a following state is $\frac{1}{2\omega}$; the particles thereafter approach or recede from each other. Mathematically,

$$T_{\mathrm{F}}(x) = \frac{1}{2\omega} + \frac{1}{2}\left[T_{\mathrm{A}}(x) + T_{\mathrm{A}}(L - x)\right], \tag{3.3.11}$$

where we emphasise here that the separation remains constant in the following state and note that the pair of terms in the square brackets results from the periodicity of the system. Substituting this into eq. 3.3.10 leads to

$$2 - 2\frac{\mathrm{d}T_{\mathrm{A}}(x)}{\mathrm{d}x} - \omega T_{\mathrm{A}}(x) + \omega T_{\mathrm{A}}(L - x) = 0. \tag{3.3.12}$$

We rearrange to find

$$\frac{\mathrm{d}T_{\mathrm{A}}(x)}{\mathrm{d}x} = 1 + \frac{\omega}{2}\left[T_{\mathrm{A}}(L - x) - T_{\mathrm{A}}(x)\right] \tag{3.3.13}$$

whose solution is

$$T_{\mathrm{A}}(x) = x + \frac{\omega x(L - x)}{2}. \tag{3.3.14}$$

This implies that

$$T_{\mathrm{L}} = T_{\mathrm{A}}(L) = L. \tag{3.3.15}$$

Hence,

$$T_1 = \frac{1}{2\omega} + \frac{L}{2}. \tag{3.3.16}$$

This completes the calculation. We shall see in the next section that a simple modification to the procedure presented above will allow us to generalise this calculation to $d \geq 2$.

### 3.3.3 Calculation of the mean return time in $d \geq 2$

To make the generalisation of the above calculation to $d \geq 2$, we introduce the notions of 'sea' and 'channel' states. Channel states comprise states wherein both walkers approach/follow each other in the same one-dimensional subdomain of the lattice, examples of which are shown in the first two panels of fig. 3.7. Sea states, meanwhile, comprise all other states as demonstrated in the remaining panels of the same figure.

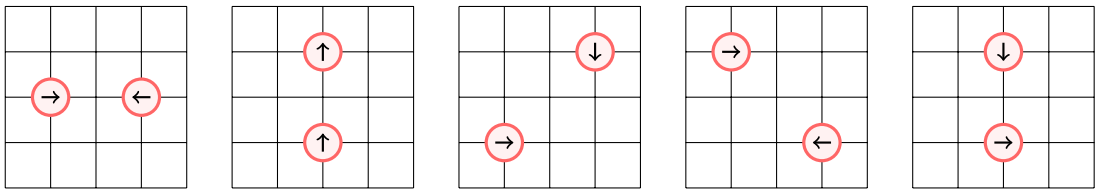

**Figure 3.7** *Examples of an approaching channel state (first panel), a following channel state (second panel) and three possible sea states (third, fourth and fifth panels) on a $5 \times 5$ square lattice. Once again, lattice sites are indicated by line intersections. Note that the final panel constitutes a sea state because the walkers are neither approaching nor following each other despite occupying the same one-dimensional sublattice; a channel state can be entered from this configuration if the bottom walker tumbles appropriately.*

We now note that, with this setup in place, the multidimensional problem considered here may be represented as a series of transient one-dimensional states that spontaneously arise due to the action of a reservoir, i.e. as long as we keep $L$ finite, and hence keep the channel width finite, channel states are guaranteed to spontaneously arise from sea states. Figure 3.8 shows the probability flow between the various types of states of the system.

#### Assumptions

In order to use the same mathematical formalism as in the previous calculation, we will assume $L$ to be large, thus allowing us to approximate the motion as

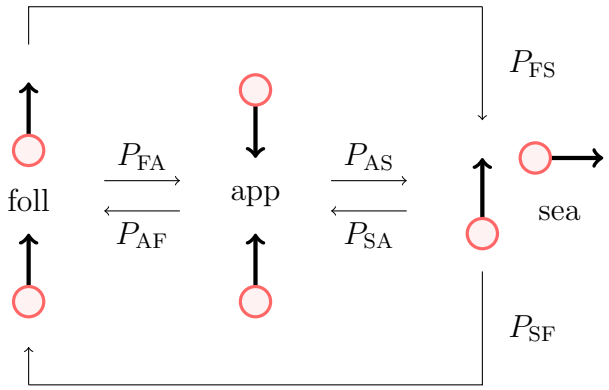


**Figure 3.8** *Probability flow diagram for transitions between the two types of channel states (following and approaching) and the sea state. The probabilities $P_{XY}$ specify the probability of entering state $Y$ from state $X$ at the points in time when a new state is chosen. Here, the states $X$ and $Y$ are one of $A$ (approaching), $F$ (following) or $S$ (sea). These probabilities are functions of $d$.*

ballistic.[2] Further, this implies that the rate at which channel states are entered from sea states is of order $\frac{1}{L^{d-1}} \ll 1$, which allows us to make two assumptions:

1. Firstly, we may assume that the mean time spent in the sea state is large and therefore independent of the initial channel-state separation from which it was entered. Simple probabilistic arguments will therefore be used to calculate this time.

2. Secondly, we may assume the separation at which a channel state is entered from the sea is uniformly distributed.

The second assumption is shown to be valid in the lower right panel of fig. 3.9.

### Modifying the $1d$ calculation

Now, from fig. 3.8 we are able to write down an expression for the mean time that elapses between jammed states, $T_{\mathrm{R}}$, based on the possibilities of entering a zero-separation following state and a sea state. Specifically, after the walkers exit a jammed state they either assume the same direction of motion (following

[2]Since we are keeping $L$ finite – contrary to the previous case – this is not strictly true. This approximation is good, however, as long as $L \gg 1$, and will allow us to write down the equations in terms of integrals instead of sums; this simplifies the mathematics and is permissible since it amounts to approximating sums to leading order in $L$. The emergent scaling behaviour discussed later in this chapter is not affected by this.

state) with probability $P_{\mathrm{AF}}$ or move off in different directions (sea state) with probability $P_{\mathrm{AS}}$. We therefore have

$$T_{\mathrm{R}} = P_{\mathrm{AF}} T_{\mathrm{F}}(0) + P_{\mathrm{AS}} T_{\mathrm{S}}. \tag{3.3.17}$$

Here we have introduced $T_{\mathrm{S}}$: the mean time taken to reach a jammed state from a sea state. From our first assumption above, this is constant. Specifically,

$$T_{\mathrm{S}} = T_{\mathrm{W}} + \frac{P_{\mathrm{SA}}}{L} \int_0^L T_{\mathrm{A}}(x)\,\mathrm{d}x + \frac{P_{\mathrm{SF}}}{L} \int_0^L T_{\mathrm{F}}(x)\,\mathrm{d}x\,. \tag{3.3.18}$$

We have introduced another quantity, $T_{\mathrm{W}}$, which measures the mean time taken to exit the sea upon entering it. The integrals then sum over contributions from entering channel states of all possible separations, where assumption 2 above is responsible for the $\frac{1}{L}$ prefactors (if we were to be more rigorous, these factors would be functions of $x$ and placed inside the integral).

To evaluate the above integrals, we require equations for $T_{\mathrm{F}}(x)$ and $T_{\mathrm{A}}(x)$. For the former, we have

$$T_{\mathrm{F}}(x) = \frac{1}{2\omega} + \frac{P_{\mathrm{FA}}}{2} \left[T_{\mathrm{A}}(x) + T_{\mathrm{A}}(L-x)\right] + P_{\mathrm{FS}} T_{\mathrm{S}}. \tag{3.3.19}$$

This a simple modification of eq. (3.3.11) where we have accounted for the possibility of entering sea states and weighted all future contributions according to fig. 3.8. Meanwhile, a similar modification to eq. (3.3.6) leads to

$$\begin{aligned} T_{\mathrm{A}}(x) = {} & \mathrm{e}^{-2\omega\delta t} \left[\delta t + T_{\mathrm{A}}(x - 2\delta t)\right] \\ & + \int_0^{\delta t} \mathrm{d}(\delta t')\, 2\omega \mathrm{e}^{-2\omega\delta t'} \left[\delta t' + P_{\mathrm{AF}} T_{\mathrm{F}}(x - 2\delta t') + P_{\mathrm{AS}} T_{\mathrm{S}}\right]. \end{aligned} \tag{3.3.20}$$

Since the sea state can be entered from an approaching state, a sea-state contribution has been added to the integrand and the weights have once more been adjusted accordingly. Carrying out a first-order expansion in $\delta t$ as before (keeping in mind that only zeroth-order terms contribute from the integrand) yields the differential equation

$$\frac{\mathrm{d}T_{\mathrm{A}}}{\mathrm{d}x} = \frac{1 + 2\omega[P_{\mathrm{AF}} T_{\mathrm{F}}(x) + P_{\mathrm{AS}} T_{\mathrm{S}} - T_{\mathrm{A}}(x)]}{2}. \tag{3.3.21}$$

We now have everything we need in order to solve for $T_{\mathrm{R}}$. Eliminating $T_{\mathrm{F}}(x)$ from

eq. (3.3.17) using eq. (3.3.19) yields

$$T_{\mathrm{R}} = \frac{P_{\mathrm{AF}}}{2\omega} + \frac{P_{\mathrm{AF}}P_{\mathrm{FA}}}{2}T_{\mathrm{A}}(L) + (P_{\mathrm{AS}} + P_{\mathrm{AF}}P_{\mathrm{FS}})T_{\mathrm{S}}, \tag{3.3.22}$$

where we have used the boundary condition $T_{\mathrm{A}}(0) = 0$, namely that two approaching particles with zero separation take zero time to meet. All that remains to do, therefore, is to calculate $T_{\mathrm{A}}(x)$ and $T_{\mathrm{S}}$. Noting

$$\int_0^L T_{\mathrm{A}}(x)\,\mathrm{d}x = \int_0^L T_{\mathrm{A}}(L-x)\,\mathrm{d}x\,, \tag{3.3.23}$$

we may substitute eq. (3.3.19) into eq. (3.3.18) and rearrange to determine that

$$T_{\mathrm{S}} = \frac{1}{1 - P_{\mathrm{SF}}P_{\mathrm{FS}}}\left[T_{\mathrm{W}} + \frac{P_{\mathrm{SF}}}{2\omega} + \frac{P_{\mathrm{SA}} + P_{\mathrm{FA}}P_{\mathrm{SF}}}{L}\int_0^L T_{\mathrm{A}}(x)\,\mathrm{d}x\right]. \tag{3.3.24}$$

Eliminating $T_{\mathrm{F}}(x)$ from eq. (3.3.21) using eq. (3.3.19) then yields

$$\frac{\mathrm{d}T_{\mathrm{A}}(x)}{\mathrm{d}x} = A + BT_{\mathrm{A}}(x) + CT_{\mathrm{A}}(L-x) \tag{3.3.25}$$

in which

$$A = \frac{1 + P_{\mathrm{AF}} + 2\omega(P_{\mathrm{AS}} + P_{\mathrm{AF}}P_{\mathrm{FS}})T_{\mathrm{S}}}{2}, \tag{3.3.26}$$

$$B = \omega\left(\frac{P_{\mathrm{AF}}P_{\mathrm{FA}}}{2} - 1\right), \tag{3.3.27}$$

$$\text{and} \quad C = \omega\left(\frac{P_{\mathrm{AF}}P_{\mathrm{FA}}}{2}\right). \tag{3.3.28}$$

We can solve this equation by defining

$$F(x) = \frac{1}{2}\left[T_{\mathrm{A}}(x) + T_{\mathrm{A}}(L-x)\right] \tag{3.3.29}$$

$$\text{and} \quad G(x) = \frac{1}{2}\left[T_{\mathrm{A}}(x) - T_{\mathrm{A}}(L-x)\right]. \tag{3.3.30}$$

Differentiation of the above gives

$$\frac{\mathrm{d}F(x)}{\mathrm{d}x} = (B-C)G(x) \tag{3.3.31}$$

$$\text{and} \quad \frac{\mathrm{d}G(x)}{\mathrm{d}x} = A + (B+C)F(x), \tag{3.3.32}$$

hence giving us

$$\frac{\mathrm{d}^2G(x)}{\mathrm{d}x^2} = (B+C)\frac{\mathrm{d}F(x)}{\mathrm{d}x} = (B^2-C^2)G(x). \tag{3.3.33}$$

Due to the antisymmetry $G(x) = -G(L-x)$, the solution must be of the form

$$G(x) = Q\sinh\left[\omega\mu\left(x-\frac{L}{2}\right)\right], \tag{3.3.34}$$

where

$$\mu = \sqrt{1-P_{\mathrm{AF}}P_{\mathrm{FA}}} \tag{3.3.35}$$

from the definitions of $B$ and $C$, and where $Q$ is a constant of integration. Differentiating $G(x)$ and substituting into eq. (3.3.32) gives us

$$F(x) = \frac{1}{\mu}\left\{\frac{A}{\omega\mu} - Q\cosh\left[\omega\mu\left(x-\frac{L}{2}\right)\right]\right\}. \tag{3.3.36}$$

Observing that

$$T_{\mathrm{A}}(x) = F(x) + G(x), \tag{3.3.37}$$

and applying our boundary condition $T_{\mathrm{A}}(0) = 0$, we arrive at

$$T_{\mathrm{A}}(x) = \frac{A}{\omega\mu^2}\left\{1 - \frac{\cosh\left[\omega\mu(x-\frac{L}{2})\right] - \mu\sinh\left[\omega\mu(x-\frac{L}{2})\right]}{\cosh\left(\frac{\omega\mu L}{2}\right) + \mu\sinh\left(\frac{\omega\mu L}{2}\right)}\right\}. \tag{3.3.38}$$

Hence

$$T_{\mathrm{A}}(L) = \frac{2A}{\omega\mu}\frac{1}{\mu+\coth\left(\frac{\omega\mu L}{2}\right)}. \tag{3.3.39}$$

We can now plug this into eq. (3.3.22) to obtain an expression for $T_{\mathrm{R}}$. One finds

$$T_{\mathrm{R}} = P_{\mathrm{AF}}P_{\mathrm{FA}}\frac{A}{\omega\mu}\frac{1}{\mu+\coth\left(\frac{\omega\mu L}{2}\right)} + \frac{P_{\mathrm{AF}}}{2\omega} + (P_{\mathrm{AS}}+P_{\mathrm{AF}}P_{\mathrm{FS}})T_{\mathrm{S}}. \tag{3.3.40}$$

Using the definitions eqs. (3.3.26) and (3.3.35), this may be written more succinctly as

$$\begin{aligned} T_{\mathrm{R}} &= (1-\mu^2)\frac{A}{\omega\mu}\frac{1}{\mu+\coth\left(\frac{\omega\mu L}{2}\right)} + \frac{A}{\omega} - \frac{1}{2\omega} \\ &= \frac{A}{\omega\mu}\frac{1+\mu\coth\left(\frac{\omega\mu L}{2}\right)}{\mu+\coth\left(\frac{\omega\mu L}{2}\right)} - \frac{1}{2\omega}. \end{aligned} \tag{3.3.41}$$

The constant $A$ still needs to be determined. This depends on $T_{\mathrm{S}}$ (eq. (3.3.26)),

which itself depends on the integral $L^{-1}\int_0^L T_{\mathrm{A}}(x)\,\mathrm{d}x$ (eq. (3.3.24)). This integral depends on $A$ again (eq. (3.3.38)), meaning we therefore have a self-consistency condition for $A$.

Evaluating the above integral, one finds

$$\begin{aligned}\frac{1}{L}\int_0^L T_{\mathrm{A}}(x)\,\mathrm{d}x &= \frac{1}{L}\frac{A}{\omega\mu^2}\left\{x - \frac{\sinh\left[\omega\mu\left(x-\frac{L}{2}\right)\right] - \mu\cosh\left[\omega\mu\left(x-\frac{L}{2}\right)\right]}{\omega\mu\left[\cosh\left(\frac{\omega\mu L}{2}\right) + \mu\sinh\left(\frac{\omega\mu L}{2}\right)\right]}\right\}\Bigg|_0^L \\ &= \frac{A\Lambda_L}{\omega\mu^2},\end{aligned} \tag{3.3.42}$$

where

$$\Lambda_L = 1 - \frac{2}{\omega\mu L}\frac{1}{\mu + \coth\left(\frac{\omega\mu L}{2}\right)}. \tag{3.3.43}$$

It thence follows from eqs. (3.3.24) and (3.3.26) that

$$A = \frac{1+P_{\mathrm{AF}}}{2} + \omega(P_{\mathrm{AS}} + P_{\mathrm{AF}}P_{\mathrm{FS}})\left\{\frac{1}{1-P_{\mathrm{SF}}P_{\mathrm{FS}}}\left[T_{\mathrm{W}} + \frac{P_{\mathrm{SF}}}{2\omega} + (P_{\mathrm{SA}} + P_{\mathrm{FA}}P_{\mathrm{SF}})\frac{A\Lambda_L}{\omega\mu^2}\right]\right\} \tag{3.3.44}$$

which can be rearranged for

$$2A = \frac{(1 + P_{\mathrm{AF}} - P_{\mathrm{FS}}P_{\mathrm{SF}} + 2(P_{\mathrm{AS}} + P_{\mathrm{AF}}P_{\mathrm{FS}})\omega T_{\mathrm{W}} + P_{\mathrm{AS}}P_{\mathrm{SF}})(1 - P_{\mathrm{AF}}P_{\mathrm{FA}})}{(1-P_{\mathrm{AF}}P_{\mathrm{FA}})(1-P_{\mathrm{FS}}P_{\mathrm{SF}}) - (P_{\mathrm{AS}} + P_{\mathrm{AF}}P_{\mathrm{FS}})(P_{\mathrm{SA}} + P_{\mathrm{FA}}P_{\mathrm{SF}})\Lambda_L}. \tag{3.3.45}$$

Expressions for the transition probabilities and the mean time spent in sea states, $T_{\mathrm{W}}$, are what remain in order for eqs. (3.3.41) and (3.3.45) to constitute a full solution to this problem. This we shall discuss now.

### Expressions for the transition probabilities and $T_{\mathrm{W}}$

Before writing down the transition probabilities, let us first remind ourselves exactly what it is that they are. As stated in fig. 3.8, the transition probability $P_{XY}$ denotes the probability that a transition from state $Y$ to state $X$ occurs at the moment in time that state $Y$ is exited. Referring to fig. 3.8, we see for example that when one of the walkers in a following state tumbles, there is some probability, $P_{\mathrm{FS}}$, that at that moment a sea state is entered, and likewise there is some probability, $P_{\mathrm{FA}} = 1 - P_{\mathrm{FS}}$, that an approaching state is entered.

With the above noted, the transition probabilities are simple to write down, since they depend only on the dimension of the system (all $\omega$ dependence is contained

in $T_{\mathrm{A}}(x)$, $T_{\mathrm{F}}(x)$ and $T_{\mathrm{S}}$). There are a total of $2d$ directions in which walkers can move along the lattice, and hence $2d-1$ *new* directions that can be chosen after a reorientation event. If transitioning from one channel state to another, then only one of these $2d-1$ directions can be adopted: a reversal. Since no directions are preferred, this tells us that

$$P_{\mathrm{AF}} = P_{\mathrm{FA}} = \frac{1}{2d-1}. \tag{3.3.46}$$

All other directions it is possible to adopt give rise to sea states. Thus,

$$P_{\mathrm{AS}} = P_{\mathrm{FS}} = \frac{2d-2}{2d-1}. \tag{3.3.47}$$

This brings us to entering channel states from sea states. Again, since no directions are favoured, it must be the case that

$$P_{\mathrm{SA}} = P_{\mathrm{SF}} = \frac{1}{2}, \tag{3.3.48}$$

i.e. the system is as likely to adopt an approaching state as it is to adopt a following state.

The calculation of $T_{\mathrm{W}}$ requires more extensive reasoning. As a reminder, $T_{\mathrm{W}}$ measures the mean time that elapses between channel states. By assuming that the system is 'randomised' sufficiently quickly after exiting a channel state, we can estimate this quantity using basic probabilistic arguments. We start by considering *orientational configurations* (OCs) of the system: the possible combinations of orientations of both particles. Since the particles are restricted to moving 'forwards' or 'backwards' along the $d$ principal axes of the lattice, there are $(2d)^2 = 4d^2$ total OCs. Of these, $4d$ of them forbid the system from accessing channel states directly due to (anti)parallel motion; there are hence $4d^2 - 4d = 4d(d-1)$ OCs which allow the system to access channel states via a single reorientation event. The probability of being in an OC that permits access to channel states after a single reorientation event is therefore $\frac{4d(d-1)}{4d^2} = \frac{d-1}{d}$. Once in such an OC, then to transition to a channel state all bar one of the walkers' coordinates must be the same, which occurs with probability $\frac{1}{L^{d-1}}$. If both of these criteria are met (that is, the system is in an appropriate OC and both walkers' coordinates coincide in the appropriate way), then with probability $\frac{2}{2d-1}$ the reorienting walker can enter a channel state, since there are $2d-1$ possible orientations that can be adopted but only 2 of them (anti-)align the

walkers. Finally, such events occur with rate[3] $\omega$ and an extra factor of 2 is needed to account for the fact that either of the two walkers could be the one in the position to actuate a channel state. Combining the foregoing, we estimate

$$T_{\mathrm{W}} = \left( \frac{d-1}{d} \cdot \frac{1}{L^{d-1}} \cdot \frac{2}{2d-1} \cdot \omega \cdot 2 \right)^{-1} = \frac{(2d-1)dL^{d-1}}{4(d-1)\omega}. \tag{3.3.49}$$

With the above all in place, we can use the expressions for $P_{\mathrm{FA}}$ and $P_{\mathrm{AF}}$ to determine an expression for $\mu$ as defined in eq. (3.3.35); namely

$$\mu = \frac{2\sqrt{d(d-1)}}{2d-1}. \tag{3.3.50}$$

Our expression for $A$ in eq. (3.3.44) simplifies considerably:

$$A = \frac{1 + dL^{d-1}}{1 - \Lambda_L}. \tag{3.3.51}$$

Finally, we find the mean time that elapses between jammed states to be

$$T_{\mathrm{R}} = \frac{L}{2}\left(1 + dL^{d-1}\right)\left[1 + \frac{2\sqrt{d(d-1)}}{2d-1}\coth\left(\frac{\sqrt{d(d-1)}}{2d-1}\,\omega L\right)\right] - \frac{1}{2\omega}. \tag{3.3.52}$$

One might be tempted to approximate $1 + dL^{d-1}$ as $dL^{d-1}$, but the subdominant term becomes important when we come to understand clustering in the extended many-body theory. We therefore refrain from dropping it.

### Comparison with simulation data

We now proceed to compare the results derived above with simulation data. Once the validity of the above results has been proven, we can begin to generalise to a many-body system.

A continuous-time Monte Carlo algorithm in which particles are assigned times for their next hops (if allowed) and reorientations was used. The event times are queued, and when the next event is carried out the associated event time is updated. Each reorientation is chosen such that no one of the possible $2d-1$ new orientations is favoured. Taking $\gamma = 1$ in the simulations, the independent system parameters are $\frac{\omega}{\gamma}$ and $L$.

[3] One sees from the final panel of fig. 3.7 that only one of walkers is able to actuate a channel state; hence, the required rate is $\omega$ and not $2\omega$.

The mean return time, $T_{\mathrm{R}}$, is calculated by recording the time at which a jammed state is exited, recording the time at which the next jammed state is entered, and then subtracting the first time from the second. Since all such return events are independent, the statistical error can be calculated in the usual way.

The comparison between the prediction in eq. (3.3.52) and the simulation data is shown in fig. 3.9. Our analysis was built upon the assumption that $L$ was large and the requirement that $\omega$ scale as $\mathcal{O}\left(\frac{1}{L}\right)$. Figure 3.9 compares our prediction with simulation data over a range of system sizes and reorientation rates both in $d = 2$ and $d = 3$. A minimum of $10^4$ jamming events were simulated for each data point shown. We find that even for small values of $L$ the predictions hold up well, which we attribute to there being large numbers of hops between the occurrence of channel states such that assumptions 1 and 2 from the previous section still apply. For larger values of $L$ and smaller values of $\omega$ the results are even more robust: the vast majority of predictions are within 3% of the values obtained from the simulations. Larger deviations of 10% or more are found for $\omega \geq 10\%$, which we neglect to show. We also verify the legitimacy of assumption 2 (that the distribution of channel-state entry separations is uniform) in the final panel of the figure.

### 3.3.4 Jamming probability in the two-particle system

The jamming probability can now be calculated from eqs. (3.3.1), (3.3.2) and (3.3.52). One finds

$$P_{\mathrm{J}} = \left\{ \omega L(1 + dL^{d-1}) \left[ 1 + \frac{2\sqrt{d(d-1)}}{2d-1} \coth\left( \frac{\sqrt{d(d-1)}}{2d-1}\, \omega L \right) \right] \right\}^{-1}, \quad (3.3.53)$$

which holds for $d \geq 2$. In the scaling limit $L \to \infty$ at fixed $\omega L \ll \gamma$, the hyperbolic cotangent may be replaced with the reciprocal of its argument, thus leading to the result

$$P_{\mathrm{J}} = \frac{1}{2dL^{d-1}\left(1 + \frac{\omega L}{2}\right)}. \quad (3.3.54)$$

In $d = 1$, the analogous result was calculated exactly to be

$$P_1 = \frac{1}{2\left(1 + \frac{\omega L}{2}\right)}. \quad (3.3.55)$$

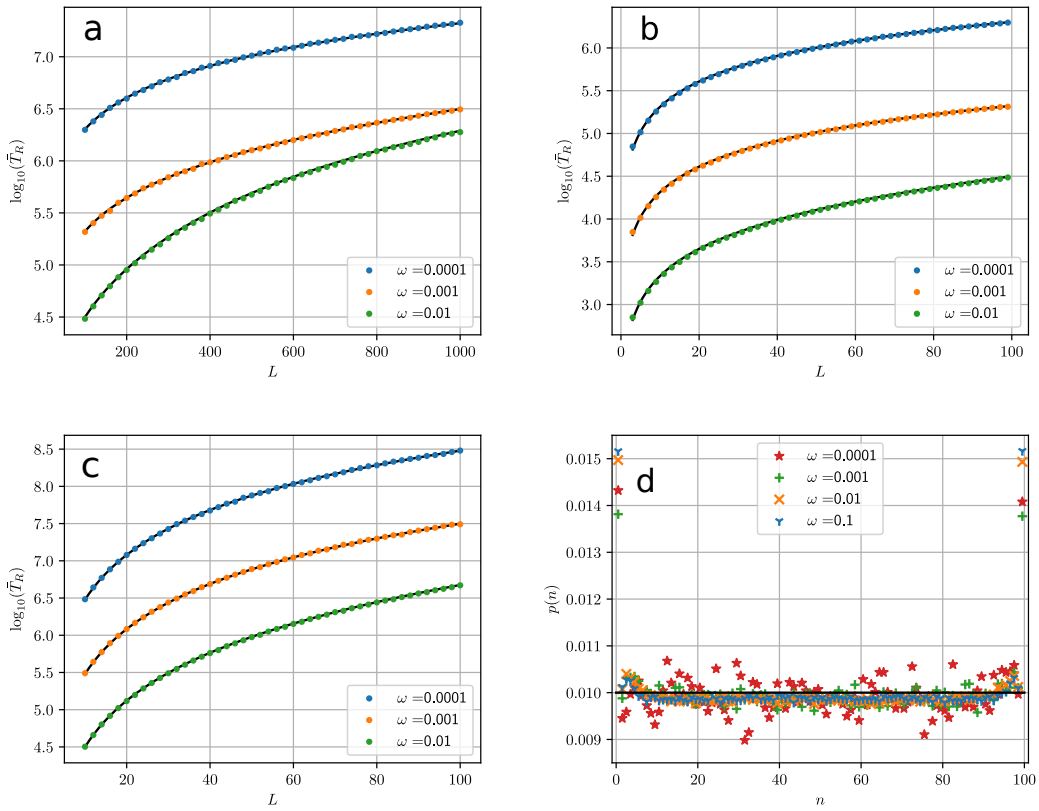


**Figure 3.9** ***a,b****: logarithmic plots of* $T_{\mathrm{R}}$ *versus* $L$ *in 2d for reorientation rates* $\omega = 10^{-\{2,3,4\}}$ *plotted atop (3.3.52) (black curves). Deviations from (3.3.52) for the* $L \gg 1$ *case (interval* $[100, 1000]$*), shown in* ***a****, lie in the range* $[-2.3, +2.1]\%$ *for* $\omega = 10^{-\{3,4\}}$ *bar one anomalous case* $(-4.5\%)$*. For* $\omega = 10^{-2}$ *deviations lie in the range* $[-0.3, -4.4]\%$*. Excluding* $L = 3$*, the corresponding deviations for smaller* $L$ *(interval* $[3, 99]$*), shown right, lie in the ranges* $[-3.2, +0.3]\%$ *and* $[-5.1, -1.6]\%$*, trending closer to zero in all cases as* $L$ *increases. Deviations for* $L = 3$ *all lie in the range* $[+7.1, +8.2]$*.* ***c****: corresponding plots for 3d (interval* $[10, 100]$*); deviations in all cases lie in the range* $[-2.8, +2.4]\%$*. As anticipated, deviations are everywhere largest for* $\omega = 10^{-2}$*. All simulations were run for a minimum of* $10^4$ *jamming events. Error bars have been omitted since in all cases they are approximately the size of or smaller than the markers.* ***d****: distribution of channel-state entry separations,* $n$*, for the set of 2d systems where* $L = 101$ *and* $\omega = 10^{-\{1,2,3,4\}}$*. A uniform entry distribution corresponds to* $p(n) = 0.01$ *(black line). A minimum of* $6 \times 10^4$ *entries were recorded in each case. Increasing noise for decreasing* $\omega$ *reflects that more simulation time is required to achieve the same number of total entries.*

We remark that this takes on precisely the same form as eq. (3.3.54). The factor $\frac{1}{dL^{d-1}}$ is understood to be the probability of finding both walkers in the same

channel, since there are $dL^{d-1}$ total channels in the lattice. Equation (3.3.54), therefore, has the simple interpretation as the $1d$ result scaled by the probability of finding both walkers in the same channel. This is because each walker is likely to traverse the system many times before reorienting in this limit, and hence we expect to see the system in the jammed state with the same probability as in $1d$ when both walkers are in the same channel. It is instructive to compare the above scenario of persistent particles to that of two random walkers (which exhibit no persistence). In the latter case, the probability of each configuration is the same: $\frac{1}{L^d-1}$, since given the first random walker is anywhere on the lattice, the second has $L^d - 1$ available sites to occupy. The probability of being on adjacent sites must therefore be $\frac{2d}{L^d-1}$ as each site has $2d$ nearest neighbours. A consequence of high persistence, therefore, is to increase the strength of attraction by a factor of $L$.

## 3.4 Clustering in a many-particle system

Having characterised two-particle jamming in our model, we now move onto a many-particle generalisation. As was emphasised in section 1.3.2, this takes us beyond previous microscopic models which are limited to one dimension and, at most, two particles. We crudely generalise our model to many particles by assuming that channel states comprising three or more particles are rare events that can be neglected, implying that we are working in a dilute regime (the probability of an $n$-particle channel state is $\mathcal{O}\left(\frac{1}{(L^{d-1})^{n-1}}\right)$ in a dilute system). We will then show how the breakdown of this approximate theory is a diagnostic for multiparticle cluster formation.

### 3.4.1 Calculation of the mean return time and jamming probability

To begin our analysis, we remark that the crucial quantity is still the jamming probability, $P_{\mathrm{J}}$, as described in eq. (3.3.1). In a system of $N$ particles, this describes the probability of finding a given walker in a jammed state. In order to calculate $P_{\mathrm{J}}$, we assume, as stated above, that channel states comprising three or more particles are low-probability events that can be neglected in our analysis. Then, a simple modification to the calculation of $T_{\mathrm{W}}$ in the previous section is

all that is required to calculate the dilute $N$-particle return time and hence also the dilute $N$-particle jamming probability. Specifically, if there are now $N-1$ available channels for each particle, then a given particle will, on average (and given the assumptions just discussed), enter a channel state $N-1$ times as quickly. We thus make the replacement $T_{\mathrm{W}} \to \frac{T_{\mathrm{W}}}{N-1}$. With this modification in place, the return time is found to be

$$T_{\mathrm{R}} = \frac{L}{2}\left[\frac{(N-1)+dL^{d-1}}{N-1}\right]\left[1+\frac{2\sqrt{d(d-1)}}{2d-1}\coth\left(\frac{\sqrt{d(d-1)}}{2d-1}\,\omega L\right)\right]-\frac{1}{2\omega}, \tag{3.4.1}$$

thus leading to the jamming probability

$$P_{\mathrm{J}} = \left\{\omega L\left[\frac{(N-1)+dL^{d-1}}{N-1}\right]\left[1+\frac{2\sqrt{d(d-1)}}{2d-1}\coth\left(\frac{\sqrt{d(d-1)}}{2d-1}\,\omega L\right)\right]\right\}^{-1}. \tag{3.4.2}$$

The subdominant term we spoke of earlier has now been scaled by the factor $N-1$. This may now be of comparable order to $dL^{d-1}$ and therefore cannot be neglected.

### 3.4.2 Critical density for clustering

We now note the following fact: since our theory works under the assumption that channel states comprise two particles only, the point at which it fails to predict the correct behaviour indicates the point at which we can no longer ignore the effects of higher-order channel states. And if higher-order channel states occur frequently in the system – in other words, there are marked local increases in density – the potential for cluster formation drastically increases.

An example of this is shown in fig. 3.10, where the simulated and predicted mean return times have been plotted against particle density, $\rho = \frac{N}{L^d}$, in the left panel of the figure for various values of $\omega$ on a $2d$ lattice where $L = 100$. The deviations from the predicted values are shown in the right panel of the figure. One sees that the prediction in eq. (3.4.1) holds well for low densities, with the deviations from the predicted values steadily increasing (e.g. for $N = 10$ particles the deviation is $\approx 3\%$, and for $N = 20$ particles the deviation is $\approx 6\%$). This we ascribe to increasingly-common occurrences of higher-order channel states. At higher densities, one sees a marked shift in the deviation from the predicted value for $\omega = 10^{-4}$ whose onset begins at $\rho \approx 0.006$. This, on the other hand, we ascribe to

a transition to cluster formation, as is evidenced by the figure insets. The reason for this is that particles which find themselves in cluster interiors have a high probability of being in jammed states (recall that this requires both particles to be adjacent and facing each other) and that, once the particle exits a jammed state, it is likely to enter a new jammed state very quickly (and in some cases immediately). If a substantial fraction of the population is found in clusters at any given time, this skews the mean return time away from that presented in eq. (3.4.1).

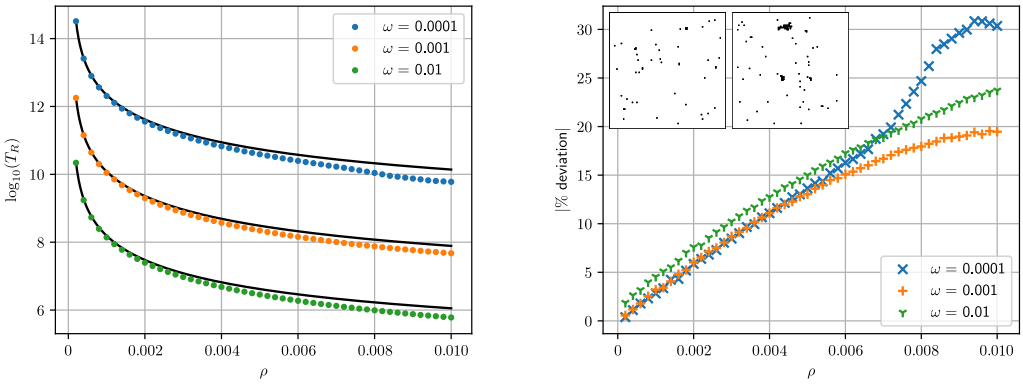


**Figure 3.10** *Left: simulation results for $T_{\mathrm{R}}$ versus $\rho$ in a 2d $L = 100$ lattice for reorientation rates $\omega = 10^{-\{2,3,4\}}$ and $\rho = [0.002, 0.010]$, plotted atop (3.4.1) (black curves). Right: deviations from (3.4.1). One notes the clustering signature for $\omega = 10^{-4}$, evidenced by the system snapshots at $\rho = 0.5\%$ and $\rho = 1.0\%$ (left and right insets, respectively). Two distinct clusters may be seen in the latter. All simulations were run for $10^6$ jamming events.*

In order to understand the above arguments more rigorously, we must determine precisely where our approximate theory breaks down. The important thing to note is that $P_{\mathrm{J}}$ is a lower bound on the probability of being in a two-particle channel state, which we denote $P_{\mathrm{C}}$, since a jammed state is a special case of such a channel state. Thus, when $P_{\mathrm{J}}$ becomes appreciably large, so does $P_{\mathrm{C}}$, and the probability of higher-order channel states grows due to the increased number of opportunities for particles to enter pre-existing two-particle channel states. We hypothesise, therefore, that when $P_{\mathrm{J}}$ becomes, say, $\mathcal{O}(1)$, that the occurrence of higher-order channel states and hence clustering is an inevitability.

To investigate this hypothesis, we choose to recast eq. (3.4.2) in terms of the

density, $\rho$, and *persistence*, $\xi$, defined as

$$\xi = \frac{1}{\omega L}. \tag{3.4.3}$$

Physically, this quantity tells us how many 'laps' of the system an unhindered walker completes between reorientation events. For clarity, we further define $c = \frac{\sqrt{d(d-1)}}{2d-1}$ (approximately equal to $\frac{1}{2}$ in all cases). It is simple to show that

$$P_{\mathrm{J}} = \frac{1}{1+\frac{d}{\rho L}} \frac{\xi}{1+2c\coth\left(\frac{c}{\xi}\right)}. \tag{3.4.4}$$

For small $\rho$, the quantity $\frac{d}{\rho L}$ becomes large and $P_{\mathrm{J}}$ is thus small. The quantity $\frac{d}{\rho L}$ is small, however, when $\rho$ is large; this causes $P_{\mathrm{J}}$ to saturate at the value $\xi\left[1+2c\coth(c\xi^{-1})\right]^{-1}$. For sufficiently high persistence lengths, therefore, this saturation value is appreciably large (to leading order the saturation value is $\frac{1}{2}$ when $\xi \gg 1$). The point which separates the two regimes can be approximately identified as the point at which $\frac{d}{\rho L} = 1$, leading to the prediction of

$$\rho^* = \frac{d}{L} \tag{3.4.5}$$

as the critical density for cluster formation. A critical number can also be identified via $\rho^* = \frac{N^*}{L^d} = \frac{d}{L}$, yielding $N^* = dL^{d-1}$. The characteristic density, therefore, corresponds to the point at which the $N-1$ and $dL^{d-1}$ terms in eqs. (3.4.1) and (3.4.2) are equal in magnitude. Physically, $dL^{d-1}$ is the number of channels in the system. This critical density/number hence corresponds to an average of one particle per channel. This is expected since we anticipate high-order channel states to arise at this density due to fluctuations; at lower densities, we expect such fluctuations to be rare events.

We note that $\rho^*$ has an intriguing property in the thermodynamic limit wherein $L \to \infty$: it vanishes. This prediction, and therefore the validity of $\rho^*$, can be tested by plotting deviations from the mean return time at different system sizes for fixed $\xi \gg 1$ (the regime where $P_{\mathrm{J}}$ saturates at non-negligible values). We plot this deviation against the parameter $\rho L$ for a set of $2d$ systems in fig. 3.11, where we see a sharpening-up of the deviations – our cluster diagnostic – at a fixed value of $\rho L \approx \frac{1}{2}$. Though this value does not agree precisely with the predicted value of $d = 2$, we remark that there is a level of arbitrariness in exactly where the saturated and unsaturated regimes of $P_{\mathrm{J}}$ meet; what matters is that $\rho^* L$ is

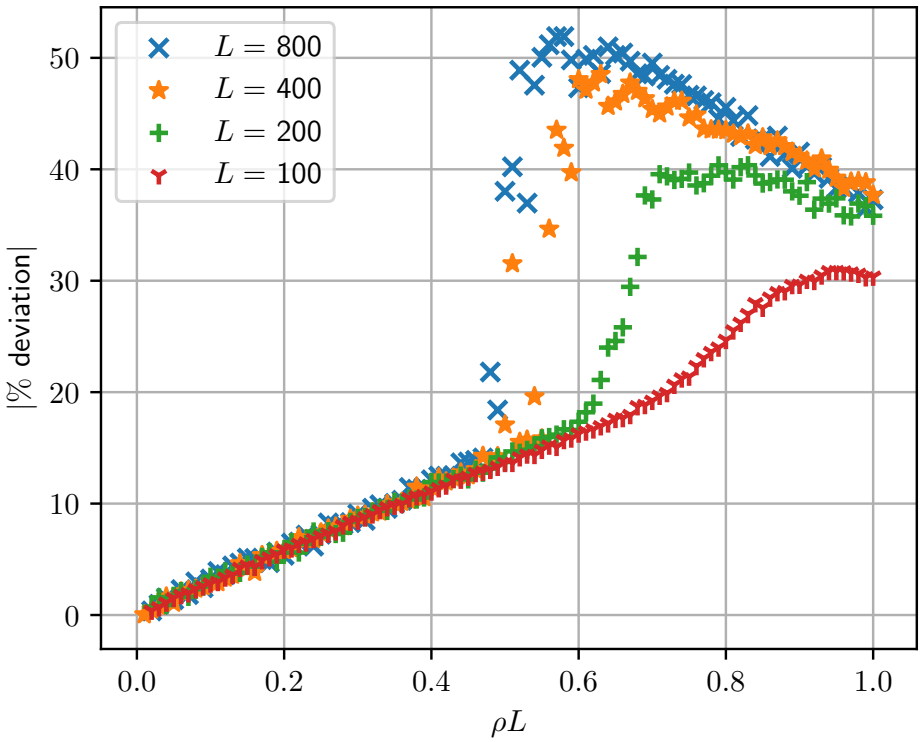


**Figure 3.11** *Absolute percentage deviations from (3.4.1) in the set of 2d systems where* $L = \{100, 200, 400, 800\}$ *and* $\omega L = 0.01$. *All simulations were run for a minimum of* $10^5$ *jamming events.*

of the same order as $d$, that is $\mathcal{O}(1)$. This therefore serves as strong evidence of the prediction above that clustering occurs at arbitrarily low densities in the thermodynamic limit, thus validating our prediction of $\rho^*$.

Now that we have confidence in our prediction of $\rho^*$, we shall provide some intuition. As noted after eq. (3.4.5), the critical density corresponds to a mean of one particle per channel. This result is much more intuitive, for if the density goes beyond this we can expect channel states of three or more particles, and therefore clustering, to become increasingly likely. To understand the counterintuitive result of a vanishing thermodynamic critical density, therefore, we need only to understand that the ratio of the number of channels in the system to the system size – that is, the density of channels – goes as $L^{-\alpha}$, where $\alpha > 0$. Since the number of channels in a system of size $L^d$ sites is $dL^{d-1}$ (again, as noted after eq. (3.4.5)), it follows that said ratio goes as $\rho^* = \frac{dL^{d-1}}{L^d} = \mathcal{O}(L^{-1})$.

## 3.5 Increasing the number of directions of motion

There are a number of possible extensions to the model presented here, though perhaps the most obvious is to lift the limitation on the walkers' directions of motion. Not only is this physically realistic (for example, in the context of bacterial dynamics), but it would allow us to probe whether or not the result of a vanishing critical clustering density in the thermodynamic limit is generic to any number of possible particle orientations. We devote this section to a discussion of the above and how one might develop suitable mathematical treatments.

### 3.5.1 Triangular lattice

A simple starting point would be to consider the triangular lattice in $d = 2$. Firstly, we note that eq. (3.4.5) can be rewritten as

$$\rho^* = \frac{2d}{2L} = \frac{\text{number of directions of motion}}{2L}. \tag{3.5.1}$$

If the calculation can be modified for the case a triangular lattice, it can be used to predict a corresponding critical density. The form of the critical density may then be instructive in telling us how it changes with increasing numbers of directions of motion (in this case, six instead of four).

The only drawback with this approach is that the domain – regardless of its shape – no longer has the property that all channels are of the same length $L$. This can be overcome by introducing a distribution of channel lengths. For a triangular domain of side length $L$ sites, there is a top-hat distribution of channel lengths from length 1 to length $L$. This has implications for the complexity of the calculation; for example, integrals such as $L^{-1}\int_0^L T_{\mathrm{A}}(x)\,\mathrm{d}x$ which appear in the expression for $T_{\mathrm{S}}$ would have to be replaced by double integrals to accommodate for the distribution of channel lengths. In principle, however, the problem should be tractable, though we do not pursue it here.

### 3.5.2 Arbitrary directions of motion on the square lattice

We can instead choose to formulate motion in arbitrary directions directly on the square lattice. This would extend previous field-theoretic work in which

diagonal hops are permitted [52] for finite-range interactions. Whilst not possible in a strict sense, the average motion of a walker over the course of many hops can be engineered to assume an arbitrary direction. There are two ways of implementing this in simulations, both of which are discussed below. A brief theoretical discussion will follow.

### Orientation-dependent hop rates

Similar to schemes implemented in [129, 130], an orientation angle $\theta$ may be assigned to each PRW when working in $d = 2$,[4] where $\theta \in [0, \frac{\pi}{2})$ is the angle as measured anticlockwise from the axis which corresponds to $\theta = 0$. For example, if the orientation of the walker is exactly north-west, the positive $y$ axis corresponds to $\theta = 0$ and thus $\theta = \frac{\pi}{4}$. Then, hops aligned with the $\theta = 0$ axis occur with mean rate $\gamma \cos\theta$ and hops aligned with the $\theta = \frac{\pi}{2}$ axis occur with mean rate $\gamma \sin\theta$. This has the desired property that the mean rate of motion in the direction $\theta$ is always $\sqrt{\gamma^2 \cos^2\theta + \gamma^2 \sin^2\theta} = \gamma$. The problem with this formulation, however, is that the motion is not perfectly linear due to the stochasticity of the hops (the situation is analogous to a biased-random-walk model in $1d$ where the ensemble mean of the motion is fixed but where individual runs are distinct).

### Bresenham formulation

An alternative approach is to make use of Bresenham's line-drawing algorithm [131]. This algorithm is designed to find the lattice path that best approximates a line segment between two pre-selected lattice points. In the context of PRWs, the pre-selected points can be chosen to correspond to reorientation events, and the set of points determined by the algorithm as the most appropriate lattice path corresponds to a run. Jamming occurs when the usual definition is satisfied: the two target sites of a pair of walkers are the sites those walkers currently occupy. Sea and channel states are also similar in definition: any configuration in which two walkers are on a collision course is an approaching state, any configuration where one walker trails the other's trajectory is a following state, and all other states are sea states.

This algorithm is long-established and its implementation relatively straightforward. One complication that arises, however, is that hop rates have to be adjusted

[4] Further angles are required to specify orientations in higher dimensions.

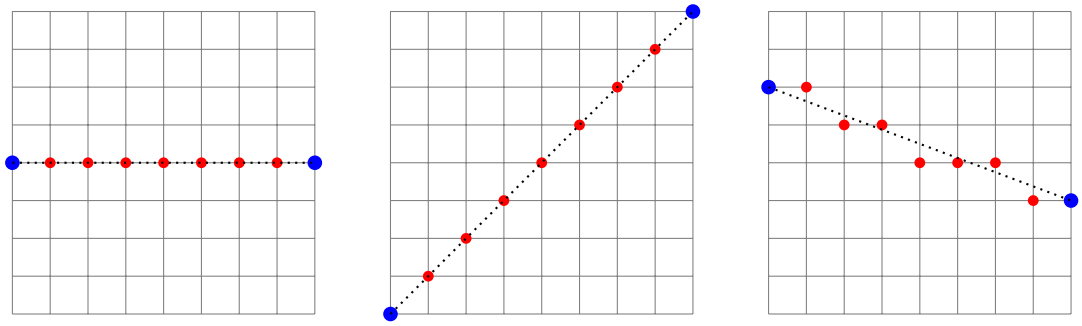

**Figure 3.12** *Three lattice paths as determined by the Bresenham line-drawing algorithm, where large blue dots indicate endpoints, small red dots indicate the lattice sites chosen by the algorithm, and where the dotted line shows the true line segment that links the two endpoints.*

to account for hops over distances greater than the lattice spacing – something which was never a consideration in the simulation work presented earlier in this chapter. We demonstrate this in fig. 3.12, wherein the lattice paths determined by the Bresenham algorithm for three different pairs of endpoints are displayed. In the left panel, all sites of the lattice path are adjacent and the hop rate need not be adjusted. In the central panel meanwhile, no hops occur between adjacent lattice sites, with all hops covering a distance of $\sqrt{2}$ times the lattice spacing. To correct for this, the (stochastic) intervals between hops must be scaled by $\sqrt{2}$. Finally, in the right panel a mixed lattice path containing both types of hop is depicted. In such cases (which form the vast majority), intervals between hops must be scaled according to each individual hop.

### Theoretical implementation

Regarding the theory, modifications to the original calculation can be made to incorporate arbitrary particle orientations. The analogues to eqs. (3.3.18)

to (3.3.20) are as follows in $d = 2$:

$$T_{\mathrm{S}} = T_{\mathrm{W}} + P_{\mathrm{SA}} \, \frac{1}{2\pi} \int_0^{2\pi} \left[ \frac{1}{\ell(\theta)} \int_0^{\ell(\theta)} T_{\mathrm{A}}(x,\theta) \, \mathrm{d}x \right] \mathrm{d}\theta + P_{\mathrm{SF}} \, \frac{1}{2\pi} \int_0^{2\pi} \left[ \frac{1}{\ell(\theta)} \int_0^{\ell(\theta)} T_{\mathrm{F}}(x,\theta) \, \mathrm{d}x \right] \mathrm{d}\theta \, ; \tag{3.5.2}$$

$$T_{\mathrm{F}}(x,\theta) = \frac{1}{2\omega} + \frac{P_{\mathrm{FA}}}{2} \left[ T_{\mathrm{A}}(x,\theta) + T_{\mathrm{A}}(\ell(\theta) - x, \theta) \right] + P_{\mathrm{FS}} T_{\mathrm{S}}; \tag{3.5.3}$$

and

$$T_{\mathrm{A}}(x,\theta) = \mathrm{e}^{-2\omega\delta t} \left[ \delta t + T_{\mathrm{A}}(x - 2\delta t, \theta) \right] + \int_0^{\delta t} \mathrm{d}(\delta t') \, 2\omega \mathrm{e}^{-2\omega\delta t'} \left[ \delta t' + P_{\mathrm{AF}} T_{\mathrm{F}}(x - 2\delta t', \theta) + P_{\mathrm{AS}} T_{\mathrm{S}} \right]. \tag{3.5.4}$$

These require some explanation. The way we treat $\theta$ is exactly the same as the way we treat $x$: it must be taken as a discrete variable in order for probabilities to remain finite, but we treat it as a continuous variable in order to approximate discrete sums as integrals and thereby simplify the mathematics. The transition probabilities will depend on the number of discretisations, which we denote $M$, since following states require that the orientations be the same and approaching states require that they be $\pi$ out of phase. Thus,

$$P_{\mathrm{AF}} = P_{\mathrm{SF}} = P_{\mathrm{SA}} = P_{\mathrm{FA}} = \frac{1}{M} \tag{3.5.5}$$

and

$$P_{\mathrm{AS}} = P_{\mathrm{FS}} = \frac{M-1}{M}. \tag{3.5.6}$$

The functions $T_{\mathrm{F}}(x,\theta)$ and $T_{\mathrm{A}}(x,\theta)$ have the same definitions as before, only the angle $\theta$ is required to specify the orientation of the channel. The distribution $\ell(\theta)$ is required since channel lengths now depend on channel orientation and the geometry of the domain. The double integral in eq. (3.5.2) sums over all channel-state entry separations (as before) for all possible channel orientations. The equations are otherwise the same as in the original calculation with a value for $T_{\mathrm{W}}$ once more chosen based on probabilistic arguments.

Considering the above, the mean return time is given by

$$T_{\mathrm{R}} = \frac{P_{\mathrm{AF}}}{2\pi} \int_0^{2\pi} T_{\mathrm{F}}(0,\theta) \, \mathrm{d}\theta + P_{\mathrm{AS}} T_{\mathrm{S}}. \tag{3.5.7}$$

Whilst we do not pursue this further here, should one be able to solve the above

equations and hence evaluate $T_{\mathrm{R}}$, it should be possible to repeat the analysis on clustering presented in the previous section. Not only would this be insightful regarding the impacts of continuous orientation versus the strongly discretised orientation studied in this chapter, but it would also be a significant step towards a physically realistic characterisation of MIPS rooted in microscopic interactions.

## 3.6 Concluding remarks and outlook

In this chapter, first-passage techniques were used to investigate lattice systems of persistent random walkers in dimension $d \geq 2$. In particular, the nature of jamming – where walkers on adjacent sites mutually block each other due to an exclusion interaction – was investigated in a two-particle system, the motivation being that jammed pairs of particles serve as nucleation sites for larger clusters. This was achieved by decomposing the system into 'sea' and 'channel' states, enabling us to expand on a previous exact calculation in $d = 1$ by treating systems for which $d \geq 2$ as quasi-one-dimensional. Some assumptions were made about the dynamics which allowed us to simplify the calculation, the veracity of which was demonstrated by comparison with Monte Carlo simulation data. The mean elapsed time between jammed states and the jamming probability in $d$ dimensions are given by eqs. (3.3.52) and (3.3.53). The latter is approximately equal to the simpler form given in eq. (3.3.54).

A dilute many-body generalisation followed straightforwardly by assuming that channel states comprising three or more particles were rare events whose effects could be neglected. By identifying the point at which the many-body generalisation breaks down, we were able to predict a critical density for the onset of clustering. This follows from the fact that the breakdown of the theory is a diagnostic for when the effects of higher-order channel states can no longer be ignored, thus implying that local increases in density which may seed multiparticle clusters are likely to occur. A critical density for cluster formation was identified from eq. (3.4.4) as $\rho^* = \frac{d}{L}$ at high persistence lengths in the scaling limit where $\frac{\omega}{\gamma} = \mathcal{O}\left(\frac{1}{L}\right)$. Strong evidence of the intriguing prediction $\rho^* \to 0$ when $L \to \infty$ – in words, that clustering can occur at arbitrarily low densities in the thermodynamic limit – was found by comparing data in fig. 3.11 from Monte Carlo simulations in $d = 2$ for increasing system sizes and identifying a clustering signature at fixed $\rho^* L$. This result serves to demonstrate the strength of effective attractions that are able to arise in systems of interacting active particles.

Given that the chosen scaling limit of our model is the most physically relevant in the context of bacterial motion, the predictions made here may have implications for clustering in bacterial populations. What remains to be seen, however, is whether removing the restrictions on the directions in which the walkers are able to move fundamentally changes the results presented here. As discussed in section 3.5, ways of approaching this might be to repeat the calculation on a triangular lattice or to incorporate arbitrary directions of motion on a square lattice. A more thorough characterisation of clustering could also be considered by going beyond the dilute limit presented here, though it is not clear at the time of writing how such a characterisation might be realised.

# Chapter 4

# A generating-function approach to a system of persistent random walkers undergoing an active contact interaction

In the previous chapter, we generalised the one-dimensional SEB model of interacting persistent random walkers (PRWs) [54] to that of many dilute PRWs in an arbitrary number of spatial dimensions. We were able to characterise the clustering behaviour of the system by examining the breakdown of our dilute approximation, with our primary finding being that of a vanishing critical density in the thermodynamic limit. Though this constitutes a significant step forward regarding microscopic models of interacting particles, it is still limited in that the particles interact by steric exclusion only. An obvious extension, therefore, is to incorporate a more generic type of interaction.

To this end, we introduce a model of PRWs in which the constituents exhibit a 'recoil' interaction. This interaction is inspired by the dynamics of the octoflagellate microalga *Pyramimonas octopus* [132], individuals of whom are observed to 'shock' at random and upon contact with each other. Motivated by this behaviour, we will incorporate recoil dynamics into our model as an example of an *active* contact interaction, that is, an interaction that is driven by the constituents. This type of interaction is much less explored than the passive type (which includes the exclusion interaction featured in the previous chapter);

as such, our aim is to ascertain what – if any – novel phenomena emerge as a consequence of this type of interaction, and how it contrasts with the passive case. The SEB model will once more provide useful comparison for this purpose.

The layout of this chapter is as follows. We will begin in section 4.1 by discussing the inspiration for the model to be introduced in section 4.2. The generating-function technique known as the *kernel* method [102] (as seen in chapter 2) will then be introduced to solve for the stationary state of our model on a discrete domain; this will be the focus of section 4.3. A special case relevant to the robustness of jamming will then be considered and discussed in section 4.4, before we conclude in section 4.5.

The work presented in this chapter was published in [3].

## 4.1 Active interactions

When modelling active matter, it is standard practice to assume passive interactions between particles. Examples are excluded-volume interactions – as implemented in the previous chapter – as well as forces that apply within some interaction radius as in [133] (linear repulsive force) and [134] (Lennard-Jones). On the other hand, *active* interactions – those which are internally driven – remain underexplored. For the case of recoil, internal driving refers to the energy expenditure required in order for a recoil to be executed, thus making collisions in this model inelastic. In chapter 3, we modified the system presented in [54] by removing constraints on particle number and dimension; in chapters 4 and 5, we will instead modify the same system to incorporate a simple active contact interaction. Thus, we will make first steps towards understanding active interactions between active particles at the microscopic level whilst, importantly, maintaining comparability to a passive analogue.

Specifically, the interaction we will study is inspired by the 'run-stop-shock' motility of *P. octopus* [132]. These microalgae have a 'run' gait, which consists of steady swimming for $\mathcal{O}(1)$ s, a 'stop' gait consisting of no swimming for $\mathcal{O}(10)$ s, and a 'shock' gait characterised by rapid locomotion over the course of sub-$\mathcal{O}(0.1)$ s time scales. The shock gait can be actuated either spontaneously or when contact is made with another object, such as a fellow microalga. The nature of these three gaits is shown in fig. 4.1.

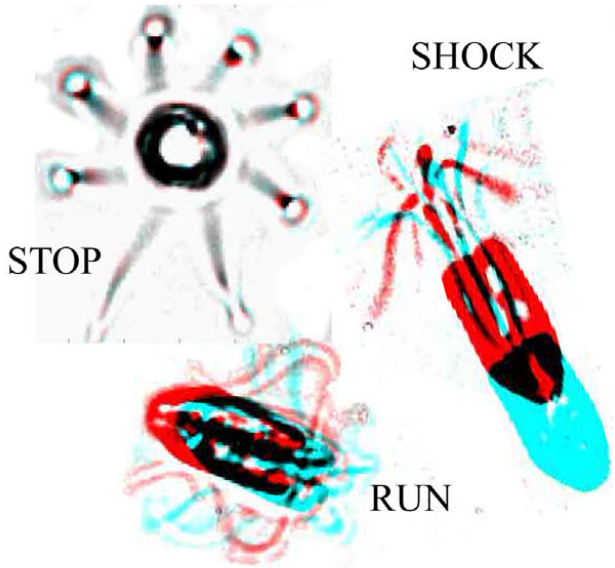


**Figure 4.1** *(Reproduced from [132].) Each of P. octopus' gaits. Each image shows an individual at some initial time, coloured red, and some later time, coloured cyan, where the time differences are 100 ms, 10 ms, and 5 ms for the stop, run, and shock gaits, respectively. We observe almost no movement during the stop gait, modest movement during the run gait, and rapid movement during the shock gait.*

The motility of *P. octopus* as described above motivates a simple model in which persistent particles run at constant speed and interact with each other upon contact via shocks. So as to avoid confusion with terminology relating to discontinuous density profiles in media, we hereafter refer to shocks as 'recoils'. For simplicity, we will consider recoils to be instantaneous; moreover, we will not consider the stop gait or spontaneous recoils at all. As such, we make no claims of correspondence to real systems of *P. octopus* microalgae. Having said this, the model we propose (whose details will be laid out in the next section) takes us beyond previous microscopic models and constitutes a first step towards a fundamental understanding of nontrivial active interactions, such as those found in biological contexts, where it is difficult to model systems in their full complexity. Furthermore, by allowing ourselves to vary the distribution of recoil lengths, we can build up a more complete picture of how a persistent particle's behaviour is affected by its contact dynamics, something that has been more fully explored in the absence of persistence [135–138].

## 4.2 The model

We begin by defining the dynamics considered in this work. Two particles inhabit a periodic lattice of $L$ sites in one dimension. Each particle has a direction of motion, denoted $+$ or $-$, and hops to the adjacent site in that direction as a Poisson process with rate $\gamma = 1$. Similarly, each particle reverses its direction of motion as a Poisson process with rate $\omega$. In addition to this, the particles experience a recoil interaction upon colliding with each other: if particle 1 hops onto the site occupied by particle 2, the latter is instantaneously displaced parallel to particle 1's direction of motion to a new separation of $n$ sites according to some distribution $\Phi(n)$, where $0 < n < L$. The form of $\Phi(n)$ is left arbitrary at this stage. After such a recoil, the particle's velocity is reversed with probability $r$; special cases include $r = 0$, that of no reversals, and $r = \frac{1}{2}$, corresponding to velocity randomisation. A schematic for the recoil dynamics is given in fig. 4.2.

Note that we refer to the active particles of this model simply as particles (or walkers) and not PRWs because we place no restriction on the value of $\omega$. Note also that, in principle, one could account for the stop gait in the manner of [63] where finite tumble duration is considered, but choose not to on the basis of simplicity; we wish instead to focus our attention on precisely how the active interaction affects the stationary distributions. So as not to distract from this aim, we leave the inclusion of the stop gait to future work.

This model is a generalisation of the SEB model, in which the case $\Phi(n) = \delta_{n,1}$ with $r = 0$ (exclusion) is considered. The more general interaction considered here – like the SEB exclusion interaction – breaks detailed balance. An example of broken detailed balance for an arbitrary recoil distribution $\Phi(n)$ is given in fig. 4.3.

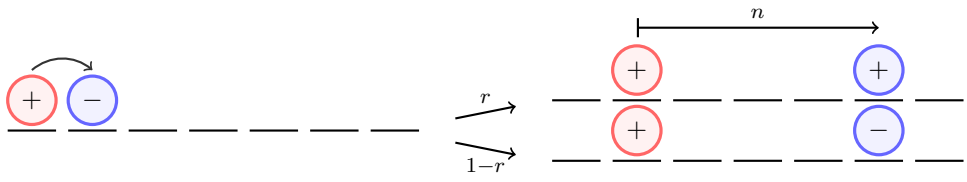


**Figure 4.2** *An illustration of the recoil interaction. The left particle successfully hops whilst the right particle is displaced to a separation of $n$ sites according to $\Phi(n)$. In addition, its velocity is reversed with probability $r$.*

The state space of this model falls naturally into four 'quadrants', corresponding

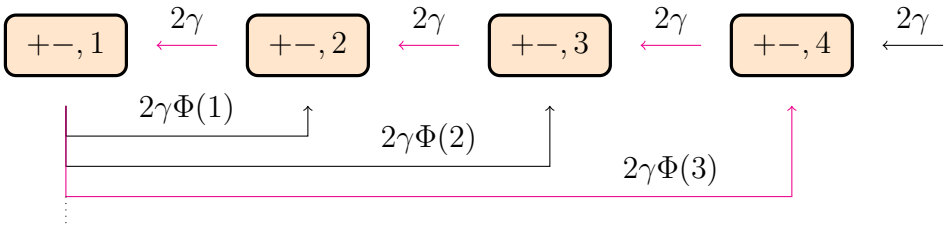


**Figure 4.3** *Demonstration of broken detailed balance when $r = 0$ for some arbitrary $\Phi(n)$ that allows for recoils to all separations. Each box represents two-particle configurations, where $+-, n$ indicates the particles are approaching each other with separation $n$. Transitions to $++$, $--$ and $-+$ are not shown. The most efficient route back to the state $+-, 1$ after a recoil to $n = 4$ from $n = 1$ requires three transitions, and thus detailed balance is broken. The flux loop associated with this set of transitions is coloured magenta.*

to the directional combinations of the particles: $++$, $+-$, $--$, and $-+$. In what follows, we aim to calculate the stationary probability distributions for the particle separations in each of the four quadrants, as well as the net distribution obtained from summing over the four quadrants. To reiterate, the importance of the stationary distributions is that, once established, we will be able to make direct comparisons to the stationary distributions derived in the passive case [54]. We will thus be able to see how the jamming signature (as highlighted in fig. 1.10) is modified with the inclusion of recoils, and what implications this may have for motility-induced phase separation (MIPS). Due to symmetry considerations (which we shall discuss shortly), it will suffice to calculate the distributions in the $++$ and $+-$ quadrants only.

## 4.3 Discrete stationary-state solution

In this section, we write down the master equations describing the evolution of the system and proceed to solve them in the steady state via the method of generating functions.

### 4.3.1 Master equations

Denoting temporal derivatives with overdots, the master equation in the ++ quadrant for $0 < n < L$ is

$$\begin{aligned}\dot{P}_{++}(n) = {} & P_{++}(n-1)I_{n>1} + P_{++}(n+1)I_{n<L-1} \\ & + \omega P_{+-}(n) + \omega P_{-+}(n) \\ & + rP_{+-}(1)\Phi(n) + rP_{-+}(L-1)\Phi(L-n) \\ & + (1-r)P_{++}(1)\Phi(n) + (1-r)P_{++}(L-1)\Phi(L-n) \\ & - 2P_{++}(n) - 2\omega P_{++}(n), \end{aligned} \tag{4.3.1}$$

where the indicator function, $I_X$, evaluates to 1 if $X$ is true and evaluates to 0 if $X$ is false, and where we remind ourselves that we have set $\gamma = 1$. The purpose of the indicator functions is to enforce the exclusion constraint that both particles are forbidden from occupying the same site. Equivalently, working on the domain $0 \leq n \leq L$ and imposing the boundary conditions

$$P_{++}(0) = P_{++}(L) = 0 \tag{4.3.2}$$

means eq. (4.3.1) reduces to

$$\begin{aligned}\dot{P}_{++}(n) = {} & [P_{++}(n-1) - 2P_{++}(n) + P_{++}(n+1)] \\ & + \omega[P_{+-}(n) - 2P_{++}(n) + P_{-+}(n)] \\ & + r[P_{+-}(1)\Phi(n) + P_{-+}(L-1)\Phi(L-n)] \\ & + (1-r)[P_{++}(1)\Phi(n) + P_{++}(L-1)\Phi(L-n)], \end{aligned} \tag{4.3.3}$$

where terms common to hopping, tumbling, and recoiling processes have been grouped together on the first, second, and third and fourth lines, respectively.

To be more specific, the origins of each term are as follows. The positive terms in the first line of eq. (4.3.3) describe hops into the desired configuration, as demonstrated in the left schematic of fig. 4.4. The central schematic of fig. 4.4 demonstrates tumbles into the correct configuration as given by the positive terms in the second line of eq. (4.3.3), whilst the right schematic of fig. 4.4 demonstrates contributions from recoils as seen in the final line of eq. (4.3.3). The negative terms correspond to processes that exit the desired configuration, as depicted in fig. 4.5.

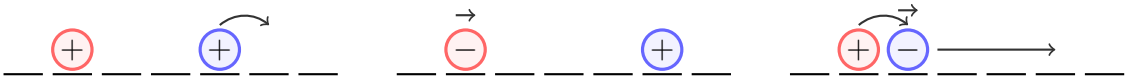

**Figure 4.4** *Example processes for entering an* $(n = 4)$ *configuration in the* $++$ *quadrant. Curved overarrows indicate hops with rate* 1*, straight overarrows indicate tumbles (into the direction of the arrow) with rate* $\omega$*, and arrows along the lattice indicate recoils to the arrow's endpoint.*

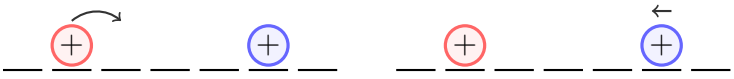

**Figure 4.5** *Example processes for exiting an* $(n = 4)$ *configuration in the* $++$ *quadrant. The same arrow convention as in fig. 4.4 is used.*

Using the same logic as above, the master equation in the $+-$ quadrant for $0 < n < L$ may be written down as

$$\begin{aligned}\dot{P}_{+-}(n) = {} & 2P_{+-}(n+1)I_{n<L-1} \\ & + \omega P_{++}(n) + \omega P_{--}(n) - 2\omega P_{+-}(n) \\ & + rP_{++}(1)\Phi(n) + rP_{--}(1)\Phi(n) + 2(1-r)P_{+-}(1)\Phi(n) \\ & - 2P_{+-}(n) - 2\omega P_{+-}(n). \end{aligned} \tag{4.3.4}$$

Working instead on the domain $0 \leq n \leq L$ and imposing the boundary condition

$$P_{+-}(L) = 0, \tag{4.3.5}$$

eq. (4.3.4) may be equivalently expressed as

$$\begin{aligned}\dot{P}_{+-}(n) = {} & 2[P_{+-}(n+1) - P_{+-}(n)] \\ & + \omega[P_{++}(n) + P_{--}(n) - 2P_{+-}(n)] \\ & + r[P_{++}(1) + P_{--}(1)]\Phi(n) + 2(1-r)P_{+-}(1)\Phi(n), \end{aligned} \tag{4.3.6}$$

where, once more, terms common to each type of process have been grouped together.

Master equations for the remaining two quadrants, $--$ and $-+$, are not required due to symmetry: since the labelling of the walkers is arbitrary, it must be true that

$$P_{\sigma_1,\sigma_2}(n) = P_{\sigma_2,\sigma_1}(L-n), \tag{4.3.7}$$

where $\sigma_i$ denotes the direction of walker $i$ for $i = 1, 2$. The $P_{-+}(L-1)$ and $P_{++}(L-1)$ terms in eq. (4.3.3) may therefore be eliminated in favour of $P_{+-}(1)$

and $P_{++}(1)$, respectively. Moreover, symmetry under the parity transformation – that which spatially reflects the system so as to produce its mirror image – implies that

$$P_{\sigma_1,\sigma_2}(n) = P_{-\sigma_2,-\sigma_1}(n), \tag{4.3.8}$$

thus enabling us to write $P_{--}(n)$ and $P_{--}(1)$ in eq. (4.3.6) as $P_{++}(n)$ and $P_{++}(1)$, respectively.

### 4.3.2 Generating-function solution of the stationary master equations

The stationary master equations are obtained by setting the time derivatives of the distributions to zero. With the foregoing symmetries in mind, the stationary master equations read

$$\begin{aligned} 0 = {} & P_{++}(n-1) - 2P_{++}(n) + P_{++}(n+1) \\ & + \omega[P_{+-}(n) + P_{-+}(n) - 2P_{++}(n)] \\ & + [rP_{+-}(1) + (1-r)P_{++}(1)][\Phi(n) + \Phi(L-n)], \end{aligned} \tag{4.3.9}$$

and

$$\begin{aligned} 0 = {} & P_{+-}(n+1) - P_{+-}(n) \\ & + \omega[P_{++}(n) - P_{+-}(n)] \\ & + [rP_{++}(1) + (1-r)P_{+-}(1)]\Phi(n). \end{aligned} \tag{4.3.10}$$

In order to solve the above equations, we introduce the generating functions

$$G_{\sigma_1,\sigma_2}(s) = \frac{1}{P_{+-}(1)} \sum_{n=1}^{L-1} P_{\sigma_1,\sigma_2}(n) s^n, \tag{4.3.11}$$

for the various combinations of $\sigma_1$ and $\sigma_2$. Multiplying both sides of eqs. (4.3.9) and (4.3.10) by $\frac{s^n}{P_{+-}(1)}$ and summing over all physical $n$ gives us the stationary master equations in generating-function space. Taking eq. (4.3.9) as an example,

one sees that

$$0 = \frac{1}{P_{+-}(1)}\sum_{n=1}^{L-1} P_{++}(n-1)s^n - \frac{2}{P_{+-}(1)}\sum_{n=1}^{L-1} P_{++}(n)s^n + \frac{1}{P_{+-}(1)}\sum_{n=1}^{L-1} P_{++}(n+1)s^n$$
$$+ \frac{\omega}{P_{+-}(1)}\sum_{n=1}^{L-1} P_{+-}(n)s^n + \frac{\omega}{P_{+-}(1)}\sum_{n=1}^{L-1} P_{-+}(n)s^n - \frac{2\omega}{P_{+-}(1)}\sum_{n=1}^{L-1} P_{++}(n)s^n$$
$$+ \left[r\frac{P_{++}(1)}{P_{+-}(1)} + (1-r)\right]\left[\sum_{n=1}^{L-1}\Phi(n)s^n + \sum_{n=1}^{L-1}\Phi(L-n)s^n\right], \tag{4.3.12}$$

One then rewrites the above in terms of the generating functions; for example, the third term may be re-expressed as

$$\frac{1}{P_{+-}(1)}\sum_{n=1}^{L-1} P_{++}(n+1)s^n = \frac{G_{++}(s)}{s} - \frac{P_{++}(1)}{P_{+-}(1)}, \tag{4.3.13}$$

where the boundary condition in eq. (4.3.2) was used. Doing this for all terms and introducing the notation

$$\kappa_L = \frac{P_{++}(1)}{P_{+-}(1)}, \tag{4.3.14}$$

as well as

$$\tilde{\Phi}(s) = \sum_{n=1}^{L-1}\Phi(n)s^n \tag{4.3.15}$$

for the generating function of the recoil distribution, one can manipulate eq. (4.3.12) into the form

$$[s - 2(1+\omega) + s^{-1}]G_{++}(s) + \omega[G_{+-}(s) + G_{-+}(s)]$$
$$= (1+s^L)\kappa_L - [r + (1-r)\kappa_L][\tilde{\Phi}(s) + s^L\tilde{\Phi}(s^{-1})], \tag{4.3.16}$$

since

$$\sum_{n=1}^{L-1}\Phi(L-n)s^n = \sum_{n=1}^{L-1}\Phi(n)s^{L-n} = s^L\tilde{\Phi}(s^{-1}). \tag{4.3.17}$$

Carrying out the same procedure for eq. (4.3.10) yields

$$[s^{-1} - (1+\omega)]G_{+-}(s) + \omega G_{++}(s) = 1 - [r\kappa_L + (1-r)]\tilde{\Phi}(s). \tag{4.3.18}$$

A further equation is required due to the presence of $G_{-+}(s)$ in eq. (4.3.16). One can write down a master equation for the $-+$ quadrant and carry out the same

procedure as above, but the symmetry in eq. (4.3.7) implies the relation

$$s^L G_{\sigma_1,\sigma_2}(s^{-1}) = G_{\sigma_2,\sigma_1}(s), \tag{4.3.19}$$

which allows us to shortcut this. Letting $s \to s^{-1}$ in eq. (4.3.18) and multiplying by $s^L$ gives

$$[s-(1+\omega)]G_{-+}(s) + \omega G_{++}(s) = s^L - [r\kappa_L + (1-r)]s^L\tilde{\Phi}(s^{-1}). \tag{4.3.20}$$

Equations (4.3.16), (4.3.18) and (4.3.20) can be cast into matrix form as

$$\begin{pmatrix} \mu(s)+\nu(s) & \omega & \omega \\ \omega & \nu(s) & 0 \\ \omega & 0 & \mu(s) \end{pmatrix} \begin{pmatrix} G_{++}(s) \\ G_{+-}(s) \\ G_{-+}(s) \end{pmatrix} = \begin{pmatrix} (1+s^L)\kappa_L - [r+(1-r)\kappa_L][\tilde{\Phi}(s) + s^L\tilde{\Phi}(s^{-1})] \\ 1-[r\kappa_L+(1-r)]\tilde{\Phi}(s) \\ s^L - [r\kappa_L+(1-r)]s^L\tilde{\Phi}(s^{-1}) \end{pmatrix}, \tag{4.3.21}$$

where

$$\mu(s) = s-(1+\omega) \qquad \text{and} \qquad \nu(s) = \mu(s^{-1}) = s^{-1}-(1+\omega)\ . \tag{4.3.22}$$

Inverting the matrix then yields

$$\frac{K(s)}{s^2}\begin{pmatrix} G_{++}(s) \\ G_{+-}(s) \\ G_{-+}(s) \end{pmatrix} = \mathsf{M}(s)\begin{pmatrix} (1+s^L)\kappa_L - [r+(1-r)\kappa_L][\tilde{\Phi}(s) + s^L\tilde{\Phi}(s^{-1})] \\ 1-[r\kappa_L+(1-r)]\tilde{\Phi}(s) \\ s^L - [r\kappa_L+(1-r)]s^L\tilde{\Phi}(s^{-1}) \end{pmatrix}, \tag{4.3.23}$$

where the *kernel*, $K(s)$, is the quartic

$$K(s) = (1+\omega)(s-z)(s-z^{-1})(s-1)(1-s) \tag{4.3.24}$$

with

$$z^{\pm 1} = (1+\omega) \pm \sqrt{\omega(2+\omega)}, \tag{4.3.25}$$

and where the matrix $\mathsf{M}(s)$ is

$$\mathsf{M}(s) = \begin{pmatrix} \mu(s)\nu(s) & -\omega\mu(s) & -\omega\nu(s) \\ -\omega\mu(s) & \mu(s)(\mu(s)+\nu(s)) - \omega^2 & \omega^2 \\ -\omega\nu(s) & \omega^2 & \nu(s)(\mu(s)+\nu(s)) - \omega^2 \end{pmatrix}. \tag{4.3.26}$$

Here, $\frac{K(s)}{s^2}$ is the determinant of the inverted matrix and may be calculated most easily by carrying out a Laplace expansion along the matrix's third row or column.

Having established the above facts, the generating functions may be determined in full by finding the value of $\kappa_L$: the only remaining unknown in the problem. This is where we make use of the kernel method as described in section 2.2: since the generating functions are finite sums (see eq. (4.3.11)) they are convergent; the left-hand side of eq. (4.3.23) must therefore vanish when $s$ is chosen to be one of the roots of the kernel (that is, when $s$ is chosen to be 1 or $z^{\pm 1}$). It can be shown that the right-hand side of eq. (4.3.23) and its first derivatives vanish at $s = 1$ for any value of $\kappa_L$, and so this provides us with no new information. Turning instead to $s = z$, requiring that $\kappa_L$ be such that the first component of eq. (4.3.23) vanishes yields

$$\begin{aligned} \omega(z^L - 1) + r\mu(z)\tilde{\Phi}_+(z) + (1-r)\omega\tilde{\Phi}_-(z) \\ + \kappa_L[-\mu(z)(z^L+1) + r\omega\tilde{\Phi}_-(z) + (1-r)\mu(z)\tilde{\Phi}_+(z)] = 0, \end{aligned} \tag{4.3.27}$$

where $\tilde{\Phi}_\pm(s)$ are the respective generating functions for the symmetric and antisymmetric components of the recoil distribution:

$$\tilde{\Phi}_\pm(s) = \sum_{n=1}^{L-1} \Phi_\pm(n) s^n = \sum_{n=1}^{L-1} [\Phi(n) \pm \Phi(L-n)] s^n. \tag{4.3.28}$$

The choice

$$\kappa_L(z) = \frac{\omega(z^L - 1) + r\mu(z)\tilde{\Phi}_+(z) + (1-r)\omega\tilde{\Phi}_-(z)}{\mu(z)(z^L+1) - r\omega\tilde{\Phi}_-(z) - (1-r)\mu(z)\tilde{\Phi}_+(z)} \tag{4.3.29}$$

is therefore required for eq. (4.3.27) to hold. It may be shown that this choice of $\kappa_L$ causes all components of eq. (4.3.23) to vanish both when $s = z$ and $s = z^{-1}$. Since this is true, our application of the kernel method is complete.

At this point, we note that $\kappa_L$ as stated in eq. (4.3.29) is invariant under the

transformation $z \to z^{-1}$. To see this, first note that

$$\kappa_L(z^{-1}) = \frac{\omega(z^{-L}-1) + r\mu(z^{-1})\tilde{\Phi}_+(z^{-1}) + (1-r)\omega\tilde{\Phi}_-(z^{-1})}{\mu(z^{-1})(z^{-L}+1) - r\omega\tilde{\Phi}_-(z^{-1}) - (1-r)\mu(z^{-1})\tilde{\Phi}_+(z^{-1})}. \tag{4.3.30}$$

Secondly, we see that

$$\tilde{\Phi}_\pm(z^{-1}) = \sum_{n=1}^{L-1}[\Phi(n) \pm \Phi(L-n)]z^{-n} = z^{-L}\sum_{n=1}^{L-1}[\pm\Phi(n) + \Phi(L-n)]z^n. \tag{4.3.31}$$

Hence

$$\tilde{\Phi}_+(z^{-1}) = z^{-L}\tilde{\Phi}_+(z) \qquad \text{and} \qquad \tilde{\Phi}_-(z^{-1}) = -z^{-L}\tilde{\Phi}_-(z). \tag{4.3.32}$$

Finally,

$$\mu(z^{-1}) = z^{-1} - (1+\omega) = -\sqrt{\omega(2+\omega)} = (1+\omega) - z = -\mu(z). \tag{4.3.33}$$

Collecting these results together implies that

$$\kappa_L(z^{-1}) = \frac{\omega(z^{-L}-1) - r\mu(z)z^{-L}\tilde{\Phi}_+(z) - (1-r)\omega z^{-L}\tilde{\Phi}_-(z)}{-\mu(z)(z^{-L}+1) + r\omega z^{-L}\tilde{\Phi}_-(z) + (1-r)\mu(z)z^{-L}\tilde{\Phi}_+(z)} \tag{4.3.34}$$

which is equal to $\kappa_L(z)$ as given by eq. (4.3.29). Since $\kappa_L(z) = \kappa_L(z^{-1})$ has been proven, we henceforth drop the argument in favour of the simpler notation $\kappa_L$.

Returning to eq. (4.3.23), multiplying by $\frac{s^2}{K(s)}$ yields the generating functions in closed form. To read off the corresponding probability distributions, expressions for the coefficients of each power of $s$ are required. This is achieved via the power-series expansion

$$\frac{s^2}{K(s)} = \frac{s^2}{(1-z^{-1}s)(1-zs)(1-s)^2} = \sum_{n=0}^{\infty} c(n)s^n, \tag{4.3.35}$$

where it can be shown that

$$c(n) = \frac{z^2}{(z^2-1)(z-1)^2}\left[\left(z^n - \frac{1}{z^n}\right) - n\left(z - \frac{1}{z}\right)\right]. \tag{4.3.36}$$

This follows from carrying out a partial-fraction decomposition of the form

$$\frac{A}{1-z^{-1}s} + \frac{B}{1-zs} + \frac{C}{1-s} + \frac{D}{(1-s)^2} \tag{4.3.37}$$

and subsequent series expansions on each term. The $z^{\pm n}$ terms in $c(n)$ come from the $\frac{1}{1-z^{\pm 1}s}$ contributions, whilst the linear term comes from the $\frac{1}{(1-s)^2}$ contribution. The constant term we expect from $\frac{1}{1-s}$ cancels with an additional constant term that originates in the $\frac{1}{(1-s)^2}$ contribution, thus leaving us with linear and exponential terms only.

From this point, one takes the Cauchy product of $\frac{s^2}{K(s)}$ with the right-hand side of eq. (4.3.23) to give polynomials in $s$. Defining the difference operators $\Delta_\pm f(n) = \pm[f(n \pm 1) - f(n)]$ and $\Delta^2 f(n) = \Delta_+ f(n) - \Delta_- f(n) = \Delta_+ f(n) - \Delta_+ f(n-1)$, we can then read off the probability distributions as

$$\begin{aligned} P_{++}(n) = \kappa_L \Delta^2 c(n) &- \mathcal{A} \sum_{m=0}^{n} c(n-m) \Delta^2 \Phi_+(m) \\ &- \frac{\omega}{1+\omega} [\Delta_- c(n) + \omega(1+\kappa_L) c(n)] \\ &+ \frac{\omega^2}{1+\omega} (1+\kappa_L) \sum_{m=0}^{n} c(n-m) \Phi_+(m) \\ &+ \frac{\omega}{1+\omega} \mathcal{B} \sum_{m=0}^{n} c(n-m) [\Delta_- \Phi(m) - \Delta_+ \Phi(L-m)] \end{aligned} \tag{4.3.38}$$

and

$$\begin{aligned} P_{+-}(n) = \Delta_- \Delta^2 c(n) &- \mathcal{B} \sum_{m=0}^{n} c(n-m) \Delta_- \Delta^2 \Phi(m) \\ &- \frac{\omega}{1+\omega} \left[\Delta_- c(n-1) + (1+\kappa_L)(\omega + \Delta_-) c(n)\right] \\ &+ \frac{\omega^2}{1+\omega} (1+\kappa_L) \sum_{m=0}^{n} c(n-m) \Phi_+(m) \\ &+ \frac{\omega}{1+\omega} \mathcal{A} \sum_{m=0}^{n} c(n-m) \Delta_- \Phi_+(m) \\ &+ \frac{\omega}{1+\omega} \mathcal{B} \sum_{m=0}^{n} c(n-m) \Delta_- \left[\Phi(m) + \Phi(m-1)\right], \end{aligned} \tag{4.3.39}$$

where

$$\mathcal{A} = r + (1-r)\kappa_L \qquad \text{and} \qquad \mathcal{B} = (1-r) + r\kappa_L. \tag{4.3.40}$$

The validity of these expressions is demonstrated in fig. 4.6. Whilst these expressions are correct and useful for evaluating the distributions numerically, they are difficult to physically interpret. There are, nevertheless, discrete cases which admit simple solutions that do not require us to algebraically evaluate

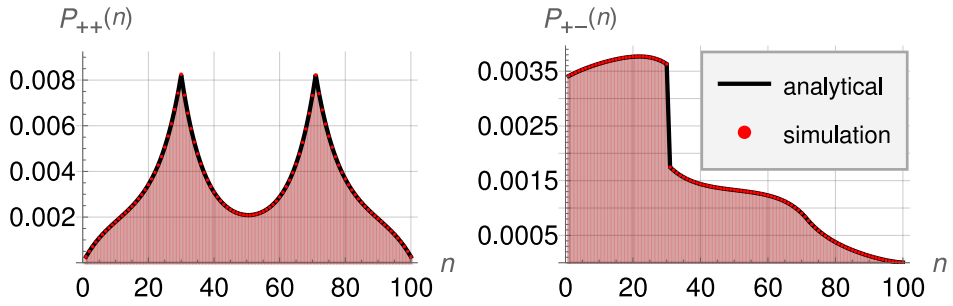


**Figure 4.6** *The distributions $P_{++}(n)$ and $P_{+-}(n)$ from eqs.* (4.3.38) *and* (4.3.39) *plotted against simulation data (see section 2.3) for $\omega = \frac{1}{100}$, $L = 101$, $\Phi(n) = \delta_{n,30}$, and $r = \frac{1}{2}$. The distributions have been normalised such that the total probability across all four quadrants is unity. The simulation data is in exact correspondence with the analytical predictions.*

eqs. (4.3.38) and (4.3.39). We shall explore one such case relevant to MIPS in the next section, before providing an alternative treatment of the general case in chapter 5.

## 4.4 The special case of partially-jamming particles with no recoil-induced reversals

We now consider an example that admits a simple solution and, importantly, one that is straightforward to interpret. This solution we obtain by returning to an earlier stage of the derivation detailed in the previous section. From there, a direct route to the solution will be presented, thus circumventing the need to work with eqs. (4.3.38) and (4.3.39). The recoil distribution we shall consider is of the form

$$\Phi(n) = u\delta_{n,1} + v\delta_{n,L-1}, \tag{4.4.1}$$

where $u + v = 1$. Additionally, we will set $r = 0$ throughout this section. This setup therefore constitutes a simple extension to the SEB case, where in addition to the jamming contribution $u\delta_{n,1}$, we also have a *particle-exchange* term, $v\delta_{n,L-1}$. The particle-exchange term switches the particles' positions such that they have, in effect, passed through each other. This interaction is equivalent to a recoil of size $L-1$ sites.

This case is of interest due to its physical relevance. In [54], it was shown that jamming is a stable phenomenon in a physically relevant continuum limit. With

the exchange contribution now in place, we are able to probe how robust a phenomenon jamming is and hence make inferences about the stability of MIPS.

### 4.4.1 Diagonalisation

In order to proceed, we first present a diagonalisation procedure that will make our task considerably easier. This procedure is important as we will use it again in chapter 5. Equation (4.3.23) may be diagonalised by firstly noting from eqs. (4.3.24) and (4.3.25) that

$$(s-z)(s-z^{-1}) = [s-(1+\omega)]^2 - \omega(2+\omega). \tag{4.4.2}$$

Expanding the right-hand side of this equation and cancelling terms then leads to

$$(s-z)(s-z^{-1}) = (s-1)(s-1) - 2\omega s. \tag{4.4.3}$$

It therefore follows that

$$\begin{aligned}\frac{K(s)}{s^2} &= \frac{(1+\omega)[(s-1)(s-1)-2\omega s](s-1)(1-s)}{s^2} \\ &= (1+\omega)[(s-1)(1-s^{-1})-2\omega](s-1)(s^{-1}-1) \\ &= (1+\omega)[2\omega-(1-s)(s^{-1}-1)](1-s)(s^{-1}-1).\end{aligned} \tag{4.4.4}$$

The factor $(1-s)(s^{-1}-1)$ in generating-function space corresponds to a second-order difference in real space (away from the domain boundaries), as is proven below for an arbitrary generating function $\tilde{h}(s)$:

$$\begin{aligned}(1-s)(s^{-1}-1)\tilde{h}(s) &= \sum_n (s-2+s^{-1})h(n)s^n \\ &= \sum_n h(n-1)s^n - 2\sum_n h(n)s^n + \sum_n h(n+1)s^n \\ &= \sum_n \{[h(n+1)-h(n)]-[h(n)-h(n-1)]\}\, s^n \\ &= \sum_n \{\Delta_+ h(n) - \Delta_+ h(n-1)\}\, s^n \\ &= \sum_n \Delta^2 h(n) s^n,\end{aligned} \tag{4.4.5}$$

where we recall the definitions of the difference operators stated prior to eq. (4.3.38). Given the above, the left-hand side of eq. (4.3.23) corresponds to

the real-space representation

$$\frac{K(s)}{s^2}\begin{pmatrix} G_{++}(s) \\ G_{+-}(s) \\ G_{-+}(s) \end{pmatrix} \;\rightleftarrows\; \frac{(1+\omega)(2\omega-\Delta^2)\Delta^2}{P_{+-}(1)}\begin{pmatrix} P_{++}(n) \\ P_{+-}(n) \\ P_{-+}(n) \end{pmatrix}. \tag{4.4.6}$$

Having dealt with the left-hand side of eq. (4.3.23), we must now deal with its right-hand side. Equations (4.3.15) and (4.4.1) imply that

$$\tilde{\Phi}(s) = us + vs^{L-1} \qquad \text{and} \qquad s^L\tilde{\Phi}(s^{-1}) = us^{L-1} + vs\ . \tag{4.4.7}$$

Matrix-multiplying the right-hand side of eq. (4.3.23) and inserting eqs. (4.3.22) and (4.4.7) explicitly, one obtains

$$\begin{pmatrix} a_{-1}s^{-1} + a_0 + a_1 s + a_2 s^2 + a_3 s^3 \\ b_{-1}s^{-1} + b_0 + b_1 s + b_2 s^2 + b_3 s^3 \\ c_{-1}s^{-1} + c_0 + c_1 s + c_2 s^2 + c_3 s^3 \end{pmatrix} + \begin{pmatrix} a_{L-3}s^{L-3} + a_{L-2}s^{L-2} + a_{L-1}s^{L-1} + a_L s^L + a_{L+1}s^{L+1} \\ b_{L-3}s^{L-3} + b_{L-2}s^{L-2} + b_{L-1}s^{L-1} + b_L s^L + b_{L+1}s^{L+1} \\ c_{L-3}s^{L-3} + c_{L-2}s^{L-2} + c_{L-1}s^{L-1} + c_L s^L + c_{L+1}s^{L+1} \end{pmatrix}, \tag{4.4.8}$$

where $a_n$, $b_n$ and $c_n$ are the constant coefficients of the $s^n$ terms and whose forms are not necessary in what follows. The notation $n$ here reflects the fact that the exponents of $s$ correspond to site locations on the lattice. With this in mind, the above polynomials are relevant only around $n = 1$ and $n = L - 1$, that is, in the boundary regions. For lattices larger than several sites, there are no monomials $s^n$ present for $3 < n < L - 3$. We therefore conclude that in the bulk of the domain for recoil distributions of the form 4.4.1, we must solve

$$\frac{(1+\omega)(2\omega-\Delta^2)\Delta^2}{P_{+-}(1)}\begin{pmatrix} P_{++}(n) \\ P_{+-}(n) \end{pmatrix} = \begin{pmatrix} 0 \\ 0 \end{pmatrix}, \tag{4.4.9}$$

where, as before, only $P_{++}(n)$ and $P_{+-}(n)$ need consideration due to the symmetries in eqs. (4.3.7) and (4.3.8). The nonzero right-hand sides that apply at the boundaries encode the boundary conditions, though the explicit form of 4.4.8 is not required in the ensuing analysis as appropriate boundary conditions can be obtained more simply. We shall see this in what follows.

### 4.4.2 Discrete solution

The solution of eq. (4.4.9) reads

$$P_{+\pm}(n) = A_{+\pm} + B_{+\pm}n + C_{+\pm}z^n + D_{+\pm}z^{L-n}. \tag{4.4.10}$$

One can verify each of these terms as solutions via direct substitution. For brevity, we henceforth refer to unknowns in the $+-$ and $++$ cases with primed and unprimed letters, respectively, i.e. $A = A_{++}$, $A' = A_{+-}$, etc.

Equation (4.3.7) allows us to simplify the case in the $++$ quadrant as

$$P_{++}(n) = A + C(z^n + z^{L-n}). \tag{4.4.11}$$

The $+-$ quadrant is more subtle; none of the unknowns can be eliminated based on symmetry considerations. Furthermore, we see from eq. (4.3.10) that

$$P_{+-}(n+1) - P_{+-}(n) = -\omega[P_{++}(n) - P_{+-}(n)] - P_{+-}(1)\Phi(n), \tag{4.4.12}$$

for the case $r = 0$ considered in this section. Hence, from our choice of recoil distribution 4.4.1 there exists a discontinuous step with magnitude proportional to $u$ from $n = 1$ to $n = 2$ (we remark from eq. (4.3.10) that this is a generic feature of our choice of $\Phi(n)$, irrespective of the value of $r$). The solution in the $+-$ quadrant thus takes the form

$$P_{+-}(n) = A' + B'n + C'z^n + D'z^{L-n} + \Delta\delta_{n,1}. \tag{4.4.13}$$

This modification to eq. (4.4.10) is permissible since the bulk solution – where eq. (4.4.9) strictly applies – remains unchanged. Substituting the above forms into eqs. (4.3.9) and (4.3.10) and simplifying yields

$$\begin{aligned} &Cz^{n-1} + Cz^{L-n+1} - 2Cz^n - 2Cz^{L-n} + Cz^{n+1} + Cz^{L-n-1} \\ &+\omega[A' + B'L + C'z^{L-n} + D'z^n + A' + C'z^n + D'z^{L-n} - 2A - 2Cz^n - 2Cz^{L-n}] = 0 \end{aligned} \tag{4.4.14}$$

and

$$\begin{aligned} &B' + C'z^{n+1} + D'z^{L-n-1} - C'z^n - D'z^{L-n} \\ &\qquad + \omega[A + Cz^n + Cz^{L-n} - A' - B'n - C'z^n - D'z^{L-n}] = 0. \end{aligned} \tag{4.4.15}$$

Matching constant and linear terms on both sides of the above equations, we deduce that

$$A' = A \qquad \text{and} \qquad B = 0. \tag{4.4.16}$$

Plugging these constraints back into eqs. (4.4.14) and (4.4.15) and comparing coefficients of $z^n$ and $z^{L-n}$, one arrives at two further equations in $C$, $C'$ and $D'$. These are

$$C'z - C' + \omega C - \omega C' = C - 2Cz + Cz^2 + \omega D'z + \omega C'z - 2\omega Cz \tag{4.4.17}$$

and

$$D'z^{-1} - D' + \omega C - \omega D' = Cz^2 - 2Cz + C + \omega C'z + \omega D'z - 2\omega Cz. \tag{4.4.18}$$

Writing as the matrix equation

$$\begin{pmatrix} z - \omega z - \omega - 1 & -\omega z \\ -\omega z & z^{-1} - \omega z - \omega - 1 \end{pmatrix} \begin{pmatrix} C' \\ D' \end{pmatrix} = (1 - \omega - 2z + z^2 - 2\omega z) C \begin{pmatrix} 1 \\ 1 \end{pmatrix} \tag{4.4.19}$$

and inverting gives us the following solution for $C'$ and $D'$ in terms of $C$:

$$\begin{pmatrix} C' \\ D' \end{pmatrix} = \frac{1-z}{1+z} \begin{pmatrix} 1 \\ -1 \end{pmatrix} C. \tag{4.4.20}$$

It remains now to solve for $A$, $C$ and $\Delta$, which we achieve by invoking the boundary conditions. Choosing to normalise the distributions by $P_{+-}(1)$, the boundary conditions become

$$\frac{P_{++}(1)}{P_{+-}(1)} = \kappa_L, \qquad \frac{P_{+-}(1)}{P_{+-}(1)} = 1 \qquad \text{and} \qquad \frac{P_{+-}(L-1)}{P_{+-}(1)} = \frac{\omega\kappa_L + v}{1+\omega}. \tag{4.4.21}$$

The last of these is obtained from eq. (4.4.12). Setting $r = 0$, $w = 0$, $\Phi(L-1) = v$ (the parameter choices made at the outset of this section), and $n = L - 1$, eq. (4.4.12) reads as

$$P_{+-}(L) - P_{+-}(L-1) = -\omega[P_{++}(L-1) - P_{+-}(L-1)] - P_{+-}(1)v. \tag{4.4.22}$$

Recalling eqs. (4.3.5) and (4.3.7), and subsequently dividing all terms by $P_{+-}(1)$ yields

$$\frac{P_{+-}(L-1)}{P_{+-}(1)} = \omega\kappa_L - \omega\frac{P_{+-}(L-1)}{P_{+-}(1)} + v, \tag{4.4.23}$$

which can then be rearranged to show the final condition of 4.4.21.

Returning to eqs. (4.4.11) and (4.4.13), these boundary conditions imply

$$\begin{aligned} 1 &= A + \frac{1-z}{1+z}(z - z^{L-1})C + \Delta, \\ \kappa_L &= A + (z + z^{L-1})C, \\ \text{and} \qquad \frac{\omega\kappa_L + v}{1+\omega} &= A - \frac{1-z}{1+z}(z - z^{L-1})C, \end{aligned} \tag{4.4.24}$$

where each constant has been renormalised according to $X \mapsto \dfrac{X}{P_{+-}(1)}$. Finally showing that

$$\kappa_L = u\frac{(z-1)(z^{L-1}+1)}{(z+1)(z^{L-1}-1)} + v, \tag{4.4.25}$$

for the case considered in this section, one can solve the above set of equations for

$$A = v + u\frac{(1-z)^2}{(1+z)(1+z^2)}\frac{1-z^L}{1-z^{L-1}}, \tag{4.4.26}$$

$$C = u\frac{1-z}{(1+z^2)(1-z^{L-1})}, \tag{4.4.27}$$

$$\text{and} \qquad \Delta = \frac{2uz}{1+z^2}. \tag{4.4.28}$$

This completes the discrete solution. To summarise,

$$P_{++}(n) = A + C(z^n + z^{L-n}) \tag{4.4.29}$$

and

$$P_{+-}(n) = A + \frac{1-z}{1+z}C(z^n - z^{L-n}) + \Delta\delta_{n,1}, \tag{4.4.30}$$

where $A$, $C$ and $\Delta$ are as above.

### 4.4.3 Continuum solution and physical interpretation

We now apply the same scaling limit as was taken in the SEB model to the above solution, so as to facilitate an easier comparison of results. We define the new domain variable

$$x = \frac{n}{L} \tag{4.4.31}$$

and the *persistence*

$$\xi = \frac{\gamma}{\omega L}. \tag{4.4.32}$$

Here, the persistence is the same quantity as that which was introduced in the previous chapter, namely it is the number of 'laps' of the system an unhindered walker completes between reorientation events. Note that we have reinstated $\gamma$. To yield a continuum, the limit $L \to \infty$ is taken such that $x$ becomes a continuous variable; furthermore, we take $\gamma \to \infty$ such that $\xi$ remains finite, ergo $\frac{\omega}{\gamma} = \mathcal{O}\left(\frac{1}{L}\right)$. A consequence of the limit taken here is that particle motion becomes ballistic. To understand this it should first be noted that, due to stochasticity on the discrete domain, particle motion (ignoring reorientations) performs a random walk relative to a ballistic trajectory. As such, after traversing $L$ sites, the mean displacement from this trajectory is $\sqrt{L}$ sites [139]. Hence, the mean displacement from the ballistic trajectory as a fraction of the system size after $\mathcal{O}(L)$ hops is $\frac{\sqrt{L}}{L} = \frac{1}{\sqrt{L}}$, which vanishes when $L \to \infty$. Taking $\gamma = \mathcal{O}(L)$ such that $\omega = \mathcal{O}(1)$, this limit therefore leaves us with walkers which move ballistically over $\mathcal{O}(L)$ lattice sites, or an $\mathcal{O}(1)$ fraction of the total system size, before reorienting after $\mathcal{O}(1)$ time scales. This scaling limit is of interest since it approximates the motion of run-and-tumble bacteria.

We now proceed with the continuum solution. We firstly recall eq. (4.3.25). Taking the negative root, it is straightforward to see that when $\omega = \frac{1}{\xi L}$,

$$z \approx 1 - \sqrt{\frac{2}{\xi L}} \tag{4.4.33}$$

for $L \gg 1$. (The choice of root here is arbitrary; we choose the smaller root for ease of calculation.) Using $n = Lx$, one sees that $z^n = z^{Lx}$ behaves as follows in the large-$L$ limit:

$$z^{Lx} \approx \left(1 - \sqrt{\frac{2}{\xi L}}\right)^{Lx} = \left[\left(1 - \sqrt{\frac{2}{\xi L}}\right)^{\sqrt{L}}\right]^{\sqrt{L}x} \xrightarrow{L\to\infty} \mathrm{e}^{-\sqrt{\frac{2L}{\xi}}x}. \tag{4.4.34}$$

Similarly,

$$z^{L(1-x)} \xrightarrow{L\to\infty} \mathrm{e}^{-\sqrt{\frac{2L}{\xi}}(1-x)}. \tag{4.4.35}$$

With these results in mind, we deduce the large-$L$ values from eqs. (4.4.26)

to (4.4.28) to be

$$A \approx v + \frac{u}{2\xi L}, \tag{4.4.36}$$

$$C \approx \frac{u}{\sqrt{2\xi L}}, \tag{4.4.37}$$

$$\text{and} \qquad \Delta \approx u\ . \tag{4.4.38}$$

Hence, using the definitions

$$p(x) = \lim_{L\to\infty} \frac{P_{++}(Lx)}{P_{+-}(1)} \qquad \text{and} \qquad q(x) = \lim_{L\to\infty} \frac{P_{+-}(Lx)}{P_{+-}(1)}\ , \tag{4.4.39}$$

we arrive at

$$p(x) = v + \frac{u}{2\xi L} + \frac{u}{\sqrt{2\xi L}} \left[ \mathrm{e}^{-\sqrt{\frac{2L}{\xi}}x} + \mathrm{e}^{-\sqrt{\frac{2L}{\xi}}(1-x)} \right] \tag{4.4.40}$$

and

$$q(x) = v + \frac{u}{2\xi L} + \frac{u}{2\xi L} \left[ \mathrm{e}^{-\sqrt{\frac{2L}{\xi}}x} - \mathrm{e}^{-\sqrt{\frac{2L}{\xi}}(1-x)} \right] + u\Theta\left(\frac{1}{L} - x\right), \tag{4.4.41}$$

where $\Theta(x)$ is the Heaviside step function.

Three interesting cases arise from these distributions. Firstly, we have the case $v = 0$ (jamming only). Then,

$$\frac{1}{\sqrt{2\xi L}} \left[ \mathrm{e}^{-\sqrt{\frac{2L}{\xi}}x} + \mathrm{e}^{-\sqrt{\frac{2L}{\xi}}(1-x)} \right] \xrightarrow{L\to\infty} \frac{1}{2L} \left[\delta(x) + \delta(1-x)\right] \tag{4.4.42}$$

and

$$L\Theta\left(\frac{1}{L} - x\right) \xrightarrow{L\to\infty} \delta(x) \tag{4.4.43}$$

on the interval $[0, 1]$, where $\delta(x)$ is the Dirac delta function, and we have

$$p(x) \propto \frac{1}{\xi} + \left[\delta(x) + \delta(1-x)\right] \qquad \text{and} \qquad q(x) \propto \frac{1}{\xi} + 2\delta(x). \tag{4.4.44}$$

This confirms the result from [54]. In the $+-$ quadrant, neither particle is able to move when adjacent to and facing its neighbour (they are jammed), thus engendering the delta-function term in $q(x)$. Since $++$ configurations can only be accessed from the $+-$ or $-+$ quadrants (via velocity reversals), this feature biases following particles into also being adjacent; the delta-function terms in $p(x)$ are a consequence of this. The manifestation of jamming as delta functions

in both of the above stationary distributions indicates that it is a strong feature of the system. To be more specific, in both quadrants the delta functions account for $\frac{2}{2+\xi^{-1}}$ of the total probability: this fraction tends closer to unity as the persistence increases, in line with the expectation that at high persistence the particles will spend most of their time jammed or in adjacent following states; otherwise, when the persistence is low, the particles behave more like random walkers and the jamming signature fades.

Secondly, we can consider the case where $v = \mathcal{O}(1)$; then, from eqs. (4.4.40) and (4.4.41), we see in the same limit that

$$p(x) \propto v \qquad \text{and} \qquad q(x) \propto v + u\Theta\left(\frac{1}{L} - x\right). \tag{4.4.45}$$

We observe that the delta-function term present in $q(x)$ for the previous case of $v = 0$ has been suppressed by $\mathcal{O}(L)$. This is understood as follows. In the previous case, particles jam, on average, for $\mathcal{O}(1)$ units of time, eventually freeing up due to a velocity reversal. In the present case, since there is an $\mathcal{O}(1)$ probability that the particles exchange, jamming occurs for $\mathcal{O}\left(\frac{1}{L}\right)$ units of time, on average, before the configuration is exited, (because $\gamma = \mathcal{O}(L)$). The jamming contribution is hence suppressed by $\mathcal{O}\left(\frac{1}{L}\right)$ relative to the fully-excluding case, and the extent to which jamming remains a feature is determined – rather intuitively – by the magnitude of $u$. In contrast to the previous case, the probability of being in a jammed state in the $+-$ quadrant is $\frac{\frac{u}{L}}{\frac{u}{L}+v\left(1-\frac{1}{L}\right)} \approx \frac{u}{vL} = \mathcal{O}\left(\frac{1}{L}\right)$. As all other separations in the $+-$ quadrant also occur with $\mathcal{O}\left(\frac{1}{L}\right)$ probability, the bias towards tumbling into the $++$ quadrant during jammed states (as was the case for $v = 0$) is lost, and $p(x)$ therefore becomes uniform.

Finally, the crossover case $v = \mathcal{O}\left(\frac{1}{L}\right)$ is considered. Letting $v = \frac{\hat{v}}{2L}$, the distributions become

$$p(x) \propto \hat{v} + \frac{1}{\xi} + [\delta(x) + \delta(1-x)] \qquad \text{and} \qquad q(x) \propto \hat{v} + \frac{1}{\xi} + 2\delta(x). \tag{4.4.46}$$

One sees that these are identical to eq. (4.4.44), only shifted upwards by an amount $\hat{v}$. The difference between the present case and the fully-excluding case of $v = 0$ is that the rate of exiting the jammed configuration via a velocity reversal is of the same order as the rate of exiting the jammed configuration via particle exchange. In the case of particle exchange, this is due to there being $\mathcal{O}(L)$ hops per unit time ($\gamma = \mathcal{O}(L)$), of which $\mathcal{O}(1)$ would result in exchange. Exiting

the jammed state via a velocity reversal also has $\mathcal{O}(1)$ probability of occurring per unit time ($\omega = \mathcal{O}(1)$). Since there are two equiprobable means of exiting a jammed state, as opposed to there being just one for the fully-excluding case, some of the probability associated with jamming in the fully-excluding case is redistributed as a uniform component. This manifests as the $\hat{v}$ terms in each distribution.

From the last two cases, we see how fragile a phenomenon jamming is in this one-dimensional system. Only when the exchange probability is $\mathcal{O}\left(\frac{1}{L}\right)$ can we sustain jamming as an emergent behaviour; anything greater than this, such as the $v = \mathcal{O}(1)$ case, suppresses jamming significantly. These results may have implications for those wishing to study more realistic models of MIPS in which the possibility of particles passing each other is accounted for.

## 4.5 Concluding remarks

In this chapter, we investigated a one-dimensional lattice system inhabited by two persistent random walkers in which the walkers experience a 'recoil' interaction upon contact. By 'contact', we mean that walker A hops onto the site occupied by walker B; this actuates an instantaneous displacement of walker B by $n$ lattice sites according to a distribution $\Phi(n)$, which we refer to as the 'recoil distribution'. The displaced walker is also assigned a reversal probability which applies after recoils.

Using generating functions, we were able to solve for the stationary distributions of the particles' separations in each of the two independent quadrants of the model: $++$ and $+-$. The forms of the resulting distributions as given in eqs. (4.3.38) and (4.3.39) were validated but are, however, difficult to interpret physically. The special case wherein particles may only jam or pass through each other with no recoil-induced reversals was treated explicitly, serving as an example of a case that admits a simple interpretation. This was achieved by deriving decoupled equations and associated boundary conditions for each of the model's two independent quadrants, which we subsequently solved. We found in a continuum limit that jamming is a feature of the system only when the probability of particle exchange is $\mathcal{O}\left(\frac{1}{L}\right)$; then, the stationary distributions are given by eq. (4.4.46). For higher-order particle-exchange probabilities, all states of the system occur with $\mathcal{O}(1)$ probability as in eq. (4.4.45). These results may have

implications for our understanding of MIPS given that, as we saw in chapter 3, two-particle jammed states serve as seeds for multiparticle clusters. For example, more biologically realistic models of MIPS may wish to account for particles being able to navigate past each other when there exists sufficient space to do so. The results of this chapter suggest that MIPS may be more unstable when such circumstances are met.

We will continue to explore the ideas presented here in the next chapter, where we will take a different approach to characterising the stationary distributions for a general class of recoil distributions. This will involve taking the scaling limit presented in section 4.4 from the outset, yielding a description in the continuum which can be solved for using standard techniques.

# Chapter 5

# Persistent random walkers undergoing an active contact interaction: a continuum solution

In the previous chapter, we investigated a system of recoiling persistent random walkers on a one-dimensional lattice. Though we derived a general solution for the resulting stationary distributions, we found them difficult to physically interpret, and instead focussed on a special case that gave us insights into the robustness of jamming. In this chapter, we will make use of the generating-function machinery of chapter 4 to derive differential equations for each of the independent stationary distributions for a general class of recoil interactions. We will then solve these equations and analyse the resulting forms.

To be more specific, we will allow for the possibility of three contributions to the recoil distribution. In addition to the jamming and exchange contributions discussed at length in the previous chapter, we will also allow for recoils into the 'bulk' of the domain. By this, we mean recoils that separate the particles by $\mathcal{O}(L)$ lattice sites. Such contributions can be 'smooth', such as a parabolic distribution across the domain, discontinuous, such as a delta distribution at some point in the domain, or a superposition of both types of contribution, such as a step. To summarise, we will be considering recoil distributions of the form

$$\Phi(n) = u\delta_{n,1} + v\delta_{n,L-1} + w\bar{\Phi}(n), \tag{5.0.1}$$

where $u + v + w = 1$ and where $\bar{\Phi}(n)$ is the normalised bulk contribution. Given that the interaction is active, it will be of interest to see precisely how the details of the recoil interaction and persistence determine the emergent behaviours of the system and, in particular, how this compares with the case of purely passive interactions.

The outline of this chapter is as follows. We will begin in section 5.1 by recalling the diagonalisation stated in the previous chapter, which we will use to derive differential equations for the stationary distributions. From information supplied to us by the master equations, we will determine and apply boundary conditions to our general solutions. We will then give an interpretation of the results in section 5.2 before finishing with concluding remarks in section 5.3.

The work presented in this chapter was published in [2, 3].

## 5.1 Continuum stationary-state solution

In this section, a continuum limit of the solutions quoted in eqs. (4.3.38) and (4.3.39) is determined via the same diagonalisation of eq. (4.3.23) that was presented in the previous chapter. To begin, we recall the diagonalisation summarised in (4.4.6):

$$\frac{K(s)}{s^2}\begin{pmatrix} G_{++}(s) \\ G_{+-}(s) \\ G_{-+}(s) \end{pmatrix} \;\rightleftarrows\; \frac{(1+\omega)(2\omega-\Delta^2)\Delta^2}{P_{+-}(1)}\begin{pmatrix} P_{++}(n) \\ P_{+-}(n) \\ P_{-+}(n) \end{pmatrix}, \tag{5.1.1}$$

where we remind the reader that $K(s)$ is the kernel in eq. (4.3.24), $\omega$ is the tumble rate as measured in units of the hop rate $\gamma$, and where, for example, $G_{++}(s)$ is the generating function of the stationary distribution $P_{++}(n)$. Since a continuum description is sought, the aim now is to turn the above difference equation into a differential equation. We take the same scaling limit as was introduced in the previous chapter, in which we have the relative position

$$x = \frac{n}{L} \tag{5.1.2}$$

and the *persistence*

$$\xi = \frac{\gamma}{\omega L}. \tag{5.1.3}$$

Enforcing $\frac{\omega}{\gamma} = \mathcal{O}\left(\frac{1}{L}\right)$ therefore implies that $\xi$ remains finite when we take $L \to \infty$ (this is the same limit we took at the start of section 4.4.3). This finite persistence is a consequence of $\mathcal{O}(L)$ hops occurring between reorientation events, that is, a finite fraction of the system size.

We must now rescale $P_{++}(n)$, $P_{+-}(n)$ and $\Phi(n)$. For the first two, we define the distributions

$$p(x) = \lim_{L\to\infty} \frac{P_{++}(Lx)}{P_{+-}(1)} \qquad \text{and} \qquad q(x) = \lim_{L\to\infty} \frac{P_{+-}(Lx)}{P_{+-}(1)} \tag{5.1.4}$$

(in keeping with the notation of section 4.4), whilst the recoil distribution (5.0.1) is rescaled as

$$\phi(x) = \lim_{L\to\infty} [L\Phi(Lx)] = u\delta\left(x - \frac{1}{L}\right) + v\delta\left(x - 1 + \frac{1}{L}\right) + w\rho(x), \tag{5.1.5}$$

where

$$\rho(x) = \lim_{L\to\infty} L\bar{\Phi}(Lx). \tag{5.1.6}$$

With these definitions in mind, it follows that

$$\begin{aligned}\lim_{L\to\infty}\left[\Delta^2\frac{P_{++}(n)}{P_{+-}(1)}\right] &= \lim_{L\to\infty}\left[\frac{P_{++}(Lx+1)}{P_{+-}(1)} - \frac{2P_{++}(Lx)}{P_{+-}(1)} + \frac{P_{++}(Lx-1)}{P_{+-}(1)}\right] \\ &= p\left(x + \frac{1}{L}\right) - 2p(x) + p\left(x - \frac{1}{L}\right) \\ &= \frac{1}{L^2}\frac{\mathrm{d}^2 p(x)}{\mathrm{d}x^2},\end{aligned} \tag{5.1.7}$$

and similarly,

$$\lim_{L\to\infty}\left[\Delta^2\frac{P_{+-}(n)}{P_{+-}(1)}\right] = \frac{1}{L^2}\frac{\mathrm{d}^2 q(x)}{\mathrm{d}x^2}. \tag{5.1.8}$$

The limiting form of the right-hand side of eq. (5.1.1) is hence

$$\frac{(1+\frac{1}{\xi L})(\frac{2}{\xi L} - \Delta^2)\Delta^2}{P_{+-}(1)}\begin{pmatrix} P_{++}(Lx) \\ P_{+-}(Lx)\end{pmatrix} \longrightarrow \left(\frac{2}{\xi L} - \frac{1}{L^2}\frac{\mathrm{d}^2}{\mathrm{d}x^2}\right)\frac{1}{L^2}\frac{\mathrm{d}^2}{\mathrm{d}x^2}\begin{pmatrix} p(x) \\ q(x)\end{pmatrix}. \tag{5.1.9}$$

We need not consider $P_{-+}(n)$ in the above since its limiting form is $q(1-x)$ (due to the particle-relabelling symmetry of eq. (4.3.7)).

The real-space representation of the right-hand side of eq. (4.3.23), i.e. the source

terms, has now to be found. We denote the right-hand side of eq. (4.3.23) by

$$\begin{pmatrix} \tilde{S}_{++}(s) \\ \tilde{S}_{+-}(s) \\ \tilde{S}_{-+}(s) \end{pmatrix}, \tag{5.1.10}$$

this being the vector of generating functions for the source terms in real space. Multiplying out the right-hand side of eq. (4.3.23) using eq. (4.3.26) for $\mathsf{M}(s)$ and reading off the coefficients of $s^n$, one finds the source term in the ++ quadrant to be (away from the boundaries)

$$\begin{aligned} S_{++}(n) = {} & A_1 w[\bar{\Phi}(n-1) + \bar{\Phi}(L-n+3)] \\ & - A_2 w[\bar{\Phi}(n-2) + \bar{\Phi}(L-n+2)] \\ & + A_3 w[\bar{\Phi}(n-3) + \bar{\Phi}(L-n+1)], \end{aligned} \tag{5.1.11}$$

where

$$A_1 = r + (1-r)\kappa_L, \tag{5.1.12}$$

$$A_2 = \omega[r\kappa_L + (1-r)] + \left[\frac{1}{1+\omega} + (1+\omega)\right][r + (1-r)\kappa_L], \tag{5.1.13}$$

$$\text{and} \quad A_3 = \frac{\omega}{1+\omega}[r\kappa_L + (1-r)] + [r + (1-r)\kappa_L]. \tag{5.1.14}$$

Using eq. (5.1.6), this can be rewritten as

$$\begin{aligned} S_{++}(Lx) = {} & \frac{A_1 w}{L}\left[\rho\left(x - \frac{1}{L}\right) + \rho\left(1 - x + \frac{3}{L}\right)\right] \\ & - \frac{A_2 w}{L}\left[\rho\left(x - \frac{2}{L}\right) + \rho\left(1 - x + \frac{2}{L}\right)\right] \\ & + \frac{A_3 w}{L}\left[\rho\left(x - \frac{3}{L}\right) + \rho\left(1 - x + \frac{1}{L}\right)\right]. \end{aligned} \tag{5.1.15}$$

To tidy this up, expansions around $x$ and $1-x$ are made where appropriate. This leads to

$$\begin{aligned} LS_{++}(Lx) \approx {} & (A_1 - A_2 + A_3) w\rho(x) + (A_1 - A_2 + A_3) w\rho(1-x) \\ & + (A_2 - 2A_3) w \frac{1}{L}\frac{\mathrm{d}\rho(x)}{\mathrm{d}x} + (2A_1 - A_2) w \frac{1}{L}\frac{\mathrm{d}\rho(1-x)}{\mathrm{d}(1-x)} \\ & + (-A_2 + 4A_3) w \frac{1}{2L^2}\frac{\mathrm{d}^2\rho(x)}{\mathrm{d}x^2} + (4A_1 - A_2) w \frac{1}{2L^2}\frac{\mathrm{d}^2\rho(1-x)}{\mathrm{d}(1-x)^2}. \end{aligned} \tag{5.1.16}$$

Higher-order derivatives can be shown to vanish in the scaling limit so need not be considered. The limiting values of the coefficients are as follows:

$$\lim_{L\to\infty}\begin{cases} +A_1 - A_2 + A_3 \\ +A_2 - 2A_3 \\ +2A_1 - A_2 \\ -A_2 + 4A_3 \\ +4A_1 - A_2 \end{cases} = \begin{cases} -(\xi L)^{-2}(1+\kappa_L) \\ -(\xi L)^{-1}[r\kappa_L + (1-r)] \\ -(\xi L)^{-1}[r\kappa_L + (1-r)] \\ +2[r + (1-r)\kappa_L] \\ +2[r + (1-r)\kappa_L] \end{cases}. \tag{5.1.17}$$

Defining $L^{-3}s_p(x) = \lim_{L\to\infty} S_{++}(Lx)$, the rescaled source term is therefore

$$s_p(x) = -\frac{1+\kappa_L}{\xi^2} w\rho_+(x) - \frac{r\kappa_L + (1-r)}{\xi} w\frac{\mathrm{d}\rho_-(x)}{\mathrm{d}x} + [r + (1-r)\kappa_L] w\frac{\mathrm{d}^2\rho_+(x)}{\mathrm{d}x^2}, \tag{5.1.18}$$

where

$$\rho_\pm(x) = \rho(x) \pm \rho(1-x) \tag{5.1.19}$$

are the symmetric and antisymmetric combinations of the bulk recoil distribution. Meanwhile, following the same procedure and defining $L^{-3}s_q(x) = \lim_{L\to\infty} S_{+-}(Lx)$ yields the following source term in the $+-$ quadrant:

$$s_q(x) = -\frac{1+\kappa_L}{\xi^2} w\rho_+(x) - \frac{1+\kappa_L}{\xi} w\frac{\mathrm{d}\rho_+(x)}{\mathrm{d}x} - \frac{r\kappa_L + (1-r)}{\xi} w\frac{\mathrm{d}\rho_-(x)}{\mathrm{d}x}. \tag{5.1.20}$$

The governing equation is therefore

$$\left(\frac{2}{\xi L} - \frac{1}{L^2}\frac{\mathrm{d}^2}{\mathrm{d}x^2}\right)\frac{1}{L^2}\frac{\mathrm{d}^2}{\mathrm{d}x^2}\begin{pmatrix} p(x) \\ q(x) \end{pmatrix} = \frac{1}{L^3}\begin{pmatrix} s_p(x) \\ s_q(x) \end{pmatrix}, \tag{5.1.21}$$

which simplifies to

$$\left(\frac{2}{\xi} - \frac{1}{L}\frac{\mathrm{d}^2}{\mathrm{d}x^2}\right)\frac{\mathrm{d}^2}{\mathrm{d}x^2}\begin{pmatrix} p(x) \\ q(x) \end{pmatrix} = \begin{pmatrix} s_p(x) \\ s_q(x) \end{pmatrix} \tag{5.1.22}$$

after cancelling the factors of $L^{-3}$. This completes the diagonalisation of the problem.

At this point, one might be tempted to drop the fourth-derivative terms on the left-hand side of eq. (5.1.22). As will be seen throughout this chapter, though, the fourth derivatives have implications for both the boundary and bulk behaviours of the stationary distributions and must therefore be kept.

### 5.1.1 Summary of solution

Before giving a detailed derivation, we summarise the full stationary solution for $p(x)$ and $q(x)$ defined in eq. (5.1.4). We find that

$$p(x) = A_p + \frac{r}{r(1-w)+w}\frac{w\xi}{2}\rho_+(x) - \frac{r(1-w)+(1-r)w}{r(1-w)+w}\frac{w}{2}\int_0^x \rho_-(y)\,\mathrm{d}y + \frac{2r(1-w)+w}{r(1-w)+w}\frac{w}{2\xi}\left[(1-x)\int_0^x y\rho_+(y)\,\mathrm{d}y + x\int_x^1 (1-y)\rho_+(y)\,\mathrm{d}y\right] \quad (5.1.23)$$

and

$$q(x) = A_q - \frac{2r(1-w)+w}{r(1-w)+w}\frac{w}{2}\int_0^x \rho_+(y)\,\mathrm{d}y - \frac{r(1-w)+(1-r)w}{r(1-w)+w}\frac{w}{2}\int_0^x \rho_-(y)\,\mathrm{d}y + \frac{2r(1-w)+w}{r(1-w)+w}\frac{w}{2\xi}\left[(1-x)\int_0^x y\rho_+(y)\,\mathrm{d}y + x\int_x^1 (1-y)\rho_+(y)\,\mathrm{d}y\right], \quad (5.1.24)$$

where $A_p$ and $A_q$ are constants that depend on the parameters of the problem, and where it is understood that $p(0) = p(1) = q(0) = q(1) = 0$ due to the exclusion condition as implemented on the lattice by eqs. (4.3.2) and (4.3.5). Note that the above distributions do not smoothly vanish at the boundaries, but instead do so discontinuously. This can be seen by evaluating eqs. (5.1.23) and (5.1.24) at $x = 0$ and $x = 1$: in contrast to the boundary values stated four lines above, the resulting values are generically nonzero. Ultimately, this behaviour is a consequence of the $\mathcal{O}\left(\frac{1}{L}\right)$ prefactor to the fourth derivative in eq. (5.1.22). We shall see why this is the case throughout the derivation, where much of our attention will be focussed on dealing with nontrivial boundary behaviours. This will require us to keep finite-size corrections throughout; only at the end of the derivation can we state the true limiting form of the solution as above.

### 5.1.2 General solutions

We now begin our derivation of the above solution. There are two methods of solving for the general solution of eq. (5.1.22), both of which will be discussed in this subsection. Necessary to both methods is the complementary function of our operator. This will be our starting point.

### Complementary function

To find the complementary function, $c(x)$, the homogeneous counterpart to eq. (5.1.22),

$$\left(\frac{2}{\xi} - \frac{1}{L}\frac{\mathrm{d}^2}{\mathrm{d}x^2}\right)\frac{\mathrm{d}^2}{\mathrm{d}x^2}\, c(x) = 0, \tag{5.1.25}$$

must be solved. The solution is

$$c(x) = A + Bx + C\mathrm{e}^{-\sqrt{\frac{2L}{\xi}}x} + D\mathrm{e}^{+\sqrt{\frac{2L}{\xi}}x}, \tag{5.1.26}$$

where $A$, $B$, $C$, and $D$ are constants of integration. Relabelling $D$ as $D\mathrm{e}^{-\sqrt{\frac{2L}{\xi}}}$ allows us to express this in the symmetrised form

$$c(x) = A + Bx + C\mathrm{e}^{-\sqrt{\frac{2L}{\xi}}x} + D\mathrm{e}^{-\sqrt{\frac{2L}{\xi}}(1-x)}. \tag{5.1.27}$$

From the above we see one way in which the fourth derivatives in eq. (5.1.22) are important: they give rise to the exponential terms which, depending on the order of the coefficients $A$, $B$, $C$ and $D$, may be of comparable order to the constant and linear terms at the domain boundaries.

### Green's function approach

With the complementary function established, the inhomogeneous solutions of eq. (5.1.22) may be sought. To find the inhomogenous solutions, we use the method of Green's functions. All Green's functions for this problem, $\mathcal{G}(x, y)$, where $y$ is an arbitrary point in the $x$ domain, must satisfy the equation

$$\frac{2}{\xi}\mathcal{G}''(x, y) - \frac{1}{L}\frac{\mathrm{d}^2\mathcal{G}''(x, y)}{\mathrm{d}x^2} = \delta(x - y), \tag{5.1.28}$$

where primes denote derivatives with respect to $x$. This is obtained by replacing the source term of eq. (5.1.22) with the point source $\delta(x-y)$. Fourier-transforming the above equation recasts it as

$$\frac{k^2}{L}\tilde{\mathcal{G}}''(k, y) + \frac{2}{\xi}\tilde{\mathcal{G}}''(k, y) = \mathrm{e}^{-iky}, \tag{5.1.29}$$

and therefore

$$\tilde{\mathcal{G}}''(k, y) = \frac{L\mathrm{e}^{-iky}}{k^2 + \frac{2L}{\xi}}. \tag{5.1.30}$$

The inverse Fourier transform is thence

$$\mathcal{G}''(x,y) = \frac{L}{2\pi}\int_{-\infty}^{+\infty} \frac{\mathrm{e}^{+ik(x-y)}}{(k+i\sqrt{\frac{2L}{\xi}})(k-i\sqrt{\frac{2L}{\xi}})}\,\mathrm{d}k\,. \tag{5.1.31}$$

The simple poles at $k = \pm i\sqrt{\frac{2L}{\xi}}$ make this amenable to contour integration. Carrying out the integration and subsequently integrating twice with respect to $x$ then yields

$$\mathcal{G}(x,y) = \frac{\xi}{4}\sqrt{\frac{\xi}{2L}}\begin{cases} \mathrm{e}^{-\sqrt{\frac{2L}{\xi}}(x-y)} + \alpha_1 x + \alpha_0, & y \le x \\ \mathrm{e}^{+\sqrt{\frac{2L}{\xi}}(x-y)} + \beta_1 x + \beta_0, & y \ge x \end{cases}. \tag{5.1.32}$$

There are four constants here that need to be determined. These can be computed by requiring continuity at $x = y$ in both the Green's function and its first derivative; two further equations can then be established by requiring that $\mathcal{G}(0,y) = \mathcal{G}(1,y) = 0$. This choice of boundary conditions is made for convenience's sake as it guarantees a particular integral which vanishes at the domain boundaries, somewhat simplifying the application of boundary conditions to the general solution (this being the sum of the particular integral and the complementary function).

Carrying out the above-described procedures, one ends up with

$$\begin{aligned}\mathcal{G}(x,y) = \frac{\xi}{4}\sqrt{\frac{\xi}{2L}}\left[\mathrm{e}^{-\sqrt{\frac{2L}{\xi}}|x-y|} - x\mathrm{e}^{-\sqrt{\frac{2L}{\xi}}(1-y)} - (1-x)\mathrm{e}^{-\sqrt{\frac{2L}{\xi}}y}\right] \\ - \frac{\xi}{2}\left[(1-x)y\Theta(x-y) + x(1-y)\Theta(y-x)\right].\end{aligned} \tag{5.1.33}$$

Once more, it is tempting to drop the terms which are subleading in $L$. The resulting Green's function is that of a regular diffusion equation, that is, it amounts to ignoring the fourth-derivative term of eq. (5.1.22) completely. We reiterate at this point that ignoring such subleading contributions leads to incomplete results.

With an appropriate Green's function established, it follows that the particular integrals and hence the general solutions to the problem have been obtained. For $p(x)$, we have

$$p(x) = A_p + B_p x + C_p\mathrm{e}^{-\sqrt{\frac{2L}{\xi}}x} + D_p\mathrm{e}^{-\sqrt{\frac{2L}{\xi}}(1-x)} + \int_0^1 \mathcal{G}(x,y)s_p(y)\,\mathrm{d}y\,, \tag{5.1.34}$$

whilst, for $q(x)$, we have

$$q(x) = A_q + B_q x + C_q \mathrm{e}^{-\sqrt{\frac{2L}{\xi}}x} + D_q \mathrm{e}^{-\sqrt{\frac{2L}{\xi}}(1-x)} + \int_0^1 \mathcal{G}(x,y) s_q(y)\,\mathrm{d}y\,. \quad (5.1.35)$$

Before proceeding further, it is first noted that the symmetry due to particle relabelling as originally stated in eq. (4.3.7) may be used to eliminate two of the unknowns in eq. (5.1.34). In the continuum, eq. (4.3.7) as applied to the ++ quadrant reads as

$$p(x) = p(1-x), \quad (5.1.36)$$

since relabelling as applied to particles moving in the same direction effects only a change in the particles' separation. This implies that

$$\begin{aligned} &A_p + B_p x + C_p \mathrm{e}^{-\sqrt{\frac{2L}{\xi}}x} + D_p \mathrm{e}^{-\sqrt{\frac{2L}{\xi}}(1-x)} + \int_0^1 \mathcal{G}(x,y) s_p(y)\,\mathrm{d}y \\ &\quad = A_p + B_p(1-x) + C_p \mathrm{e}^{-\sqrt{\frac{2L}{\xi}}(1-x)} + D_p \mathrm{e}^{-\sqrt{\frac{2L}{\xi}}x} + \int_0^1 \mathcal{G}(1-x,y) s_p(y)\,\mathrm{d}y\,. \end{aligned} \quad (5.1.37)$$

It may be seen from eq. (5.1.33) that the Green's function is symmetric under the transformation $(x,y) \mapsto (1-x, 1-y)$, that is, $G(x,y) = G(1-x,1-y)$, and that, from eqs. (5.1.18) and (5.1.19), the source term is symmetric under the transformation $x \mapsto 1-x$, that is, $s_p(x) = s_p(1-x)$. Letting $u = 1-y$, the first of these symmetries implies that

$$\begin{aligned} \int_0^1 \mathcal{G}(1-x,y) s_p(y)\,\mathrm{d}y &= \int_1^0 \mathcal{G}(1-x,1-u) s_p(1-u)\,\mathrm{d}(-u) \\ &= \int_0^1 \mathcal{G}(x,u) s_p(u)\,\mathrm{d}u\,. \end{aligned} \quad (5.1.38)$$

It is therefore required that the complementary function also be symmetric in order for $p(x) = p(1-x)$ to be fulfilled. We conclude that

$$B_p = 0 \qquad \text{and} \qquad D_p = C_p\ . \quad (5.1.39)$$

This means we can write

$$p(x) = A_p + C_p \left[\mathrm{e}^{-\sqrt{\frac{2L}{\xi}}x} + \mathrm{e}^{-\sqrt{\frac{2L}{\xi}}(1-x)}\right] + \int_0^1 \mathcal{G}(x,y) s_p(y)\,\mathrm{d}y\,. \quad (5.1.40)$$

No symmetries can be used to simplify $q(x)$ in an analogous way.

At this point we can manipulate the integrands of eqs. (5.1.34) and (5.1.35) into a form which is not only more amenable to the application of boundary conditions, but is also easier to work with when the recoil distribution contains discontinuities in the bulk of the domain. This we do by moving the derivatives on the recoil distribution onto the Green's function. Integration by parts tells us that

$$\int_0^1 \mathcal{G}(x,y)\frac{\mathrm{d}f(y)}{\mathrm{d}y}\,\mathrm{d}y = \text{constant} - \int_0^1 \frac{\partial\mathcal{G}(x,y)}{\partial y}f(y)\,\mathrm{d}y \tag{5.1.41}$$

$$\text{and}\quad \int_0^1 \mathcal{G}(x,y)\frac{\mathrm{d}^2f(y)}{\mathrm{d}y^2}\,\mathrm{d}y = \text{constant} + \int_0^1 \frac{\partial^2\mathcal{G}(x,y)}{\partial y^2}f(y)\,\mathrm{d}y\,. \tag{5.1.42}$$

The constant terms here may be dropped since they can be absorbed into $A_p$. As such, the general solutions in eqs. (5.1.35) and (5.1.40) may be re-expressed as

$$\begin{aligned} p(x) = A_p + C_p\left[\mathrm{e}^{-\sqrt{\frac{2L}{\xi}}x} + \mathrm{e}^{-\sqrt{\frac{2L}{\xi}}(1-x)}\right] &- \frac{1+\kappa_L}{\xi^2}w\int_0^1 \mathcal{G}(x,y)\rho_+(y)\,\mathrm{d}y \\ &+ \frac{r\kappa_L+(1-r)}{\xi}w\int_0^1 \frac{\partial\mathcal{G}(x,y)}{\partial y}\rho_-(y)\,\mathrm{d}y \\ &+ [r+(1-r)\kappa_L]w\int_0^1 \frac{\partial^2\mathcal{G}(x,y)}{\partial y^2}\rho_+(y)\,\mathrm{d}y \end{aligned} \tag{5.1.43}$$

and

$$\begin{aligned} q(x) = A_q + B_q x + C_q\mathrm{e}^{-\sqrt{\frac{2L}{\xi}}x} + D_q\mathrm{e}^{-\sqrt{\frac{2L}{\xi}}(1-x)} &- \frac{1+\kappa_L}{\xi^2}w\int_0^1 \mathcal{G}(x,y)\rho_+(y)\,\mathrm{d}y \\ &+ \frac{1+\kappa_L}{\xi}w\int_0^1 \frac{\partial\mathcal{G}(x,y)}{\partial y}\rho_+(y)\,\mathrm{d}y + \frac{r\kappa_L+(1-r)}{\xi}w\int_0^1 \frac{\partial\mathcal{G}(x,y)}{\partial y}\rho_-(y)\,\mathrm{d}y\,. \end{aligned} \tag{5.1.44}$$

We may now get a flavour for how the Green's function interacts with the recoil distribution to determine the stationary distributions. Generally speaking, $\rho(x)$ – the bulk part of the continuum recoil distribution – may be decomposed as a sum over continuous and discontinuous pieces. Specifically,

$$\begin{aligned} \rho(x) &= \sum_i a_i\delta(x-x_i) + \sum_j b_j\Theta(x-x_j) + \sum_k c_k\Theta(x_k-x) + d\bar{\rho}(x) \\ &=: \psi(x) + d\bar{\rho}(x), \end{aligned} \tag{5.1.45}$$

where $\psi(x)$ captures all discontinuous contributions, $\bar{\rho}(x)$ is continuous and normalised to unity, $d = 1 - \sum_i a_i - \sum_j b_j(1-x_j) - \sum_k c_k x_k$, and where all $x_{i,j,k}$ are taken to be in the bulk of the domain. We can investigate how each

type of term in the above contributes to the integrals

$$\int_0^1 \mathcal{G}(x,y)\rho_+(y)\,\mathrm{d}y\,, \quad \int_0^1 \frac{\partial\mathcal{G}(x,y)}{\partial y}\rho_\pm(y)\,\mathrm{d}y \quad \text{and} \quad \int_0^1 \frac{\partial^2\mathcal{G}(x,y)}{\partial y^2}\rho_+(y)\,\mathrm{d}y \tag{5.1.46}$$

that we see in eqs. (5.1.43) and (5.1.44). The full list of contributions is given in appendix A; here, we note only the most interesting features. Firstly, we see that delta functions in the recoil distribution give rise to $\mathcal{O}(1)$ contributions in the resulting stationary distributions, effecting exponential smoothing either side of a discontinuous jump:

$$\int_0^1 \frac{\partial\mathcal{G}(x,y)}{\partial y}\delta(y-x_0)\,\mathrm{d}y = \frac{\xi}{4}\mathrm{e}^{-\sqrt{\frac{2L}{\xi}}(x-x_0)}\Theta(x-x_0) - \frac{\xi}{4}\mathrm{e}^{-\sqrt{\frac{2L}{\xi}}(x_0-x)}\Theta(x_0-x) - \frac{\xi}{2}\Theta(x-x_0) + \frac{\xi}{2}x\,. \tag{5.1.47}$$

Though $L$ is relatively small, one can see this effect in the right panel of fig. 4.6. Most of the interesting behaviour, however, can be seen to derive from the Green's function's second derivative. We have

$$\int_0^1 \frac{\partial^2\mathcal{G}(x,y)}{\partial y^2}\rho_+(y)\,\mathrm{d}y = \int_0^1 \frac{\partial^2\mathcal{G}(x,y)}{\partial y^2}\psi_+(y)\,\mathrm{d}y + \int_0^1 \frac{\partial^2\mathcal{G}(x,y)}{\partial y^2}\bar{\rho}_+(y)\,\mathrm{d}y\,, \tag{5.1.48}$$

where $\psi_+(x)$ is defined as the symmetrised version of $\psi(x)$ by analogy with the symmetrised recoil distribution defined in eq. (5.1.19). The integral over $\psi_+(y)$ gives rise to two interesting features. The first of these can be seen from

$$\int_0^1 \frac{\partial^2\mathcal{G}(x,y)}{\partial y^2}\delta(y-x_0)\,\mathrm{d}y = \frac{1}{2}\sqrt{\frac{\xi L}{2}}\mathrm{e}^{-\sqrt{\frac{2L}{\xi}}|x-x_0|}\,. \tag{5.1.49}$$

We hence observe that delta functions are smoothed out to exponential cusps of magnitude $\mathcal{O}(\sqrt{L})$. This effect can be seen in the left panel of fig. 4.6. The second feature is the exponential smoothing of step functions, as seen from the

following:

$$\int_0^1 \frac{\partial^2 \mathcal{G}(x,y)}{\partial y^2}\Theta(y-x_0)\,\mathrm{d}y = \frac{\xi}{4}\mathrm{e}^{-\sqrt{\frac{2L}{\xi}}(x_0-x)}\Theta(x_0-x) - \frac{\xi}{4}\mathrm{e}^{-\sqrt{\frac{2L}{\xi}}(x-x_0)}\Theta(x-x_0) + \frac{\xi}{2}\Theta(x-x_0) - \frac{\xi}{4}\mathrm{e}^{-\sqrt{\frac{2L}{\xi}}(1-x)} - \frac{\xi}{4}x\ ; \qquad (5.1.50)$$

$$\int_0^1 \frac{\partial^2 \mathcal{G}(x,y)}{\partial y^2}\Theta(x_0-y)\,\mathrm{d}y = \frac{\xi}{4}\mathrm{e}^{-\sqrt{\frac{2L}{\xi}}(x-x_0)}\Theta(x-x_0) - \frac{\xi}{4}\mathrm{e}^{-\sqrt{\frac{2L}{\xi}}(x_0-x)}\Theta(x_0-x) + \frac{\xi}{2}\Theta(x_0-x) - \frac{\xi}{4}\mathrm{e}^{-\sqrt{\frac{2L}{\xi}}x} - \frac{\xi}{4}(1-x)\ . \qquad (5.1.51)$$

We now turn to the second integral on the right-hand side of eq. (5.1.48), whose leading-order contribution is given by

$$\int_0^1 \frac{\partial^2 \mathcal{G}(x,y)}{\partial y^2}\bar{\rho}_+(y)\,\mathrm{d}y = \frac{\xi}{2}\bar{\rho}_+(x) + \text{complementary terms}\ . \qquad (5.1.52)$$

We need not consider the complementary terms (terms given in eq. (5.1.26) which solve eq. (5.1.25)) since they can later be absorbed into the complementary contribution to the general solution. We observe that the smooth contribution becomes 'imprinted' in the stationary distributions. The origin of this effect is straightforward to explain. The magnitude of a recoil event is sampled directly from the recoil distribution, and when a ++ configuration is entered following a recoil of magnitude $x$, a separation of magnitude $x$ persists for a time proportional to the persistence. The imprint arises as a result of many samplings of the recoil distribution during such events. We will discuss this effect (and others) in more detail once we have dealt with the +− quadrant.

For all contributions to $\psi(x)$ considered above, the resultant exponential smoothing becomes increasingly sharp for increasing $\sqrt{L}$. In the continuum limit $L \to \infty$, the smoothings become perfectly sharp (i.e. perfect steps and/or delta functions) such that all features of the recoil distribution – continuous or discontinuous – become imprinted exactly. We remark that this behaviour derives mathematically from the exponential terms in the Green's function, which themselves have their origins in the fourth-order term of eq. (5.1.22). We will elaborate on the physical origins of this later.

### Convolution approach

Alternatively, one can simply 'spot' that the solution of eq. (5.1.22) is the convolution

$$\left( \begin{array}{c} p(x) \\ q(x) \end{array} \right) = \sqrt{\frac{L}{2\xi}} \int_0^1 \left( \begin{array}{c} u_p(y) \\ u_q(y) \end{array} \right) \mathrm{e}^{-\sqrt{\frac{2L}{\xi}}|x-y|} \, \mathrm{d}y \ , \tag{5.1.53}$$

where $u_p(x)$ and $u_q(x)$ are solutions of the second-order equation

$$\frac{2}{\xi} \frac{\mathrm{d}^2}{\mathrm{d}x^2} \left( \begin{array}{c} u_p(x) \\ u_q(x) \end{array} \right) = \left( \begin{array}{c} s_p(x) \\ s_q(x) \end{array} \right) \ , \tag{5.1.54}$$

which is obtained when one drops the fourth-derivative term in eq. (5.1.22). To see that eq. (5.1.53) is indeed correct, it is noted that

$$\frac{\partial^2}{\partial x^2} \mathrm{e}^{-\sqrt{\frac{2L}{\xi}}|x-y|} = \sqrt{\frac{2L}{\xi}} \left\{ \begin{array}{ll} +\sqrt{\frac{2L}{\xi}} \mathrm{e}^{-\sqrt{\frac{2L}{\xi}}|x-y|} & x \neq y \\ -2\delta(x-y) & x = y \end{array} \right. \ . \tag{5.1.55}$$

Hence,

$$\begin{aligned} \frac{\mathrm{d}^2}{\mathrm{d}x^2} \left( \begin{array}{c} p(x) \\ q(x) \end{array} \right) &= \sqrt{\frac{L}{2\xi}} \int_0^1 \left( \begin{array}{c} u_p(y) \\ u_q(y) \end{array} \right) \frac{\partial^2}{\partial x^2} \mathrm{e}^{-\sqrt{\frac{2L}{\xi}}|x-y|} \, \mathrm{d}y \\ &= \sqrt{\frac{L}{2\xi}} \int_0^1 \left( \begin{array}{c} u_p(y) \\ u_q(y) \end{array} \right) \left[ \frac{2L}{\xi} \mathrm{e}^{-\sqrt{\frac{2L}{\xi}}|x-y|} - 2\sqrt{\frac{2L}{\xi}} \delta(x-y) \right] \mathrm{d}y \\ &= \frac{2L}{\xi} \left[ \left( \begin{array}{c} p(x) \\ q(x) \end{array} \right) - \left( \begin{array}{c} u_p(x) \\ u_q(x) \end{array} \right) \right] \ . \end{aligned} \tag{5.1.56}$$

It therefore follows that

$$\begin{aligned} &\left( \frac{2}{\xi} - \frac{1}{L} \frac{\mathrm{d}^2}{\mathrm{d}x^2} \right) \frac{\mathrm{d}^2}{\mathrm{d}x^2} \sqrt{\frac{L}{2\xi}} \int_0^1 \left( \begin{array}{c} u_p(y) \\ u_q(y) \end{array} \right) \mathrm{e}^{-\sqrt{\frac{2L}{\xi}}|x-y|} \, \mathrm{d}y \\ &\quad = \frac{2L}{\xi} \left[ \frac{2}{\xi} \left( \begin{array}{c} p(x) \\ q(x) \end{array} \right) - \frac{2}{\xi} \left( \begin{array}{c} u_p(x) \\ u_q(x) \end{array} \right) - \frac{2}{\xi} \left( \begin{array}{c} p(x) \\ q(x) \end{array} \right) + \frac{2}{\xi} \left( \begin{array}{c} u_p(x) \\ u_q(x) \end{array} \right) \right] \\ &\qquad + \frac{2L}{\xi} \frac{1}{L} \frac{\mathrm{d}^2}{\mathrm{d}x^2} \left( \begin{array}{c} u_p(x) \\ u_q(x) \end{array} \right) \\ &\quad = \left( \begin{array}{c} s_p(x) \\ s_q(x) \end{array} \right) \ , \end{aligned} \tag{5.1.57}$$

thus verifying eq. (5.1.53). Hence, eqs. (5.1.34) and (5.1.35) may be equivalently stated as

$$p(x) = A_p + B_p x + C_p \mathrm{e}^{-\sqrt{\frac{2L}{\xi}}x} + D_p \mathrm{e}^{-\sqrt{\frac{2L}{\xi}}(1-x)} + \sqrt{\frac{L}{2\xi}} \int_0^1 u_p(y) \mathrm{e}^{-\sqrt{\frac{2L}{\xi}}|x-y|} \, \mathrm{d}y \ , \tag{5.1.58}$$

and

$$q(x) = A_q + B_q x + C_q \mathrm{e}^{-\sqrt{\frac{2L}{\xi}}x} + D_q \mathrm{e}^{-\sqrt{\frac{2L}{\xi}}(1-x)} + \sqrt{\frac{L}{2\xi}} \int_0^1 u_q(y) \mathrm{e}^{-\sqrt{\frac{2L}{\xi}}|x-y|} \, \mathrm{d}y \, . \tag{5.1.59}$$

In this way, we see that the solution is a smearing of the solution to the second-order equation in eq. (5.1.54) over a region of size $\frac{1}{\sqrt{L}}$.[1] We will elaborate on this shortly.

With the Green's function[2]

$$\mathcal{H}(x,y) = -\frac{\xi}{2} \left[ (1-x) y \Theta(x-y) + x(1-y)\Theta(y-x) \right] , \tag{5.1.60}$$

it is straightforward to write down the explicit forms of $u_p(x)$ and $u_q(x)$. These are

$$\begin{aligned} u_p(x) = {} & \frac{r + (1-r)\kappa_L}{2} w \xi \rho_+(x) - \frac{r\kappa_L + (1-r)}{2} w \int_0^x \rho_-(y) \, \mathrm{d}y \\ & + \frac{1+\kappa_L}{2\xi} w \left[ (1-x) \int_0^x y \rho_+(y) \, \mathrm{d}y + x \int_x^1 (1-y) \rho_+(y) \, \mathrm{d}y \right] \end{aligned} \tag{5.1.61}$$

and

$$\begin{aligned} u_q(x) = {} & -\frac{r\kappa_L + (1-r)}{2} w \int_0^x \rho_-(y) \, \mathrm{d}y - \frac{1+\kappa_L}{2} w \int_0^x \rho_+(y) \, \mathrm{d}y \\ & + \frac{1+\kappa_L}{2\xi} w \left[ (1-x) \int_0^x y \rho_+(y) \, \mathrm{d}y + x \int_x^1 (1-y) \rho_+(y) \, \mathrm{d}y \right] . \end{aligned} \tag{5.1.62}$$

As was done in the previous section, symmetry arguments may be used to simplify $p(x)$. It is simple to verify that eq. (5.1.61) obeys the symmetry $u_p(x) = u_p(1-x)$,

[1] To demonstrate this, $\mathrm{e}^{-\sqrt{\frac{2L}{\xi}}x}\Big|_{x=\frac{a}{\sqrt{L}}} = \mathrm{e}^{-\sqrt{\frac{2}{\xi}}a} = \mathcal{O}(1)$, whilst $\mathrm{e}^{-\sqrt{\frac{2L}{\xi}}x}\Big|_{x=a} = \mathrm{e}^{-\sqrt{\frac{2L}{\xi}}a} \approx 0$.

[2] The appropriate boundary conditions on the particular integral can be set by complementary terms.

from which we deduce

$$\int_0^1 u_p(y)\mathrm{e}^{-\sqrt{\frac{2L}{\xi}}|(1-x)-y|}\,\mathrm{d}y = \int_1^0 u_p(1-y)\mathrm{e}^{-\sqrt{\frac{2L}{\xi}}|(1-x)-(1-y)|}\,\mathrm{d}(-y)$$
$$= \int_0^1 u_p(y)\mathrm{e}^{-\sqrt{\frac{2L}{\xi}}|x-y|}\,\mathrm{d}y\,. \tag{5.1.63}$$

It thus follows from $p(x) = p(1-x)$ that the complementary contributions to $p(x)$ as written in eq. (5.1.58) must also be symmetric under the mapping $x \mapsto 1-x$. Hence,

$$p(x) = A_p + C_p\left[\mathrm{e}^{-\sqrt{\frac{2L}{\xi}}x} + \mathrm{e}^{-\sqrt{\frac{2L}{\xi}}(1-x)}\right] + \sqrt{\frac{L}{2\xi}}\int_0^1 u_p(y)\mathrm{e}^{-\sqrt{\frac{2L}{\xi}}|x-y|}\,\mathrm{d}y\,. \tag{5.1.64}$$

We now return to the smearing effect alluded to above. For large $L$, where eq. (5.1.22) is valid, this will not be noticeable unless the second-order solutions feature discontinuities (in line with what was discussed regarding the Green's function solution). To see this, we consider $u_p(x) = u_0 + \Gamma\delta(x-x_0)$; one finds

$$p(x) = u_0 + \Gamma\sqrt{\frac{L}{2\xi}}\mathrm{e}^{-\sqrt{\frac{2L}{\xi}}|x-x_0|}\,. \tag{5.1.65}$$

We see that the delta function has become a cusp whose sharpness increases with $\sqrt{L}$ in accordance with what was found using the Green's function. To demonstrate that this behaviour is correct, we investigate the recoil distribution $\phi(x) = \delta\left(x - \frac{1}{4}\right)$ whose dominant contribution is such that

$$\bar{p}(x) := \frac{1}{\sqrt{L}}\ln\left[\sqrt{\frac{2\xi}{L}}p(x)\right] = -\sqrt{\frac{2}{\xi}}\left|x-\frac{1}{4}\right| + \mathcal{O}\left(\frac{1}{\sqrt{L}}\right). \tag{5.1.66}$$

We see in fig. 5.1 that we approach the dominant behaviour as $L$ becomes sufficiently large.

### 5.1.3 Particular integrals

With the general solutions now in place, it remains to find the particular integrals of the problem. This we do by deriving a set of boundary conditions from the discrete master equations, after which we may apply them to the general solutions in either of eqs. (5.1.43) and (5.1.44) or eqs. (5.1.58) and (5.1.59). Here, we choose

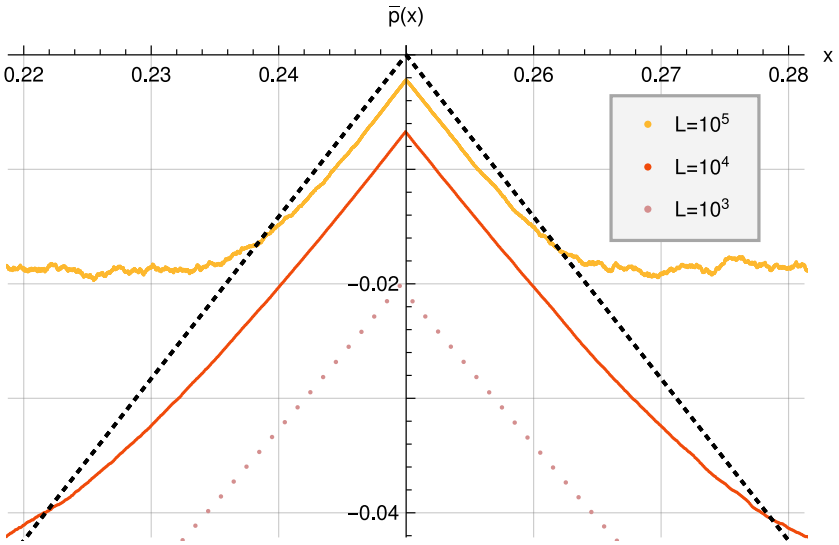


**Figure 5.1** *Limiting behaviour of $\bar{p}(x)$ for the recoil distribution $\phi(x) = \delta\left(x - \frac{1}{4}\right)$ and for system parameters $\xi = 1$ and $r = 1$. The black dotted line corresponds to the $L \to \infty$ limit of $\bar{p}(x)$. We see the simulation data (see section 2.3) approaching this limit as $L$ is increased.*

to work with eqs. (5.1.43) and (5.1.44).

### The ++ quadrant

Since there are two constants of integration to solve for in the ++ quadrant, $A_p$ and $C_p$, we choose to find expressions for $p(x)$ and its first derivative at the left boundary. We will make use of the stationary master equation in eq. (4.3.9), which may be equivalently expressed as

$$\begin{aligned} &P_{++}(n+1) - P_{++}(n) \\ &\quad = P_{++}(n) - P_{++}(n-1) - [rP_{+-}(1) + (1-r)P_{++}(1)](1-w)\delta_{n,1} + \mathcal{O}\left(\frac{1}{L}\right) \end{aligned} \tag{5.1.67}$$

for $n \ll L$. In particular, the base case of $n = 1$ can be shown to read

$$\frac{P_{++}(2)}{P_{+-}(1)} = \kappa_L + \frac{\chi_{r,w} + rw\xi\rho_+(0)}{r(1-w)+w}\frac{1}{\sqrt{2\xi L}} + \mathcal{O}\left(\frac{1}{L}\right), \tag{5.1.68}$$

where we have made use of the excluding boundary conditions stated in eq. (4.3.2), recalled the definition of $\kappa_L$, and defined

$$\chi_{r,w} = w - r(1-w) - [r(1-w) + w(1-r)](u-v). \tag{5.1.69}$$

The general case of $n > 1$ meanwhile reads

$$\frac{P_{++}(n+1)}{P_{+-}(1)} - \frac{P_{++}(n)}{P_{+-}(1)} = \frac{P_{++}(n)}{P_{+-}(1)} - \frac{P_{++}(n-1)}{P_{+-}(1)} + \mathcal{O}\left(\frac{1}{L}\right). \tag{5.1.70}$$

Iterating and making use of the base case $n = 1$, it follows that for $n \ll L$,

$$\frac{P_{++}(n)}{P_{+-}(1)} = \kappa_L + \frac{\chi_{r,w} + rw\xi\rho_+(0)}{r(1-w)+w}\frac{n-1}{\sqrt{2\xi L}} + \mathcal{O}\left(\frac{1}{L}\right). \tag{5.1.71}$$

This immediately implies

$$\begin{aligned}\left.\frac{\mathrm{d}p(x)}{\mathrm{d}x}\right|_{x\approx 0} &= \lim_{L\to\infty}\left[\frac{P_{++}(n+1) - P_{++}(n)}{L^{-1}P_{+-}(1)}\right] \\ &= \frac{\chi_{r,w} + rw\xi\rho_+(0)}{r(1-w)+w}\sqrt{\frac{L}{2\xi}}\end{aligned} \tag{5.1.72}$$

is the derivative near the left boundary of the domain. We note here that the boundary behaviours[3] depend only on the system parameters $\xi$, $r$, $u$ and $v$, as well as $\rho(0)$ and $\rho(1)$. Given that these parameters are fixed, the boundary behaviours are independent of the details of the recoil distribution in the bulk of the domain. This is demonstrated in the left panel of fig. 5.2.

The second boundary condition follows immediately from our expression for $\kappa_L$ – eq. (4.3.29). When $r > 0$ and/or $w > 0$, one finds

$$\begin{aligned}p\left(x = \frac{1}{L}\right) &= \lim_{L\to\infty}\kappa_L \\ &= \frac{r(1-w)}{r(1-w)+w} + \frac{\chi_{r,w} + rw\xi\rho_+(0)}{[r(1-w)+w]^2}\frac{1}{\sqrt{2\xi L}} + \mathcal{O}\left(\frac{1}{L}\right).\end{aligned} \tag{5.1.73}$$

It turns out the case $r = w = 0$ has to be treated specially when using the current approach. Since we have already presented the solution to this special case in chapter 4, we will not discuss it further.

With the boundary conditions (5.1.72) and (5.1.73) established, they may now be

[3]This applies at both boundaries due to symmetry; the only difference in the derivative is a necessary factor of $-1$.

applied to our general solution. We firstly recall that we can express eq. (5.1.43) as

$$p(x) = A_p + C_p\left[\mathrm{e}^{-\sqrt{\frac{2L}{\xi}}x} + \mathrm{e}^{-\sqrt{\frac{2L}{\xi}}(1-x)}\right] - \frac{1+\kappa_L}{\xi^2}w\int_0^1 \mathcal{G}(x,y)\rho_+(y)\,\mathrm{d}y$$
$$+ \frac{r\kappa_L + (1-r)}{\xi}w\int_0^1 \frac{\partial\mathcal{G}(x,y)}{\partial y}\rho_-(y)\,\mathrm{d}y$$
$$+ [r+(1-r)\kappa_L]w\left[\int_0^1 \frac{\partial^2\mathcal{G}(x,y)}{\partial y^2}\psi_+(y)\,\mathrm{d}y + \frac{\xi}{2}\bar{\rho}_+(x)\right]. \qquad (5.1.74)$$

This form is useful since the integral over $\psi_+(y)$ does not contribute to leading order in either application of the boundary conditions. Noting that[4]

$$\mathcal{G}(0,y) = \left.\frac{\partial\mathcal{G}(x,y)}{\partial y}\right|_{x=0} = \left.\frac{\partial^2\mathcal{G}(x,y)}{\partial y^2}\right|_{x=0} = 0, \qquad (5.1.75)$$

we deduce the relation

$$A_p + C_p + \frac{rw}{r(1-w)+w}\frac{\xi}{2}\rho_+(0) = \frac{r(1-w)}{r(1-w)+w} \qquad (5.1.76)$$

by working to leading order in $L$ (since $\bar{\rho}_+(0) = \rho_+(0)$ due to our restriction that $\psi(x)$ contain discontinuities in the bulk of the domain only).

Secondly, it may be shown from eq. (5.1.33) that[5]

$$\left.\frac{\partial\mathcal{G}(x,y)}{\partial x}\right|_{x=0} = \frac{\xi}{4}\mathrm{e}^{-\sqrt{\frac{2L}{\xi}}y} + \frac{\xi}{4}\sqrt{\frac{\xi}{2L}}\left[\mathrm{e}^{-\sqrt{\frac{2L}{\xi}}y} - \mathrm{e}^{-\sqrt{\frac{2L}{\xi}}(1-y)}\right] - \frac{\xi}{2}(1-y), \qquad (5.1.77)$$

and

$$\left.\frac{\partial^2\mathcal{G}(x,y)}{\partial x\partial y}\right|_{x=0} = -\frac{1}{2}\sqrt{\frac{\xi L}{2}}\mathrm{e}^{-\sqrt{\frac{2L}{\xi}}y} - \frac{\xi}{4}\left[\mathrm{e}^{-\sqrt{\frac{2L}{\xi}}y} + \mathrm{e}^{-\sqrt{\frac{2L}{\xi}}(1-y)}\right] + \frac{\xi}{2}. \qquad (5.1.78)$$

Working to leading order, we find that, for the first derivative at $x = 0$,

$$-\sqrt{\frac{2L}{\xi}}C_p = \frac{\chi_{r,w} + rw\xi\rho_+(0)}{r(1-w)+w}\sqrt{\frac{L}{2\xi}}\,. \qquad (5.1.79)$$

We remark here that the Green's function's third derivative would also contribute

[4]Strictly speaking the evaluations should be taken at $x = \frac{1}{L}$, but this yields subleading corrections only.

[5]Again, one need not worry about subleading corrections, thus making evaluation at $x = 0$ legitimate.

were it not for the fact that $\psi_+(x) = 0$ in the boundary regions. Had we not re-expressed $p(x)$ with the imprint term, extra care would have to be taken to ensure that all contributions are accounted for since, in general, $\bar{\rho}_+(0) \neq 0$.

Solving eqs. (5.1.76) and (5.1.79) for $A_p$ and $C_p$, one finds

$$A_p = \frac{1}{2}\frac{2r(1-w) + \chi_{r,w}}{r(1-w) + w} \tag{5.1.80}$$

$$\text{and} \quad C_p = -\frac{1}{2}\frac{\chi_{r,w} + rw\xi\rho_+(0)}{r(1-w) + w}, \tag{5.1.81}$$

which completes our solution of $p(x)$. We will now move on to derive and apply the boundary conditions in the $+-$ quadrant, after which we will give a joint interpretation of our results.

### The $+-$ quadrant

As was noted earlier, the $+-$ quadrant requires more thought than the $++$ quadrant since there are four constants of integration: $A_q$, $B_q$, $C_q$, and $D_q$. To this end, we will derive expressions for $q(x)$ and its derivatives at both domain boundaries. We start with the $+-$ stationary master equation, eq. (4.3.10); this may be equivalently expressed as

$$P_{+-}(n+1) = (1+\omega)P_{+-}(n) - \lambda(n) \tag{5.1.82}$$

where

$$\lambda(n) = \omega P_{++}(n) + [rP_{++}(1) + (1-r)P_{+-}(1)]\Phi(n). \tag{5.1.83}$$

Iterating in the same way as was done for eq. (5.1.71) and noting that the base case $n = 1$ is simply our choice of normalisation

$$\frac{P_{+-}(1)}{P_{+-}(1)} = 1, \tag{5.1.84}$$

one finds that for $n \ll L$,

$$\begin{aligned}\frac{P_{+-}(n)}{P_{+-}(1)} = 1 - u[r\kappa_L + (1-r)]\left(1 - \frac{1}{\xi L}\right) I_{n>1} \\ + (1 - \kappa_L - [r\kappa_L + (1-r)][u + w\xi\rho(0)])\,\frac{n-1}{\xi L} + \mathcal{O}\left(\frac{1}{L^{\frac{3}{2}}}\right),\end{aligned} \tag{5.1.85}$$

where $I_{n>1}$ is the indicator function introduced in section 4.3. We note the discontinuous step between $n = 1$ and $n = 2$ for $u > 0$ which we encountered an example of in section 4.4.2. The above relationship therefore implies that

$$\begin{aligned}\left.\frac{\mathrm{d}q(x)}{\mathrm{d}x}\right|_{x\approx 0} &= \lim_{L\to\infty}\left[\frac{P_{+-}(n+1)-P_{+-}(n)}{L^{-1}P_{+-}(1)}\right] \\ &= -2u[r\kappa_L+(1-r)]\left(L-\frac{1}{\xi}\right)\Theta\left(\frac{1}{L}-x\right) \\ &\quad +\frac{1}{\xi}\left\{1-\kappa_L-[r\kappa_L+(1-r)][u+w\xi\rho(0)]\right\}. \end{aligned} \tag{5.1.86}$$

The step function marks the discontinuity. We also see that

$$\begin{aligned} q(x\approx 0) &= \lim_{L\to\infty}\left[1-u[r\kappa_L+(1-r)]\left(1-\frac{1}{\xi L}\right)\right] \\ &= 1-u[r\kappa_L+(1-r)] \end{aligned} \tag{5.1.87}$$

when $x \neq \dfrac{1}{L}$.

It remains to find the corresponding boundary conditions near $x = 1$. Recalling eq. (4.3.5), a similar analysis to the above only iterated from $n = L - 1$ yields

$$\begin{aligned}\frac{P_{+-}(L-n)}{P_{+-}(1)} &= v[r\kappa_L+(1-r)]\left(1-\frac{1}{\xi L}\right) \\ &\quad +(\kappa_L-[r\kappa_L+(1-r)][v-w\xi\rho(1)])\,\frac{n-1}{\xi L}+\mathcal{O}\left(\frac{1}{L^{\frac{3}{2}}}\right)\end{aligned} \tag{5.1.88}$$

once more for $n \ll L$. From this, we deduce

$$\left.\frac{\mathrm{d}q(x)}{\mathrm{d}x}\right|_{x\approx 1} = \lim_{L\to\infty}\left[\frac{P_{+-}(L-n+1)-P_{+-}(L-n)}{L^{-1}P_{+-}(1)}\right] \tag{5.1.89}$$

$$= -\frac{\kappa_L-[r\kappa_L+(1-r)][v-w\xi\rho(1)]}{\xi} \tag{5.1.90}$$

and

$$q(x\approx 1) = \lim_{L\to\infty} v[r\kappa_L+(1-r)]\left(1-\frac{1}{\xi L}\right) \tag{5.1.91}$$

$$= v[r\kappa_L+(1-r)]. \tag{5.1.92}$$

As was the case in the ++ quadrant, we note that the boundary behaviours in the $+-$ and $-+$ quadrants are independent of the details of the recoil distribution

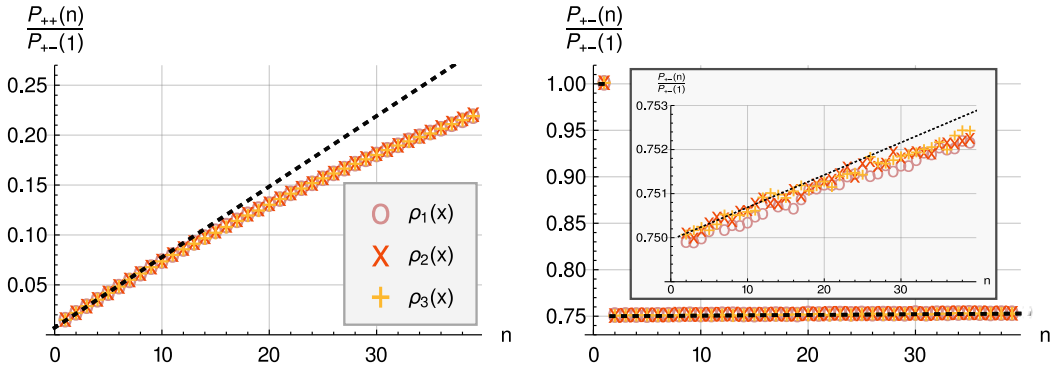


**Figure 5.2** *Common behaviours at the left boundaries in the ++ (left panel) and +− (right panel) quadrants for the distinct recoil distributions* $\rho_1(x) = 3x(1-x) + \frac{1}{4}\delta(x) + \frac{1}{4}\delta(1-x)$, $\rho_2(x) = \Pi(2x-1) + \frac{1}{4}\delta(x) + \frac{1}{4}\delta(1-x)$, *and* $\rho_3(x) = \frac{1}{2}\delta(\frac{1}{2}-x) + \frac{1}{4}\delta(x) + \frac{1}{4}\delta(1-x)$. *Here,* $\Pi(x)$ *is defined to be the top-hat function of unit width centred at the origin. The system parameters for which the simulations (see section 2.3) were run are* $L = 10^4$, $\xi = 1$ *and* $r = 0$. *The dotted black lines show the common boundary behaviours as predicted by eqs.* (5.1.71) *and* (5.1.85). *All simulated cases show good agreement with the predicted boundary behaviours. The small discrepancy between the pink circles and the predicted curve in the +− quadrant is attributed to the* $\mathcal{O}(L^{-3/2})$ *corrections in eq.* (5.1.85).

in the bulk of the domain; each of the boundary expressions above are therefore universal when $\xi$, $r$, $u$, $v$, $\rho(0)$ and $\rho(1)$ are fixed. For the +− quadrant, this behaviour is verified in the right panel of fig. 5.2.

The boundary conditions may now be applied to eq. (5.1.44). Accommodating for the step near $x = 0$, recalling eq. (5.1.75), and working to leading order in $L$ provides us with

$$A_q + C_q = 1 - u[r\kappa_L + (1-r)] \tag{5.1.93}$$

and

$$B_q - \sqrt{\frac{2L}{\xi}}C_q + \left(\frac{1}{2\xi} + 1\right)(1+\kappa_L)w - \frac{1+\kappa_L}{4}w\rho_+(0) - \frac{r\kappa_L + (1-r)}{4}w\rho_-(0) = \frac{1-\kappa_L - [r\kappa_L + (1-r)][u + w\xi\rho(0)]}{\xi}\,. \tag{5.1.94}$$

The latter was arrived at by considering the terms in eqs. (5.1.77) and (5.1.78) which yield $\mathcal{O}(1)$ contributions when integrated, these being

$$-\frac{\xi}{2}(1-y), \qquad -\frac{1}{2}\sqrt{\frac{\xi L}{2}}\mathrm{e}^{-\sqrt{\frac{2L}{\xi}}y} \qquad \text{and} \qquad \frac{\xi}{2}.$$

To leading order, we thus conclude that

$$C_q = \mathcal{O}\left(\frac{1}{\sqrt{L}}\right). \tag{5.1.95}$$

Using

$$\mathcal{G}(1,y) = \left.\frac{\partial \mathcal{G}(x,y)}{\partial y}\right|_{x=1} = 0, \tag{5.1.96}$$

as well as

$$\left.\frac{\partial \mathcal{G}(x,y)}{\partial x}\right|_{x=1} = -\frac{\xi}{4}\mathrm{e}^{-\sqrt{\frac{2L}{\xi}}(1-y)} + \frac{\xi}{4}\sqrt{\frac{\xi}{2L}}\left[\mathrm{e}^{-\sqrt{\frac{2L}{\xi}}y} - \mathrm{e}^{-\sqrt{\frac{2L}{\xi}}(1-y)}\right] + \frac{\xi}{2}y \tag{5.1.97}$$

$$\text{and} \quad \left.\frac{\partial^2 \mathcal{G}(x,y)}{\partial x \partial y}\right|_{x=1} = -\frac{1}{2}\sqrt{\frac{\xi L}{2}}\mathrm{e}^{-\sqrt{\frac{2L}{\xi}}(1-y)} - \frac{\xi}{4}\left[\mathrm{e}^{-\sqrt{\frac{2L}{\xi}}y} + \mathrm{e}^{-\sqrt{\frac{2L}{\xi}}(1-y)}\right] + \frac{\xi}{2}\,, \tag{5.1.98}$$

the equations to be satisfied near $x = 1$ may be shown to be

$$A_q + B_q + D_q = v[r\kappa_L + (1-r)] \tag{5.1.99}$$

and

$$B_q + \sqrt{\frac{2L}{\xi}}D_q + \left(-\frac{1}{2\xi} + 1\right)(1+\kappa_L)w - \frac{1+\kappa_L}{4}w\rho_+(0) - \frac{r\kappa_L + (1-r)}{4}w\rho_-(1)$$
$$= -\frac{\kappa_L - [r\kappa_L + (1-r)][v - w\xi\rho(1)]}{\xi}. \tag{5.1.100}$$

We hence conclude that

$$D_q = \mathcal{O}\left(\frac{1}{\sqrt{L}}\right). \tag{5.1.101}$$

Combining eqs. (5.1.93), (5.1.94), (5.1.99) and (5.1.100), it is simple to solve for $A_q$ and $B_q$. One finds

$$A_q = 1 - \frac{r(1-2w)+w}{r(1-w)+w}u \tag{5.1.102}$$

$$\text{and} \quad B_q = -1 + \frac{r(1-2w)+w}{r(1-w)+w}(1-w) \tag{5.1.103}$$

to leading order. We note that, in contrast to the ++ quadrant, the exponential complementary terms give only subleading contributions to the solution. The

interpretation of this is that the exponential terms in the ++ quadrant describe how the particles follow each other but with a separation that slowly diffuses due to the stochastic nature of particle hops. The probability of small separations, therefore, rapidly drops off, since such diffusion permits particle collisions that actuate recoils to greater separations. As the system size transitions from finite to infinite, the exponents diverge and the exponential terms tend towards perfectly sharp steps.

More rigorously, the reasons for the above are as follows. Suppose two particles follow each other for $\mathcal{O}(L)$ hops – the typical number of hops spent in the ++ quadrant before reorientation. Random-walk theory [139] tells us that the mean displacement from the particles' initial separation at the time of reorientation is therefore proportional to $\sqrt{L}$. As a fraction of the system size in the continuum limit, this is proportional to $\lim_{L\to\infty} \frac{\sqrt{L}}{L} = \lim_{L\to\infty} \frac{1}{\sqrt{L}} = 0$, meaning that only particles which are infinitesimally separated can collide and hence be displaced away from each other. For finite $L$, on the other hand, the effect is noticeable on the scale of the system size; taking $L = 100$ as an example, we see that $\frac{1}{\sqrt{L}} = \frac{1}{10}$. Hence, following particles that are separated by approximately $\sqrt{L} = 10$ sites exhibit a significant collision probability before a reorientation occurs, after which they recoil to a new separation. If recoils favour separations of size $\Delta n > \sqrt{L}$, the net effect is to deplete probability density in the boundary regions of size $\sqrt{L}$. Conversely, when recoil separations of size $\Delta n < \sqrt{L}$ are favoured, the opposite effect occurs in which probability accumulates in the boundary regions. We saw an example of the latter case in the previous chapter when $w = 0$ and $v = \mathcal{O}\left(\frac{1}{L}\right)$; see eq. (4.4.46). The model of [54] corresponding to $v = 0$, whose results were rederived in eq. (4.4.44), also exhibits this feature.

In the +− quadrant, particles approach each other with a diffusive drift around a ballistically shrinking separation; hence, the number of hops executed in the boundary region of size $\mathcal{O}(\sqrt{L})$ is $\mathcal{O}(\sqrt{L})$ – in contrast to $\mathcal{O}(L)$ for following particles. We ascribe the $\mathcal{O}(\sqrt{L})$ difference in exponential prefactors between the two quadrants to these facts.

We also remark that the exponential smearing of delta functions highlighted in eq. (5.1.49) and noted in the ++ discussion is never present in the +− quadrant, since the second derivative of the Green's function is absent in eq. (5.1.44). The highest-order contribution to $q(x)$ that arises from delta functions in the recoil distribution is therefore $\mathcal{O}(1)$: see eq. (5.1.47). The fact that this differs from the ++ quadrant by $\mathcal{O}(\sqrt{L})$ is exactly analogous to the situation at the boundaries.

Suppose the recoil distribution is $\phi(x) = \delta(x - x_0)$. When a recoil takes place into the ++ quadrant the particles follow each other, with their separation described by a random walk about the recoil distance, $x_0$. This has the said effect of smearing an 'imprint' of the delta function in $p(x)$. When a recoil takes place into the +− quadrant, however, the particles immediately begin to approach each other, thus meaning that probability in the +− quadrant does not accumulate at $x_0$, but rather in the region $0 \leq x \leq x_0$. In summary, a state of fixed separation up to an error of $\mathcal{O}(\sqrt{L})$ persists for $\mathcal{O}(L)$ hops, whilst a state of shrinking separation occupies a region of the same size over the course of $\mathcal{O}(\sqrt{L})$ hops, hence the $\mathcal{O}(\sqrt{L})$ difference between the contributions in eqs. (5.1.47) and (5.1.49). Furthermore, the asymmetry of the contribution in eq. (5.1.47) is a consequence of the fact that approaching particles can never recede from each other after a recoil event. Hence, we expect probability to accumulate in the region $0 < x \leq x_0$ and to rapidly drop off in the region $x_0 < x \leq 1$. This manifests as a discontinuity in eq. (5.1.47) proportional to the persistence: a high persistence allows for many consecutive recoils into the +− quadrant, and thus greater probability accumulation in the region $0 < x \leq x_0$.

### 5.1.4 Full solutions

We now collect together the results of this section in order to establish the limiting forms in eqs. (5.1.23) and (5.1.24). We established a differential equation, eq. (5.1.22), for the stationary distributions $p(x)$ and $q(x)$, whose source terms are stated in eqs. (5.1.18) and (5.1.20). In each case, the solution comprises two parts. The first part is a complementary piece composed of constant, linear, and exponential terms. As we have already stated, the exponential terms decay rapidly away from the boundaries as $\mathcal{O}(\sqrt{L})$, meaning that when we take $L \to \infty$, they form perfectly sharp steps. Hence, these terms vanish if the system is not of finite size, thus leaving only the constant and linear terms. In the case of $p(x)$, the symmetry of eq. (5.1.36) implies that the linear term has coefficient 0. The constant term was then determined to be that given in eq. (5.1.80). In the case of $q(x)$, symmetry considerations cannot be used to eliminate terms. The constant term and linear coefficient were found to be as stated in eqs. (5.1.102) and (5.1.103), respectively.

The second part of the solution is that which gives rise to the source terms when inserted into eq. (5.1.22). These manifest as the integral terms in eqs. (5.1.43)

and (5.1.44) with the limiting value of $\kappa_L$ – given by the $\mathcal{O}(1)$ term of eq. (5.1.73) – substituted appropriately into the prefactors. (We remind ourselves here that the limiting form of $\kappa_L$ for the case $r = w = 0$ depends on the order of limits, hence requiring a different treatment such as the one given in section 4.4.) We reiterate that no exponential smoothing of discontinuities occurs in the continuum limit: sharp features such as delta functions remain sharp. The decomposition of $\rho(x)$ into discontinuous terms, $\psi(x)$, and continuous terms, $\bar{\rho}(x)$, as in eq. (5.1.45) is thus no longer relevant; in particular, we emphasise that the imprint becomes exact for all contributions to the recoil distribution. Because of this, one needs only the results

$$\int_0^1 \mathcal{G}(x,y)\rho_+(y)\,\mathrm{d}y = -\frac{\xi}{2}(1-x)\int_0^x y\rho_+(y)\,\mathrm{d}y - \frac{\xi}{2}x\int_x^1 (1-y)\rho_+(y)\,\mathrm{d}y\,, \tag{5.1.104}$$

$$\int_0^1 \frac{\partial\mathcal{G}(x,y)}{\partial y}\rho_\pm(y)\,\mathrm{d}y = \frac{\xi}{2}(1\pm 1)x - \frac{\xi}{2}\int_0^x \rho_\pm(y)\,\mathrm{d}y\,, \tag{5.1.105}$$

and

$$\int_0^1 \frac{\partial^2\mathcal{G}(x,y)}{\partial y^2}\rho_+(y)\,\mathrm{d}y = \frac{\xi}{2}\rho_+(x) - \frac{\xi}{4}\rho_+(0) - \frac{\xi}{4}\rho_+(0)\mathrm{e}^{-\sqrt{\frac{2L}{\xi}}x} - \frac{\xi}{4}\rho_+(0)\mathrm{e}^{-\sqrt{\frac{2L}{\xi}}(1-x)}. \tag{5.1.106}$$

Substituting the above equations into eqs. (5.1.43) and (5.1.44) yields the non-constant terms of eqs. (5.1.23) and (5.1.24). The complementary terms are then added to provide the full solution. Note that in the case of $q(x)$ all linear terms cancel, thus leaving the constant term as the only complementary contribution.

## 5.2 Interpretation

Having established the continuum solutions, a physical interpretation will now be given. In this section, we restrict ourselves to the case $u = v = 0$, $w = 1$ (unless stated otherwise) for which no particle exchange ($v = 0$) and no jamming ($u = 0$) can occur. We shall not consider finite-size corrections in this section since they have already been discussed. For our choice of parameters, by eqs. (5.1.23)

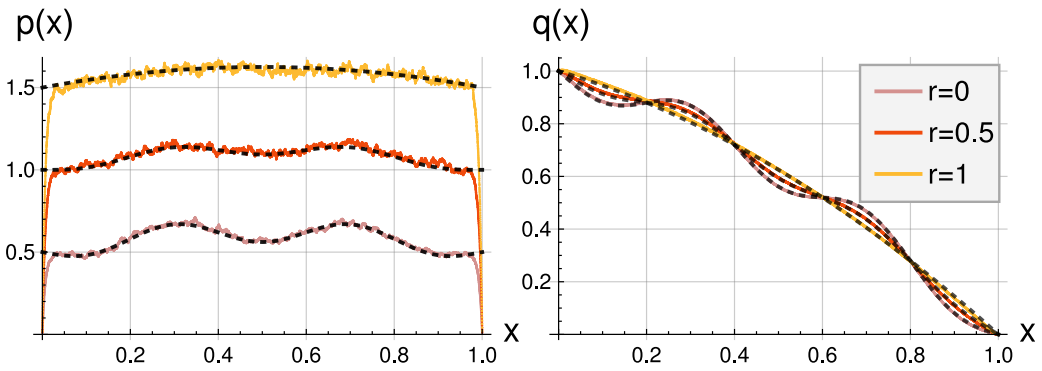


**Figure 5.3** *Comparison between the analytical predictions for the stationary distributions in eqs.* (5.2.1) *and* (5.2.2) *(dashed black lines) and simulation data (see section 2.3) for* $\rho(x) = \cos(5\pi x) + 1$, $\xi = 1$, $L = 10^4$ *and* $r = 0, 0.5, 1$. *Monte Carlo distributions were obtained by averaging over* $10^{10}$ *units of time. We note how the imprint becomes increasingly apparent for decreasing* $r$.

and (5.1.24) the stationary distributions are

$$p(x) = \frac{1}{2} + \frac{1}{2\xi}\left[(1-x)\int_0^x y\rho_+(y)\,\mathrm{d}y + x\int_x^1 (1-y)\rho_+(y)\,\mathrm{d}y\right] - \frac{1-r}{2}\int_0^x \rho_-(y)\,\mathrm{d}y + \frac{r\xi}{2}\rho_+(x) \tag{5.2.1}$$

and

$$q(x) = 1 + \frac{1}{2\xi}\left[(1-x)\int_0^x y\rho_+(y)\,\mathrm{d}y + x\int_x^1 (1-y)\rho_+(y)\,\mathrm{d}y\right] - \frac{1}{2}\int_0^x \rho_+(y)\,\mathrm{d}y - \frac{1-r}{2}\int_0^x \rho_-(y)\,\mathrm{d}y\,, \tag{5.2.2}$$

where we remind the reader that $\rho_+(x)$ and $\rho_-(x)$ are, respectively, the symmetrised and antisymmetrised recoil distributions as defined in eq. (5.1.19). Additionally, the stationary distribution of particle separations over all quadrants, which we denote by $Q(x)$, is given by

$$\begin{aligned} Q(x) &= p(x) + p(1-x) + q(x) + q(1-x) \\ &= 2p(x) + q(x) + q(1-x). \end{aligned} \tag{5.2.3}$$

We validate eqs. (5.2.1) and (5.2.2), and therefore eq. (5.2.3) by extension, in fig. 5.3.

### 5.2.1 Boundary behaviours

We begin by investigating the system's behaviours at the boundaries. The fact that sharp steps emerge in the ++ quadrant linking the constraint of vanishing probability at $x = 0$ to the bulk solution for $0 < x < 1$ leads to the counterintuitive result that $p(x)$ has discontinuous derivatives at its boundaries. What is less obvious is that the same is true in the +− quadrant. We see this by returning to the lattice formulation; in particular, we turn to eq. (5.1.86) which, for the parameter choices made in this section, can be shown to yield

$$q'(0) = \frac{1 - (1 - r)\xi\rho(0)}{\xi}. \tag{5.2.4}$$

This is the derivative in the boundary region, whose width as a fraction of the overall lattice size is $\frac{\sqrt{L}}{L} = \frac{1}{\sqrt{L}}$. If instead we choose to evaluate the derivative of the bulk solution at $x = 0$ via eq. (5.2.2), for which the boundary region of width $\frac{1}{\sqrt{L}}$ has been 'squeezed' to zero size after taking the continuum limit, one finds

$$q'(0) = \frac{1 - \xi\rho_+(0) - (1 - r)\xi\rho_-(0)}{2\xi}. \tag{5.2.5}$$

This is the bulk derivative and hence applies infinitesimally far from $x = 0$, whilst the previous derivative applies exactly at $x = 0$ once the continuum limit is taken (to reiterate, the boundary region is squeezed to size zero). These two expressions are distinct and we thus conclude that $q'(0)$ is discontinuous. An analogous result may be shown for $q'(1)$.

The discontinuous derivatives of $p(x)$ and $q(x)$ at the boundaries for the case $w = 1$ given in eqs. (5.2.1) and (5.2.2) are, in fact, a feature of the general case stated in eqs. (5.1.23) and (5.1.24), where the expressions for the lattice and bulk derivatives are correspondingly more complicated. An example of this nontrivial boundary behaviour in the general case is shown in fig. 5.4. Due to these facts, we must be wary of the naïve application of boundary conditions; only at the level of the lattice can the boundary behaviours be rigorously determined.

### 5.2.2 Regimes of persistence

We now turn our attention to the different physical regimes which arise as a result of the dynamics (keeping in mind that we are still working with $w = 1$).

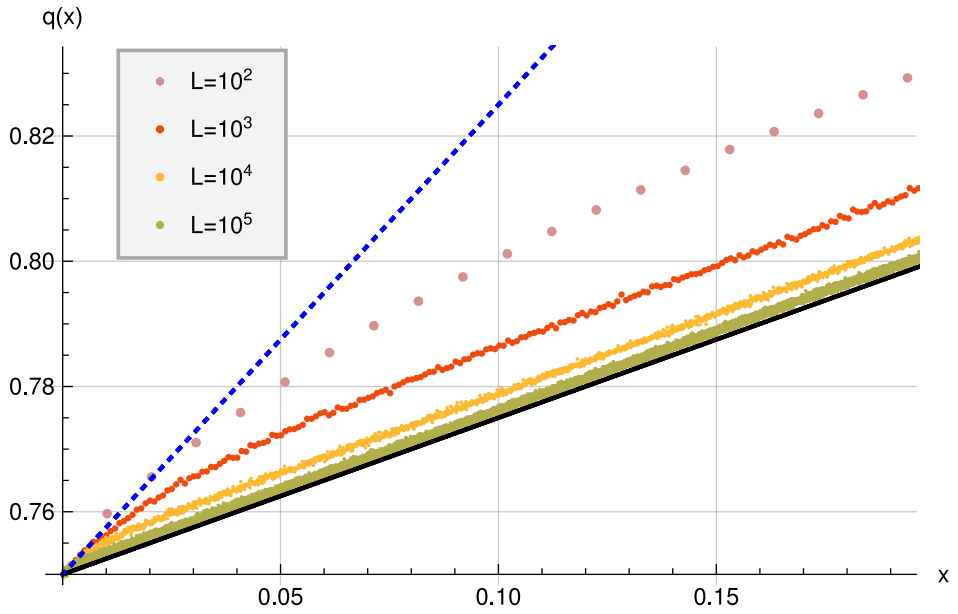


**Figure 5.4** *Behaviour near the left boundary in the +− quadrant. Simulation data (see section 2.3) were obtained for different $L$ with the recoil distribution $\phi(x) = \Pi(2x-1) + \frac{1}{4}\delta(x) + \frac{1}{4}\delta(1-x)$ and for system parameters $\xi = 1$ and $r = 0$. Here, $\Pi(x)$ is the top-hat function of unit width centred at the origin. As $L \to \infty$ for this example, the derivative of $q(x)$ should, at any fixed $x$ shown, approach that of the solid black line which is obtained from the bulk solution. At finite $L$, the derivative of $q(x)$ should approach that of the dashed blue line which derives instead from the lattice solution. Note that for $L = 100$ there are higher-order corrections in $L$ which obscure the latter limit.*

We see from the continuum stationary distributions – eqs. (5.2.1) and (5.2.2) – that there are contributions at three orders of persistence. In the regime of high persistence, $\xi \gg 1$, the imprint term in eq. (5.2.1) dominates when $r \neq 0$. The origin of this effect was discussed earlier, but we recapitulate it here. In the continuum limit, particle collisions, and therefore recoils, are only possible in the $+-$ quadrant, since separations in the $++$ quadrant remain fixed due to ballistic particle motion. Recoils into the $++$ quadrant are therefore possible only for nonzero values of $r$, and fix the separation of the particles (again, due to ballistic motion) for a time scale that is determined by the persistence: this is why both $r$ and $\xi$ appear as prefactors. The symmetrised recoil distribution features since a recoil- and reversal-induced separation $x$ in the $++$ quadrant can arise either from the $+-$ quadrant when $x = 0$ or from the $-+$ quadrant when $x = 1$. Mathematically, this symmetrisation is necessary to ensure symmetry constraints are met. We remark here that the imprint term can either be attractive (where probability is maximal around the midpoint of the domain) or repulsive (where probability is maximal near the boundaries) depending on the profile of $\rho(x)$, in contrast to passively-interacting particles of high persistence which most often behave attractively.

Conversely, in the regime of low persistence, $\xi \ll 1$, both particles behave diffusively: reorientations occur so rapidly relative to hops that the direction of motion at each hop is effectively random. The distinction between quadrants is lost as a result. This behaviour is confirmed by eqs. (5.2.1) and (5.2.2), in which both approach the same limiting forms under this regime. Naturally, these limiting forms stem from the diffusive contribution to the Green's function or, equivalently, solve the stationary diffusion equation $p''(x) = q''(x) = -\rho_+(x)$ with absorbing boundaries. Since $\rho_+(x) \geq 0$ everywhere, $p(x)$ and $q(x)$ have negative curvature everywhere. Furthermore, symmetry under $x \mapsto 1 - x$ implies that the respective profiles are peaked at $x = \frac{1}{2}$, meaning that all effective interactions in the regime of low persistence are repulsive. We therefore conclude that a transition from effective repulsion to effective attraction is possible for appropriate recoil distributions upon increasing the persistence length.

We finish by discussing the regime of intermediate persistence, $\xi = \mathcal{O}(1)$, in which all terms in the stationary distributions contribute. Besides constant terms, this comprises integrals over the (anti)symmetrised recoil distributions on the interval $0 < y \leq x$, which we ascribe to advection as a consequence of persistence. Of interest is that these terms are able to induce an effective attraction even when

both the imprint and diffusive contributions favour effective repulsion. We explore this idea below.

### 5.2.3 Reentrant states

As stated above, it is possible to find stationary distributions which are attractive at intermediate persistent lengths but are otherwise repulsive. This means that continuously varying the persistence length from high persistence to low persistence (or vice versa) sees the net distribution of separations, $Q(x)$ (see eq. (5.2.3)), transition from repulsive to attractive before transitioning back to repulsive. We term transitions of this type *reentrant*. In order to characterise reentrancy, we must investigate the curvature of $Q(x)$ at $x = \frac{1}{2}$, reminding ourselves that negative curvature implies repulsion whilst positive curvature implies attraction. From eqs. (5.2.1) to (5.2.3), it is possible to show that

$$Q''\left(\frac{1}{2}\right) = 2r\rho''\left(\frac{1}{2}\right)\xi - 4(1-r)\rho'\left(\frac{1}{2}\right) - 4\rho\left(\frac{1}{2}\right)\xi^{-1}. \tag{5.2.6}$$

The roots of the above quadratic are given by

$$\xi_{\pm} = \frac{(1-r)\rho'(\frac{1}{2}) \pm \sqrt{(1-r)^2\rho'(\frac{1}{2})^2 + 2r\rho(\frac{1}{2})\rho''(\frac{1}{2})}}{r\rho''(\frac{1}{2})}\,. \tag{5.2.7}$$

To ensure that these roots are real and distinct, we require that the discriminant be positive. This amounts to requiring

$$-\frac{(1-r)^2\rho'(\frac{1}{2})^2}{2r\rho(\frac{1}{2})} < \rho''\left(\frac{1}{2}\right). \tag{5.2.8}$$

Furthermore, in order for reentrancy to be possible, the imprint term must have negative curvature. In combination with the above inequality, this implies the stricter constraint

$$-\frac{(1-r)^2\rho'(\frac{1}{2})^2}{2r\rho(\frac{1}{2})} < \rho''\left(\frac{1}{2}\right) < 0. \tag{5.2.9}$$

Finally, we require that $\xi_{\pm}$ both be positive (negative values imply an unphysical reorientation rate). Since the denominator of eq. (5.2.7) is negative, we require that the numerator also be negative. We note that $\rho\left(\frac{1}{2}\right) \neq 0$ by virtue of the negative-curvature constraint $\rho''\left(\frac{1}{2}\right) < 0$; hence, the only possibility is $\rho\left(\frac{1}{2}\right) > 0$.

This implies

$$\sqrt{(1-r)^2\rho'\left(\frac{1}{2}\right)^2 + 2r\rho\left(\frac{1}{2}\right)\rho''\left(\frac{1}{2}\right)} < (1-r)\rho'\left(\frac{1}{2}\right). \tag{5.2.10}$$

For $\xi_\pm$ to both be positive, therefore, we must have that

$$\rho'\left(\frac{1}{2}\right) < 0. \tag{5.2.11}$$

This and 5.2.9 give the constraints that must be satisifed in order for reentrancy to be a feature of the system. If this is the case, attractive states occur when $\xi_+ < \xi < \xi_-$. Physically, we interpret attractive reentrant states as arising when particle separation is advected towards the boundaries from the central region, but not to such an extent that the imprint term dominates.

We now consider the example of $\rho(x) = \frac{3}{2}(1-x^2)$, for which $\rho_+(x)$ is peaked at $x = \frac{1}{2}$. Clearly, 5.2.11 is satisfied. Constraint 5.2.9, on the other hand, manifests as $-\frac{(1-r)^2}{r} < -3$. The only physical solutions to this are $r < \frac{5-\sqrt{21}}{2} \approx 0.209$. Thus, if we pick $r$ to satisfy this constraint, the system is reentrant. This is demonstrated in fig. 5.5 for $r = \frac{1}{20}$, for which we have $\xi_+ \approx 0.825$ and $\xi_- \approx 18.2$.

## 5.3 Concluding remarks and outlook

In this chapter, we extended the work of the previous chapter in which a one-dimensional system of recoiling persistent random walkers was investigated. In particular, we saw how the stationary state could be derived for recoil distributions which incorporate jamming, particle exchange, and bulk displacements. The derived stationary distributions are stated in eqs. (5.1.23) and (5.1.24).

Specifically, we set out to improve the interpretability of the discrete results obtained in chapter 4 so as to facilitate a better understanding of the physics. This was achieved in section 5.1 via a novel diagonalisation rooted in the kernel method, building upon ideas which were introduced in section 4.4. The regime $L \gg 1$ was considered for ease of calculation, and led to the governing fourth-order differential equation 5.1.22 for each quadrant in which the coefficient of the fourth-derivative term was $\mathcal{O}(L)$ lower than the remaining terms in the equation. This was found to have significant consequences at the domain boundaries,

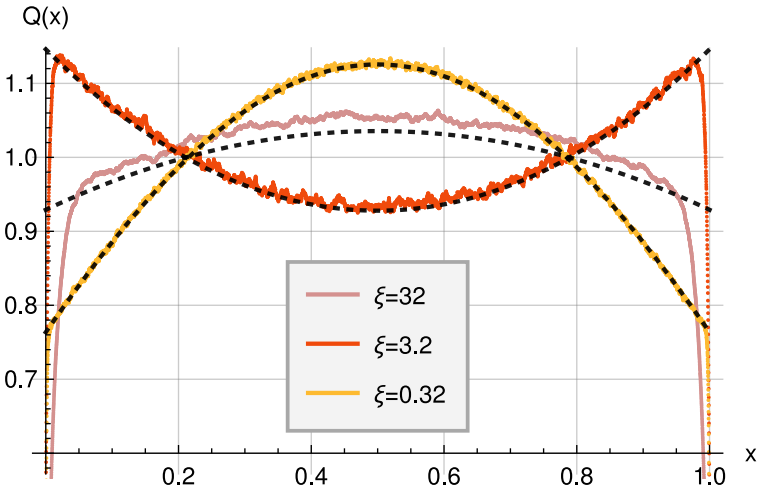


**Figure 5.5** *Distributions of particle separations at high, low, and intermediate persistent lengths for* $\rho(x) = \frac{3}{2}(1-x^2)$ *and* $r = \frac{1}{20}$. *Analytical predictions (black dashed lines) are compared with distributions obtained from Monte Carlo simulations (see section 2.3) on a lattice of* $L = 10^5$ *sites and averaged over up to* $10^{13}$ *units of time. These distributions are consistent with our prediction for attraction when* $0.825 < \xi < 18.2$ *and for repulsion otherwise. The discrepancy evident for* $\xi = 32$ *is due to finite-size corrections, where depleted probability in the boundary regions is compensated for by increased probability in the bulk.*

engendering, for example, discontinuities in both quadrants of the continuum limit $L \to \infty$. This was demonstrated in fig. 5.4. We conclude from this that a naïve application of the zero-flux condition, though it may seem intuitive in this problem given that both particles are foribidden from occupying the same site, and as is often assumed when solving other physical problems, leads to incorrect results. Furthermore, a rigorous treatment such as that presented here allows us to characterise finite-size corrections to features in the resultant stationary distributions, namely exponential smoothing of discontinuities as was demonstrated in fig. 5.1.

From the above, we take away that the importance of studying microscopic models cannot be understated. Here, we introduced a novel kind of interaction – that which is active, or driven by the constituents – and found that only a rigorous treatment at the microscopic level is capable of accurately capturing the subtle physical behaviours that emerge; jumping to a continuum description and using intuition as a guide is mathematically dangerous. On account of this, the methods developed here may be applicable in a wide variety of problems, and may serve as a means of rectifying incorrect results which derive from naïve physical assumptions.

We also showed how the model studied here has intriguing emergent behaviours. One such behaviour was that of reentrancy, in which the walkers are able to experience an effective attraction even when both the 'diffusive' and 'imprint' regimes are effectively repulsive. We derived the necessary conditions for this to occur for recoil distributions that feature bulk displacements only. Said conditions are given by eqs. (5.2.9) and (5.2.11), and were validated in fig. 5.5. We also noted how highly persistent particles can be attractive or repulsive depending on the details of the recoil distribution. This is courtesy of the imprint, which reproduces the symmetrised recoil distribution as a contribution to the stationary distribution in the ++ quadrant (see eq. (5.1.23)), and is in contrast to short-range excluding particles, which are generally attractive. These results imply that a tunable persistence length for an active particle could be exploited to engineer on demand an effective attraction to, or repulsion from, other objects to achieve some goal. At the more abstract level of the state space, we appreciate from reentrancy how tuning the parameter responsible for the rate at which different quadrants are accessed, $\omega$, is associated with contrasting emergent behaviours.

To build on the preliminary analysis of chapter 4 and the findings stated above, it would be interesting to conduct a many-body investigation to see how the details of the recoil distribution affect the onset of motility-induced phase separation. Given the level of complexity involved in the exact calculation for two particles presented here, this would likely have to be approached with computational or approximate analytical techniques – especially if we were to consider higher-dimensional domains (which are more likely to be of biological relevance). This consideration serves to highlight how readily complex behaviours are able to arise in active systems with few constituents and simple rules of interaction, which in itself puts the complexity of many-body active systems into perspective.

Although an exact many-body and/or higher-dimensional generalisation of this problem are out of reach with present analytical techniques, some extensions to this model may be made that admit exact solutions. On the question of the robustness of jamming discussed in the previous chapter and briefly above, as well as its consequences for motility-induced phase separation, one could look at contributions to the recoil distribution that scale neither as $\mathcal{O}(1)$ (jamming and exchange) nor as $\mathcal{O}(L)$ (bulk displacements). Perhaps the most pertinent example is that of $\mathcal{O}(\sqrt{L})$ scalings, which may serve to model short-range displacements, for example. Given that the boundary region is of size $\sqrt{L}$ sites, the implications of such an interaction may be significant, and could lead to further insights into

the nature of jamming at the microscopic level.

# Chapter 6

# A stochastic generalisation of a one-dimensional cellular automaton

In the previous three chapters, we have considered *interacting-particle systems* (IPS) [20]: systems of multiple particles which execute events in continuous time and which interact with each other. The study of IPS has been of major historical importance regarding investigation into nonequilibrium systems. This is because the rules of IPS are simple to state – thus making them straightforward to formulate mathematically and simulate on a computer – but are not so simple that they fail to capture complex emergent behaviours. For these reasons, seminal studies concerning IPS, such as those which provided exact solutions to the TASEP [25, 26], have proved physically insightful in addition to being fruitful regarding inspiration for further research [140–142].

An alternative model-based approach to investigating nonequilibrium systems is in the setting of cellular automata (CA), whose details we reviewed in the introduction. CA may be viewed as the discrete-time analogue to IPS; they therefore afford comparable ease of mathematical formulation to IPS and an even simpler implementation on a computer. Furthermore, as we saw for the game of life in section 1.4, CA are also capable of generating rich and complex emergent behaviours. That CA can be straightforwardly engineered to break detailed balance thus makes them a natural choice of model system through which we can probe fundamental nonequilibrium processes and the complexity that emerges therefrom.

In this chapter, we shall review a class of deterministic one-dimensional CA known

as *reversible cellular automata* (RCA) [143]. In particular, we shall review the nonequilibrium properties and stationary state of the *rule-150* RCA, which we use as the basis of a stochastic generalisation that retains some of the symmetries of the rule-150 RCA whilst allowing for greater mixing of configurations. It is the aim of this chapter to establish precisely how the structure of the state space changes as a consequence of this increased mixing.

We now summarise the content of this chapter. We introduce RCA and the specific example of the rule-150 RCA in section 6.1, whose nonequilibrium properties and stationary state we shall review. We will then introduce a stochastic generalisation of the rule-150 RCA in section 6.2 before investigating its state space in section 6.3, whose structure it is the aim of this chapter to ascertain; in particular, we will show that a lower bound on the number of subspaces given a system size of $L$ sites asymptotically grows as $\phi^{\frac{L}{4}}$, where $\phi$ is the golden ratio. We will thereafter give concluding remarks and discuss future directions in which this work could be taken in section 6.4.

## 6.1 Reversible cellular automata

We begin by reviewing the class of CA that inspired the work of this chapter, first introduced in [143]. This will serve to familiarise the reader with the mathematical formalism we will use throughout this chapter as well as to build intuition for the kinds of systems we will be investigating. We will then look at the specific example of the rule-150 RCA whose stationary state was solved for in [144], and for which a simple stochastic generalisation will be introduced in section 6.2.

### 6.1.1 Review of reversible cellular automata

The CA considered in [143] comprise one-dimensional lattices of length $L$ whose sites each have a binary variable associated with them. Whilst not stipulated in [143], we will take $L$ to be even and the lattice to be periodic. The binary variable at site $i$, where $i = 0, 1, 2, ..., L-1$, we refer to as the *occupation number* of site $i$; this we denote $n_i$, where $n_i = 0, 1$. If $n_i = 0$, site $i$ is said to be *empty*, and if $n_i = 1$, we say site $i$ is *occupied*. The dynamics is such that staggered updates occur in discrete time, $t$: on even time steps ($t = 2k,\ k \in \mathbb{N}_0$), sites of

even index ($i = 2j,\ j \in \{0, 1, ..., \frac{L}{2} - 1\}$) are updated, whilst on odd time steps ($t = 2k{+}1,\ k \in \mathbb{N}_0$), sites of odd index ($i = 2j{+}1,\ j \in \{0, 1, ..., \frac{L}{2} - 1\}$) are updated. The update of site $i$ is deterministic and depends entirely on its current occupation number, $n_i$, and on the occupation numbers of its nearest neighbours, $n_{i-1}$ and $n_{i+1}$. Specifically, updates for a particular model are encoded by a local three-site function

$$f_i = f(n_{i-1}, n_i, n_{i+1}), \tag{6.1.1}$$

where $f_i$ denotes the occupation of site $i$ after the update. We remark that the staggered dynamics makes the CA considered here different to those introduced by Wolfram [77] and reviewed in section 1.4, whose updates are fully parallel. A consequence of the staggered dynamics is that the order in which the sublattices are updated matters. We demonstrate how the ordering of sublattice updates affects the resultant trajectories with the simple example of a 4-site lattice whose update rule is such that the occupation of site $i$ changes if both of its neighbours have the same occupations. Starting from the configuration 0000 and recalling that the left-most site has index $i = 0$, updating even-indexed sites first yields the trajectory

$$0000 \xrightarrow{\text{e}} 1010 \xrightarrow{\text{o}} 1111 \xrightarrow{\text{e}} 0101 \xrightarrow{\text{o}} 0000 \tag{6.1.2}$$

after four updates. Meanwhile, updating odd-indexed sites first yields the different trajectory

$$0000 \xrightarrow{\text{o}} 0101 \xrightarrow{\text{e}} 1111 \xrightarrow{\text{o}} 1010 \xrightarrow{\text{e}} 0000\ . \tag{6.1.3}$$

Here, 'e' and 'o' denote updates on even and odd sites, respectively; we will continue to use this notation throughout this chapter except in situations where the parity of the site index is ambiguous. We note from this example the importance of sticking to the aforementioned update convention in which even-indexed sites are updated on even-parity time steps.

Since there are eight possible inputs to the local three-site function 6.1.1, there exist $2^8 = 256$ possible combinations of updates/outputs. We denote the three-site inputs as $c_j$, where $j = 0, ..., 7$ correspond to the decimal representations of the binary strings $(n_{i-1}, n_i, n_{i+1})$. This is summarised in fig. 6.1, where the decimal representation of a binary string is found by evaluating $\sum_{i=0}^{L-1} 2^i \delta_{n_i,1}$, that is, the significance of each digit decreases from right to left (as opposed to the usual convention in which significance decreases from left to right).

With this convention of labelling binary numbers, we can usefully label each of

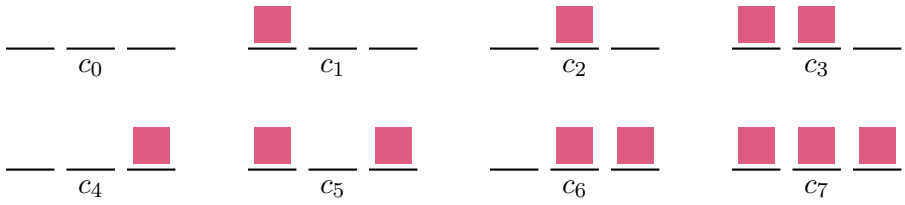


**Figure 6.1** *Showing all possible three-site inputs to the three-site update function 6.1.1, where the site indices increase from left to right. Filled squares correspond to occupied sites and empty sites are left blank. The decimal representation of each three-site binary string, to be read right-to-left, is shown below in each case. For example, the upper-right panel is represented by binary string* 110*, whose decimal representation is* 3 *when read from right to left (*011*).*

the 256 CA of the kind described in this section via a simple mapping. Each such CA has a unique set of outputs for each three-site configuration depicted in fig. 6.1. Listing the outputs $f(c_0), ..., f(c_7)$ in order yields a unique eight-digit binary string for every CA. Converting such a binary string into a decimal representation (remembering to read from right to left) yields a decimal number which can be used to label a particular CA. As an example, consider the CA whose binary representation is 01010101, that is to say, this CA's outputs are $f(c_{2m}) = 0$ and $f(c_{2m+1}) = 1$ for $m = 0, 1, 2, 3$. The decimal representation of this number is given by $2^7 + 2^5 + 2^3 + 2 = 170$, and as such this particular CA is known as the 'rule-170 cellular automaton',[1]

Now, if we focus solely on the CA of the kind we are considering that exhibit symmetry under both the parity transformation and time reversal, we are left with just eight of the possible 256 CA [143]. Explicitly, symmetry under the parity transformation implies that

$$f(n_{i-1}, n_i, n_{i+1}) = f(n_{i+1}, n_i, n_{i-1}) \ , \tag{6.1.4}$$

whilst symmetry under time reversal implies that

$$f(n_{i-1}, f(n_{i-1}, n_i, n_{i+1}), n_{i+1}) = n_i \ . \tag{6.1.5}$$

From fig. 6.1, symmetry under the parity transformation tells us that $c_1$ and $c_4$ are no longer independent. The same can be said for $c_3$ and $c_6$, meaning that eq. (6.1.4) implies a total of two constraints. Regarding time-reversal symmetry, we must have, for example, that $f(c_2) = 1 - f(c_0)$. We can understand this by

[1]Note that this naming convention is independent of the update scheme used.

considering all cases. If $f(c_0) = 0$ and $f(c_2) = 1$, then we have

$$000 \to 000 \qquad \text{and} \qquad 010 \to 010 \ . \tag{6.1.6}$$

If instead we have $f(c_0) = 1$ and $f(c_2) = 0$, then

$$000 \to 010 \qquad \text{and} \qquad 010 \to 000 \ . \tag{6.1.7}$$

Both of the above pairs of transitions obey time-reversal symmetry. Conversely, if $f(c_0) = 0$ and $f(c_2) = 0$, then we have

$$000 \to 000 \qquad \text{and} \qquad 010 \to 000 \ , \tag{6.1.8}$$

whilst for $f(c_0) = 1$ and $f(c_2) = 1$,

$$000 \to 010 \qquad \text{and} \qquad 010 \to 010 \ , \tag{6.1.9}$$

neither of which obey time-reversal symmetry. Thus, only two of the possible four combinations of updates are permissible. By similar reasoning, we must also have $f(c_3) = 1 - f(c_1)$ and $f(c_7) = 1 - f(c_5)$, meaning that eq. (6.1.5) implies a total of three constraints. For each constraint stated here, the number of possible update schemes halves; given that there are five constraints (two from eq. (6.1.4) and three from eq. (6.1.5)), we are thus left with $2^{8-5} = 2^3 = 8$ CA. This subset of CA are termed *reversible cellular automata* (RCA) due to the symmetries they exhibit.

The RCA described above have decimal representations 51, 54, 105, 108, 147, 150, 201 and 204. Rules 54, 150 and 201 have been the subject of much interest in physics circles; this is largely because exact stationary solutions have been found, allowing us to understand macroscopic properties from the underlying microscopic dynamics. For example, an exact stationary solution of the open-boundary rule-54 CA, which features interacting quasiparticles, was first solved in [145], and has since triggered a flurry of further research [146]: such works include boundary generalisations [147, 148], large-deviation statistics [149], and applications in quantum mechanics [150]. Exact stationary solutions of the interacting rule-201 CA [151] and noninteracting rule-150 CA [144] have also been found. We will discuss the latter in what follows, for we shall go on to consider one of its stochastic generalisations as the topic of this chapter.

### 6.1.2 Reversible cellular automaton 150

As stated, we will now look at the rule-150 RCA in more detail [144]. Not only will this serve to build our intuition for RCA, but it will also make for useful comparison when we introduce and work with its stochastic analogue from section 6.2 onwards.

We begin by stating the update rules. The rule-150 dynamics corresponds to the updates

$$f(c_0) = f(0,0,0) = 0 \tag{6.1.10}$$
$$f(c_1) = f(1,0,0) = 1 \tag{6.1.11}$$
$$f(c_2) = f(0,1,0) = 1 \tag{6.1.12}$$
$$f(c_3) = f(1,1,0) = 0 \tag{6.1.13}$$
$$f(c_4) = f(0,0,1) = 1 \tag{6.1.14}$$
$$f(c_5) = f(1,0,1) = 0 \tag{6.1.15}$$
$$f(c_6) = f(0,1,1) = 0 \tag{6.1.16}$$
$$\text{and} \qquad f(c_7) = f(1,1,1) = 1. \tag{6.1.17}$$

One can see that this has decimal representation 150, for the binary string 01101001 maps to $2^7 + 2^4 + 2^2 + 2 = 150$. In addition to the parity-inversion and time-reversal symmetries, it is noted that the above dynamics exhibits particle-hole (occupied-empty) symmetry: the set of update rules above is reproduced when each rule is restated as

$$f(1 - n_{i-1}, 1 - n_i, 1 - n_{i+1}) = 1 - f_i. \tag{6.1.18}$$

An alternative representation of the foregoing dynamics is

$$f_i = n_{i-1} + n_i + n_{i+1} \pmod 2 \ . \tag{6.1.19}$$

In summary, the occupation number of the central site switches value when its neighbouring sites' occupation numbers differ. This *kinetic constraint* is reminiscent of the continuous-time Fredrickson-Andersen Ising model [152] in which spins may flip only when at least one of its neighbouring spins is in an 'up' state. For the rule-150 RCA, precisely one 'spin' (site) must be in an 'up' (occupied) state, thus making it a discrete-time analogue of the 'exclusive one-

spin-facilitated' Fredrickson-Anderson model [153].

### Quasiparticles

We will now gain a feel for the emergent behaviours of the dynamics. For both clarity and brevity, we introduce a new notation $X_m$ to denote a domain of variable $X$ of length $m$ sites. As an example, in this shorthand notation the configuration 00000011011111 (in which we remind the reader that the left-most digit has index $i = 0$) is represented as $0_6 1_2 0_1 1_5$. If a domain straddles the periodic boundary, we denote it explicitly. The configuration 00011111110000 is represented as $0_3 1_7 0_4$, for example, notwithstanding that there exists only one domain of empty sites. From now on, we will use the term 'domain' to refer specifically to a domain of occupied sites.

In fig. 6.2 we see how two domains comprising an even number of sites separated by an even number of empty sites evolve through time. Specifically, we have the initial configuration $0_8 1_8 0_4 1_{12} 0_8$, where the first ($i = 8$; $i = 20$) and last ($i = 15$; $i = 31$) sites of the domains have even and odd parity, respectively. The effect of the dynamics is such that both domains move deterministically with velocity $+1$. Conversely, in fig. 6.3 we increase the gap size between the two domains by one site such that an odd number of sites now separates them, that is, we have the initial configuration $0_8 1_8 0_5 1_{12} 0_7$. The lower domain instead moves with velocity $-1$ such that both domains cross each other. We note that after the point of intersection, the trajectories of the domains remain as if no intersection took place at all; the domains are therefore *noninteracting*.

As stated, the domains described above comprise even numbers of sites. When the domain length is odd, the domain walls do not move in parallel and instead move with opposite velocities, as can be seen in figs. 6.4 and 6.5 for initial configurations $0_9 1_{21} 0_{10}$ and $0_{10} 1_{21} 0_9$, respectively. We observe sign flips in the velocities of the domain walls when the initial configuration is shifted by one site. Additionally, we observe time-reversal symmetry between the two evolutions in figs. 6.4 and 6.5.

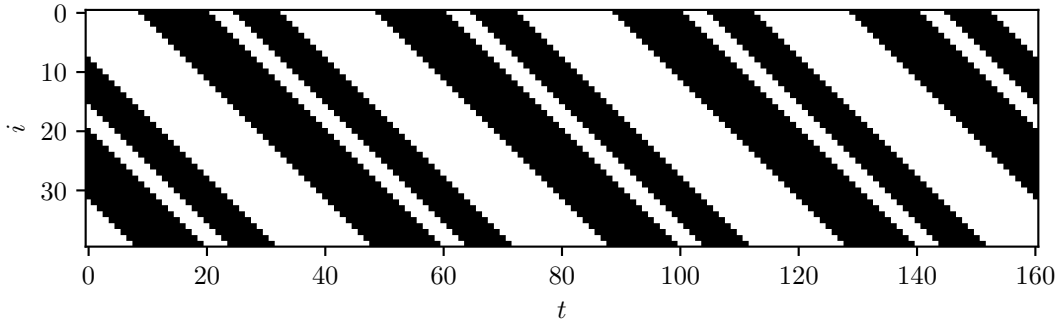


**Figure 6.2** *Evolution of the rule-150 RCA on a periodic lattice of $L$=40 sites over 160 time steps with initial configuration $0_8 1_8 0_4 1_{12} 0_8$. Black and white cells indicate occupied and unoccupied sites, respectively. The domains move deterministically with speed $+1$.*

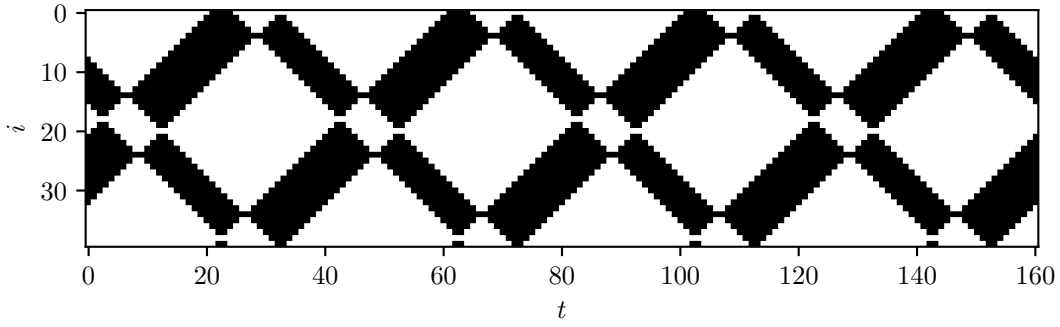


**Figure 6.3** *Evolution of the rule-150 RCA on a periodic lattice of $L$=40 sites over 160 time steps with initial configuration $0_8 1_8 0_5 1_{12} 0_7$. Black and white cells indicate occupied and unoccupied sites, respectively. The 8-site domain moves deterministically with speed $+1$ whilst the 12-site domain moves deterministically with speed $-1$. The domains pass through each other unaffected.*

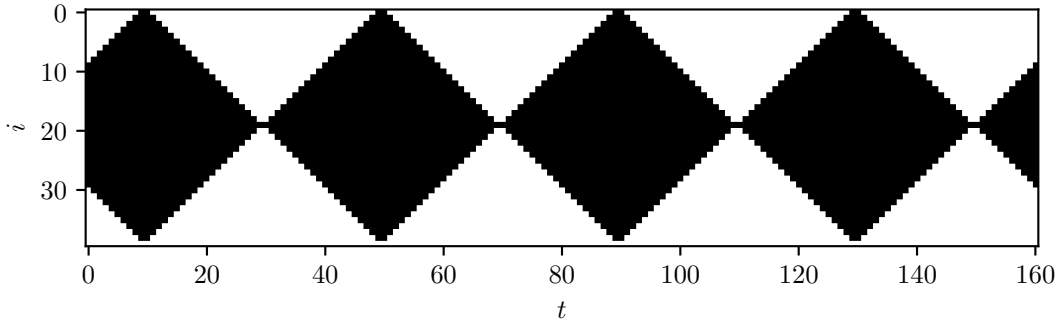


**Figure 6.4** *Evolution of the rule-150 RCA on a periodic lattice of $L$=40 sites over 160 time steps with initial configuration $0_9 1_{21} 0_{10}$. Black and white cells indicate occupied and unoccupied sites, respectively. The domain grows in size as its walls recede from each other, shrinking again after the walls meet and pass through each other.*

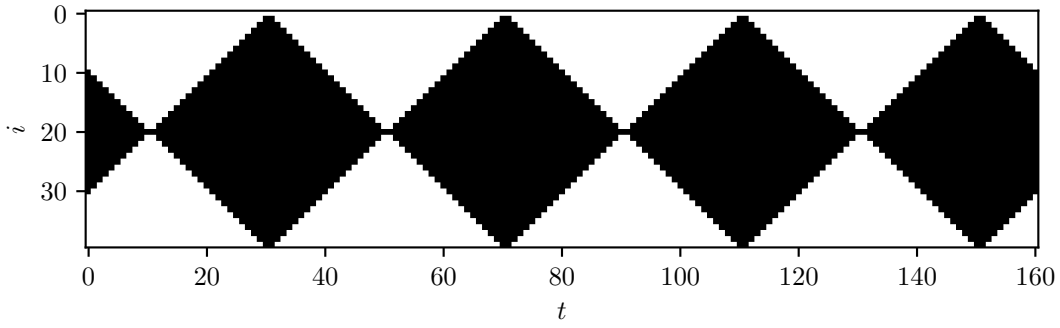


**Figure 6.5** *Evolution of the rule-150 RCA on a periodic lattice of L=40 sites over 160 time steps with initial configuration* $0_{10}1_{21}0_9$ *– a downward shift of the initial configuration in fig. 6.4 by one site. Black and white cells indicate occupied and unoccupied sites, respectively. The result of the shift is a sign flip in the domain-wall velocities, thus evolving identically to fig. 6.4 in reverse time.*

Considering the above observations, it is possible to characterise the dynamics in terms of domain walls (01 or 10 pairs), which we henceforth refer to as *quasiparticles* in line with [144].[2] We note both from the update rules and the above figures that quasiparticles always move ballistically. Furthermore, the velocity of a quasiparticle at time $t$, $v_t(n_i, 1-n_i)$, can be determined via

$$v_t(n_i, 1-n_i) = \begin{cases} -1, & \text{if } \; i+t=0 \pmod 2 \\ +1, & \text{if } \; i+t=1 \pmod 2 \end{cases} . \tag{6.1.20}$$

The configurations 010 and 101, each of which features one positive-moving quasiparticle and one negative-moving quasiparticle, correspond to points in space-time at which quasiparticles meet before passing through each other. Since quasiparticles are noninteracting, the numbers of positive- and negative-moving quasiparticles is fixed by the initial configuration. Finally, the numbers of quasiparticles in configuration $\mathcal{C}$ of the lattice are constrained by

$$N_{\mathcal{C}}^{+} - N_{\mathcal{C}}^{-} = 0 \pmod 2 , \tag{6.1.21}$$

where $N_{\mathcal{C}}^{+}$ and $N_{\mathcal{C}}^{-}$ denote the numbers of positive- and negative-moving quasiparticles, respectively. In words, the difference in the numbers of each type of quasiparticle is always even. To understand why this is so, we first understand that any configuration can be constructed from a lattice of empty sites simply

[2]These quasiparticles are sometimes referred to as *solitons* in the literature due to their localised forms and the property that they emerge unaffected after collisions with other such quasiparticles [154].

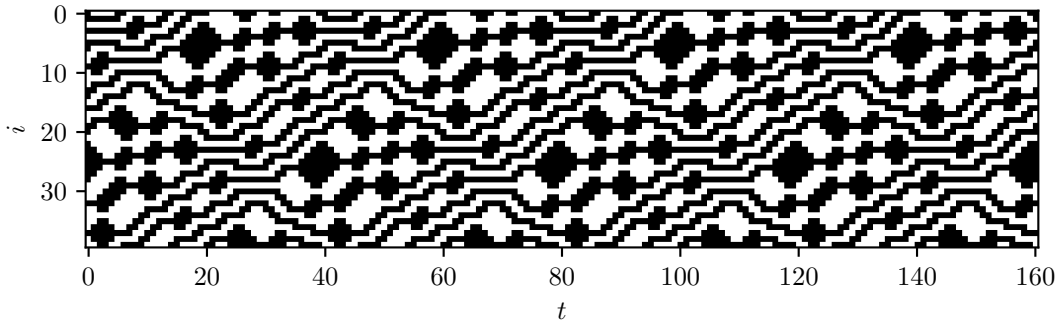


**Figure 6.6** *Evolution of the rule-150 RCA on a periodic lattice of $L$=40 sites over 160 time steps from a random initial configuration in which $N_{\mathcal{C}}^{+} = 8$ and $N_{\mathcal{C}}^{-} = 12$. Black and white cells indicate occupied and unoccupied sites, respectively. Quasiparticles occur when the occupation number changes from one site to the next, as characterised by eq.* (6.1.20)*. One observes a net current in the negative-i direction as a consequence of the mismatch in quasiparticle numbers.*

by adding domains of appropriate lengths. For example, in order to construct the configuration $0_2 1_4 0_3 1_3$, we first start with the configuration $0_{12}$ and add the 4- and 3-site domains in the appropriate places. Given that all configurations can be constructed in this way, the numbers of quasiparticles can be determined by considering how the insertion of each domain impacts the numbers $N_{\mathcal{C}}^{+}$ and $N_{\mathcal{C}}^{-}$. By eq. (6.1.20), inserting a domain of even length is guaranteed to add two quasiparticles of the same type, whilst inserting a domain of odd length adds one quasiparticle of each type. Given that the $0_L$ configuration is such that $N_{\mathcal{C}}^{+} = N_{\mathcal{C}}^{-} = 0$, these facts imply that the difference $N_{\mathcal{C}}^{+} - N_{\mathcal{C}}^{-}$ is always even. The only exceptions are when we add a single domain of length $L$ or add no domains at all, in which case $N_{\mathcal{C}}^{+} = N_{\mathcal{C}}^{-} = 0$ and eq. (6.1.21) still holds. By eq. (6.1.20), our example of $0_2 1_4 0_3 1_3$ obeys $N_{\mathcal{C}}^{+} - N_{\mathcal{C}}^{-} = \pm 2$, where the sign depends on the parity of the time step, and is therefore consistent with eq. (6.1.21).

In fig. 6.6 we plot the evolution of a system from a random initial condition in which we have $N_{\mathcal{C}}^{+} = 8$ and $N_{\mathcal{C}}^{-} = 12$. Since we have $N_{\mathcal{C}}^{+} - N_{\mathcal{C}}^{-} = -4$, a net current can be seen to move in the negative spatial direction.

### Nonequilibrium properties

Having characterised the rule-150 RCA in terms of quasiparticles, we are now able to discuss it in the context of detailed balance – or lack thereof. We remark

from the preceding discussion that distinct configurational sectors – subsets of the state space which do not communicate with each other – arise as a consequence of the dynamics. For example, the $0_L$ and $1_L$ states are fixed points of the system: if initialised in either of these configurations, all other configurations are inaccessible. Another example of a sector is the set of configurations in which a 2-site domain travels ballistically round the lattice. Whether these configurations are cycled through 'forwards' or 'backwards' depends on the parity of the time steps and site indices by eq. (6.1.20). If we suppose the lattice configuration is 011000 on an even time step, the trajectory

$$011000 \xrightarrow{\text{e}} 110000 \xrightarrow{\text{o}} 100001 \xrightarrow{\text{e}} 000011 \xrightarrow{\text{o}} 000110 \xrightarrow{\text{e}} 001100 \xrightarrow{\text{o}} 011000 \quad (6.1.22)$$

ensues: the quasiparticles move with negative velocity. Meanwhile, starting from an odd time step yields

$$011000 \xrightarrow{\text{e}} 001100 \xrightarrow{\text{o}} 000110 \xrightarrow{\text{e}} 000011 \xrightarrow{\text{o}} 100001 \xrightarrow{\text{e}} 110000 \xrightarrow{\text{o}} 011000, \quad (6.1.23)$$

in which the quasiparticles move with positive velocity. This demonstrates that the time period for each trajectory (the time taken to return to the automaton's initial configuration) is $L$. This is true in general since all quasiparticles are noninteracting and move with the speed $|\pm 1| = 1$; hence, after $L$ time steps all quasiparticles return to their initial positions to reproduce the configuration in which the system was initialised. Though all trajectories are periodic over $L$ time steps, this allows for some trajectories whose time periods are divisors of $L$ (for example, the 00110011 configuration has time period 4 and not 8).

At the level of sectors, detailed balance holds since there is no probability flux between them. The flux from one sector to another is therefore 'balanced' by the flux in the reverse direction in the sense that both are zero, meaning their difference is also zero. This holds pairwise for all sectors. For the system as a whole to exhibit detailed balance, detailed balance must also hold *within* each sector. We know this is not true in general, though, since we observe quasiparticle currents (as demonstrated in (6.1.22) and (6.1.23)), meaning that flux is directed in the state space. In the context considered here, we can only sensibly define transitions between states as being full lattice updates, that is, a transition is composed of two time steps. We therefore see that there is no direct reverse transition one could take to go back from the 100001 configuration in (6.1.22) to the 011000 configuration; one has to go through the 000110 configuration first.

There is therefore no pairwise flux balance between the two states, and detailed balance is broken. It suffices to find one sector for which detailed balance is broken in order for us to say that detailed balance is broken for the system as a whole, but we can go further by saying that all sectors bar $0_L$ and $1_L$ comprise combinations of deterministically moving quasiparticles, meaning broken detailed balance is generic to all sectors.

### Stationary state: patch-state ansatz

Having discussed its various physical features, we now present the stationary state of the rule-150 RCA before giving a derivation. The stationary weight of configuration $\mathcal{C}$ for the rule-150 RCA is given by [144]

$$P(\mathcal{C}) = \frac{1}{Z}\xi^{N_{\mathcal{C}}^{+}}\omega^{N_{\mathcal{C}}^{-}}, \tag{6.1.24}$$

where $\frac{1}{Z}$ is the normalisation and where $\xi$ and $\omega$ are parameters corresponding to the weights of each sector: since each sector constitutes a disjoint subset of state-space configurations, the stationary state will be determined by the sector weights in the initial ensemble. For example, $\xi = \omega = 1$ corresponds to sectors weighted such that all configurations are equiprobable, i.e. $p(\mathcal{C}) = Z^{-1}$ for all $\mathcal{C}$.

The weights in eq. (6.1.24) were calculated via a *patch-state ansatz* in [144]. For the model considered here, the patch-state ansatz takes the form

$$P(\mathcal{C}) \;\propto\; X_{n_1n_2}X'_{n_2n_3}X_{n_3n_4}\;...\;X'_{n_{N-2}n_{N-1}}X_{n_{N-1}n_N}X'_{n_Nn_1}, \tag{6.1.25}$$

where $X_{00}$, $X_{10}$, $X_{01}$, $X_{11}$, and their primed counterparts comprise eight scalars to be determined. To see how this can be used to derive eq. (6.1.24), we start with the description of the stationary state in terms of the state vector

$$\mathsf{p} = \sum_{\mathcal{C}} P(\mathcal{C})\hat{\mathsf{e}}_{\mathcal{C}}, \tag{6.1.26}$$

where $\hat{\mathsf{e}}_{\mathcal{C}}$ denotes the unit vector associated with configuration $\mathcal{C}$. We now consider the action of an operator $\mathcal{T}_i$ which effects the update rule (6.1.19) at site $i$. One full update consists of applying $\mathcal{T}_i$ for all even $i$ followed by applying $\mathcal{T}_i$ for all odd $i$. In order that $\mathsf{p}$ correctly describes the stationary state, we must recover $\mathsf{p}$

after one full update. Mathematically,

$$(\mathcal{T}_1 ... \mathcal{T}_{L-1})(\mathcal{T}_0 ... \mathcal{T}_{L-2})\mathsf{p} = \mathsf{p}, \tag{6.1.27}$$

where it is understood that all $\mathcal{T}_i$ for which $i$ has the same parity commute, since it does not matter in which order we update each sublattice as the result is always the same. Locally, the operator $\mathcal{T}_i =: \mathcal{T}$ for all $i$ is given by

$$\mathcal{T} = \begin{pmatrix} 1 & 0 & 0 & 0 & 0 & 0 & 0 & 0 \\ 0 & 0 & 0 & 1 & 0 & 0 & 0 & 0 \\ 0 & 0 & 1 & 0 & 0 & 0 & 0 & 0 \\ 0 & 1 & 0 & 0 & 0 & 0 & 0 & 0 \\ 0 & 0 & 0 & 0 & 0 & 0 & 1 & 0 \\ 0 & 0 & 0 & 0 & 0 & 1 & 0 & 0 \\ 0 & 0 & 0 & 0 & 1 & 0 & 0 & 0 \\ 0 & 0 & 0 & 0 & 0 & 0 & 0 & 1 \end{pmatrix} \tag{6.1.28}$$

in the basis where row/column $j$ is associated with configuration $j$ (zero-indexed) in the decimal representation of the three-site outputs $(n_{i-1}, n_i, n_{i+1})$. (The specific operator $\mathcal{T}_i$ is a $2^L$-by-$2^L$ matrix since it acts on $\mathsf{p}$.) The form of $\mathcal{T}$ becomes clear when we act it on the possible configurations of a three-site system:

$$\begin{pmatrix} 1 & 0 & 0 & 0 & 0 & 0 & 0 & 0 \\ 0 & 0 & 0 & 1 & 0 & 0 & 0 & 0 \\ 0 & 0 & 1 & 0 & 0 & 0 & 0 & 0 \\ 0 & 1 & 0 & 0 & 0 & 0 & 0 & 0 \\ 0 & 0 & 0 & 0 & 0 & 0 & 1 & 0 \\ 0 & 0 & 0 & 0 & 0 & 1 & 0 & 0 \\ 0 & 0 & 0 & 0 & 1 & 0 & 0 & 0 \\ 0 & 0 & 0 & 0 & 0 & 0 & 0 & 1 \end{pmatrix} \begin{pmatrix} \delta_{n_0,0}\ \delta_{n_1,0}\ \delta_{n_2,0} \\ \delta_{n_0,1}\ \delta_{n_1,0}\ \delta_{n_2,0} \\ \delta_{n_0,0}\ \delta_{n_1,1}\ \delta_{n_2,0} \\ \delta_{n_0,1}\ \delta_{n_1,1}\ \delta_{n_2,0} \\ \delta_{n_0,0}\ \delta_{n_1,0}\ \delta_{n_2,1} \\ \delta_{n_0,1}\ \delta_{n_1,0}\ \delta_{n_2,1} \\ \delta_{n_0,0}\ \delta_{n_1,1}\ \delta_{n_2,1} \\ \delta_{n_0,1}\ \delta_{n_1,1}\ \delta_{n_2,1} \end{pmatrix} = \begin{pmatrix} \delta_{n_0,0}\ \delta_{n_1,0}\ \delta_{n_2,0} \\ \delta_{n_0,1}\ \delta_{n_1,1}\ \delta_{n_2,0} \\ \delta_{n_0,0}\ \delta_{n_1,1}\ \delta_{n_2,0} \\ \delta_{n_0,1}\ \delta_{n_1,0}\ \delta_{n_2,0} \\ \delta_{n_0,0}\ \delta_{n_1,1}\ \delta_{n_2,1} \\ \delta_{n_0,1}\ \delta_{n_1,0}\ \delta_{n_2,1} \\ \delta_{n_0,0}\ \delta_{n_1,0}\ \delta_{n_2,1} \\ \delta_{n_0,1}\ \delta_{n_1,1}\ \delta_{n_2,1} \end{pmatrix}. \tag{6.1.29}$$

We see that the rows corresponding to $(1,0,0)$, $(1,1,0)$, $(0,0,1)$ and $(0,1,1)$ configurations are flipped by the action of $\mathcal{T}$ whilst the remaining configurations are left unaffected in accordance with the rules of the model.

An important feature of $\mathcal{T}$ that we see from eq. (6.1.28) is that it is self-inverse, this being a necessary consequence of time-reversal symmetry. Because of this,

we see that

$$(\mathcal{T}_1...\mathcal{T}_{L-1})(\mathcal{T}_1...\mathcal{T}_{L-1})(\mathcal{T}_0...\mathcal{T}_{L-2})\mathsf{p} = \mathbb{1}(\mathcal{T}_0...\mathcal{T}_{L-2})\mathsf{p} = (\mathcal{T}_0...\mathcal{T}_{L-2})\mathsf{p}, \tag{6.1.30}$$

and thus by eq. (6.1.27), at stationarity we have

$$(\mathcal{T}_0...\mathcal{T}_{L-2})\mathsf{p} = (\mathcal{T}_1...\mathcal{T}_{L-1})\mathsf{p}. \tag{6.1.31}$$

Substituting the patch-state ansatz (6.1.25) into eq. (6.1.31), one can find a solution by forcing each $\hat{\mathsf{e}}_{\mathcal{C}}$ component to be equal. Doing so yields

$$\begin{aligned} X_{f_0,n_1}X'_{n_1,f_2}X_{f_2,n_3}\ ...\ X'_{n_{N-3},f_{N-2}}X_{f_{N-2},n_{N-1}}X'_{n_{N-1},f_0} \\ = X_{n_0,f_1}X'_{f_1,n_2}X_{n_2,f_3}\ ...\ X'_{f_{N-3},n_{N-2}}X_{n_{N-2},f_{N-1}}X'_{f_{N-1},n_0}. \end{aligned} \tag{6.1.32}$$

This amounts to just two conditions:

$$X_{00}X'_{00} = X_{11}X'_{11} \qquad \text{and} \qquad X_{01}X'_{10} = X_{10}X'_{01}\ . \tag{6.1.33}$$

To see this, we may consider the example of a 4-site system. From each of the 16 possible starting configurations, two independent equations arise. Starting from the 1000 configuration, one arrives at the condition

$$X_{10}X'_{00}X_{00}X'_{01} = X_{11}X'_{10}X_{01}X'_{11}, \tag{6.1.34}$$

whilst starting from the 0100 configuration, one arrives at

$$X_{11}X'_{11}X_{10}X'_{01} = X_{01}X'_{10}X_{00}X'_{00}. \tag{6.1.35}$$

All other configurations either yield the same conditions (for example, the starting configuration 0010 yields eq. (6.1.34) due to cyclic symmetry of the patch-state ansatz) or yield equations that provide us with no information (such as the 0000 or 1111 configurations whose left- and right-hand sides are the same). Multiplying the left- and right-hand sides of eqs. (6.1.34) and (6.1.35) and subsequently equating them yields the second of eq. (6.1.33). Substituting this result into either of eq. (6.1.34) or eq. (6.1.35) then completes the derivation of eq. (6.1.33).

We are free to set the normalisation in any way we like. We may therefore choose

$$X_{00}X'_{00} = X_{11}X'_{11} = 1. \tag{6.1.36}$$

Moreover, since the patch-state ansatz is a product of scalars, it is determined only up to the gauge transformation

$$X_{n_i,n_{i+1}} \mapsto g_{n_i} X_{n_i,n_{i+1}} h^{-1}_{n_{i+1}} \qquad \text{and} \qquad X'_{n_i,n_{i+1}} \mapsto h_{n_i} X'_{n_i,n_{i+1}} g^{-1}_{n_{i+1}}, \tag{6.1.37}$$

where $g_0$, $g_1$, $h_0$ and $h_1$ are scalars. Since this change of gauge involves four new scalars, we are free to set four of our patch-state scalars in any way we like. In accordance with eq. (6.1.36), we may choose

$$X_{00} = X'_{00} = X_{01} = X'_{01} = 1. \tag{6.1.38}$$

Substituting these values into eq. (6.1.33), we arrive at the following solution:

$$X_{00} = X'_{00} = 1; \tag{6.1.39}$$

$$X_{10} = X'_{10} = \alpha; \tag{6.1.40}$$

$$X_{01} = X'_{01} = 1; \tag{6.1.41}$$

$$\text{and} \qquad X^{-1}_{11} = X'_{11} = \beta, \tag{6.1.42}$$

where $\alpha$ and $\beta$ are arbitrary (as was discussed after eq. (6.1.24), the stationary weights are parametrised since they depend on the details of the initial ensemble). In order to arrive at the form in eq. (6.1.24), we make one further gauge transformation. Recalling eq. (6.1.20), we note that, starting from an even time step (as is implied in this calculation by eq. (6.1.27)), the scalars $X_{10}$ and $X_{01}$ correspond to negative-velocity quasiparticles, whilst $X'_{10}$ and $X'_{01}$ correspond to quasiparticles with positive velocity. It is therefore natural to seek a change of gauge that sets $X_{10} = X_{01} = \omega$, $X'_{10} = X'_{01} = \xi$, and all other components to 1. In this way, the exponents of $\xi$ and $\omega$ in each weight count the numbers of each type of quasiparticle so as to take on the form of eq. (6.1.24). Setting $\alpha = \xi\omega$, $\beta = \frac{\omega}{\xi}$, $g_0 = h_0 = 1$, $g_1 = \frac{1}{\xi}$ and $h_1 = \frac{1}{\omega}$, one arrives at the gauge we seek:

$$X_{00} = X'_{00} = 1; \tag{6.1.43}$$

$$X_{10} = X_{01} = \omega; \tag{6.1.44}$$

$$X'_{10} = X'_{01} = \xi; \tag{6.1.45}$$

$$\text{and} \qquad X_{11} = X'_{11} = 1. \tag{6.1.46}$$

An equivalent matrix-product solution for the stationary state is detailed in appendix B.

## 6.2 The model

Having reviewed the properties and stationary solution of the deterministic rule-150 RCA, we now introduce a stochastic generalisation. In particular, we introduce stochastic update rules which preserve many features of the original system whilst allowing for the creation and annihilation of quasiparticle pairs. As we shall see, these alterations effect increased mixing of configurations; it will therefore be of interest to see how this mixing determines into which sectors the various configurations of the system fall.

The stochastic generalisation we consider here is as follows. We retain all rules (6.1.10) to (6.1.14) as well as rule (6.1.16), and make rules (6.1.15) and (6.1.17) stochastic according to

$$f(c_5) = f(1,0,1) = \begin{cases} 0 & \text{with probability } p \\ 1 & \text{with probability } q \end{cases} \tag{6.2.1}$$

$$\text{and} \quad f(c_7) = f(1,1,1) = \begin{cases} 1 & \text{with probability } p \\ 0 & \text{with probability } q \end{cases} , \tag{6.2.2}$$

where $p+q=1$. Previously, the occupation of a site changed value when exactly one of its nearest neighbours was occupied; now, the situation is the same only with the additional feature that the occupation can change with probability $q$ given that *both* neighbours are occupied.

Given that quasiparticles are domain walls, we see how the above rules are able to create and annihilate quasiparticle pairs, each pair here comprising exactly one positive-moving quasiparticle and one negative-moving quasiparticle. Thus, the nature of the new update rules means that the constraint described by eq. (6.1.21) – that the difference $N_{\mathcal{C}}^{+} - N_{\mathcal{C}}^{-}$ is even – still holds: by eq. (6.1.20), a quasiparticle pair is created by the transition $111 \to 101$ whilst a quasiparticle pair is annihilated by the transition $101 \to 111$, meaning the difference of constraint (6.1.21), $N_{\mathcal{C}}^{+} - N_{\mathcal{C}}^{-}$, stays fixed since $(N_{\mathcal{C}}^{+} \pm 1) - (N_{\mathcal{C}}^{-} \pm 1) = N_{\mathcal{C}}^{+} - N_{\mathcal{C}}^{-}$. We demonstrate quasiparticle creation and annihilation with examples in fig. 6.7. Furthermore, we note from fig. 6.7 that the system is no longer periodic in time as a consequence of the stochastic updates.

Regarding symmetries, we make the following deductions. Since the inputs $c_5$ and $c_7$ are spatially symmetric, we retain symmetry under parity inversion.

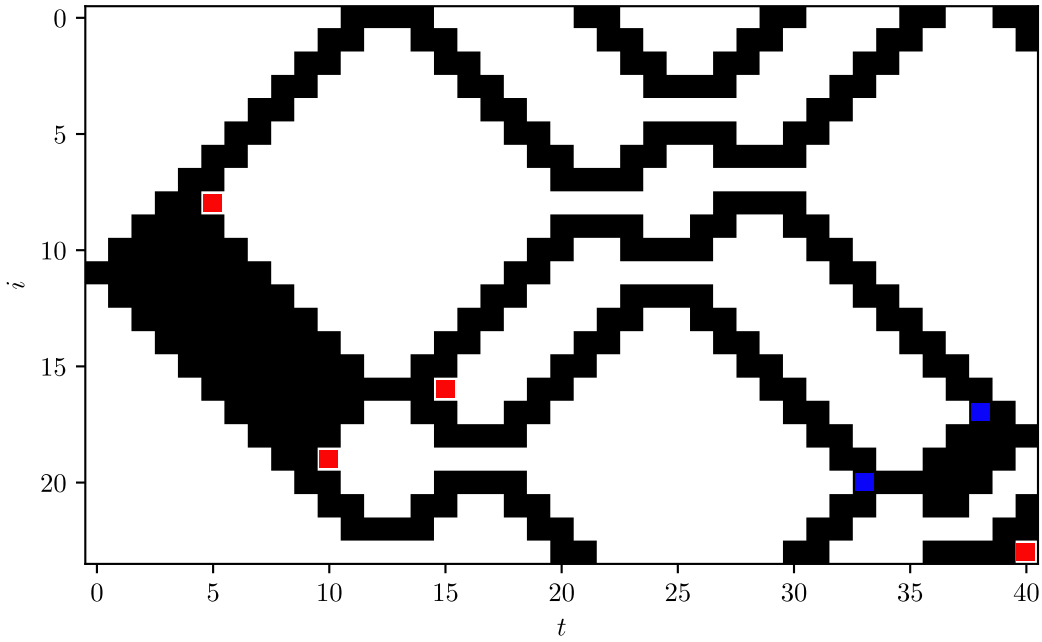


**Figure 6.7** *Evolution of the stochastic rule-150 CA on a periodic lattice of $L$=24 sites over 40 time steps with $q = \frac{1}{5}$ and initial configuration $0_{11}1_1 0_{12}$. Black and white cells indicate occupied and unoccupied sites, respectively. Quasiparticles occur when the occupation number changes from one site to the next, as characterised by eq.* (6.1.20)*. Points where quasiparticle pairs are created and annihilated are marked by red and blue squares, respectively. We note how the stochasticity has destroyed the periodicity of the trajectory: unlike the deterministic system, the stochastic system is not guaranteed to return to its initial state after $L$ time steps.*

Time-reversal symmetry is broken since the stochasticity implies that running time forward to some final configuration is not guaranteed to produce the same trajectory as that which is produced by starting from the final configuration and updating the system in reverse time. Taking 1111 to be the final configuration, the possible transitions

$$0101 \to 1111 \qquad \text{and} \qquad 1111 \to 1111 \tag{6.2.3}$$

exemplify this broken symmetry. Finally, we recognise also that particle-hole symmetry is broken. For example, particle-hole symmetry as applied to the deterministic transition

$$0000 \to 0000 \tag{6.2.4}$$

would imply that

$$1111 \to 1111, \tag{6.2.5}$$

which is inconsistent with the stochastic rule (6.2.2). To summarise, the introduction of the stochastic update rules (6.2.1) and (6.2.2) breaks two of the four symmetries of the deterministic system: time-reversal (eq. (6.1.5)) and particle-hole (eq. (6.1.18)) symmetry are broken whilst parity-inversion (eq. (6.1.4)) and the quasiparticle constraint (eq. (6.1.21)) still hold. Given the similarities between the deterministic and stochastic systems, it will be of interest to see how the broken symmetries effected by the stochasticity alter the emergent behaviours. For clarity in what follows, we hereafter refer to the stochastic system as the 'rule-150 stochastic cellular automaton (SCA)'.[3]

Like the rule-150 RCA, we once again see that detailed balance is broken. The evolution of the configuration 011000, for example, is unchanged after the inclusion of the stochastic update rules, and one once more sees the domain travel ballistically round the lattice. Trajectories involving stochastic updates are also able to break detailed balance. As may be seen from the trajectory

$$011011 \xrightarrow{\text{e}} 110001 \xrightarrow{\text{o}} 100000 \xrightarrow{\text{e}} 100000 \xrightarrow{\text{o}} 110001, \tag{6.2.6}$$

the rule-150 SCA is able to reach the configuration 100000 from 011011 in one full lattice update (two time steps) via rule (6.2.1), but the deterministic nature of the full lattice update that follows leaves no scope for returning to 011011 in as many steps. Thus, detailed balance does not hold.

[3]We keep in mind that other stochastic generalisations of the rule-150 RCA are possible. The term 'rule-150 SCA' is taken to mean that considered in this chapter only.

## 6.3 Characterising sectors

Having noted that quasiparticle creation and annihilation mixes configurations of the rule-150 RCA that do not communicate, it will be of interest to see to what extent this mixing occurs. In this section, we will investigate the details of this mixing and characterise the configurational sectors of the rule-150 SCA that emerge from its dynamics.

### 6.3.1 Distribution of configurations in each sector

We begin by establishing that the configurations of each sector are uniformly mixed. This we do by firstly showing that a uniform distribution of all configurations is stationary, from which uniform mixing within sectors is inferred.

We start by writing the probability of finding the system in configuration $\mathcal{C}'$ after a single sublattice update as

$$P(\mathcal{C}') = \sum_{\mathcal{C}} P(\mathcal{C}'|\mathcal{C})P(\mathcal{C}), \tag{6.3.1}$$

where $P(\mathcal{C}'|\mathcal{C})$ is the conditional probability that, given the system is in configuration $\mathcal{C}$, the system enters configuration $\mathcal{C}'$ after one sublattice update. Equation (6.3.1) expresses the fact that it is now possible for multiple configurations $\mathcal{C}$ to yield $\mathcal{C}'$ when updated, and hence that contributions from all such $\mathcal{C}$ need now be accounted for. If a uniform distribution over all configurations is a solution to the above equation at stationarity, it must be true that

$$\alpha = \sum_{\mathcal{C}} P(\mathcal{C}'|\mathcal{C})\alpha, \tag{6.3.2}$$

where $\alpha$ is a constant. Equivalently,

$$\sum_{\mathcal{C}} P(\mathcal{C}'|\mathcal{C}) = 1. \tag{6.3.3}$$

We therefore aim to prove eq. (6.3.3). The conditional probabilities may be expressed explicitly as

$$P(\mathcal{C}'|\mathcal{C}) = \prod_i P(n'_i|n_{i-1}, n_i, n_{i+1}) \prod_j \delta(n'_j, n_j), \tag{6.3.4}$$

where $\delta(a,b)$ denotes the Kronecker delta and where it is understood that $i$ and $j$ have different parities (for this proof, the choice is arbitrary). Here, the product over $i$ describes a sublattice update, and the product over $j$ expresses the fact that the second sublattice must remain unchanged (due to the staggered dynamics). In order to evaluate the sum on the left-hand side of eq. (6.3.3), an expression for $P(n_i'|n_{i-1},n_i,n_{i+1})$ is required. We may write

$$P(n_i'|n_{i-1},n_i,n_{i+1}) = \frac{1}{2}[1 - 2qn_{i-1}n_{i+1}(2n_i-1)(2n_i'-1) + (2n_{i-1}-1)(2n_i-1)(2n_{i+1}-1)(2n_i'-1)], \quad (6.3.5)$$

which one can verify reproduces the outputs of rules (6.1.10) to (6.1.14), (6.1.16), (6.2.1) and (6.2.2). Briefly, the first and third terms in the square brackets together reproduce the deterministic update rules (6.1.10) to (6.1.17), whilst the second term is only nonzero when both of site $i$'s nearest neighbours are occupied – as applies to the stochastic update rules (6.2.1) and (6.2.2). The construction of the second term is such that, in combination with the first and third terms, the output is $q$ if $n_i \neq n_i'$ and is $1-q$ otherwise.

We now return to the left-hand side of eq. (6.3.3). Summing over all configurations $\mathcal{C}$ amounts to summing over all possible values of $n_i$ and $n_j$. From eq. (6.3.4), we therefore have

$$\sum_{\mathcal{C}} P(\mathcal{C}'|\mathcal{C}) = \prod_i \sum_{n_i} P(n_i'|n_{i-1},n_i,n_{i+1}) \prod_j \sum_{n_j} \delta(n_j',n_j). \quad (6.3.6)$$

The first of the sums on the right-hand side of eq. (6.3.6) can be expanded via eq. (6.3.5) as

$$\sum_{n_i=0}^{1} P(n_i'|n_{i-1},n_i,n_{i+1}) = \frac{1}{2}\sum_{n_i=0}^{1}(1) - qn_{i-1}n_{i+1}(2n_i'-1)\sum_{n_i=0}^{1}(2n_i-1) + \frac{1}{2}(2n_{i-1}-1)(2n_{i+1}-1)(2n_i'-1)\sum_{n_i=0}^{1}(2n_i-1)\ . \quad (6.3.7)$$

The second and third terms above evaluate to 0; we therefore see that

$$\sum_{n_i=0}^{1} P(n_i'|n_{i-1},n_i,n_{i+1}) = 1. \quad (6.3.8)$$

The remaining sum of eq. (6.3.6) is simple to evaluate. Since we have $n_j = n'_j$ for all $j$ (as this sublattice is not being updated), then

$$\sum_{n_j=0}^{1} \delta(n'_j, n_j) = 1 \tag{6.3.9}$$

as only one of $n_j = 0$ or $n_j = 1$ will be equal to $n'_j$. Thus, by eq. (6.3.6),

$$\sum_{\mathcal{C}} P(\mathcal{C}'|\mathcal{C}) = \prod_i 1 \prod_j 1 = 1. \tag{6.3.10}$$

The condition of eq. (6.3.3) therefore holds for the rule-150 SCA dynamics. That a uniform distribution is a stationary solution of the dynamics implies that all configurations within a particular sector are uniformly distributed (it would not otherwise be possible to find a specific weighting of sectors that renders all configurations equiprobable). We therefore recognise that establishing the configurational structure of the rule-150 SCA's state space boils down to establishing how the state space is divided into sectors. In what follows, we will use simulation data to characterise these sectors, thus giving us a more complete view of the rule-150 SCA's state space and how it contrasts with that of the rule-150 RCA.

### 6.3.2 Counting sectors

As motivated above, we now wish to characterise the rule-150 SCA's configurational sectors. Using a simple Monte Carlo algorithm to simulate the dynamics (as described in section 2.3), it is possible to count the number of sectors for a given system size $L$. To do this, one starts with the $0_L$ configuration and evolves the system forward in time for a sufficiently large number of time steps, recording every configuration that has been accessed. One then looks at the next configuration (in numerical order, remembering that digits are read from right to left) that has yet to be accessed, and uses that as an initial condition (this is the $1_1 0_{L-1}$ configuration for both CA considered in this chapter since only the $0_L$ configuration is accessed from the $0_L$ initial condition). One then records the accessed configurations from this new initial condition and so on until all configurations have been accessed. Simulations in each sector were run for $T \gg 2^L$ time steps in the case of the rule-150 SCA and for $T = L$ time steps in the case of the rule-150 RCA to ensure all configurations of each sector were

| L | RCA | SCA |
|---|---|---|
| 4 | 9 | 3 |
| 6 | 20 | 4 |
| 8 | 51 | 5 |
| 10 | 136 | 6 |
| 12 | 414 | 8 |
| 14 | 1300 | 9 |
| 16 | 4371 | 12 |
| 18 | 15084 | 15 |
| 20 | 53508 | 20 |
| 22 | 192700 | 25 |
| 24 | 703346 | 37 |

**Table 6.1** *Sector counts for each CA. In the middle column, we tabulate the number of sectors of the rule-150 RCA for each value of L shown in the left column. We likewise do the same for the rule-150 SCA in the right column (we set $q = \frac{1}{2}$ when running simulations to ensure a high rate of mixing). We observe that the SCA exhibits a strong degree of mixing relative to the RCA.*

accessed. In table 6.1, we tabulate the number of sectors for increasing values of $L$ for both the rule-150 RCA and SCA. We observe significantly more mixing in the state space of the SCA, with $\mathcal{O}(10^3)$ more sectors in the state space of the RCA for the cases $L = 18$ and $L = 20$.

### RCA sectors

We will now spend some time understanding the sector counts from table 6.1. To begin, we can understand the RCA sector counts using a simple argument. As discussed previously, it is generally true that the trajectories of the rule-150 RCA are periodic over $L$ time steps. The number of sectors may thus be estimated by $\frac{2^L}{L}$ : the total number of configurations divided by the approximate number of configurations in each sector. Since this function is not restricted to integer outputs, we define the estimator function to be

$$S_R(L) := \left\lfloor \frac{2^L}{L} \right\rceil, \tag{6.3.11}$$

where the notation $\lfloor x \rceil$ denotes the nearest integer $x$ rounds to. The function $S_R(L)$ will, of course, underestimate the number of sectors since, as was alluded to earlier, not all sectors are periodic over $L$ time steps; some trajectories are

| L | $S_R(L)$ | True | Relative error |
|---|---|---|---|
| 4 | 4 | 9 | 55.6% |
| 6 | 11 | 20 | 45.0% |
| 8 | 32 | 51 | 37.3% |
| 10 | 102 | 136 | 25.0% |
| 12 | 341 | 414 | 17.6% |
| 14 | 1170 | 1300 | 10.0% |
| 16 | 4096 | 4371 | 6.3% |
| 18 | 14564 | 15084 | 3.4% |
| 20 | 52429 | 53508 | 2.0% |
| 22 | 190650 | 192700 | 1.1% |
| 24 | 699051 | 703346 | 0.6% |

**Table 6.2** *Comparing the estimated and true sector counts of the rule-150 RCA. The relative errors on $S_R(L)$ decrease as $L$ becomes larger.*

instead periodic over divisors of $L$. We therefore recognise $S_R(L)$ as a lower bound on the true sector count. We compare $S_R(L)$ with the true sector counts in table 6.2, where we observe increasingly good agreement for increasingly large values of $L$.

### SCA sectors

We now turn our attention to the SCA sector counts. Since the stochastic update rules forbid periodic trajectories in general, the argument used above regarding the RCA no longer holds. Instead, we shall use simulation results to guide us.

As was described at the start of this section, sectors are counted by initialising the automaton in the configuration whose associated numerical value is the smallest of the configurations that have yet to be accessed. Each sector may therefore be assigned an identifying binary string corresponding to said numerical value. In table 6.3, we tabulate the first 40 binary strings that label sectors of the $L$=32 SCA. We see that, with the exception of sector 2, all strings are composed of consecutive 00, 01 and 11 pairs. As can be shown from simulations, the first four binary sector identifiers (0000..., 1000..., 1100... and 1101...) are common to all systems for which $L \geq 6$. Thereafter, a pattern can be identified; we describe this pattern in what follows.

We can generate binary identifiers for sectors 5 onwards by carrying out the following steps:

| Sector index | Binary identifier of sector |
|---|---|
| 1 | 00 00 00 00 00 00 00 00 00 00 00 00 00 00 00 00 |
| 2 | 10 00 00 00 00 00 00 00 00 00 00 00 00 00 00 00 |
| 3 | 11 00 00 00 00 00 00 00 00 00 00 00 00 00 00 00 |
| 4 | 11 01 00 00 00 00 00 00 00 00 00 00 00 00 00 00 |
| 5 | 11 00 11 00 00 00 00 00 00 00 00 00 00 00 00 00 |
| 6 | 11 00 11 01 00 00 00 00 00 00 00 00 00 00 00 00 |
| 7 | 11 00 00 11 00 00 00 00 00 00 00 00 00 00 00 00 |
| 8 | 11 00 00 00 11 00 00 00 00 00 00 00 00 00 00 00 |
| 9 | 11 00 11 00 11 00 00 00 00 00 00 00 00 00 00 00 |
| 10 | 11 00 11 00 11 01 00 00 00 00 00 00 00 00 00 00 |
| 11 | 11 00 00 00 00 11 00 00 00 00 00 00 00 00 00 00 |
| 12 | 11 00 11 00 00 11 00 00 00 00 00 00 00 00 00 00 |
| 13 | 11 00 00 11 00 11 00 00 00 00 00 00 00 00 00 00 |
| 14 | 11 00 00 00 00 00 11 00 00 00 00 00 00 00 00 00 |
| 15 | 11 00 11 00 00 00 11 00 00 00 00 00 00 00 00 00 |
| 16 | 11 00 00 11 00 00 11 00 00 00 00 00 00 00 00 00 |
| 17 | 11 00 00 00 11 00 11 00 00 00 00 00 00 00 00 00 |
| 18 | 11 00 11 00 11 00 11 00 00 00 00 00 00 00 00 00 |
| 19 | 11 00 11 00 11 00 11 01 00 00 00 00 00 00 00 00 |
| 20 | 11 00 00 00 00 00 00 11 00 00 00 00 00 00 00 00 |
| 21 | 11 00 11 00 00 00 00 11 00 00 00 00 00 00 00 00 |
| 22 | 11 00 00 11 00 00 00 11 00 00 00 00 00 00 00 00 |
| 23 | 11 00 00 00 11 00 00 11 00 00 00 00 00 00 00 00 |
| 24 | 11 00 11 00 11 00 00 11 00 00 00 00 00 00 00 00 |
| 25 | 11 00 00 00 00 11 00 11 00 00 00 00 00 00 00 00 |
| 26 | 11 00 11 00 00 11 00 11 00 00 00 00 00 00 00 00 |
| 27 | 11 00 00 11 00 11 00 11 00 00 00 00 00 00 00 00 |
| 28 | 11 00 00 00 00 00 00 00 11 00 00 00 00 00 00 00 |
| 29 | 11 00 11 00 00 00 00 00 11 00 00 00 00 00 00 00 |
| 30 | 11 00 00 11 00 00 00 00 11 00 00 00 00 00 00 00 |
| 31 | 11 00 00 00 11 00 00 00 11 00 00 00 00 00 00 00 |
| 32 | 11 00 11 00 11 00 00 00 11 00 00 00 00 00 00 00 |
| 33 | 11 00 00 00 00 11 00 00 11 00 00 00 00 00 00 00 |
| 34 | 11 00 11 00 00 11 00 00 11 00 00 00 00 00 00 00 |
| 35 | 11 00 00 11 00 11 00 00 11 00 00 00 00 00 00 00 |
| 36 | 11 00 00 00 00 00 11 00 11 00 00 00 00 00 00 00 |
| 37 | 11 00 11 00 00 00 11 00 11 00 00 00 00 00 00 00 |
| 38 | 11 00 00 11 00 00 11 00 11 00 00 00 00 00 00 00 |
| 39 | 11 00 00 00 11 00 11 00 11 00 00 00 00 00 00 00 |
| 40 | 11 00 11 00 11 00 11 00 11 00 00 00 00 00 00 00 |

**Table 6.3** *The first 40 binary identifiers of sectors of the rule-150 SCA for* $L = 32$. *Binary identifiers represent the configurations of sectors whose associated numerical values are the smallest of any configuration in the sector.*

1. Firstly, one writes down strings of the form $1_2 0_{2m} 1_2 0_{L-2m-4}$, where $m = 1, \ ... \ , \ \lfloor \frac{L}{4} \rfloor - 1$ .

2. Secondly, one replaces the $0_{2m}$ substrings for each $m$ with all substrings of the form $0_{2k_1} 1_2 0_{2k_2} 1_2 ... 1_2 0_{2k_\alpha}$, where all $k_i$ are positive integers such that for each $m$ we have $m = \sum_i k_i + \alpha - 1$. All resulting strings – including the starting string – are sector identifiers.

3. Thirdly, if one is able to generate a string of the form $1_2 0_2 1_2 0_2 ... 1_2 0_2 1_2 0_{L-2m-4}$ in step 2, that is, if $m$ is odd such that $k_1 = ... = k_\alpha = 1$ is possible, an additional binary identifier of the form $1_2 0_2 1_2 0_2 ... 1_2 0_2 1_2 0_1 1_1 0_{L-2m-6}$ is generated.

We will demonstrate the above algorithm for finding sector identifiers using the example of $L = 32$ in table 6.3. (Though $L = 32$ is a specific example, the algorithm described above works for all $L$.) Carrying out the above steps yields the following:

1. We will focus on one string only in this example. Let us consider the string $1_2 0_{10} 1_2 0_{18}$ ($m = 5 < \lfloor \frac{L}{4} \rfloor = 8$).

2. We now generate all combinations of strings as described in step 2 above. From the $0_{10}$ substring, we generate $0_2 1_2 0_6$, $0_4 1_2 0_4$, $0_6 1_2 0_2$, and $0_2 1_2 0_2 1_2 0_2$. Explicitly, we have the following sector identifiers:

$$
\begin{aligned}
&11\ 00\ 00\ 00\ 00\ 00\ 11\ 00\ 00\ 00\ 00\ 00\ 00\ 00\ 00\ 00\ ; \\
&11\ 00\ 11\ 00\ 00\ 00\ 11\ 00\ 00\ 00\ 00\ 00\ 00\ 00\ 00\ 00\ ; \\
&11\ 00\ 00\ 11\ 00\ 00\ 11\ 00\ 00\ 00\ 00\ 00\ 00\ 00\ 00\ 00\ ; \\
&11\ 00\ 00\ 00\ 11\ 00\ 11\ 00\ 00\ 00\ 00\ 00\ 00\ 00\ 00\ 00\ ; \\
&11\ 00\ 11\ 00\ 11\ 00\ 11\ 00\ 00\ 00\ 00\ 00\ 00\ 00\ 00\ 00\ .
\end{aligned}
$$

3. Finally, since the final string above is of the form required in step 3, we also generate the string

$$11\ 00\ 11\ 00\ 11\ 00\ 11\ 01\ 00\ 00\ 00\ 00\ 00\ 00\ 00\ 00\ . \tag{6.3.12}$$

Let us now compare the generated strings with table 6.3. Our chosen starting string was the binary identifier of sector 14. The strings generated in step 2

| Sector index | Binary identifier of sector |
|---|---|
| 1 | 00 00 00 00 00 00 00 00 |
| 2 | 10 00 00 00 00 00 00 00 |
| 3 | 11 00 00 00 00 00 00 00 |
| 4 | 11 01 00 00 00 00 00 00 |
| 5 | 11 00 11 00 00 00 00 00 |
| 6 | 11 00 11 01 00 00 00 00 |
| 7 | 11 00 00 11 00 00 00 00 |
| 8 | 11 00 00 00 11 00 00 00 |
| 9 | 11 00 11 00 11 00 00 00 |
| 10 | 11 00 11 00 11 01 00 00 |
| 11 | 11 00 11 00 00 11 00 00 |
| 12 | 11 00 11 00 11 00 11 00 |

**Table 6.4** *All binary identifiers of sectors for $L = 16$. We see that $1_20_61_20_6$ is a valid identifier corresponding to $m = 3$, but that incrementing $m$ by 1 yields $1_20_81_20_4$. This is not a valid identifier since it is translationally symmetric to $1_20_41_20_8$ (the identifier corresponding to $m = 2$).*

correctly correspond to the identifiers of sectors 15, 16, 17 and 18, respectively. Sector 19's identifier is correctly generated in step 3.

At this point, we make some remarks. Firstly, it is important that $m$ be less than $\lfloor \frac{L}{4} \rfloor$, for if we relax this requirement we are able to generate binary strings which are not sector identifiers. As an example, we consider the case in which $L$ is a multiple of 4 such that $\lfloor \frac{L}{4} \rfloor = \frac{L}{4}$. Then, the maximum value of $m$ generates the binary string $1_20_{L/2-2}1_20_{L/2-2}$, which is a valid identifier. Incrementing $m$ beyond its maximum value, however, yields the string $1_20_{L/2}1_20_{L/2-4}$. This string is not a valid identifier since its associated sector has identifier $1_20_{L/2-4}1_20_{L/2}$ ($m = \frac{L}{4}-2$): the $1_20_{L/2}1_20_{L/2-4}$ configuration is reached from the $1_20_{L/2-4}1_20_{L/2}$ configuration – whose decimal representation is smaller – after $\frac{L}{2}+2$ time steps. An example of this is shown in table 6.4 for $L = 16$. Some valid strings can indeed be generated using higher values of $m$, but one has to be wary of what is and what is not a valid identifier. For a system of infinite size, the algorithm for generating identifiers is valid for all values of $m$ and hence none of the foregoing caveats apply.

Secondly, the fact that we mostly generate identifiers comprising isolated 11 domains is a consequence of the fact that, like the RCA, such domains travel ballistically in the SCA; the form of all such configurations is therefore preserved in their respective sectors up to translations. Since such sectors contain $L$ configurations at most, we conclude that, when $L$ is sufficiently large, sectors

| Binary identifier | $L = 12$ | $L = 16$ | $L = 20$ |
|---|---|---|---|
| 00 00 00 00 00 00 00 00 00 00 | 1 | 1 | 1 |
| 10 00 00 00 00 00 00 00 00 00 | 1847 | 25739 | 369511 |
| 11 00 00 00 00 00 00 00 00 00 | 12 | 16 | 20 |
| 11 01 00 00 00 00 00 00 00 00 | 1968 | 32016 | 503860 |
| 11 00 11 00 00 00 00 00 00 00 | 12 | 16 | 20 |
| 11 00 11 01 00 00 00 00 00 00 | 246 | 7240 | 154970 |
| 11 00 00 11 00 00 00 00 00 00 | 6 | 16 | 20 |
| 11 00 00 00 11 00 00 00 00 00 | – | 8 | 20 |
| 11 00 11 00 11 00 00 00 00 00 | 4 | 16 | 20 |
| 11 00 11 00 11 01 00 00 00 00 | – | 448 | 19280 |
| 11 00 00 00 00 11 00 00 00 00 | – | – | 10 |
| 11 00 11 00 00 11 00 00 00 00 | – | 16 | 20 |
| 11 00 00 11 00 11 00 00 00 00 | – | – | 20 |
| 11 00 11 00 00 00 11 00 00 00 | – | – | 20 |
| 11 00 00 11 00 00 11 00 00 00 | – | – | 20 |
| 11 00 11 00 11 00 11 00 00 00 | – | 4 | 20 |
| 11 00 11 00 11 00 11 01 00 00 | – | – | 710 |
| 11 00 11 00 11 00 00 11 00 00 | – | – | 20 |
| 11 00 11 00 00 11 00 11 00 00 | – | – | 10 |
| 11 00 11 00 11 00 11 00 11 00 | – | – | 4 |

**Table 6.5** *Populations of all sectors for $L = 12$, $L = 16$, and $L = 20$. We see that sector populations are high for those sectors whose identifiers feature a* 01 *pair due to increased mixing via quasiparticle creation and annihilation.*

whose identifiers contain 01 pairs (those of all other sectors bar the $0_L$ sector) must be highly populated. We see this to be true in table 6.5, where we tabulate the populations of each sector for different values of $L$. That this is the case is because sectors containing 01 pairs are the only sectors which feature negative-velocity quasiparticles, and are also the only ones which are able to generate or destroy quasiparticles of any type (for example, 11010000 destroys quasiparticles if it updates to 01111000). In summary, all configurations which feature any number of negative-velocity quasiparticles belong to sectors that feature 01 pairs in their identifiers, and that this is true accounts for the disparity in the RCA and SCA sector counts seen in table 6.1.

We finish this section by describing how one can count sectors of the SCA systematically. In the algorithm described above, we see that the majority of sector identifiers are generated in step 2, where the resulting strings are of the form $1_2 0_{2k_1} 1_2 0_{2k_2} 1_2 ... 1_2 0_{2k_\alpha} 1_2 0_{L-2m-4}$. To reiterate, we have freedom in step 2 to

choose the form of the $0_{2k_1-2}1_2...1_20_{2k_\alpha-2}$ substring,[4] with each valid choice made corresponding to a new sector identifier. Given that there are $n = m-2$ pairs of digits in each such substring, denoting

$$X_n = \text{number of substrings of the form } ...00 \tag{6.3.13}$$

$$\text{and} \qquad Y_n = \text{number of substrings of the form } ...11 \tag{6.3.14}$$

leads to the following coupled recurrence relations:

$$X_{n+1} = X_n + Y_n \tag{6.3.15}$$

$$\text{and} \qquad Y_{n+1} = X_n \ . \tag{6.3.16}$$

Equation (6.3.15) follows from the fact that we can validly append 00 to any substring, whilst eq. (6.3.16) follows from the fact that appending 11 is only allowed if the current substring ends in 00 – as per the requirements of step 2. Combining eqs. (6.3.15) and (6.3.16) leads to the decoupled Fibonacci recurrence relations

$$X_{n+2} = X_{n+1} + X_n \tag{6.3.17}$$

$$\text{and} \qquad Y_{n+2} = Y_{n+1} + Y_n \ . \tag{6.3.18}$$

Defining $F_n := X_n + Y_n$ to be the total number of valid substrings, it follows that $F_m = F_{n+2}$ also obeys the Fibonacci recurrence relation

$$F_m = F_{m-1} + F_{m-2} \ . \tag{6.3.19}$$

Since this recurrence relation is second-order, two values must be specified to generate the entire sequence. To reiterate, the strings from which we can generate valid sector identifiers in step 2 are of the form $1_20_{2m}1_20_{L-2m-4}$. The simplest two such strings are $1_20_21_20_{L-6}$ and $1_20_41_20_{L-6}$, for which we have $m = 1$ and $m = 2$, respectively. We therefore set $F_1 = F_2 = 1$, since the only strings that can be generated by applying step 2 to $1_20_21_20_{L-6}$ and $1_20_41_20_{L-6}$ are themselves. It hence follows that, given a string of the form $1_20_{2m}1_20_{L-2m-4}$, we generate $F_m$ sector identifiers by application of step 2, where $F_m$ is the $m$th Fibonacci number.

Given the above facts, we can define a measure for the sector count of the $L$-site

[4] We have freedom only over the substring $0_{2k_1-2}1_2...1_20_{2k_\alpha-2}$ and not $0_{2k_1}1_2...1_20_{2k_\alpha}$ since it is required that the former be bookended by $0_2$ pairs so as to avoid consecutive $1_2$ pairs.

SCA. We define $S_S(L)$ to be a lower bound on the true sector count, where

$$S_S(L) = 4 + \sum_{m=1}^{\lfloor \frac{L}{4} \rfloor - 1} \left[ \delta_{m \bmod 2,\ 1} + F_m \right] \ . \tag{6.3.20}$$

Here, the 4 counts the first four sectors (whose identifiers have identical forms for $L \geq 6$). We then sum the remaining sectors by summing over the Fibonacci numbers, adding 1 whenever $m$ is odd to account for the additional configurations of step 3. The only exception to this is $L = 8$, where we do not add 1 to avoid counting/generating an identifier that contains three consecutive 1s. The summation index runs up to $\lfloor \frac{L}{4} \rfloor - 1$ since, as we have discussed, this is the largest value of $m$ which is guaranteed to generate valid sector identifiers. Equation (6.3.20) is a lower bound since, as has also been discussed, larger values of $m$ may generate valid identifiers, but this is not guaranteed in every case. The lower bound of eq. (6.3.20) is valid only for $L \geq 10$ due to the non-conforming case of $L = 8$ mentioned above.

Evaluating the sum in eq. (6.3.20) yields

$$S_S(L) = 3 + \left\lceil \frac{1}{2} \left( \left\lfloor \frac{L}{4} \right\rfloor - 1 \right) \right\rceil + F_{\lfloor \frac{L}{4} \rfloor + 1} \tag{6.3.21}$$

since

$$\sum_{m=1}^{N} \delta_{m \bmod 2,\ 1} = \left\lceil \frac{1}{2} N \right\rceil \tag{6.3.22}$$

and

$$\sum_{m=1}^{N} F_m = F_{N+2} - 1. \tag{6.3.23}$$

Equation (6.3.23) may be proved by induction. Assuming eq. (6.3.23) is correct, we have

$$\sum_{m=1}^{N+1} F_m = \sum_{m=1}^{N} F_m + F_{N+1} = F_{N+2} + F_{N+1} - 1 = F_{N+3} - 1 = F_{(N+1)+2} - 1. \tag{6.3.24}$$

Thus, if it holds for $N$ then it also holds for $N + 1$. The base case $N = 1$ reads

$$\sum_{m=1}^{1} F_m = F_1. \tag{6.3.25}$$

Since $F_3 - 1 = F_3 - F_2 = F_1$, we see that the base case holds. We hence conclude

that eq. (6.3.23) is correct.

For large $L$, the dominant term in eq. (6.3.21) is $F_{\lfloor \frac{L}{4} \rfloor + 1}$. Thus,

$$\frac{S_S(L+4)}{S_S(L)} \sim \frac{\phi^{\lfloor \frac{L}{4} \rfloor + 1} - \varphi^{\lfloor \frac{L}{4} \rfloor + 1}}{\phi^{\lfloor \frac{L}{4} \rfloor} - \varphi^{\lfloor \frac{L}{4} \rfloor}} \sim \phi \ , \tag{6.3.26}$$

where $\phi = \frac{1+\sqrt{5}}{2} \approx 1.6180$ is the golden ratio, $\varphi = \frac{1-\sqrt{5}}{2} \approx -0.6180$ is the conjugate of the golden ratio, and where we have used the exact expression $F_m = \frac{\phi^m - \varphi^m}{\sqrt{5}}$. Given that $|\varphi| < 1$, the lower bound on the sector count, eq. (6.3.21), grows asymptotically as

$$S_S(L) \sim \phi^{\frac{L}{4}} = \left( \sqrt[4]{\phi} \right)^L \approx 1.1278^L. \tag{6.3.27}$$

A corresponding upper bound, denoted $S_U(L)$, can also be established by letting the value of $m$ run to $\frac{L}{2} - 3$ in eq. (6.3.20). This amounts to writing down all strings of the form $1_2 0_{2m} 1_2 0_{L-2m-4}$ starting from $1_2 0_2 1_2 0_{L-6}$ and ending at $1_2 0_{L-6} 1_2 0_2$ in step 1, and subsequently carrying out steps 2 and 3 as usual. As has already been alluded to, this will overcount the number of sectors since some of the generated strings will not be valid identifiers (the starting and ending strings provide an example; the latter, $1_2 0_{L-6} 1_2 0_2$, is not a valid sector identifier since it is translationally equivalent to the former, $1_2 0_2 1_2 0_{L-6}$). We therefore have that

$$S_U(L) = 4 + \sum_{m=1}^{\frac{L}{2}-3} \left[ \delta_{m \bmod 2,\, 1} + F_m \right] \ . \tag{6.3.28}$$

Evaluating this sum yields

$$S_U(L) = 3 + \left\lceil \frac{L}{4} - \frac{3}{2} \right\rceil + F_{\frac{L}{2}-1} \ . \tag{6.3.29}$$

In fig. 6.8 we demonstrate the validity of the lower and upper bounds obtained in eqs. (6.3.21) and (6.3.29) with the true sector counts tabulated in table 6.1.

For large $L$, we see from eq. (6.3.29) that

$$\frac{S_U(L+4)}{S_U(L)} \sim \frac{\phi^{\frac{L}{2}+1} - \varphi^{\frac{L}{2}+1}}{\phi^{\frac{L}{2}-1} - \varphi^{\frac{L}{2}-1}} \sim \phi^2 \ . \tag{6.3.30}$$

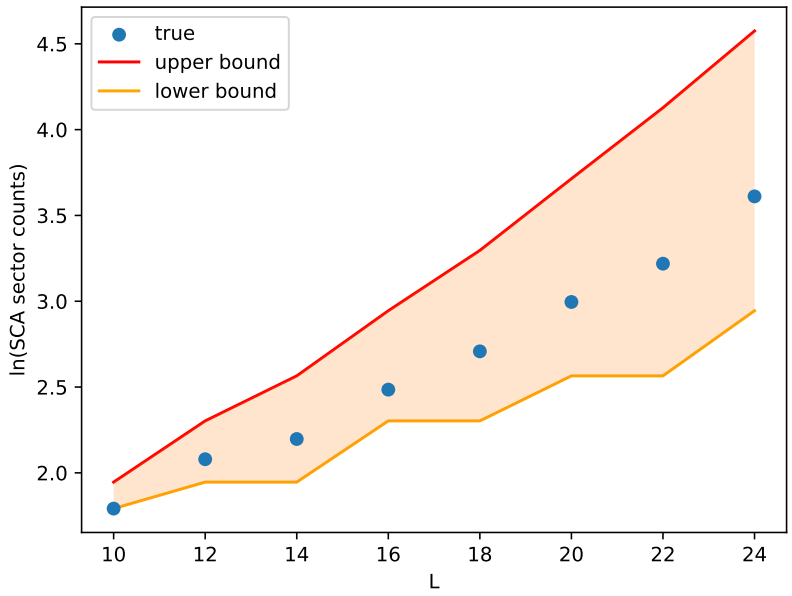


**Figure 6.8** *Comparison of the true SCA sector counts from table 6.1 with the lower and upper bounds of eqs.* (6.3.21) *and* (6.3.29) *plotted on a natural-logarithmic scale over the range* $10 \leq L \leq 24$ *(we recall that eq.* (6.3.21) *is valid only when* $L \geq 10$*). We observe that all sector counts lie on or within the two bounds.*

The upper bound on the sector count therefore grows asymptotically as

$$S_U(L) \sim \phi^{\frac{L}{2}} = \left(\sqrt{\phi}\right)^L \approx 1.2720^L. \tag{6.3.31}$$

The bounds on the growth rates in eqs. (6.3.27) and (6.3.31) allow us to appreciate the difference in sector growth rates between the SCA and RCA as tabulated in table 6.1. Specifically, by eq. (6.3.11), the ratio of the lower bound on the RCA growth rate to the upper bound on the SCA growth rate is approximately $\frac{1}{L}\frac{2^L}{\sqrt{\phi}^L} \approx \frac{1.5723^L}{L}$. Using instead the lower bound on the SCA growth rate, this ratio becomes $\frac{1}{L}\frac{2^L}{\sqrt[4]{\phi}^L} \approx \frac{1.7733^L}{L}$. The true ratio will, of course, fall between these two bounds, and clearly grows very rapidly for large $L$.

We remark finally that a more thorough analysis would yield an exact count for the number of sectors as a function of system size. We leave this to future work, but note that the growth rate established in eqs. (6.3.20) and (6.3.27) serves as a precise description for the way in which the sector count diverges in the case of infinite system size, this being a consequence of the pattern in identifiers remaining unbroken (there is no upper limit of $m$ in step 1 for infinite systems).

## 6.4 Concluding remarks and outlook

In this chapter, we investigated a stochastic generalisation of a one-dimensional system known as a reversible cellular automaton (RCA), whose site occupations change in discrete time based on nearest-neighbour occupations. RCA are so called because of the parity-inversion and time-reversal symmetries they exhibit. Here, we focussed specifically on the rule-150 RCA, whose update rules are stated in eqs. (6.1.10) to (6.1.17). The generalisation we considered replaced the deterministic rules of eqs. (6.1.15) and (6.1.17) with the stochastic rules of eqs. (6.2.1) and (6.2.2). We referred to this generalisation as the 'rule-150 SCA'. Whilst the rule-150 SCA breaks time-reversal symmetry and the particle-hole symmetry of the rule-150 RCA, it retains parity-inversion symmetry as well as the constraint of eq. (6.1.21) regarding the counting of quasiparticles.

In section 6.3.1, we showed that a uniform distribution of configurations solves the stationary master equation of the rule-150 SCA, implying that the configurations within each sector of the SCA's state space are equiprobable. Understanding the state space of the rule-150 SCA therefore becomes a matter of understanding the sectors of the system. Using simulations, we counted the numbers of sectors in each of the RCA and SCA state spaces, noting a stark contrast in the growth rates as the system size, $L$, is increased (see table 6.1). Moreover, we assigned an identifying label to each sector consisting of a binary string whose value is the smallest of all configurations within the sector. By tabulating sector identifiers obtained from simulation runs (table 6.3), we were able to establish a pattern. From this, we showed that a lower bound on the number of sectors for the $L$-site SCA is related to the Fibonacci numbers, after which we inferred the asymptotic growth rate of the lower bound be exponential according to $\phi^{\frac{L}{4}}$, where $\phi$ is the golden ratio. This is significantly less than the growth rate of the corresponding lower bound for the RCA, which goes as $\frac{2^L}{L}$. We found that most configurations of the SCA were those comprising arrangements of positive-velocity 11 domains, whose trajectories are periodic over $L$ time steps. The remaining sectors are less numerous – significantly so when $L$ is large. Aside from the $0_L$ configuration (which constitutes its own sector), all other sectors feature a single negative-velocity quasiparticle which allows for the creation and annihilation of quasiparticles by the stochastic update rules; we hence conclude that such sectors are highly populated and well-mixed.

There are many possible extensions to the work presented here. One could further

this work by establishing the true sector count for the $L$-site SCA and not a lower bound. This would involve establishing the pattern of identifiers that emerges after the pattern corresponding to the lower bound breaks (as a reminder, the breaking of this pattern was highlighted in table 6.4). One could also investigate the highly mixed sectors (those containing 01 pairs) more deeply with regards to precisely how populous each such sector is and why such sectors do not mix with each other. More broadly, a full set of solutions to the stationary master equation – perhaps via a matrix-product ansatz – would allow for a deeper analysis via the calculation of the nonequilibrium partition function, from which all statistical properties of the system could be derived exactly. Further stochastic generalisations (of the rule-150 RCA as well as other RCA) could also be considered if one wishes to learn more generally about the partitioning of the state space given a particular set of update rules.

# Chapter 7

# Conclusions and outlook

In this thesis, we have formulated and studied three nonequilibrium model systems with the aim of establishing their emergent properties and the ways in which these arise as a consequence of broken detailed balance at the microscopic level. We now summarise these models and the conclusions drawn from them individually, before moving on to draw broader conclusions that apply to this thesis as a whole.

The first model we investigated (chapter 3) consisted of a dilute gas of on-lattice persistent random walkers (PRWs) which interact via exclusion in $d$ dimensions, where $d \geq 2$. We predicted that after taking a continuum scaling limit the critical density for multiparticle clustering becomes vanishingly small and discovered good agreement between this prediction and simulation results.

The second model we investigated (chapters 4 and 5) comprises two on-lattice PRWs in one dimension which undergo an interaction wherein the walkers are instantaneously displaced upon contact, an action known as recoil. In the same continuum limit as that which was taken in the first model, we established a number of facts. Firstly, we found that jamming in a purely excluding system is a relatively weak phenomenon which can be made to disappear by adding a small particle-exchange probability. Then, for general recoil interactions, we established the existence of reentrant states in which the walkers are effectively attractive for a finite range of tumble rates and are otherwise repulsive, as well as nontrivial boundary behaviours which require care to be correctly handled.

The third and final model we looked at (chapter 6) was a one-dimensional cellular

automaton (CA) whose update rules were a stochastic generalisation of the previously-studied deterministic rule-150 CA's update rules. From simulation results, we were able to establish the structure of the system's state space and hence a lower bound on the growth rate of the number of state-space sectors with system size. We found that this growth rate is related to the Fibonacci numbers, and is significantly slower than that for the rule-150 CA due to increased mixing engendered by the stochasticity.

Regarding the many-PRW model, that we observe clustering at arbitrarily low densities in the thermodynamic limit is indicative of the strength of effective attractions in the system. This is an intriguing result in light of the findings of section 4.4, where we concluded that the addition of a particle-exchange interaction to the purely-excluding, one-dimensional SEB model showed that jamming was a relatively unstable phenomenon. Though particle exchange was not included in the many-PRW model, the higher dimensionality allows the walkers to escape two-particle jammed states via tumbling into orientations perpendicular to the orientations of their jamming partners – something which is not possible in the SEB case where tumbles in jammed states always retain adjacency. Such tumbling in the multidimensional PRW system, which we here define to have rate $\bar{\omega}$, thus plays an analogous role to particle exchange in the one-dimensional system introduced in section 4.4, since both are means of immediately exiting jammed states without first having to go through a reversal (as is the case in the SEB model). We now compare these two scenarios, first noting that $\bar{\omega} = \frac{2d-2}{2d-1}\omega$ since there are $2d-1$ total tumble orientations and $2d-2$ tumble orientations excluding reversals. Since, $\bar{\omega} \propto \omega$ and $\frac{\omega}{\gamma} = \mathcal{O}\left(\frac{1}{L}\right)$, it follows that $\frac{\bar{\omega}}{\gamma} = \mathcal{O}\left(\frac{1}{L}\right)$. Thus, $\bar{\omega}$ tumbles in the multidimensional system are analogous to a particle-exchange probability of $v = \mathcal{O}\left(\frac{1}{L}\right)$ in the one-dimensional system of section 4.4 in that the rate of escape from jammed states in both cases is of the same order. In the latter case, jamming was found to be of comparable strength to that of the purely-excluding regime, that is, we saw in each of the cases $v = 0$ and $v = \mathcal{O}\left(\frac{1}{L}\right)$ that the stationary probability associated with jamming is $\mathcal{O}(1)$. If one were to incorporate an $\mathcal{O}\left(\frac{1}{L}\right)$ particle exchange probability into the multidimensional system, we might therefore expect clustering to remain stable (since the rate of escape from jammed states would remain of the same order after the introduction of particle exchange). By extension, we may conjecture that clustering in the multidimensional system be more unstable given an $\mathcal{O}(1)$ particle-exchange probability, for this is analogous to setting $\frac{\bar{\omega}}{\gamma} = \mathcal{O}(1)$, for which two-particle jammed states (the seeds for larger clusters) would persist

only ephemerally due to the significant decrease in activity/persistence. Thus, it is perhaps the case that the critical density for clustering in the multidimensional system with an additional $\mathcal{O}(1)$ exchange ineraction is not vanishingly small in the thermodynamic limit. In order to investigate this, one could attempt to modify the calculation of chapter 3 to account for particle exchange. One could also attempt to establish a critical clustering density directly from simulations.

On the subject of using one-dimensional systems as a guide for what might happen in multidimensional systems, we reiterate the approach taken in chapter 3. There, we found an approximate solution to a first-passage problem in many dimensions by treating the system as consisting of sea and channel states. As a reminder, channels refer to one-dimensional sublattices of the multidimensional domain, whilst the sea refers to the rest of the domain. The sea serves as a reservoir from which particles may enter or leave channels; in this way, the multidimensional problem becomes a quasi-one-dimensional one. That this approach was successful gives us confidence that the same approach could be adapted to the case of recoiling PRWs studied in chapters 4 and 5. One could then survey the effects different types of recoil interaction have on the existence of multiparticle clusters.

In the recoil model, we saw how the stationary distribution of particle separations could be controlled by tuning the persistence. Specifically, appropriate tuning can be used to engineer an effective attraction/repulsion. That such behaviour is possible in a simple two-particle system suggests that emergent behaviours in the corresponding many-particle system may also be nontrivially sensitive to changes in microscopic conditions. It is tempting to suggest that parameter choices corresponding to an effective attraction at the two-particle level would give rise to clustering in the presence of many particles; and likewise that no clustering would be seen otherwise. Given the level of complexity that emerges out of the simple two-particle model, perhaps instead the emergent behaviours of the many-body system are more nuanced. At present, analytical techniques are not at the level required to solve this many-body problem exactly, but approximate methods (such as that described in the paragraph above) and simulation work for different recoil distributions and parameter choices could prove insightful.

In the stochastic CA model, we noted how the added stochasticity effected increased mixing of configurations, greatly reducing the number of state-space sectors. We also noted how the emergent behaviours of the recoil model are determined by the level of persistence: for an infinite persistence length, $\xi \to \infty$, the recoil system becomes stuck in one of the model's four quadrants ($++$, $+-$,

$--$ or $-+$) – that which it was initialised in; whilst for finite persistence lengths, the quadrants are able to mix. As was alluded to in section 5.3, we can view this at the level of the state space. The rate at which different quadrants are accessed, $\omega = \frac{1}{\xi L}$, determines the dominant contribution to the system's overall behaviour. In our analysis of the stochastic CA, we found that previously unmixed sectors mix for any nonzero stochastic transition probability, $q$, to create new sectors with high configurational populations. Perhaps, like the recoil model, the rate at which the system mixes different sectors can be used to say something useful about its emergent behaviours. Since we were focussed solely on establishing the structure of the state space, tuning the value of $q$ was not important in our analysis (as long as $0 < q < 1$, mixing will occur). Perhaps a survey of behaviours for different values of $q$ would be worthwhile, therefore, so that we can make comparisons with the recoil system with the hope of being able to say something more general about the effects of stochasticity on nonequilibrium emergent properties.

Finally, we conclude by emphasising the importance of microscopic models with regards to the study of nonequilibrium systems. We start by noting that many models of active systems (to use an example) are imprecise in the sense that approximations and phenomenology are often used to make simplifications. Whilst such models may still provide useful insights, there is no guarantee that they are physically consistent at the microscopic level; one therefore has to be careful if one wishes to use them as a guide for learning about nonequilibrium systems. Fundamentally, the Universe is a nonequilibrium process, or may be equivalently viewed as a collection of nonequilibrium subprocesses that feed into each other. One can therefore learn a great deal about the Universe by studying microscopic models, for they are likely to be applicable to a wide range of real, physical processes (whether or not we currently realise what those processes are). This makes them invaluable as a tool for building intuition about how our Universe operates at a fundamental level. Microscopic models are also of great pedagogical use too, owing to their simplicity of formulation and, in some cases such as the TASEP and the recoil model presented in this thesis, known exact solutions. As awareness of nonequilibrium statistical mechanics and its importance increases, perhaps it will become increasingly common to present exact solutions to nonequilibrium microscopic models in pedagogical settings, much in the same way that we present exact Ising model calculations when teaching equilibrium statistical mechanics. Then, the next generation of statistical physicists can build upon current known methods and develop entirely new ones, helping to increase the span of exact solutions and thereby giving us

a larger pool of results from which we can draw general conclusions. In this way, perhaps, we may eventually arrive at a general theory of nonequilibrium statistical physics.

# Appendix A

# Leading-order contributions to weighted integrals over the Green's function and its derivatives

In this appendix, we give the leading-order contributions to the integrals

$$\int_0^1 \mathcal{G}(x,y)\rho_+(y)\,\mathrm{d}y\,, \quad \int_0^1 \frac{\partial \mathcal{G}(x,y)}{\partial y}\rho_\pm(y)\,\mathrm{d}y \quad \text{and} \quad \int_0^1 \frac{\partial^2 \mathcal{G}(x,y)}{\partial y^2}\rho_+(y)\,\mathrm{d}y \tag{A.0.1}$$

given that

$$\rho(x) = \sum_i a_i \delta(x - x_i) + \sum_j b_j \Theta(x - x_j) + \sum_k c_k \Theta(x_k - x) + d\bar{\rho}(x). \tag{A.0.2}$$

As stated in the main text, all $x_{i,j,k}$ are taken to be in the bulk of the domain. Using

$$\begin{aligned}\mathcal{G}(x,y) = \frac{\xi}{4}\sqrt{\frac{\xi}{2L}}\left[\mathrm{e}^{-\sqrt{\frac{2L}{\xi}}|x-y|} - x\mathrm{e}^{-\sqrt{\frac{2L}{\xi}}(1-y)} - (1-x)\mathrm{e}^{-\sqrt{\frac{2L}{\xi}}y}\right] \\ - \frac{\xi}{2}\left[(1-x)y\Theta(x-y) + x(1-y)\Theta(y-x)\right]\end{aligned} \tag{A.0.3}$$

as stated in eq. (5.1.33), differentiation yields

$$\frac{\partial \mathcal{G}(x,y)}{\partial y} = \frac{\xi}{4}\Bigg[\mathrm{e}^{-\sqrt{\frac{2L}{\xi}}|x-y|}\Theta(x-y) - \mathrm{e}^{-\sqrt{\frac{2L}{\xi}}|x-y|}\Theta(y-x) \\ -x\mathrm{e}^{-\sqrt{\frac{2L}{\xi}}(1-y)} + (1-x)\mathrm{e}^{-\sqrt{\frac{2L}{\xi}}y}\Bigg] - \frac{\xi}{2}[\Theta(x-y)-x] \tag{A.0.4}$$

$$\text{and} \quad \frac{\partial^2 \mathcal{G}(x,y)}{\partial y^2} = \frac{1}{2}\sqrt{\frac{\xi L}{2}}\left[\mathrm{e}^{-\sqrt{\frac{2L}{\xi}}|x-y|} - x\mathrm{e}^{-\sqrt{\frac{2L}{\xi}}(1-y)} - (1-x)\mathrm{e}^{-\sqrt{\frac{2L}{\xi}}y}\right]. \tag{A.0.5}$$

Using the above, we can show the following leading-order contributions to the above integrals:

$$\int_0^1 \mathcal{G}(x,y)\delta(y-x_0)\,\mathrm{d}y = -\frac{\xi}{2}(1-x)x_0\Theta(x-x_0) - \frac{\xi}{2}x(1-x_0)\Theta(x_0-x); \tag{A.0.6}$$

$$\int_0^1 \mathcal{G}(x,y)\Theta(y-x_0)\,\mathrm{d}y = -\frac{\xi}{4}x(1-x)^2 - \frac{\xi}{4}(1-x)(x^2-x_0^2)\Theta(x-x_0) \\ + \frac{\xi}{4}x[(1-x)^2-(1-x_0)^2]\Theta(x_0-x); \tag{A.0.7}$$

$$\int_0^1 \mathcal{G}(x,y)\Theta(x_0-y)\,\mathrm{d}y = -\frac{\xi}{4}(1-x)x^2 + \frac{\xi}{4}(1-x)(x^2-x_0^2)\Theta(x-x_0) \\ - \frac{\xi}{4}x[(1-x)^2-(1-x_0^2)]\Theta(x_0-x); \tag{A.0.8}$$

$$\int_0^1 \mathcal{G}(x,y)\bar{\rho}_+(y)\,\mathrm{d}y = -\frac{\xi}{2}(1-x)\int_0^x y\bar{\rho}_+(y)\,\mathrm{d}y \\ - \frac{\xi}{2}x\int_x^1 (1-y)\bar{\rho}_+(y)\,\mathrm{d}y\,; \tag{A.0.9}$$

$$\int_0^1 \frac{\partial \mathcal{G}(x,y)}{\partial y}\delta(y-x_0)\,\mathrm{d}y = \frac{\xi}{4}\mathrm{e}^{-\sqrt{\frac{2L}{\xi}}(x-x_0)}\Theta(x-x_0) - \frac{\xi}{4}\mathrm{e}^{-\sqrt{\frac{2L}{\xi}}(x_0-x)}\Theta(x_0-x) - \frac{\xi}{2}\Theta(x-x_0) + \frac{\xi}{2}x; \tag{A.0.10}$$

$$\int_0^1 \frac{\partial \mathcal{G}(x,y)}{\partial y}\Theta(y-x_0)\,\mathrm{d}y = \frac{\xi}{2}x_0\Theta(x-x_0) + \frac{\xi}{2}x\Theta(x_0-x) - \frac{\xi}{2}x_0x; \tag{A.0.11}$$

$$\int_0^1 \frac{\partial \mathcal{G}(x,y)}{\partial y}\Theta(x_0-y)\,\mathrm{d}y = \frac{\xi}{2}x_0x - \frac{\xi}{2}x_0\Theta(x-x_0) - \frac{\xi}{2}x\Theta(x_0-x); \tag{A.0.12}$$

$$\int_0^1 \frac{\partial \mathcal{G}(x,y)}{\partial y}\bar{\rho}_{\pm}(y)\,\mathrm{d}y = \frac{\xi}{2}(1\pm 1)x - \frac{\xi}{2}\int_0^x \bar{\rho}_{\pm}(y)\,\mathrm{d}y\,; \tag{A.0.13}$$

$$\int_0^1 \frac{\partial^2 \mathcal{G}(x,y)}{\partial y^2}\delta(y-x_0)\,\mathrm{d}y = \frac{1}{2}\sqrt{\frac{\xi L}{2}}\mathrm{e}^{-\sqrt{\frac{2L}{\xi}}|x-x_0|}; \tag{A.0.14}$$

$$\int_0^1 \frac{\partial^2 \mathcal{G}(x,y)}{\partial y^2}\Theta(y-x_0)\,\mathrm{d}y = \frac{\xi}{4}\mathrm{e}^{-\sqrt{\frac{2L}{\xi}}(x_0-x)}\Theta(x_0-x) - \frac{\xi}{4}\mathrm{e}^{-\sqrt{\frac{2L}{\xi}}(x-x_0)}\Theta(x-x_0) + \frac{\xi}{2}\Theta(x-x_0) - \frac{\xi}{4}\mathrm{e}^{-\sqrt{\frac{2L}{\xi}}(1-x)} - \frac{\xi}{4}x; \tag{A.0.15}$$

$$\int_0^1 \frac{\partial^2 \mathcal{G}(x,y)}{\partial y^2}\Theta(x_0-y)\,\mathrm{d}y = \frac{\xi}{4}\mathrm{e}^{-\sqrt{\frac{2L}{\xi}}(x-x_0)}\Theta(x-x_0) - \frac{\xi}{4}\mathrm{e}^{-\sqrt{\frac{2L}{\xi}}(x_0-x)}\Theta(x_0-x) + \frac{\xi}{2}\Theta(x_0-x) - \frac{\xi}{4}\mathrm{e}^{-\sqrt{\frac{2L}{\xi}}x} - \frac{\xi}{4}(1-x); \tag{A.0.16}$$

and

$$\int_0^1 \frac{\partial^2 \mathcal{G}(x,y)}{\partial y^2}\bar{\rho}_{+}(y)\,\mathrm{d}y = \frac{\xi}{2}\bar{\rho}_{+}(x) - \frac{\xi}{4}\bar{\rho}_{+}(0) - \frac{\xi}{4}\bar{\rho}_{+}(0)\mathrm{e}^{-\sqrt{\frac{2L}{\xi}}x} - \frac{\xi}{4}\bar{\rho}_{+}(0)\mathrm{e}^{-\sqrt{\frac{2L}{\xi}}(1-x)}. \tag{A.0.17}$$

# Appendix B

# Matrix-product solution of the rule-150 RCA stationary state

In [144], the patch-state ansatz detailed in section 6.1.2 was used to construct an equivalent matrix-product solution. For completeness, we outline this derivation here.

In the matrix-product formulation, the weight of configuration $\mathcal{C}$ is posited to take the form

$$P(\mathcal{C}) = \mathrm{Tr}\Big[\mathsf{X}_{n_0}\hat{\mathsf{X}}_{n_1}\mathsf{X}_{n_2}\ ...\ \hat{\mathsf{X}}_{n_{L-3}}\mathsf{X}_{n_{L-2}}\hat{\mathsf{X}}_{n_{L-1}}\Big]. \tag{B.0.1}$$

Here, we distinguish the sublattice corresponding to odd site indices with hatted matrices, giving four matrices in total that need to be solved for: $\mathsf{X}_0$, $\mathsf{X}_1$, $\hat{\mathsf{X}}_0$, and $\hat{\mathsf{X}}_1$. The trace is chosen here over an inner product to reflect the system's translational invariance: due to periodicity, it must be true that

$$\begin{aligned} P(n_0, n_1, ..., n_{L-2}, n_{L-1}) &= P(n_2, n_3, ..., n_0, n_1) \\ &= ... \\ &= P(n_{L-2}, n_{L-1}, ..., n_{L-4}, n_{L-3}). \end{aligned} \tag{B.0.2}$$

The trace operation is invariant under cyclic permutations, thus making it a suitable operation for extracting weights from the matrix products.

Inserting eq. (B.0.1) explicitly, the state vector of eq. (6.1.26) may be written as

$$\mathsf{p} = \sum_{\mathcal{C}} \mathrm{Tr}\Big[\mathsf{X}_{n_0}\hat{\mathsf{X}}_{n_1}\mathsf{X}_{n_2}\ ...\ \hat{\mathsf{X}}_{n_{L-3}}\mathsf{X}_{n_{L-2}}\hat{\mathsf{X}}_{n_{L-1}}\Big]\hat{\mathsf{e}}_{\mathcal{C}}. \tag{B.0.3}$$

The action of $\mathcal{T}_i$ is therefore such that

$$\mathcal{T}_i \mathsf{p} = \sum_{\mathcal{C}} \mathrm{Tr}\Big[ \ ... \ \hat{\mathsf{X}}_{n_{i-1}} \mathsf{X}_{f_i} \hat{\mathsf{X}}_{n_{i+1}} \ ... \ \Big] \hat{\mathsf{e}}_{\mathcal{C}}. \tag{B.0.4}$$

We recall from eq. (6.1.27) that $\mathsf{p}$ must be recovered after applying updates at all even sites followed by updates at all odd sites if it is to describe the stationary state. With this in mind, we can implement a suitable *cancellation mechanism*. The simplest possible cancellation mechanism is one in which

$$\begin{aligned}(\mathcal{T}_0 ... \mathcal{T}_{L-2}) \sum_{\mathcal{C}} \mathrm{Tr}\Big[ \mathsf{X}_{n_0} \hat{\mathsf{X}}_{n_1} \mathsf{X}_{n_2} \ ... \ \hat{\mathsf{X}}_{n_{L-3}} \mathsf{X}_{n_{L-2}} \hat{\mathsf{X}}_{n_{L-1}} \Big] \hat{\mathsf{e}}_{\mathcal{C}} \\ = \sum_{\mathcal{C}} \mathrm{Tr}\Big[ \hat{\mathsf{X}}_{n_0} \mathsf{X}_{n_1} \hat{\mathsf{X}}_{n_2} \ ... \ \mathsf{X}_{n_{L-3}} \hat{\mathsf{X}}_{n_{L-2}} \mathsf{X}_{n_{L-1}} \Big] \hat{\mathsf{e}}_{\mathcal{C}}\end{aligned} \tag{B.0.5}$$

and

$$\begin{aligned}(\mathcal{T}_1 ... \mathcal{T}_{L-1}) \sum_{\mathcal{C}} \mathrm{Tr}\Big[ \hat{\mathsf{X}}_{n_0} \mathsf{X}_{n_1} \hat{\mathsf{X}}_{n_2} \ ... \ \mathsf{X}_{n_{L-3}} \hat{\mathsf{X}}_{n_{L-2}} \mathsf{X}_{n_{L-1}} \Big] \hat{\mathsf{e}}_{\mathcal{C}} \\ = \sum_{\mathcal{C}} \mathrm{Tr}\Big[ \mathsf{X}_{n_0} \hat{\mathsf{X}}_{n_1} \mathsf{X}_{n_2} \ ... \ \hat{\mathsf{X}}_{n_{L-3}} \mathsf{X}_{n_{L-2}} \hat{\mathsf{X}}_{n_{L-1}} \Big] \hat{\mathsf{e}}_{\mathcal{C}}.\end{aligned} \tag{B.0.6}$$

The effect at each time step is to switch unhatted matrices for hatted matrices and vice versa such that after two time steps (one full lattice update) we end up with $\mathsf{p}$ once more. We demonstrate the precise implementation of this in fig. B.1. Noting the commutative property stated above, we begin by applying $\mathcal{T}_i$, where $i$ is arbitrary. This transforms the product $\hat{\mathsf{X}}_{n_{i-1}} \mathsf{X}_{n_i} \hat{\mathsf{X}}_{n_{i+1}}$ into $\mathsf{Y}_{n_{i-1}} \hat{\mathsf{X}}_{n_i} \mathsf{Z}_{n_{i+1}}$, where $\mathsf{Y}_0$, $\mathsf{Y}_1$, $\mathsf{Z}_0$ and $\mathsf{Z}_1$ are *auxiliary matrices* which are only temporarily introduced. Next, we apply $\mathcal{T}_{i-2}$ and $\mathcal{T}_{i+2}$ to the products $\hat{\mathsf{X}}_{n_{i-3}} \mathsf{X}_{n_{i-2}} \mathsf{Y}_{n_{i-1}}$ and $\mathsf{Z}_{n_{i+1}} \mathsf{X}_{n_{i+2}} \hat{\mathsf{X}}_{n_{i+3}}$, respectively, transforming them into $\mathsf{Y}_{n_{i-3}} \hat{\mathsf{X}}_{n_{i-2}} \mathsf{X}_{n_{i-1}}$ and $\mathsf{X}_{n_{i+1}} \hat{\mathsf{X}}_{n_{i+2}} \mathsf{Z}_{n_{i+3}}$. As per fig. B.1, we continue in this manner until only one site, site $j$ (that which is diametrically opposite site $i$), is yet to be updated. We enforce that the application of $\mathcal{T}_j$ to the product $\mathsf{Z}_{n_{j-1}} \mathsf{X}_{n_j} \mathsf{Y}_{n_{j+1}}$ yields $\mathsf{X}_{n_{j-1}} \hat{\mathsf{X}}_{n_j} \mathsf{X}_{n_{j+1}}$ so as to ensure all unhatted matrices have become hatted and vice versa. Applying this procedure to the second sublattice restores the original state.

We now return to eq. (B.0.4). In order for eq. (B.0.4) to be consistent with the cancellation mechanism described above, we require that

$$\hat{\mathsf{X}}_{n_{i-1}} \mathsf{X}_{f_i} \hat{\mathsf{X}}_{n_{i+1}} = \mathsf{Y}_{n_{i-1}} \hat{\mathsf{X}}_{n_i} \mathsf{Z}_{n_{i+1}}. \tag{B.0.7}$$

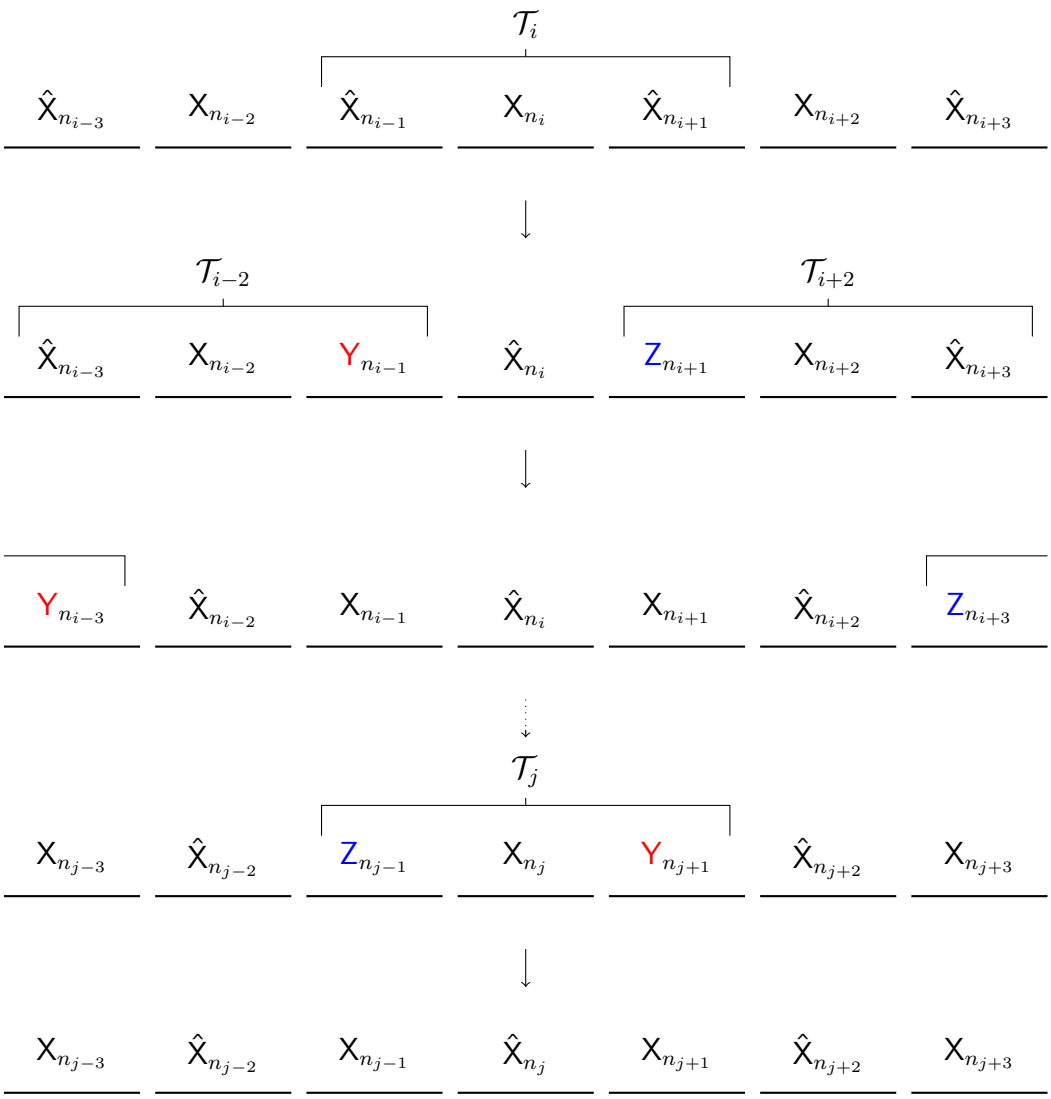


**Figure B.1** *A diagrammatic representation of the matrix-product algebra at an arbitrary timestep. Here, site $j$ is diametrically opposite site $i$ on the lattice. The net result of these operations is that all hatted matrices become unhatted and vice versa via the action of the auxiliary matrices $\mathsf{Y}_0$, $\mathsf{Y}_1$, $\mathsf{Z}_0$, and $\mathsf{Z}_1$.*

Applying the same logic to the products $\hat{\mathsf{X}}_{n_{i-1}}\mathsf{X}_{n_i}\mathsf{Y}_{n_{i+1}}$, $\mathsf{Z}_{n_{i-1}}\mathsf{X}_{n_i}\hat{\mathsf{X}}_{n_{i+1}}$ and $\mathsf{Z}_{n_{i-1}}\mathsf{X}_{n_i}\mathsf{Y}_{n_{i+1}}$, we further deduce that

$$\hat{\mathsf{X}}_{n_{i-1}}\mathsf{X}_{f_i}\mathsf{Y}_{n_{i+1}} = \mathsf{Y}_{n_{i-1}}\hat{\mathsf{X}}_{n_i}\mathsf{X}_{n_{i+1}} \ , \tag{B.0.8}$$

$$\mathsf{Z}_{n_{i-1}}\mathsf{X}_{f_i}\hat{\mathsf{X}}_{n_{i+1}} = \mathsf{X}_{n_{i-1}}\hat{\mathsf{X}}_{n_i}\mathsf{Z}_{n_{i+1}} \ , \tag{B.0.9}$$

$$\text{and} \quad \mathsf{Z}_{n_{i-1}}\mathsf{X}_{f_i}\mathsf{Y}_{n_{i+1}} = \mathsf{X}_{n_{i-1}}\hat{\mathsf{X}}_{n_i}\mathsf{X}_{n_{i+1}} \ . \tag{B.0.10}$$

This algebra amounts to 32 matrix equations corresponding to all possible combinations of subscripts in eqs. (B.0.7) to (B.0.10). In [144], the matrices

that satisfy the above algebra and reconstruct eq. (6.1.24) (up to normalisation) were shown to be

$$\mathsf{X}_0 = \begin{pmatrix} 1 & \xi \\ 0 & 0 \end{pmatrix} \qquad \text{and} \qquad \mathsf{X}_1 = \begin{pmatrix} 0 & 0 \\ \xi & 1 \end{pmatrix} \tag{B.0.11}$$

whilst

$$\hat{\mathsf{X}}_0 = \begin{pmatrix} 1 & \omega \\ 0 & 0 \end{pmatrix} \qquad \text{and} \qquad \hat{\mathsf{X}}_1 = \begin{pmatrix} 0 & 0 \\ \omega & 1 \end{pmatrix} . \tag{B.0.12}$$

# Bibliography


[1] M J Metson, M R Evans, and R A Blythe. Jamming of multiple persistent random walkers in arbitrary spatial dimension. *Journal of Statistical Mechanics: Theory and Experiment*, 2020:103207, 2020.

[2] M J Metson, M R Evans, and R A Blythe. Tuning attraction and repulsion between active particles through persistence. *Europhysics Letters*, 141: 41001, 2023.

[3] M J Metson, M R Evans, and R A Blythe. From a microscopic solution to a continuum description of active particles with a recoil interaction in one dimension. *Physical Review E*, 107:044134, 2023.

[4] J C Maxwell. Illustrations of the dynamical theory of gases. part I. On the motions and collisions of perfectly elastic spheres. *The London, Edinburgh, and Dublin Philosophical Magazine and Journal of Science*, 19:19, 1860.

[5] J C Maxwell. Illustrations of the dynamical theory of gases. part II. On the process of diffusion of two or more kinds of moving particles among one another. *The London, Edinburgh, and Dublin Philosophical Magazine and Journal of Science*, 20:21, 1860.

[6] L E Boltzmann. *Wissenschaftliche Abhandlungen*, volume 1, chapter 5: Studien über das Gleichgewicht der lebendigen Kraft zwischen bewegten materiellen Punkten, page 49. Cambridge University Press, 2012.

[7] L D Landua and E M Lifshitz. *Course of Theoretical Physics: Statistical Physics*, volume 5. Butterworth-Heinemann, 3rd edition, 1980.

[8] R Bowley and M Sánchez. *Introductory Statistical Mechanics*. Oxford University Press, 2nd edition, 1999.

[9] K Huang. *Introduction to Statistical Physics*. Routledge, 2nd edition, 2009.

[10] P M Chaikin and T C Lubensky. *Principles of Condensed Matter Physics*. Cambridge University Press, 1995.

[11] J Zinn-Justin. *Phase Transitions and Renormalization Group*. Oxford University Press, 2007.

[12] C Kittel. *Introduction to Solid State Physics*. John Wiley & Sons, global edition, 2018.

[13] R A L Jones. *Soft Condensed Matter*. Oxford University Press, 2002.

[14] N Duric. *Advanced Astrophysics*. Cambridge University Press, 2003.

[15] A Zee. *Group Theory in a Nutshell for Physicists*. Princeton University Press, 2016.

[16] D H Ackley, G E Hinton, and T J Sejnowski. A learning algorithm for Boltzmann machines. *Cognitive Science*, 9:147, 1985.

[17] Y Bahri, J Kadmon, J Pennington, S S Schoenholz, J Sohl-Dickstein, and S Ganguli. Statistical mechanics of deep learning. *Annual Review of Condensed Matter Physics*, 11:501, 2020.

[18] C Castellano, S Fortunato, and V Loreto. Statistical physics of social dynamics. *Reviews of Modern Physics*, 81:591, 2009.

[19] R N Mantegna and H E Stanley. *Introduction to Econophysics: Correlations and Complexity in Finance*. Cambridge University Press, 1999.

[20] T M Liggett. *Interacting Particle Systems*. Springer, 2012.

[21] T M Liggett. *Stochastic Interacting Systems: Contact, Voter and Exclusion Processes*. Springer, 1999.

[22] C Domb, R K P Zia, B Schmittmann, and J L Lebowitz. *Statistical Mechanics of Driven Diffusive Systems*. Elsevier Science, 1995.

[23] M R Evans and T Hanney. Nonequilibrium statistical mechanics of the zero-range process and related models. *Journal of Physics A: Mathematical and General*, 38:R195, 2005.

[24] T M Liggett. Ergodic theorems for the asymmetric simple exclusion process II. *The Annals of Probability*, 5:795, 1977.

[25] B Derrida, E Domany, and D Mukamel. An exact solution of a one-dimensional asymmetric exclusion model with open boundaries. *Journal of Statistical Physics*, 69:667, 1992.

[26] B Derrida, M R Evans, V Hakim, and V Pasquier. Exact solution of a 1d asymmetric exclusion model using a matrix formulation. *Journal of Physics A: Mathematical and General*, 26:1493, 1993.

[27] R A Blythe and M R Evans. Nonequilibrium steady states of matrix-product form: a solver's guide. *Journal of Physics A: Mathematical and Theoretical*, 40:R333, 2007.

[28] A J Wood, R A Blythe, and M R Evans. Rényi entropy of the totally asymmetric exclusion process. *Journal of Physics A: Mathematical and Theoretical*, 50:475005, 2017.

[29] P L Krapivsky, S Redner, and E Ben-Naim. *A Kinetic View of Statistical Physics*. Cambridge University Press, 2010.

[30] R Livi and P Politi. *Nonequilibrium Statistical Physics: a Modern Perspective*. Cambridge University Press, 2017.

[31] F P Kelly. *Reversibility and Stochastic Networks*. Cambridge University Press, 2011.

[32] C W Gardiner. *Handbook of Stochastic Methods for Physics, Chemistry and the Natural Sciences*. Springer-Verlag, 2nd edition, 1985.

[33] G Grimmett and D Stirzaker. *Probability and Random Processes*. Oxford University Press, 4th edition, 2020.

[34] N G van Kampen. *Stochastic Processes in Physics and Chemistry*. Elsevier, 3rd edition, 2007.

[35] D S Lemons and A Gythiel. Paul Langevin's 1908 paper "On the theory of Brownian motion" ["sur la théorie du mouvement brownien," C. R. Acad. Sci. (Paris) 146, 530 (1908)]. *American Journal of Physics*, 65:1079, 1997.

[36] Bernt K. Øksendal. *Stochastic Differential Equations: an Introduction with Applications*. Springer, 6th edition, 2003.

[37] R Stinchcombe. Stochastic non-equilibrium systems. *Advances in Physics*, 50:431, 2001.

[38] E Seneta. *Non-negative Matrices: an Introduction to Theory and Applications*. Allen & Unwin, 1973.

[39] S Ramaswamy. The mechanics and statistics of active matter. *Annual Review of Condensed Matter Physics*, 1:323, 2010.

[40] M C Marchetti, J F Joanny, S Ramaswamy, T B Liverpool, J Prost, M Rao, and R A Simha. Hydrodynamics of soft active matter. *Reviews of Modern Physics*, 85:1143, 2013.

[41] M E Cates and J Tailleur. Motility-induced phase separation. *Annual Review of Condensed Matter Physics*, 6:219, 2015.

[42] J Elgeti, R G Winkler, and G Gompper. Physics of microswimmers – single particle motion and collective behavior: a review. *Reports on Progress in Physics*, 78:056601, 2015.

[43] C Bechinger, R Di Leonardo, H Löwen, C Reichhardt, G Volpe, and G Volpe. Active particles in complex and crowded environments. *Reviews of Modern Physics*, 88, 2016.

[44] T Vicsek, A Czirók, E Ben-Jacob, I Cohen, and O Shochet. Novel type of phase transition in a system of self-driven particles. *Physical Review Letters*, 75:1226, 1995.

[45] J Toner and Y Tui. Long-range order in a two-dimensional dynamical XY model: how birds fly together. *Physical Review Letters*, 75:4326, 1995.

[46] J Toner and Y Tui. Flocks, herds, and schools: a quantitative theory of flocking. *Physical Review E*, 58:4828, 1998.

[47] J M Kosterlitz and D J Thouless. Ordering, metastability and phase transitions in two-dimensional systems. *Journal of Physics C: Solid State Physics*, 6:1181, 1973.

[48] N D Mermin and H Wagner. Absence of ferromagnetism or antiferromagnetism in one- or two-dimensional isotropic Heisenberg models. *Physical Review Letters*, 17:1133, 1966.

[49] S Coleman. There are no Goldstone bosons in two dimensions. *Communications in Mathematical Physics*, 31:259, 1973.

[50] E Bertin, M Droz, and G Grégoire. Boltzmann and hydrodynamic description for self-propelled particles. *Physical Review E*, 74:022101, 2006.

[51] T Ihle. Kinetic theory of flocking: derivation of hydrodynamic equations. *Physical Review E*, 83:030901, 2011.

[52] A G Thompson, J Tailleur, M E Cates, and R A Blythe. Lattice models of nonequilibrium bacterial dynamics. *Journal of Statistical Mechanics: Theory and Experiment*, 2011:P02029, 2011.

[53] R Soto and R Golestanian. Run-and-tumble dynamics in a crowded environment: persistent exclusion process for swimmers. *Physical Review E*, 89:012706, 2014.

[54] A B Slowman, M R Evans, and R A Blythe. Jamming and attraction of interacting run-and-tumble random walkers. *Physical Review Letters*, 116: 218101, 2016.

[55] H C Berg and D A Brown. Chemotaxis in *Escherichia coli* analysed by three-dimensional tracking. *Nature*, 239:500, 1972.

[56] H C Berg and R A Anderson. Bacteria swim by rotating their flagellar filaments. *Nature*, 245:380–382, 1973.

[57] M J Schnitzer. Theory of continuum random walks and application to chemotaxis. *Physical Review E*, 48:2553, 1993.

[58] J Tailleur and M E Cates. Statistical mechanics of interacting run-and-tumble bacteria. *Physical Review Letters*, 100:218103, 2008.

[59] R M Donlan. Biofilms: microbial life on surfaces. *Emerging Infectious Diseases*, 8:881, 2002.

[60] P Stoodley, L Hall-Stoodley, and J W Costerton. Bacterial biofilms: from the natural environment to infectious diseases. *Nature Reviews Microbiology*, 2:95, 2004.

[61] H-C Flemming, J Wingender, U Szewzyk, P Steinberg, S A Rice, and S Kjelleberg. Biofilms: an emergent form of bacterial life. *Nature Reviews Microbiology*, 14:563, 2016.

[62] E Mallmin, R A Blythe, and M R Evans. Exact spectral solution of two interacting run-and-tumble particles on a ring lattice. *Journal of Statistical Mechanics: Theory and Experiment*, 2019:013204, 2019.

[63] A B Slowman, M R Evans, and R A Blythe. Exact solution of two interacting run-and-tumble random walkers with finite tumble duration. *Journal of Physics A: Mathematical and Theoretical*, 50:375601, 2017.

[64] D Saintillan and M J Shelley. Instabilities and pattern formation in active particle suspensions: kinetic theory and continuum simulations. *Physical Review Letters*, 100:178103, 2008.

[65] D Saintillan and M J Shelley. Instabilities, pattern formation, and mixing in active suspensions. *Physics of Fluids*, 20:123304, 2008.

[66] G Subramanian and D L Koch. Critical bacterial concentration for the onset of collective swimming. *Journal of Fluid Mechanics*, 632:359, 2009.

[67] D Saintillan and M J Shelley. *Complex Fluids in Biological Systems: Experiment, Theory, and Computation*, chapter 9: Theory of Active Suspensions, page 319. Springer, 2015.

[68] M Doi and S F Edwards. *The Theory of Polymer Dynamics*. Oxford University Press, 1988.

[69] M Gardner. The fantastic combinations of John Conway's new solitaire game 'Life'. *Scientific American*, 223:120, 1970.

[70] A Adamatzky. *Game of Life Cellular Automata*. Springer, 2010.

[71] B Chopard and M Droz. *Cellular Automata Modelling of Physical Systems*. Cambridge University Press, 1998.

[72] P Sarkar. A brief history of cellular automata. *ACM Computing Surveys*, 32:80, 2000.

[73] E R Berlekamp, J H Conway, and R K Guy. *Winning Ways for Your Mathematical Plays*, volume 4. Routledge, 2nd edition, 2004.

[74] J von Neumann. The general and logical theory of automata. In *Cerebral Mechanisms in Behavior: the Hixon Symposium / edited by L A Jeffress*, page 1. Wiley, 1951.

[75] S Ulam. On some mathematical problems connected with patterns of growth of figures. In *Proceedings of Symposia in Applied Mathematics*, volume 14, page 215. American Mathematical Society, 1962.

[76] A Ilachinski. *Cellular Automata: a Discrete Universe*. World Scientific Publishing Company, 2001.

[77] S Wolfram. Statistical mechanics of cellular automata. *Reviews of Modern Physics*, 55:601, 1983.

[78] S Wolfram. Cellular automata as models of complexity. *Nature*, 311:419, 1984.

[79] S Wolfram. Universality and complexity in cellular automata. *Physica D: Nonlinear Phenomena*, 10:1, 1984.

[80] O Martin, A M Odlyzko, and S Wolfram. Algebraic properties of cellular automata. *Communications in Mathematical Physics*, 93:219, 1984.

[81] S Wolfram. *A new kind of science*. Wolfram Media Inc, 2002.

[82] U Frisch, B Hasslacher, and Y Pomeau. Lattice-gas automata for the Navier-Stokes equation. *Physical Review Letters*, 56:1505, 1986.

[83] S Wolfram. Cellular automaton fluids 1: basic theory. *Journal of Statistical Physics*, 45:471, 1986.

[84] D d'Humieres, P Lallemand, and U Frisch. Lattice gas models for 3d hydrodynamics. *Europhysics Letters*, 2:291, 1986.

[85] D A Wolf-Gladrow. *Lattice-gas Cellular Automata and Lattice Boltzmann Models: an Introduction*. Springer, 2004.

[86] G Y Vichniac. Simulating physics with cellular automata. *Physica D: Nonlinear Phenomena*, 10:96, 1984.

[87] J Krug and H Spohn. Universality classes for deterministic surface growth. *Physical Review A*, 38:4271, 1988.

[88] D E Wolf, M Schreckenberg, and A Bachem. *Traffic and granular flow*. World Scientific, 1996.

[89] K Nagel and H J Herrmann. Deterministic models for traffic jams. *Physica A: Statistical Mechanics and its Applications*, 199:254, 1993.

[90] R Fisch, J Gravner, and D Griffeath. Threshold-range scaling of excitable cellular automata. *Statistics and Computing*, 1:23, 1991.

[91] J Gravner and D Griffeath. Threshold growth dynamics. *Transactions of the American Mathematical Society*, page 837, 1993.

[92] P Bak, K Chen, and C Tang. A forest-fire model and some thoughts on turbulence. *Physics Letters A*, 147:297, 1990.

[93] B Drossel and F Schwabl. Self-organized critical forest-fire model. *Physical Review Letters*, 69:1629, 1992.

[94] P Grassberger. Critical behaviour of the Drossel-Schwabl forest-fire model. *New Journal of Physics*, 4:17, 2002.

[95] B Chopard. A cellular automata model of large-scale moving objects. *Journal of Physics A: Mathematical and General*, 23:1671, 1990.

[96] B W-C Chan. Lenia: biology of artificial life. *Complex Systems*, 28:251, 2019.

[97] B W-C Chan. Lenia and expanded universe. In *ALIFE 2020: The 2020 Conference on Artificial Life*, page 221, 2020.

[98] M A Bedau, J S McCaskill, N H Packard, S Rasmussen, C Adami, D G Green, T Ikegami, K Kaneko, and T S Ray. Open problems in artificial life. *Artificial Life*, 6:363, 2000.

[99] S Redner. *A Guide to First-passage Processes*. Cambridge University Press, 2001.

[100] S Redner. A first look at first-passage processes. *Physica A: Statistical Mechanics and its Applications*, page 128545, 2023.

[101] H S Wilf. *Generatingfunctionology*. Academic Press, 1990.

[102] H Prodinger. The kernel method: a collection of examples. *Séminaire Lotharingien de Combinatoire*, 50:19, 2004.

[103] M E J Newman and G T Barkema. *Monte Carlo Methods in Statistical Physics*. Clarendon Press, 1999.

[104] D T Gillespie. Exact stochastic simulation of coupled chemical reactions. *Journal of Physical Chemistry*, 81:2340, 1977.

[105] R Furth. Analysis on the Brownian motion of a single particle. *Annalen der Physik*, 53:177, 1917.

[106] G I Taylor. Diffusion by continuous movements. *Proceedings of the London Mathematical Society*, 20:196, 1922.

[107] S Goldstein. On diffusion by discontinuous movements, and on the telegraph equation. *The Quarterly Journal of Mechanics and Applied Mathematics*, 4:129, 1951.

[108] Marián Boguñá, Josep M. Porrà, and Jaume Masoliver. Generalization of the persistent random walk to dimensions greater than 1. *Physical Review E*, 58:6992, 1998.

[109] M Boguñá, J M Porrà, and J Masoliver. Persistent random walk model for transport through thin slabs. *Physical Review E*, 59:6517, 1999.

[110] M Miri and H Stark. Persistent random walk in a honeycomb structure: light transport in foams. *Physical Review E*, 68:031102, 2003.

[111] M Miri and H Stark. Modelling light transport in dry foams by a coarse-grained persistent random walk. *Journal of Physics A: Mathematical and General*, 38:3743, 2005.

[112] S Fujita, Y Okamura, and J T Chen. Theory of polymer conformation based on the correlated walk model. *The Journal of Chemical Physics*, 72: 3993, 1980.

[113] D Bhat and M Gopalakrishnan. Memory, bias, and correlations in bidirectional transport of molecular-motor-driven cargoes. *Physical Review E*, 88:042702, 2013.

[114] H Wu, B-L Li, T A Springer, and W H Neill. Modelling animal movement as a persistent random walk in two dimensions: expected magnitude of net displacement. *Ecological Modelling*, 132:115, 2000.

[115] L Angelani, R Di Leonardo, and M Paoluzzi. First-passage time of run-and-tumble particles. *The European Physical Journal E*, 37:59, 2014.

[116] E Mallmin, R A Blythe, and M R Evans. A comparison of dynamical fluctuations of biased diffusion and run-and-tumble dynamics in one dimension. *Journal of Physics A: Mathematical and Theoretical*, 52:425002, 2019.

[117] K Malakar, V Jemseena, A Kundu, K V Kumar, S Sabhapandit, S N Majumdar, S Redner, and A Dhar. Steady state, relaxation and first-passage properties of a run-and-tumble particle in one-dimension. *Journal of Statistical Mechanics: Theory and Experiment*, page 043215, 2018.

[118] K Malakar, A Das, A Kundu, K V Kumar, and A Dhar. Steady state of an active Brownian particle in a two-dimensional harmonic trap. *Physical Review E*, 101:022610, 2020.

[119] F Mori, P Le Doussal, S N Majumdar, and G Schehr. Universal survival probability for a d-dimensional run-and-tumble particle. *Physical Review Letters*, 124:090603, 2020.

[120] A K Hartmann, S N Majumdar, H Schawe, and G Schehr. The convex hull of the run-and-tumble particle in a plane. *Journal of Statistical Mechanics: Theory and Experiment*, 2020:053401, 2020.

[121] K Proesmans, R Toral, and C van den Broeck. Phase transitions in persistent and run-and-tumble walks. *Physica A: Statistical Mechanics and its Applications*, 552:121934, 2019.

[122] M E Cates. Active field theory. In *Active Matter and Nonequilibrium Statistical Physics*, volume 112 of *Lecture Notes of the Les Houches Summer School*, page 180. Oxford University Press, 2022.

[123] A Das, A Dhar, and A Kundu. Gap statistics of two interacting run and tumble particles in one dimension. *Journal of Physics A: Mathematical and Theoretical*, 53:345003, 2020.

[124] N Sepúlveda and R Soto. Coarsening and clustering in run-and-tumble dynamics with short-range exclusion. *Physical Review E*, 94:022603, 2016.

[125] M Kourbane-Houssene, C Erignoux, T Bodineau, and J Tailleur. Exact hydrodynamic description of active lattice gases. *Physical Review Letters*, 120:268003, 2018.

[126] B Partridge and C F Lee. Critical motility-induced phase separation belongs to the Ising universality class. *Physical Review Letters*, 123:068002, 2019.

[127] S Zhang, A Chong, and B D Hughes. Persistent exclusion processes: inertia, drift, mixing, and correlation. *Physical Review E*, 100:042415, 2019.

[128] C Reichhardt and C J O Reichhardt. Directional locking effects for active matter particles coupled to a periodic substrate. *Physical Review E*, 102: 042616, 2020.

[129] A Manacorda and A Puglisi. Lattice model to derive the fluctuating hydrodynamics of active particles with inertia. *Physical Review Letters*, 119:208003, 2017.

[130] S Chatterjee, M Mangeat, and H Rieger. Polar flocks with discretized directions: the active clock model approaching the Vicsek model. *Europhysics Letters*, 138:41001, 2022.

[131] J E Bresenham. Algorithm for computer control of a digital plotter. *IBM Systems Journal*, 4:25, 1965.

[132] K Y Wan and R E Goldstein. Time irreversibility and criticality in the motility of a flagellate microorganism. *Physical Review Letters*, 121:058103, 2018.

[133] Y Fily and M C Marchetti. Athermal phase separation of self-propelled particles with no alignment. *Physical Review Letters*, 108:235702, 2012.

[134] G S Redner, M F Hagan, and A Baskaran. Structure and dynamics of a phase-separating active colloidal fluid. *Physical Review Letters*, 110:055701, 2013.

[135] G M Schütz, R Ramaswamy, and M Barma. Pairwise balance and invariant measures for generalized exclusion processes. *Journal of Physics A: Mathematical and General*, 29:837, 1996.

[136] M Alimohammadi, V Karimipour, and M Khorrami. Exact solution of a one-parameter family of asymmetric exclusion processes. *Physical Review E*, 57:6370, 1998.

[137] M D Jara. Non-equilibrium scaling limit for a tagged particle in the simple exclusion process with long jumps. *Communications on Pure and Applied Mathematics*, 62:198, 2007.

[138] C Bernardin and B O Jimenez. Fractional Fick's law for the boundary driven exclusion process with long jumps. *Latin American Journal of Probability and Mathematical Statistics*, 14:473, 2017.

[139] G H Weiss and R J Rubin. Random walks: theory and selected applications. *Advances in Chemical Physics*, 52:363, 1983.

[140] D Chowdhury, L Santen, and A Schadschneider. Statistical physics of vehicular traffic and some related systems. *Physics Reports*, 329:199, 2000.

[141] D Helbing. Traffic and related self-driven many-particle systems. *Reviews of Modern Physics*, 73:1067, 2001.

[142] T Chou, K Mallick, and R K P Zia. Non-equilibrium statistical mechanics: from a paradigmatic model to biological transport. *Reports on Progress in Physics*, 74:116601, 2011.

[143] A Bobenko, M Bordemann, C Gunn, and U Pinkall. On two integrable cellular automata. *Communications in Mathematical Physics*, 158:127, 1993.

[144] J W P Wilkinson, T Prosen, and J P Garrahan. Exact solution of the "rule 150" reversible cellular automaton. *Physical Review E*, 105:034124, 2022.

[145] T Prosen and C Mejía-Monasterio. Integrability of a deterministic cellular automaton driven by stochastic boundaries. *Journal of Physics A: Mathematical and Theoretical*, 49:185003, 2016.

[146] B Buča, K Klobas, and T Prosen. Rule 54: exactly solvable model of nonequilibrium statistical mechanics. *Journal of Statistical Mechanics: Theory and Experiment*, 2021:074001, 2021.

[147] T Prosen and B Buča. Exact matrix product decay modes of a boundary driven cellular automaton. *Journal of Physics A: Mathematical and Theoretical*, 50:395002, 2017.

[148] A Inoue and S Takesue. Two extensions of exact nonequilibrium steady states of a boundary-driven cellular automaton. *Journal of Physics A: Mathematical and Theoretical*, 51:425001, 2018.

[149] B Buča, J P Garrahan, T Prosen, and M Vanicat. Exact large deviation statistics and trajectory phase transition of a deterministic boundary driven cellular automaton. *Physical Review E*, 100:020103, 2019.

[150] S Gopalakrishnan and B Zakirov. Facilitated quantum cellular automata as simple models with non-thermal eigenstates and dynamics. *Quantum Science and Technology*, 3:044004, 2018.

[151] J W P Wilkinson, K Klobas, T Prosen, and J P Garrahan. Exact solution of the Floquet-PXP cellular automaton. *Physical Review E*, 102:062107, 2020.

[152] G H Fredrickson and H C Andersen. Kinetic Ising model of the glass transition. *Physical Review Letters*, 53:1244, 1984.

[153] L Causer, I Lesanovsky, M C Bañuls, and J P Garrahan. Dynamics and large deviation transitions of the XOR-Fredrickson-Andersen kinetically constrained model. *Physical Review E*, 102:052132, 2020.

[154] P G Drazin and R S Johnson. *Solitons: an Introduction*. Cambridge University Press, 2nd edition, 1989.